Measurement of the Branching Fraction and Time Dependent CP Asymmetry in $\mathrm{B}^0 \to \mathrm{D}^{*-}\mathrm{D}^{*+}\mathrm{K}^0_\mathrm{S}$ Decays at the Belle Experiment

Martin Ritter

München 2013

Measurement of the Branching Fraction and Time Dependent CP Asymmetry in $\mathrm{B}^0 \to \mathrm{D}^{*-}\mathrm{D}^{*+}\mathrm{K}^0_\mathrm{S}$ Decays at the Belle Experiment

Martin Ritter

Dissertation
an der Physik
der Ludwig–Maximilians–Universität
München

vorgelegt von
Martin Ritter
aus Landsberg am Lech

München, den 29.11.2013

Erstgutachter: Prof. Dr. Christian Kiesling
Zweitgutachter: Prof. Dr. Jochen Schieck
Tag der mündlichen Prüfung: 25.02.2014

Contents

Zusammenfassung

Warum existieren wir? CP-Verletzung ist ein integraler Bestandteil dieser Frage, da ihr Verständnis notwendig ist, um die in unserem Universum beobachtete Asymmetrie zwischen Materie und Antimaterie zu erklären. Dementsprechend wurden bereits mehrere Experimente zur Vermessung der CP-Verletzung geplant und auch durchgeführt. Mit Belle II wird bald ein weiteres Experiment diese Messungen verbessern. Belle II basiert auf dem Design des erfolgreichen Belle Experimentes am KEKB Beschleuniger, der mit einer Luminosität von $2.11 \times 10^{34}\,\mathrm{cm}^{-2}\mathrm{s}^{-1}$ momentan den Weltrekord hält.

Das System der B-Mesonen weist eine sehr reichhaltige Zerfallsstruktur auf und viele dieser Zerfallskanäle und ihre CP-Asymmetrie wurden bereits von Belle vermessen. Der bekannteste davon, $\mathrm{B}^0 \to \mathrm{J}/\psi\mathrm{K}^0_\mathrm{S}$, erlaubt eine präzise Vermessung von $\sin 2\phi_1$. Dieses Ergebnis hinterlässt aber eine zweifache Ambiguität für den Wert des Winkels ϕ_1 im CKM-Dreieck. Der Zerfallskanal $\mathrm{B}^0 \to \mathrm{D}^{*-}\mathrm{D}^{*+}\mathrm{K}^0_\mathrm{S}$ ist zwar experimentell wesentlich herausfordernder, erlaubt aber auch die Messung von $\cos 2\phi_1$ um diese Ambiguität aufzulösen.

In den ersten Kapiteln dieser Arbeit werden wir das Prinzip dieser Messung vorstellen und präsentieren die Ergebnisse für die Messung des Verzweigungsverhältnisses und der zeitabhängigen CP-Verletzungs-Parameter mit den endgültigen Daten des Belle Experiments. Diese enthalten 772 Millionen $\mathrm{B\overline{B}}$ Paare, aufgezeichnet an der $\Upsilon(4\mathrm{S})$ Resonanz. Für das Verzweigungsverhältnis erhalten wir einen Wert von

$$\mathcal{B}\Big(\mathrm{B}^0 \to \mathrm{D}^{*-}\mathrm{D}^{*+}\mathrm{K}^0_\mathrm{S}\Big) = \Big(5.35^{+0.35}_{-0.34}(\mathrm{stat}) \pm 0.57(\mathrm{syst})\Big) \times 10^{-3},$$

welcher mit dem aktuellen, weltweiten Mittelwert gut übereinstimmt. Aus einem Drei-Parameter-Fit, sensitiv auf $\cos 2\phi_1$, extrahieren wir in der zur Zeit präzisesten Messung die CP-Parameter

$$\begin{aligned} J_c/J_0 &= 0.37 \pm 0.10(\mathrm{stat}) \pm 0.02(\mathrm{syst}), \\ (2J_{s1}/J_0)\sin(2\phi_1) &= 0.30 \pm 0.16(\mathrm{stat}) \pm 0.03(\mathrm{syst}), \\ (2J_{s2}/J_0)\cos(2\phi_1) &= 0.16 \pm 0.16(\mathrm{stat}) \pm 0.03(\mathrm{syst}). \end{aligned}$$

Mit diesem Ergebnis können wir, unter der Annahme, dass $(2J_{s2}/J_0)$ positiv ist, einen negativen Wert von $\cos 2\phi_1$ mit einer Sicherheit von 85 % ausschliessen.

Schlussendlich beschreiben wir die Implementierung der Vertexdetektorgeometrie für das Belle II Experiment. Diese Fortführung des Belle Experiments soll die integrierte Luminosität vom Belle um einen Faktor 50 erhöhen und erhält unter anderem einen neuen Vertexdetektor. Um Ereignisse korrekt simulieren zu können, ist eine präzise Beschreibung der Sensorgeometrie und des Detektormaterials notwendig.

Abstract

Why do we exist? CP violation is an integral part of this question as its understanding is crucial to explain the matter-antimatter asymmetry observed in our universe. Several experiments were designed and carried out to precisely measure CP violation, especially in the B meson system where large asymmetries where predicted and found. With Belle II and LHCb, two new experiments are going to improve the existing measurements. Belle II will be based on the very successful Belle experiment at the KEKB collider, currently holding the world record on luminosity with $2.11 \times 10^{34}\,\mathrm{cm}^{-2}\mathrm{s}^{-1}$.

The B meson system has a very rich decay topology and many of theses decay modes and their CP asymmetry parameters have already been measured at Belle. The most famous decay channel, $\mathrm{B}^0 \to \mathrm{J}/\psi\mathrm{K}^0_\mathrm{S}$, poses very tight constraints on $\sin 2\phi_1$ but leaves a twofold ambiguity on the actual value of the angle ϕ_1 in the CKM triangle. The decay mode $\mathrm{B}^0 \to \mathrm{D}^{*-}\mathrm{D}^{*+}\mathrm{K}^0_\mathrm{S}$, while experimentally much more challenging, offers the unique possibility to also extract $\cos 2\phi_1$ and thus resolve this ambiguity.

In the first chapters of this thesis we present the principle of this measurement and the results for the branching fraction and the time-dependent CP violation parameters of $\mathrm{B}^0 \to \mathrm{D}^{*-}\mathrm{D}^{*+}\mathrm{K}^0_\mathrm{S}$ decays. These results are obtained from the final data sample of the Belle experiment containing 772 million $\mathrm{B\overline{B}}$ pairs collected at the $\Upsilon(4\mathrm{S})$ resonance with the Belle detector at the KEKB asymmetric-energy e^+ e^-– collider.

We obtain the branching fraction

$$\mathcal{B}\Big(\mathrm{B}^0 \to \mathrm{D}^{*-}\mathrm{D}^{*+}\mathrm{K}^0_\mathrm{S}\Big) = \Big(5.35^{+0.35}_{-0.34}(\mathrm{stat}) \pm 0.57(\mathrm{syst})\Big) \times 10^{-3},$$

which is in agreement with the current world average. In a 3 parameter fit sensitive to $\cos 2\phi_1$, we extract the currently most precise values for the CP parameters

$$\begin{aligned} J_c/J_0 &= 0.37 \pm 0.10(\mathrm{stat}) \pm 0.02(\mathrm{syst}), \\ (2J_{s1}/J_0)\sin(2\phi_1) &= 0.30 \pm 0.16(\mathrm{stat}) \pm 0.03(\mathrm{syst}), \\ (2J_{s2}/J_0)\cos(2\phi_1) &= 0.16 \pm 0.16(\mathrm{stat}) \pm 0.03(\mathrm{syst}). \end{aligned}$$

This allows us to exclude a negative value for $\cos 2\phi_1$ at a 85 % confidence under the assumption that that $(2J_{s2}/J_0)$ is positive.

Finally, we describe the implementation of the vertex detector geometry for the upcoming Belle II experiment. The upgrade to Belle aims to increase the integrated luminosity by a factor of 50 and will receive, among other upgrades, a completely new vertex detector. To produce simulated events, a precise description of the sensor geometry and material budget is needed.

Introduction

Over the last 30 years, particle physics has been a very vivid and successful area of research, revealing many fundamental and interesting aspects of our universe. Yet many unresolved mysteries remain.

Cosmology and field theory predict that the universe was created in a Big Bang, with extremely high temperatures, way beyond the energy scales achievable by present-day accelerators. This initial ultra-high energy density inevitably gives rise to the creation of particle-antiparticle pairs which leads to two possible scenarios: either the particle-antiparticle pairs could annihilate, ultimately leaving a sea of photons in which we could not exist, or there should be equal amounts of matter and antimatter, somehow separated to prevent annihilation. Yet, although the observed proton to photon ratio is about 10^{-9}, no evidence for significant amounts of antimatter could be established over cosmological distances. Thus, the excess of matter over antimatter has to be explained by an asymmetry between the way matter and antimatter interact. In 1976, Sakharov formulated a mechanism to generate this cosmological matter asymmetry based on three conditions [1]:

- Non-conservation of baryonic charge
- Deviation from the thermal equilibrium
- Breaking of the matter-antimatter symmetry (breaking of the C and CP symmetry)

The Standard Model (SM) of particle physics describes the known elementary particles and their interactions very successfully and has been verified with high precision [2]. It contains three generations of fermions: quarks and leptons which are the fundamental matter particles and possess spin $\frac{1}{2}$. These particles exchange field quanta, called gauge bosons, which mediate the forces between them. They follow from local gauge invariance according to the symmetry group of the SM, $SU_C(3) \times SU_L(2) \times U_Y(1)$.

Although the SM has been verified to a high degree of precision there are still some tensions and aspects which are not completely satisfactory, including the large number of parameters which can only be deduced by experiments, like for example the ones needed for the flavour mixing; or the fact that the SM does not describe the Dark Matter and the Dark Energy and thus only accounts for approx. 5 % of the known universe [3–5].

CP violation was discovered in 1964 in the Kaon system [6] and could be integrated into the SM in 1972 by Kobayashi and Maskawa using only one CP-violating phase, the KM phase [7]. Since this formalism is only possible for more than two quark generations,

they predicted a minimum of three quarks in addition to the three quarks known at that time. Then in 1980, based on the observation of a surprisingly long lifetime of the B mesons, Bigi, Carter and Sanda pointed out that the $B^0\overline{B}^0$ system may show large time-dependent CP asymmetries [8–10]. Two dedicated experiments where commissioned to explore these asymmetries: BABAR [11] in the USA and Belle [12] in Japan. And indeed, a large CP violation in the B meson sector was observed by 2001 in $B^0 \to J/\psi K^0_S$ decays by both collaborations [13, 14]. This measurement is sensitive to $\sin(2\phi_1)$ so a twofold ambiguity $\phi_1 \to \pi/2 - \phi_1$ remains. The decay mode $B^0 \to D^{*-}D^{*+}K^0_S$ addresses this ambiguity. Although it is experimentally much more challenging than $B^0 \to J/\psi K^0_S$, theory shows that it might allow to extract $\cos(2\phi_1)$ and solve the ambiguity on ϕ_1.

As it can be shown [15] that the amount of CP violation in the SM cannot explain the observed matter-antimatter asymmetry and new sources of CP violation are needed besides the single KM phase now present in the SM:. These sources could enter the observed CP asymmetries via loop diagrams. This makes CP violation sensitive to detect new physics in a range from 600 GeV to more than ~ 500 TeV, depending on the amount of flavour violation of these new physics [16]. But to challenge the SM, high precision measurements with very high statistics are needed. The planned upgrade to Belle, Belle II [17], will start operation in 2016 and increase the statistics from Belle by a factor of 50 till 2028. For this upgrade, a precise simulation of the detector response is needed which requires, among other things, a detailed description of the material of all sub-detectors.

In the following chapter, the principles of CP violation measurements will be presented and the reason to measure the decay channel $B^0 \to D^{*-}D^{*+}K^0_S$ will be motivated. An overview of the Belle experiment will be given in Chapter 2. In Chapter 3 we will describe the methods used to select and reconstruct $B^0 \to D^{*-}D^{*+}K^0_S$ events from the Belle data. The extraction of the branching fraction, $\mathcal{B}(B^0 \to D^{*-}D^{*+}K^0_S)$ will be presented in Chapter 4 and Chapter 5 shows the measurement of the time dependent CP violation in $B^0 \to D^{*-}D^{*+}K^0_S$ decays. Finally, Chapter 6 will give an outlook on the upcoming Belle II upgrade, focussing on the new vertex detector and the implementation of its geometry in the simulation.

Chapter 1

Physics motivation

In this chapter, the basic principles of CP violation measurements are developed. Starting with a short introduction about basic symmetry operations, the time evolution of neutral mesons is discussed. The principles of CP violation will be presented and the observables will be defined. A brief outline of the experimental techniques utilized to measure these observables is given.

1.1 C, P and T Symmetry

Symmetries are very important in physics since every operation which leaves a system invariant corresponds to a conservation law according to Noether's theorem [18]. For example, rotational symmetry corresponds to the conservation of angular momentum and invariance under translations in space or time corresponds to the conservation laws of momentum and energy, respectively. Important discrete symmetries in the Standard Model (SM) are the Charge C, Parity P and Time Conjugation T:

Charge conjugation transforms a particle q into its antiparticle $\overline{q}$, leaving mass, momentum and spin invariant, but inverting the quantum numbers like flavour and electric charge

$$C\,|q\rangle = |\overline{q}\rangle \tag{1.1}$$

Parity transformation is a discrete operation which mirrors the physical system in space, thus the coordinate $\boldsymbol{x}$, momentum $\boldsymbol{p}$ and angular momentum $\boldsymbol{l} \equiv \boldsymbol{x} \times \boldsymbol{p}$ transform as follows:

$$\boldsymbol{x} \xrightarrow{P} -\boldsymbol{x} \qquad \boldsymbol{p} \xrightarrow{P} -\boldsymbol{p} \qquad \boldsymbol{l} \xrightarrow{P} \boldsymbol{l} \tag{1.2}$$

It can be seen that we can distinguish between two types of vectors: Polar vectors $\boldsymbol{V}$ that change their sign and axial vectors $\boldsymbol{A}$ which are invariant under parity transformation. This also leads to the distinction of scalars $S = \boldsymbol{V} \cdot \boldsymbol{V} = \boldsymbol{A} \cdot \boldsymbol{A} \xrightarrow{P} S$ and pseudoscalars $P = \boldsymbol{V} \cdot \boldsymbol{A} \xrightarrow{P} -P$.

Time conjugation reflects t into $-t$ while leaving $\boldsymbol{x}$ unchanged, thus representing a reversal of motion

$$\boldsymbol{x} \xrightarrow{T} \boldsymbol{x} \qquad \boldsymbol{p} \xrightarrow{T} -\boldsymbol{p} \qquad \boldsymbol{l} \xrightarrow{T} -\boldsymbol{l} \tag{1.3}$$

Until the 1950s, P and C conservation were believed to be fundamental conservation laws like the conservations of energy and momentum. Trying to explain the $\theta - \tau$ puzzle in 1956, Tsung-Dao Lee and Chen Ning Yang pointed out that, while verified in strong and electromagnetic interactions, parity conservation was hitherto untested in weak decays [19]. They proposed several direct experimental tests and in the same year, Chien-Shiung Wu et al. demonstrated [20] that parity is violated maximally in weak decays, i.e. the weak interaction only couples to left-handed particles.

Soon after, Landau pointed out that the combined transformation CP and the time reversal T are still conserved [21]. This seemed to be very important since it can be shown quite generally that violation of CPT would also lead to a violation of Lorentz invariance. To be precise, the CPT theorem states that any Lorentz invariant local quantum field theory with a Hermitian Hamiltonian must preserve CPT symmetry [22]. Thus if CP is violated, also T needs to be broken to conserve CPT.

1.2 Flavour Physics

The SM describes the interaction of three generations of quarks and leptopns. The quarks consist of one up-type and one down-type quark in each generation. Each of these 6 quarks, which are shown in Figure 1.1, is assigned a quantum number called "flavour". These quantum numbers are conserved in electromagnetic and strong interaction, but not in the weak interaction. Cabibbo was the first to explain the long lifetimes of the strange particles, the kaons, by describing them as a mixing between the known quarks using only one free parameter, the Cabibbo angle $\theta_C = 13.04°$ [23]:

$$\begin{pmatrix} \mathrm{d}' \\ \mathrm{s}' \end{pmatrix} = \underbrace{\begin{pmatrix} \cos\theta_C & \sin\theta_C \\ -\sin\theta_C & \cos\theta_C \end{pmatrix}}_{\mathbf{V}^{\mathrm{C}}} \begin{pmatrix} \mathrm{d} \\ \mathrm{s} \end{pmatrix} \tag{1.4}$$

d', s' are the so called "flavour eigenstates" which are transformed into each other in weak interactions. Since the squared elements of $\mathbf{V}^{\mathrm{C}}$ describe the probability for one quark to transform into another flavour state, probability preservation dictates this matrix to be unitary. This mixing formalism can be extended to three quark generations as will be seen in Section 1.4.

1.3 Neutral Meson Mixing

In the Kaon system, decays of both K^0 and $\overline{\mathrm{K}}^0$ to the same final state were observed. This also requires the existence of a transition between K^0 and $\overline{\mathrm{K}}^0$. Since K^0 and $\overline{\mathrm{K}}^0$ have

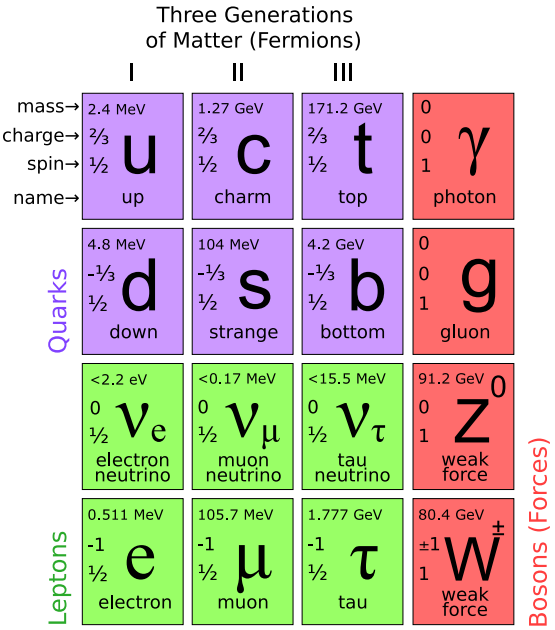

Figure 1.1: Particle-Generations in the Standard Model [24].

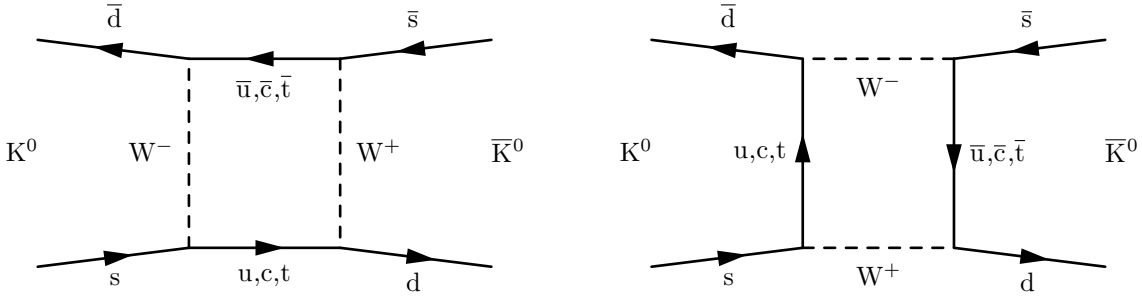

Figure 1.2: Leading Feynman diagrams contributing to Kaon-oscillation.

different flavour, this transition is called flavour mixing. As a consequence, these mesons may oscillate between particle and antiparticle before decaying, a process of second order in Weak Interactions. The two leading Feynman diagrams contributing to the Kaon oscillation are shown in Figure 1.2. This is a rare second order process due to the small value of the Fermi constant.

For the neutral Kaon system, this oscillation can be described by diagonalizing the Hamiltonian of the generic two-dimensional wave function

$$|\psi(t)\rangle = \psi_1(t)\,|\mathrm{K}^0\rangle + \psi_2(t)\,|\overline{\mathrm{K}}^0\rangle = \begin{pmatrix}\psi_1\\ \psi_2\end{pmatrix} \tag{1.5}$$

evolving in time according to the Schrödinger equation with the Hamiltonian $\mathbf{H}$ consisting

of the mass and decay matrices $\mathbf{M}$ and $\mathbf{\Gamma}$ [25, 26].

$$i\frac{d}{dt}\begin{pmatrix}\psi_1\\ \psi_2\end{pmatrix} = \left(\mathbf{M} - \frac{i}{2}\mathbf{\Gamma}\right)\begin{pmatrix}\psi_1\\ \psi_2\end{pmatrix} \tag{1.6}$$

The off-diagonal elements of this Hamiltonian are associated with flavour changing transitions, $\mathrm{K}^0 \leftrightarrow \overline{\mathrm{K}}^0$, so $H_{12} = H_{21}^*$ is required for CP to be conserved. Assuming that the K^0 couples to itself in the same way as the $\overline{\mathrm{K}}^0$, therefore assuming CPT-invariance, the diagonal elements have to be equal: $H_{11} = H_{22} = M - \frac{i}{2}\Gamma$. Diagonalizing the Hamiltonian yields two eigenvalues with their corresponding eigenstates

$$\mu_{1,2} = M - \frac{i}{2}\Gamma \pm \sqrt{\left(M_{12} - \frac{i}{2}\Gamma_{12}\right)\left(M_{12}^* - \frac{i}{2}\Gamma_{12}^*\right)} \tag{1.7}$$

$$\begin{aligned} |\mathrm{K}_1\rangle &= p\,|\mathrm{K}^0\rangle + q\,|\overline{\mathrm{K}}^0\rangle \quad \text{for } \mu_1 \\ |\mathrm{K}_2\rangle &= p\,|\mathrm{K}^0\rangle - q\,|\overline{\mathrm{K}}^0\rangle \quad \text{for } \mu_2 \end{aligned} \tag{1.8}$$

$$\text{with} \quad \frac{q}{p} = \sqrt{\frac{M_{12}^* - \frac{i}{2}\Gamma_{12}^*}{M_{12} - \frac{i}{2}\Gamma_{12}}} \quad \text{and the normalization} \quad \sqrt{p^2+q^2} = 1 \tag{1.9}$$

These eigenstates represent the physical mass-eigenstates. The masses and lifetimes for these states can be obtained from the eigenvalues

$$m_{1,2} = \mathrm{Re}(\mu_{1,2}) \qquad\qquad \Gamma_{1,2} = -2\,\mathrm{Im}(\mu_{1,2}) \tag{1.10}$$

If CP is conserved, it is evident that $p = q = 1$. From $CP\,|\mathrm{K}^0\rangle = |\overline{\mathrm{K}}^0\rangle$ follows

$$CP\,|\mathrm{K}_1\rangle = +\,|\mathrm{K}_1\rangle \qquad\qquad CP\,|\mathrm{K}_2\rangle = -\,|\mathrm{K}_2\rangle$$

Since $CP\,|2\pi\rangle = +\,|2\pi\rangle$ and $CP\,|3\pi\rangle = -\,|3\pi\rangle$, CP-invariance dictates

$$\mathrm{K}_1 \to 2\pi \nleftarrow \mathrm{K}_2 \quad \text{and} \quad \mathrm{K}_1 \nrightarrow 3\pi \leftarrow \mathrm{K}_2 \tag{1.11}$$

The mass difference $\Delta m = m_2 - m_1$ between K_1 and K_2 is a very small quantity $\Delta m_K/m_K \simeq 7 \times 10^{-15}$ and it is a remarkable achievement of experimental physics and quantum mechanics that it can be measured at all. The value for Δm can be determined by measuring the oscillation frequency.

The lifetime difference $\Delta\Gamma = \Gamma_1 - \Gamma_2$ is mainly governed by phase space. Since three pions have an invariant mass of about 420 MeV and the K^0 with about 500 MeV is only slightly larger, this decay is suppressed fo the Kaon system. The lifetime of the CP-odd state K_2 is roughly 600 times the lifetime of the CP-even state K_1, which can decay into $\pi\pi$. Assuming CP is conserved, the mass-eigenstates K_1 and K_2 were are also identified as CP eigenstates and the identifiers K_S^0 and K_L^0 were chosen for the short and the long lived state, respectively.

The derivation above can be applied without change to the heavier mesons D and B. Yet due to their higher masses no phase space restriction applies for the decay. The differences in lifetime for these mass eigenstates is negligible. Accordingly, the mass eigenstates in these systems are denoted with subscript H and L for the heavy and light states, respectively.

The time evolution of the mass eigenstates (or CP eigenstates if CP is conserved) for any neutral meson M is exponential in time and given by

$$\begin{aligned} |M_1(t)\rangle &= e^{-i\mu_1 t}\,|M_1\rangle = e^{-i(m_1-\frac{i}{2}\Gamma_1)t}\left(p\,|M^0\rangle + q\,|\overline{M}^0\rangle\right) \\ |M_2(t)\rangle &= e^{-i\mu_2 t}\,|M_2\rangle = e^{-i(m_2-\frac{i}{2}\Gamma_2)t}\left(p\,|M^0\rangle - q\,|\overline{M}^0\rangle\right) \end{aligned} \tag{1.12}$$

Using Eq. 1.8 we solve these equations to obtain the time evolution of M^0 and $\overline{M}^0$

$$\begin{aligned} |M^0(t)\rangle &= g_+(t)\,|M^0\rangle + \frac{q}{p} g_-(t)\,|\overline{M}^0\rangle \\ |\overline{M}^0(t)\rangle &= g_+(t)\,|\overline{M}^0\rangle + \frac{p}{q} g_-(t)\,|M^0\rangle \end{aligned} \tag{1.13}$$

with

$$g_\pm = \frac{1}{2}\left(e^{-i(m_1-\frac{i}{2}\Gamma_1)t} \pm e^{-i(m_2-\frac{i}{2}\Gamma_2)t}\right) \tag{1.14}$$

Quantitative results for the mixing probabilities for Kaons and B-mesons can be seen in Figure 1.3. One can clearly see the influence of the lifetime difference in the Kaon system, since this prevents full oscillation: An initial pure K^0 will never convert to a pure $\overline{\mathrm{K}}^0$, as opposed to the B system.

1.4 CP violation

In 1964, James Cronin, Val Fitch and co-workers found evidence of CP violation [6], winning the Nobel-Prize in 1980. They intended to set an upper limit to the branching fraction of $\mathrm{K}^0_\mathrm{L} \to \pi\pi$ but discovered a branching ratio of

$$\mathcal{B}\left(\mathrm{K}^0_\mathrm{L} \to \pi^+\pi^-\right) = (2.0 \pm 0.4) \times 10^{-3} \tag{1.15}$$

With CP violation established, the mixing parameters p and q are no longer equal, making it necessary to change the definition of K^0_S and K^0_L to be mixtures of the CP eigenstates with a small, complex mixing parameter ε

$$\begin{aligned} |\mathrm{K}^0_\mathrm{S}\rangle &= \frac{1}{\sqrt{1+|\varepsilon|^2}}\left(|\mathrm{K}_1\rangle - \varepsilon\,|\mathrm{K}_2\rangle\right) \\ |\mathrm{K}^0_\mathrm{L}\rangle &= \frac{1}{\sqrt{1+|\varepsilon|^2}}\left(|\mathrm{K}_1\rangle + \varepsilon\,|\mathrm{K}_2\rangle\right) \end{aligned} \tag{1.16}$$

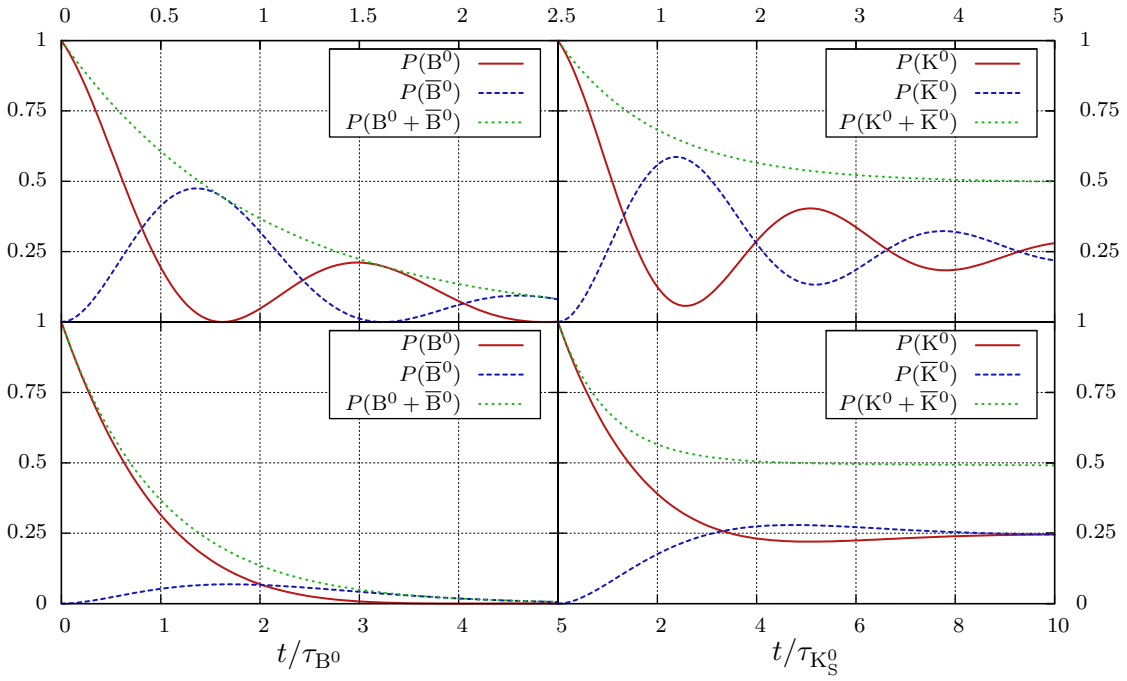

Figure 1.3: Mixing probability for a B^0 (left) and a K^0 (right) as functions of their lifetimes. The top row shows the probabilities for a Δm 5 times the measured value (bottom row).

With Equations 1.9 and 1.11, this leads to the following relations

$$p = \frac{1+\varepsilon}{\sqrt{2(1+|\varepsilon|^2)}} \qquad q = \frac{1-\varepsilon}{\sqrt{2(1+|\varepsilon|^2)}} \qquad \frac{p}{q} = \frac{1-\varepsilon}{1+\varepsilon} \tag{1.17}$$

To describe CP violation in the SM, an additional, irreducible complex phase has to be present in the flavour transition matrix. A unitary, complex $n \times n$ matrix contains n^2 free parameters, $2n-1$ of these represent global phases which are physically irrelevant. Apart from the $n(n-1)/2$ rotations, the number of remaining parameters which can contribute to CP violation is given by

$$n_{CP} = (n-1)(n-2)/2 \tag{1.18}$$

Thus CP violation cannot be explained with only two quark generations since this will leave only one real angle as parameter. Kobayashi and Maskawa postulated their model predicting 3 quark generations, which allows for one complex CP-violating phase, in 1972 [7]. This was two years before the discovery of the charm quark, five years before the discovery of the b-quark and 20 years before the discovery of the t-quark. For this work, after their scheme was verified with the B system, they were awarded the Nobel Prize in 2008.

Their model is an extension of the Cabibbo mixing (Eq. 1.4) for three generations

with a 3×3 mixing matrix, the CKM-matrix.

$$\begin{pmatrix} \mathrm{d}' \\ \mathrm{s}' \\ \mathrm{b}' \end{pmatrix} = \underbrace{\begin{pmatrix} V_{ud} & V_{us} & V_{ub} \\ V_{cd} & V_{cs} & V_{cb} \\ V_{td} & V_{ts} & V_{tb} \end{pmatrix}}_{\mathbf{C}_{CKM}} \begin{pmatrix} \mathrm{d} \\ \mathrm{s} \\ \mathrm{b} \end{pmatrix} \tag{1.19}$$

This CKM matrix has a non-vanishing complex phase (δ_{13}) and three real Euler angles θ_{12}, θ_{23}, θ_{13}. The standard parametrization [3] of this matrix is given by

$$\mathbf{C}_{CKM} = \begin{pmatrix} c_{12}c_{13} & s_{12}c_{13} & s_{13}e^{-i\delta_{13}} \\ -s_{12}c_{23} - c_{12}s_{23}s_{13}e^{i\delta_{13}} & c_{12}c_{23} - s_{12}s_{23}s_{13}e^{i\delta_{13}} & s_{23}c_{13} \\ s_{12}s_{23} - c_{12}c_{23}s_{13}e^{i\delta_{13}} & -c_{12}s_{23} - s_{12}c_{23}s_{13}e^{i\delta_{13}} & c_{23}c_{13} \end{pmatrix} \tag{1.20}$$

where s_{ij} and c_{ij} are the sines and the cosines of the three mixing angles θ_{12}, θ_{23}, θ_{13}. The angle θ_{12} is identical to the Cabibbo angle $\theta_C = 13.04°$. The structure of CP violation can better be seen in the Wolfenstein representation [27], which expands the CKM matrix in orders of $\lambda = \sin\theta_c = 0.2257^{+0.0009}_{-0.0010}$ and is written in terms of three other parameters $A = 0.814^{+0.814}_{-0.022}$, $\rho = 0.135^{+0.031}_{-0.016}$ and $\eta = 0.349^{+0.015}_{-0.017}$. This parametrization is unitary to all orders of λ [3].

$$\mathbf{C}_{CKM} = \begin{pmatrix} 1 - \lambda^2/2 & \lambda & A\lambda^3(\rho - i\eta) \\ -\lambda & 1 - \lambda^2/2 & A\lambda^2 \\ A\lambda^3(1 - \rho - i\eta) & -A\lambda^2 & 1 \end{pmatrix} + \mathcal{O}(\lambda^4) \tag{1.21}$$

1.4.1 Unitarity Triangle

The unitarity requirement for the CKM matrix can be used to establish relations among the different matrix elements, such as

$$\sum_k V_{ik} V_{jk}^* = 0 \tag{1.22}$$

Since the matrix contains complex values, these constraints can be visualized as triangles in the complex plane with the sides $V_{ik}V_{jk}^*$. It can be shown that all unitarity triangles have the same area [28], which is proportional to the amount of CP violation in the SM. By looking at the Wolfenstein parametrization one can see that this triangle is almost degenerate for the relations between adjacent columns. Whereas the sides of the triangle

$$\underset{\mathcal{O}(\lambda^3)}{V_{ud}V_{ub}^*} + \underset{\mathcal{O}(\lambda^3)}{V_{cd}V_{cb}^*} + \underset{\mathcal{O}(\lambda^3)}{V_{td}V_{tb}^*} = 0 \tag{1.23}$$

are all of the same order in λ. Therefore, the angles in this triangle have to be naturally large. Due to this, [8–10] predicted large CP asymmetries for some decay of B mesons due to the comparable size of the decay and oscillation amplitudes.

It is convenient to normalize this triangle by the real number ($V_{cd}V_{cb}^*$), which results in this side being exactly $(0, 0)$ to $(1, 0)$ in the complex plane. Since the imaginary part of

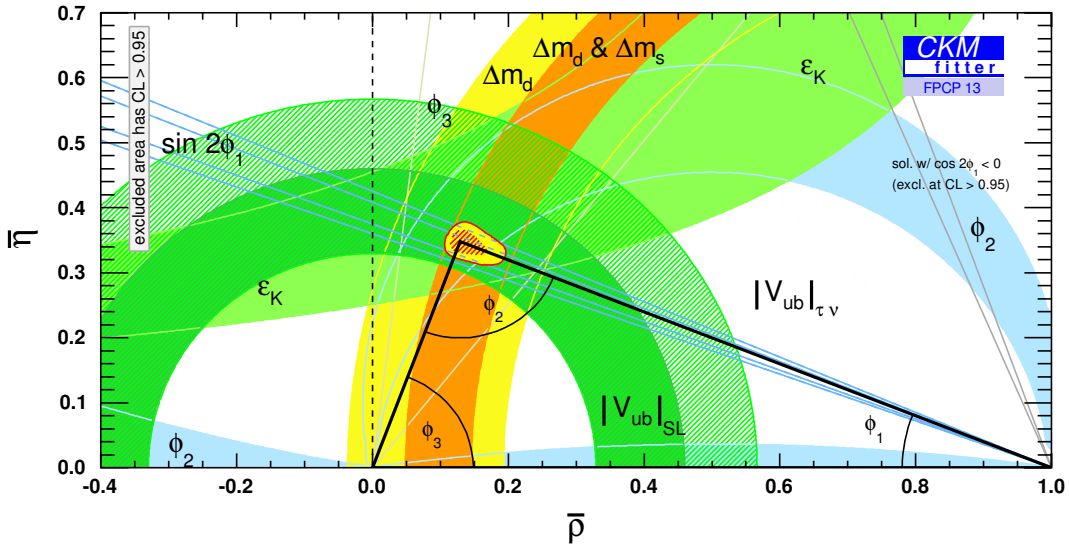

Figure 1.4: Current constraints on the CKM Triangle [29].

$V_{cd}V_{cb}^*$ is almost zero except for higher order contributions $\sim \mathcal{O}(\lambda^5)$, this normalization can be approximated as a simple scaling of the triangle. The coordinates of the top corner $(\overline{\rho}, \overline{\eta})$ and the angles of the rescaled triangle are given by

$$\overline{\rho} \equiv \left(1 - \frac{\lambda^2}{2}\right)\rho \qquad \overline{\eta} \equiv \left(1 - \frac{\lambda^2}{2}\right)\eta \tag{1.24}$$

$$\phi_1 \equiv \arg\left(-\frac{V_{cd}V_{cb}^*}{V_{td}V_{tb}^*}\right) \qquad \phi_2 \equiv \arg\left(-\frac{V_{td}V_{tb}^*}{V_{ud}V_{ub}^*}\right) \qquad \phi_3 \equiv \arg\left(-\frac{V_{ud}V_{ub}^*}{V_{cd}V_{cb}^*}\right) \tag{1.25}$$

Since sides and angles of this triangle can be measured using the B meson system and the triangle is supposed to be well conditioned, the SM can be tested by verifying the closing of this triangle. If any of the possible unitarity triangles does not close exactly, the unitarity of the CKM matrix would be broken, proving the incompleteness of the SM and therefore the existence of new physics beyond the SM. The current results of these measurements can be seen in Figure 1.4. So far, the results are in good agreement with the CKM model within the uncertainties, yet discrepancies could show up once the constraints are tightened further [30]. To achieve this, high precision measurements with very high statistics are needed.

1.4.2 Time Dependent CP violation

The time evolution for neutral B mesons is given by Equation 1.13

$$\begin{aligned} |\mathrm{B}^0(t)\rangle &= g_+(t)\,|\mathrm{B}^0\rangle + \frac{q}{p} g_-(t)\,|\overline{\mathrm{B}}^0\rangle \\ |\overline{\mathrm{B}}^0(t)\rangle &= g_+(t)\,|\mathrm{B}^0\rangle + \frac{p}{q} g_-(t)\,|\overline{\mathrm{B}}^0\rangle \end{aligned} \tag{1.26}$$

With the average mass $\overline{m} = (m_H + m_L)/2$ and the average lifetime $\overline{\Gamma} = (\Gamma_H + \Gamma_L)/2$, the functions $g_\pm$ (see Eq. 1.14) can be written as

$$g_\pm = \frac{1}{2} e^{-i\overline{m}t} e^{-\frac{1}{2}\overline{\Gamma}t} \left(e^{i\Delta m t/2} e^{-\Delta\Gamma t/4} \pm e^{-i\Delta m t/2} e^{\Delta\Gamma t/4} \right) \tag{1.27}$$

Since $\Delta\Gamma/\Gamma \sim \mathcal{O}(10^{-3})$ in the B^0 system, the lifetime difference between the two mass eigenstates can be ignored ($\Delta\Gamma = 0$). The lifetime is redefined as $\Gamma \equiv \overline{\Gamma} = \Gamma_L = \Gamma_H$ and Equation 1.27 becomes

$$g_\pm = e^{-\Gamma t/2} \frac{e^{i\Delta m t/2} \pm e^{-i\Delta m t/2}}{2} \tag{1.28}$$

where $e^{-i\overline{m}t}$ is removed by a phase convention. Thus the time evolution of the B^0 and the $\overline{\mathrm{B}}^0$ is

$$\begin{aligned} |\mathrm{B}^0(t)\rangle &= e^{-\Gamma t/2} \left(\cos(\frac{\Delta m t}{2})\,|\mathrm{B}^0\rangle + i\frac{q}{p} \sin(\frac{\Delta m t}{2})\,|\overline{\mathrm{B}}^0\rangle \right) \\ |\overline{\mathrm{B}}^0(t)\rangle &= e^{-\Gamma t/2} \left(\cos(\frac{\Delta m t}{2})\,|\overline{\mathrm{B}}^0\rangle + i\frac{p}{q} \sin(\frac{\Delta m t}{2})\,|\mathrm{B}^0\rangle \right) \end{aligned} \tag{1.29}$$

Consider the case where both B^0 and $\overline{\mathrm{B}}^0$ decay into the same CP eigenstate f_{CP}. The decay amplitudes can be written as

$$A_{CP} = \langle f_{CP}|\mathrm{B}^0\rangle \qquad\qquad \overline{A}_{CP} = \langle f_{CP}|\overline{\mathrm{B}}^0\rangle \tag{1.30}$$

Using the time evolution from Equation 1.29, the time-dependent decay amplitudes are

$$\begin{aligned} A_{CP}(t) &= A_{CP} e^{-\Gamma t/2} \left(\cos(\frac{\Delta m t}{2}) + i\lambda_{CP} \sin(\frac{\Delta m t}{2}) \right) \\ \overline{A}_{CP}(t) &= \overline{A}_{CP} e^{-\Gamma t/2} \left(\cos(\frac{\Delta m t}{2}) + \frac{i}{\lambda_{CP}} \sin(\frac{\Delta m t}{2}) \right) \end{aligned} \tag{1.31}$$

with

$$\lambda_{CP} = \frac{q}{p} \frac{\overline{A}_{CP}}{A_{CP}}. \tag{1.32}$$

With Equation 1.32, three distinct types of CP violation can be distinguished. Typical Feynman diagrams for each type of CP observable can be seen in Figure 1.5. These types can be classified as

***CP* violation in decay** or direct CP violation occurs when $|\overline{A}_f/A_{\overline{f}}| \neq 1$. This is the only type of CP violation possible in charged meson decays (since they cannot mix with their antiparticles).

***CP* violation in mixing** or indirect CP violation is defined by $|p/q| \neq 1$. This is the case for the first observed CP violation in the Kaon system and corresponds to an asymmetry in the flavour oscillation $M^0 \to \overline{M}^0 \to M^0$.

***CP* violation by interference of mixing and decay** can be observed in neutral decays where B^0 and $\overline{\mathrm{B}}^0$ have a common final state f, preferentially a pure CP eigenstate. A non-vanishing interference between a direct decay $M^0 \to f$ and a decay via mixing $M^0 \to \overline{M}^0 \to f$ is expected when

$$\mathrm{Im}\,(\lambda_{CP}) \neq 0$$

The B^0-oscillations are dominated by top-quark contributions because of $V_{tb} \gg V_{cb} \gg V_{ub}$ and GIM cancellations [31]. This leads to $p/q \simeq 1$ and allows to write λ_{CP} in the B-System as

$$|\lambda_{CP}|^2 = \frac{|\overline{A}_{CP}|^2}{|A_{CP}|^2} \tag{1.33}$$

Finally, the time dependent decay rates can be obtained from Equation 1.31

$$\begin{aligned}
\Gamma\left(\mathrm{B}^0 \to f_{CP}\right) &= |\,\langle f_{CP}|\mathrm{B}^0(t)\rangle\,|^2 \\
&= \frac{e^{-\Gamma t}}{2}|A_{CP}|^2\Big[(|\lambda_{CP}|^2+1) - (|\lambda_{CP}|^2-1)\cos(\Delta m t) - 2\,\mathrm{Im}(\lambda_{CP})\sin(\Delta m t)\Big] \\
\Gamma\left(\overline{\mathrm{B}}^0 \to f_{CP}\right) &= |\,\langle f_{CP}|\overline{\mathrm{B}}^0(t)\rangle\,|^2 \\
&= \frac{e^{-\Gamma t}}{2}|A_{CP}|^2\Big[(|\lambda_{CP}|^2+1) - (|\lambda_{CP}|^2-1)\cos(\Delta m t) + 2\,\mathrm{Im}\left(\frac{1}{\lambda_{CP}}\right)\sin(\Delta m t)\Big]
\end{aligned} \tag{1.34}$$

With CP violation, a difference between the time dependent decay rates (Eq. 1.34) of B^0 to $\overline{\mathrm{B}}^0$ to the same finalstate f_{CP} can be observed. Since these effects are expected to be small, it is advantageous to look at the asymmetry between these decays. Many systematic errors will be canceled in this measurement. This time-dependent asymmetry is then given by

$$a_{CP}(t) = \frac{\Gamma\left(\overline{\mathrm{B}}^0 \to f_{CP};t\right) - \Gamma\left(\mathrm{B}^0 \to f_{CP};t\right)}{\Gamma\left(\overline{\mathrm{B}}^0 \to f_{CP};t\right) + \Gamma\left(\mathrm{B}^0 \to f_{CP};t\right)} \tag{1.35}$$

Using Equations 1.31 and 1.34, this asymmetry can be expressed using two CP parameters

$$a_{CP}(t) = \mathcal{A}_{CP}\sin(\Delta m t) + \mathcal{S}_{CP}\cos(\Delta m t) \tag{1.36}$$

$$\mathcal{A}_{CP} = \frac{|\lambda_{CP}|^2 - 1}{|\lambda_{CP}|^2 + 1} \qquad \mathcal{S}_{CP} = \frac{2\,\mathrm{Im}(\lambda_{CP})}{|\lambda_{CP}|^2 + 1} \tag{1.37}$$

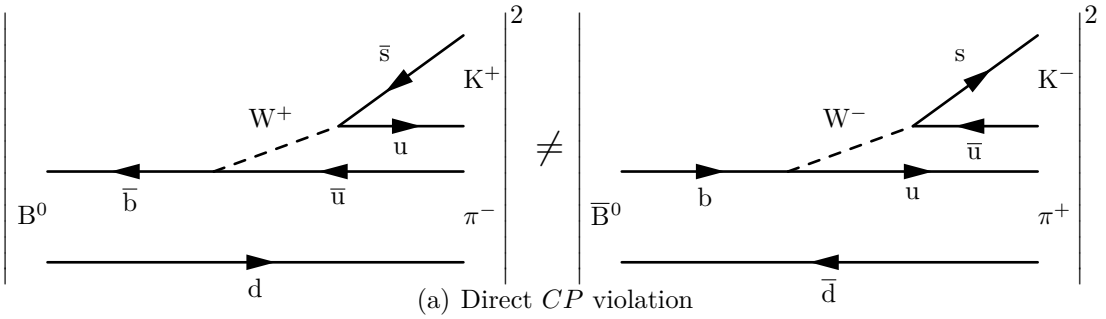

(a) Direct CP violation

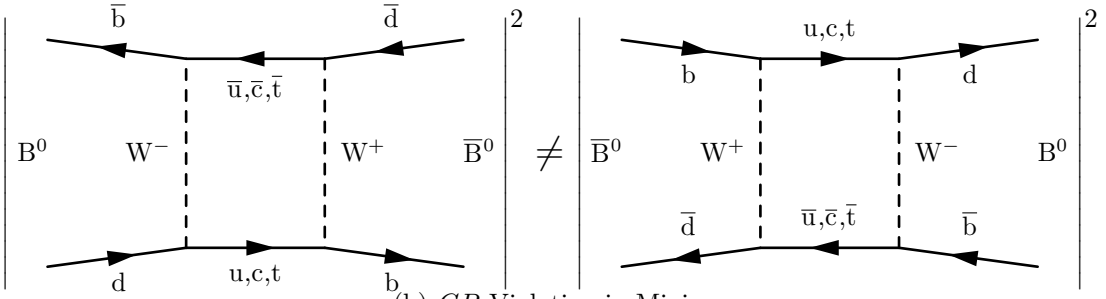

(b) CP Violation in Mixing

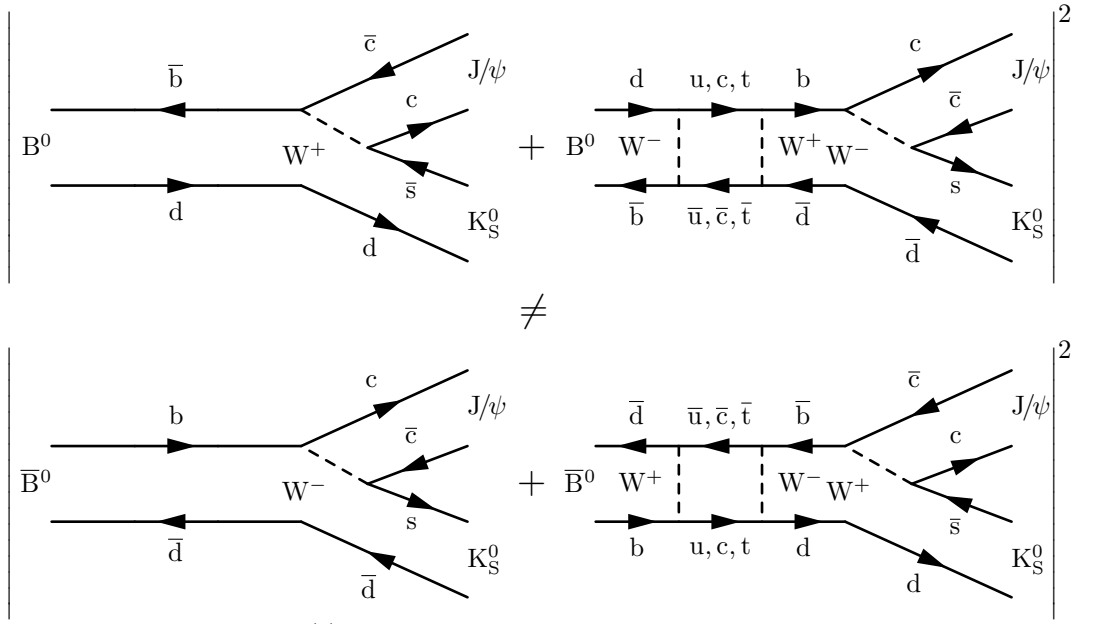

(c) CP Violation via Mixing and Decay

Figure 1.5: Examples for the three different types of CP observables. CP violation can be observed if the decay rates, and thus the squared Feynman amplitudes differ for B^0 and $\overline{B}^0$.

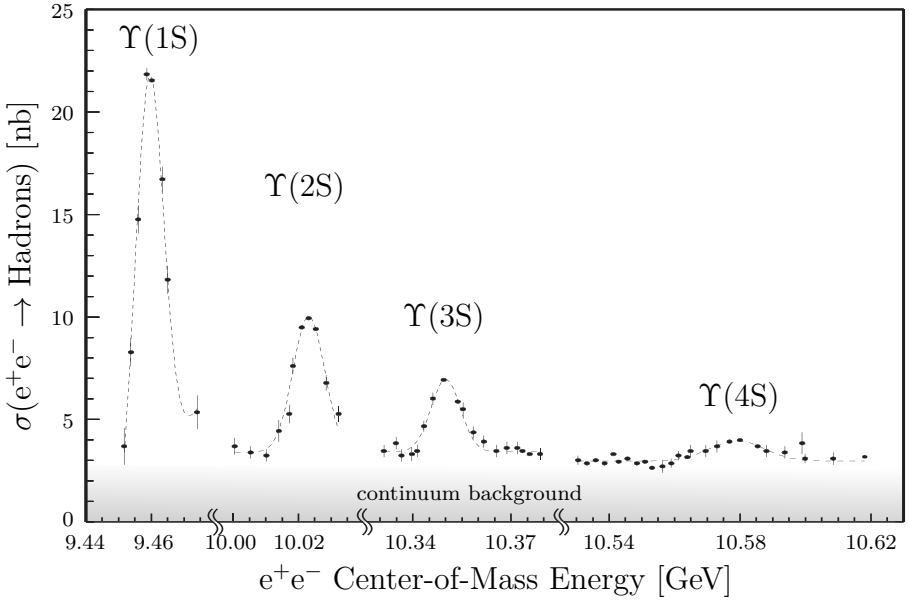

Figure 1.6: Hadronic cross section for e^+e^- collisions as function of the e^+e^- center-of-mass energy in the region at and above the $\Upsilon(1S)$ [32].

In this asymmetry, $\mathcal{A}_{CP}$ corresponds to effects of direct CP violation and $\mathcal{S}_{CP}$ to the mixing-induced CP violation. This is because $\mathcal{A}_{CP}$ will only differ from zero if $|\lambda_{CP}|^2 \neq 1$. From Equation 1.33 then follows $|\overline{A}_{CP}/A_{CP}| \neq 1$.

1.4.3 Measurement of CP violation

Due to the short lifetime of the B^0 of about 1.5 ps, it is impossible to resolve the CP asymmetry by a time measurement. Furthermore, the time-dependent decay asymmetry (Eq. 1.36) requires that the flavour of the B meson is known. For a CP eigenstate, both B^0 and $\overline{B}^0$ can decay into the same final state. Therefore the knowledge whether the B^0 or the $\overline{B}^0$ has decayed into the CP eigenstate f_{CP} is a non-trivial experimental issue.

To create B-mesons in an e^+e^- machine with low background, $B\overline{B}$ pairs are produced at the $\Upsilon(4S)$ resonance. The $\Upsilon(4S)$ is one of the hadronic $b\overline{b}$ resonances (see Figure 1.6) and is exactly at the production threshold for $B\overline{B}$ meson pair production. This is the lowest energy where B mesons can be produced and they are therefore essentially at rest in the center of mass system. Running at the $\Upsilon(4S)$ also has the benefit of high $B\overline{B}$ yields as about one third of all hadron events at that energy are $B\overline{B}$ events.

The two B mesons are in a state with quantum numbers $J^{PC} = 1^{--}$ from the $\Upsilon(4S)$ since P and C are conserved in strong interactions. Due to B^0 being a pseudoscalar particle, the $B\overline{B}$ system must have an orbital angular momentum $L = 1$ (p-wave). This state must be antisymmetric, therefore Bose-Einstein statistics forbids the states B^0B^0 and $\overline{B}^0\overline{B}^0$ which necessarily must be a symmetric state. As a consequence, the two B mesons cannot oscillate independently, so that a state B^0B^0 or $\overline{B}^0\overline{B}^0$ cannot occur at any

time: The $\mathrm{B}^0\overline{\mathrm{B}}^0$ pair therefore must oscillate coherently,

$$|\mathrm{B}_1(t_1), \mathrm{B}_2(t_2)\rangle = \frac{1}{\sqrt{2}}\left(|\mathrm{B}_1^0(t_1)\rangle\,|\overline{\mathrm{B}}_2^0(t_2)\rangle - |\overline{\mathrm{B}}_1^0(t_1)\rangle\,|\mathrm{B}_2^0(t_2)\rangle\right). \tag{1.38}$$

Substitution of Equation1.31 and $\Delta t = t_2 - t_1$ yields

$$\begin{aligned}|\mathrm{B}_1(t_1), \mathrm{B}_2(t_2)\rangle = \frac{1}{\sqrt{2}}e^{\frac{-\Gamma(t_1+t_2)}{2}}\Bigg[&\cos\Big(\frac{\Delta m\Delta t}{2}\Big)\Big(\,|\mathrm{B}_1^0\rangle\,|\overline{\mathrm{B}}_2^0\rangle - |\overline{\mathrm{B}}_1^0\rangle\,|\mathrm{B}_2^0\rangle\,\Big)\\ &+ i\sin\Big(\frac{\Delta m\Delta t}{2}\Big)\Big(\frac{q}{p}\,|\mathrm{B}_1^0\rangle\,|\overline{\mathrm{B}}_2^0\rangle - \frac{p}{q}\,|\overline{\mathrm{B}}_1^0\rangle\,|\mathrm{B}_2^0\rangle\,\Big)\Bigg]\end{aligned} \tag{1.39}$$

Once one of the two mesons decays, the other one is free to oscillate. If we can measure the flavour of one of the two B's, determined by a flavour-specific decay, which is called "tag side", the exact flavour and time evolution of the other B is known. In the specific case where one B meson decays to a flavour specific state $\mathrm{B}_{\mathrm{tag}}$ and the other B decays to a CP eigenstate, B_{CP}, the time-dependent decay rates become

$$\begin{aligned}\Gamma(f_{CP}, f_{\mathrm{tag}}) =&|\,\langle f_{CP}, f_{\mathrm{tag}}|\mathrm{B_{CP}(t_{CP})}, \mathrm{B_{tag}(t_{tag})}\rangle\,|^2\\ =&\frac{1}{4}e^{-\Gamma(t_{CP}+t_{\mathrm{tag}})}A_{CP}^2A_{\mathrm{tag}}^2\\ &\Big[(|\lambda_{CP}|^2+1) - (|\lambda_{CP}|^2-1)\cos(\Delta m\Delta t) - 2\,\mathrm{Im}(\lambda_{CP})\sin(\Delta m\Delta t)\Big]\\ \Gamma(f_{CP}, \overline{f}_{\mathrm{tag}}) =&|\,\langle f_{CP}, \overline{f}_{\mathrm{tag}}|\mathrm{B_{CP}(t_{CP})}, \mathrm{B_{tag}(t_{tag})}\rangle\,|^2\\ =&\frac{1}{4}e^{-\Gamma(t_{CP}+t_{\mathrm{tag}})}A_{CP}^2A_{\mathrm{tag}}^2|\frac{p}{q}|^2\\ &\Big[(|\lambda_{CP}|^2+1) + (|\lambda_{CP}|^2-1)\cos(\Delta m\Delta t) + 2\,\mathrm{Im}(\lambda_{CP})\sin(\Delta m\Delta t)\Big]\end{aligned} \tag{1.40}$$

with the decay amplitude $A_{\mathrm{tag}} = \langle f_{\mathrm{tag}}|\mathrm{B}^0\rangle = \langle\overline{f}_{\mathrm{tag}}|\overline{\mathrm{B}}^0\rangle$. The resulting time-dependent CP asymmetry,

$$\begin{aligned}a_{CP}(\Delta t) &= \frac{\Gamma\left(f_{CP}, \overline{f}_{\mathrm{tag}}\right) - \Gamma\left(f_{CP}, f_{\mathrm{tag}}\right)}{\Gamma\left(f_{CP}, \overline{f}_{\mathrm{tag}}\right) + \Gamma\left(f_{CP}, f_{\mathrm{tag}}\right)}\\ &= \mathcal{A}_{CP}\sin\left(\Delta m\Delta t\right) + \mathcal{S}_{CP}\cos\left(\Delta m\Delta t\right),\end{aligned} \tag{1.41}$$

retains its form in Δt when compared to Equation 1.35. The CP-violating parameters can be extracted as a physical observable if Δt and the flavour of $\mathrm{B}_{\mathrm{tag}}$ can be determined. If Equation 1.40 is normalized to unity in the region $-\infty < \Delta t < \infty$ we obtain the probability of finding f_{CP} at time Δt and a given flavour tag $q = +1$ (-1) for $\mathrm{B}_{\mathrm{tag}} = \mathrm{B}^0$ $(\overline{\mathrm{B}}^0)$,

$$\mathcal{P}(\Delta t, q) = \frac{e^{-|\Delta t|/\tau_{\mathrm{B}^0}}}{4\tau_{\mathrm{B}^0}}\Big[1 + q\Big(\mathcal{A}_{CP}\cos\left(\Delta m\Delta t\right) + \mathcal{S}_{CP}\sin\left(\Delta m\Delta t\right)\Big)\Big]. \tag{1.42}$$

Figure 1.7 shows this probability for two different, arbitrary values for the CP parameters $\mathcal{A}_{CP}$ and $\mathcal{S}_{CP}$ and the resulting CP asymmetry a_{CP}

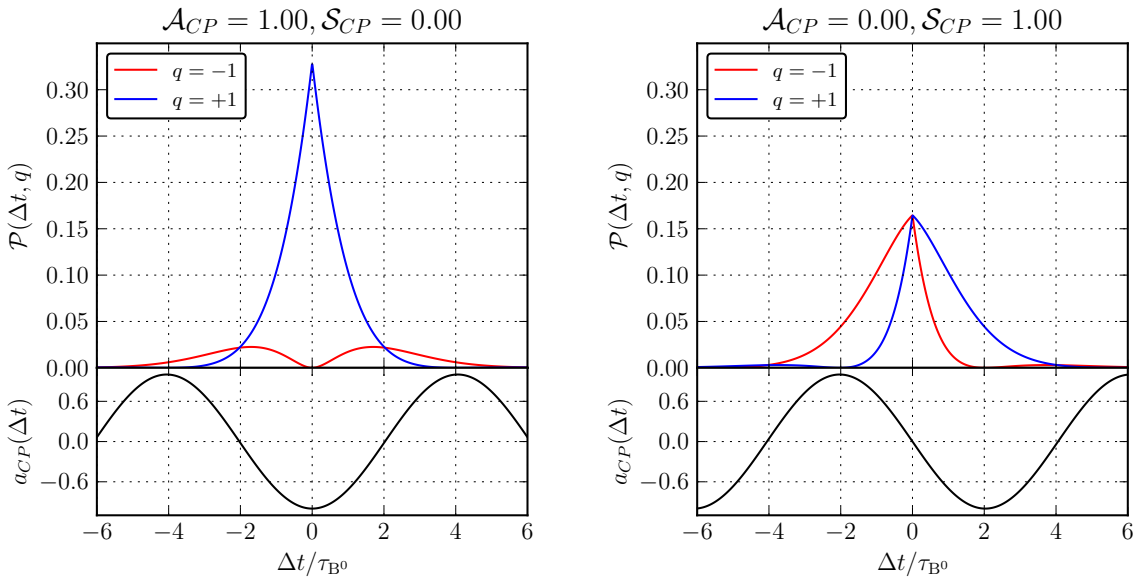

(a) Direct CP violation

(b) Mixing-induced CP violation

Figure 1.7: Two different examples how CP violation can manifest in the probability $\mathcal{P}(\Delta t, q)$ and the resulting CP asymmetry a_{CP}. In the case of no CP violation the distributions for $q = +1$ and $q = -1$ would match and the asymmetry would disappear.

Using asymmetric beam energies, the $\Upsilon(4S)$ system is boosted in beam direction (z in Belle). As the B mesons have very low momentum the $\Upsilon(4S)$ frame they fly almost parallel to the boost direction. This makes it possible to measure the distance Δz between the decay vertices of the B . Since the boost of the system is known, the time Δt can be determined using

$$\Delta t = \frac{\Delta z}{\langle \beta\gamma \rangle c} \tag{1.43}$$

Yet even for a boost of $\beta\gamma = 1$, the mean flight distance of the B^0 is only $\sim 400\,\mu\mathrm{m}$. High precision vertexing using silicon technology is required to be able to determine Δz.

A schematic decay of $\mathrm{B}^0 \to \mathrm{J}/\psi \mathrm{K}^0_{\mathrm{S}}$ is shown in Figure 1.8. Due to the low theoretical uncertainties, the large branching fraction and the high reconstruction efficiencies [33], this channel can be considered a golden mode for the time dependent the CP measurement. The dominant Feynman diagrams contributing to this channel can be seen in Figure 1.5(c) In Figure 1.8, the flavour of the tag side B^0 meson can be obtained using a semileptonic tag: Charge conservation dictates that a single lepton emitted from a B^0 decay has to be positively charged and vice versa for $\overline{\mathrm{B}}^0$. Therefore semileptonic decays can be used to determine the flavour of one of the two B^0 mesons.

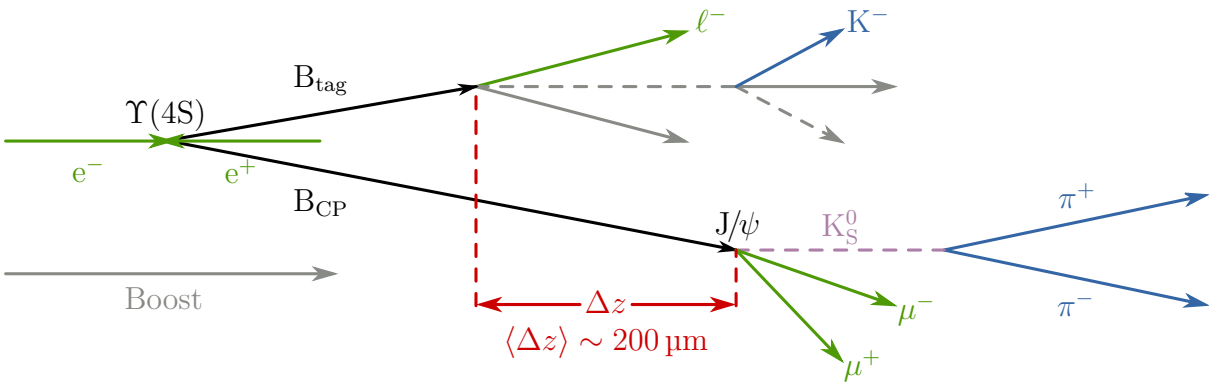

Figure 1.8: Simple schematic of $B^0\overline{B}^0$ decaying in the case of the golden channel $J/\psi K^0_S$.

1.5 Time-Dependent CP violation in $B^0 \to D^{*-}D^{*+}K^0_S$

The leading process for $B^0 \to D^{*-}D^{*+}K^0_S$ is shown in Figure 1.9. Like $B^0 \to J/\psi K^0_S$, it contains the $b \to c\bar{c}s$ transition. However, due to the external emission of the W boson, this process is not colour suppressed, and the branching fraction is enhanced relative to $B^0 \to J/\psi K^0_S$. According to [34] the penguin contribution is expected to be negligible, meaning that no direct CP violation is expected.

The D^* is a vector (spin 1) resonance. For vector-vector decay modes the final state in general is an admixture of CP odd and even eigenstates, because s, p and d partial waves with different CP parities can contribute [34]. This tends to dilute or cancel the overall asymmetry. Furthermore there is an additional dilution if there is a resonance in the final state. The decay amplitudes $B \to f$ and $\overline{B} \to \overline{f}$ differ because the resonance bands in the Dalitz plot can be populated differently. This causes additional mismatch of the B and $\overline{B}$ amplitudes which further dilutes the CP asymmetry.

However, if there is a resonant contribution it may be used to extract $\cos(2\phi_1)$. Since other decay channels are only sensitive to $\sin(2\phi_1)$ there is a $\phi_1 \to \pi/2 - \phi_1$ ambiguity. Being potentially sensitive to $\cos(2\phi_1)$ makes this decay mode so interesting despite the experimental difficulties as it can be used to resolve this ambiguity on ϕ_1.

Following [34], we define amplitudes which take into account the polarisation of the $D^{*\pm}$ mesons,

$$\begin{aligned} A_{\lambda_1,\lambda_2} &\equiv A\left[B^0(p) \to D^{*+}_{\lambda_1}(p_+)D^{*-}_{\lambda_2}(p_-)K^0_S(p_k)\right] \\ \overline{A}_{\lambda_1,\lambda_2} &\equiv A\left[\overline{B}^0(p) \to D^{*+}_{\lambda_1}(p_+)D^{*-}_{\lambda_2}(p_-)K^0_S(p_k)\right], \end{aligned} \tag{1.44}$$

where p, p_+, p_- and p_k are the 4-momenta of B^0, D^{*+}, D^{*-} and K^0_S, and λ_1 and λ_2 are the polarisation indices of the D^{*+} and D^{*-}, respectively. Using the time-dependent amplitude for an oscillating B^0 ($\overline{B}^0$) from equation 1.31 and $\lambda_{CP} = e^{-i2\phi_1}$, we obtain

$$\begin{aligned} A_{\lambda_1,\lambda_2}(t) &= A_{\lambda_1,\lambda_2}\cos(\frac{\Delta m t}{2}) + ie^{-2i\phi_1}\overline{A}_{\lambda_1,\lambda_2}\sin(\frac{\Delta m t}{2}) \\ \overline{A}_{\lambda_1,\lambda_2}(t) &= \overline{A}_{\lambda_1,\lambda_2}\cos(\frac{\Delta m t}{2}) + ie^{2i\phi_1}A_{\lambda_1,\lambda_2}\sin(\frac{\Delta m t}{2}) \end{aligned} \tag{1.45}$$

dropping the $e^{-\Gamma t/2}$ for convenience. Integrating over the phase space angles and summing over the polarisations, the time-dependent squared amplitude becomes

$$\begin{aligned} |A(s^+,s^-;t)|^2 &= \frac{1}{2}\Big[G_0(s^+,s^-) + G_c(s^+,s^-)\cos(\Delta m t) - G_s(s^+,s^-)\sin(\Delta m t)\Big] \\ |\overline{A}(s^-,s^+;t)|^2 &= \frac{1}{2}\Big[G_0(s^-,s^+) - G_c(s^-,s^+)\cos(\Delta m t) + G_s(s^-,s^+)\sin(\Delta m t)\Big] \end{aligned} \tag{1.46}$$

with

$$\begin{aligned} G_0(s^+,s^-) &= |A(s^+,s^-)|^2 + |\overline{A}(s^+,s^-)|^2 \\ G_c(s^+,s^-) &= |A(s^+,s^-)|^2 - |\overline{A}(s^+,s^-)|^2 \\ G_s(s^+,s^-) &= -2\sin(2\phi_1)\,\mathrm{Re}(\overline{A}A^*) + 2\cos(2\phi_1)\,\mathrm{Im}(\overline{A}A^*) \\ &= -2\sin(2\phi_1)G_{s1}(s^+,s^-) + 2\cos(2\phi_1)G_{s2}(s^+,s^-) \end{aligned} \tag{1.47}$$

and the Dalitz variables $s^+ = (p_+ + p_k)^2$ and $s^- = (p_- + p_k)^2$. It is more convenient to replace s^+ and s^- by $y = \cos\theta$ and E_k where θ is the angle between the D^{*+} and the K^0_S in the rest frame of the two D^* mesons (see Figure 1.10) and E_k is the K^0_S energy in the B^0 rest frame. Note that $s^+ \leftrightarrow s^-$ corresponds to $y \leftrightarrow -y$. If we neglect penguin contributions to the amplitude there is no CP violation which implies that

$$A(\boldsymbol{p}'_k, E_k) = \overline{A}(-\boldsymbol{p}'_k, E_k) \tag{1.48}$$

where $\boldsymbol{p}'_k$ is the momentum of the K^0_S in the boosted frame. This leads to

$$\begin{aligned} G_0(y,E_k) &= G_0(-y,E_k) \\ G_c(y,E_k) &= -G_c(-y,E_k) \\ G_{s1}(y,E_k) &= G_{s1}(-y,E_k) \\ G_{s2}(y,E_k) &= -G_{s2}(-y,E_k). \end{aligned} \tag{1.49}$$

Integration of Equation 1.46 over half of the phase space region, taken as $y \geq 0$ ($y \leq 0$) for B^0 ($\overline{\mathrm{B}}^0$) decay, yields

$$\begin{aligned} \Gamma(t, y \geq 0) &= \frac{1}{2}\Big[J_0 + J_c\cos(\Delta m t) + 2J_{s1}\sin(2\phi_1)\sin(\Delta m t) - 2J_{s2}\cos(2\phi_1)\sin(\Delta m t)\Big] \\ \overline{\Gamma}(t, y \leq 0) &= \frac{1}{2}\Big[J_0 + J_c\cos(\Delta m t) - 2J_{s1}\sin(2\phi_1)\sin(\Delta m t) - 2J_{s2}\cos(2\phi_1)\sin(\Delta m t)\Big] \end{aligned} \tag{1.50}$$

where J_0, J_c, J_{s1} and J_{s2} represent the integrated functions $G_0(y,E_k)$, $G_c(y,E_k)$, $G_{s1}(y,E_k)$ and $G_{s2}(y,E_k)$ over the half phase space region $y \geq 0$ which is equivalent to $s^+ \geq s^-$. Finally we can write down the time-dependent CP asymmetry as

$$\frac{\overline{\Gamma}(t) - \Gamma(t)}{\overline{\Gamma}(t) + \Gamma(t)} = \eta_y \frac{J_c}{J_0}\cos(\Delta m t) - \left(\frac{2J_{s1}}{J_0}\sin(2\phi_1) + \eta_y\frac{2J_{s2}}{J_0}\cos(2\phi_1)\right)\sin(\Delta m t) \tag{1.51}$$

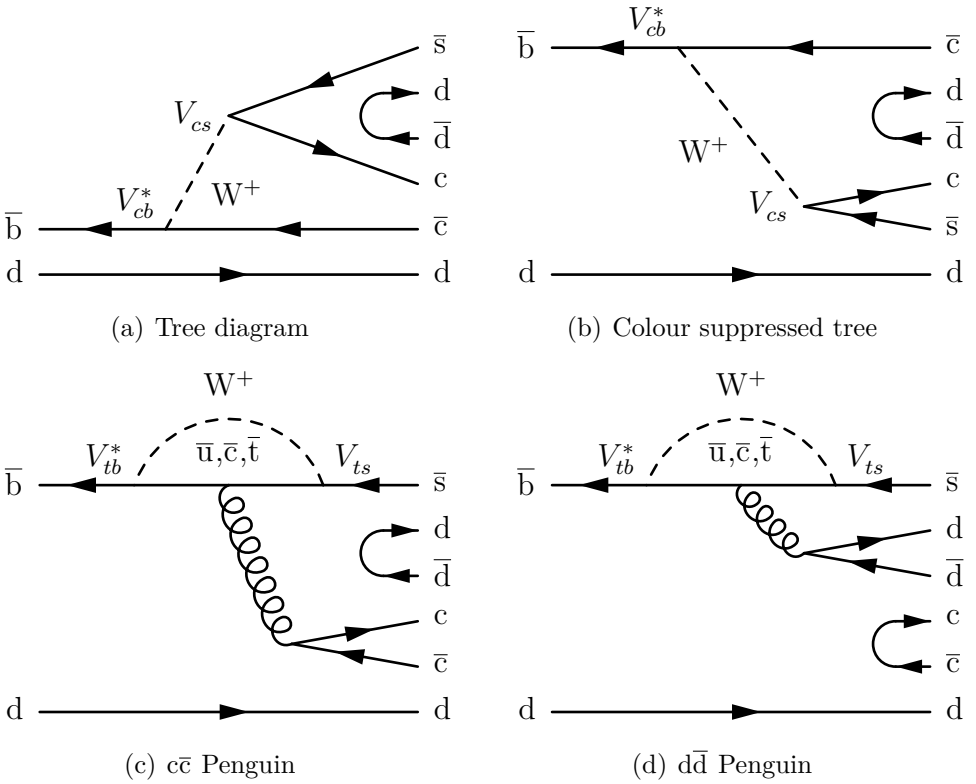

Figure 1.9: Leading Feynman diagrams for $B^0 \to D^{*-}D^{*+}K^0_S$.

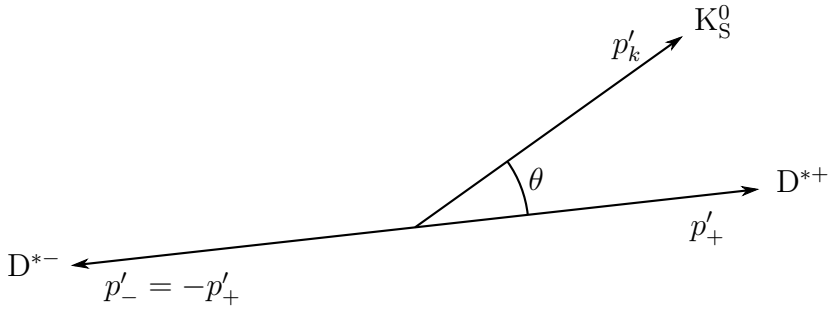

Figure 1.10: Schematics of the D^{*+} D^{*-} rest frame and the definition of θ. p'_+, p_- and p'_k are the boosted 4-momenta of the D^{*+}, D^{*-} and K^0_S in this frame.

with $\eta_y = +1$ (-1) for $s^+ \geq s^-$ $(s^+ \leq s^-)$. From this distribution we can extract the time-dependent CP violating parameters J_c/J_0, $(2J_{s1}/J_0)\sin(2\phi_1)$, $(2J_{s2}/J_0)\cos(2\phi_1)$ for $\mathrm{B}^0 \to \mathrm{D}^{*-}\mathrm{D}^{*+}\mathrm{K}^0_\mathrm{S}$. Similar to Equation 1.42, the probability of finding f_{CP} at time Δt for a given flavour tag q is given by

$$\mathcal{P}(\Delta t, q) = \frac{\exp -|\Delta t|/\tau_{\mathrm{B}^0}}{4\tau_{\mathrm{B}^0}}\Big\{1 + q\Big[\eta_y \frac{J_c}{J_0}\cos(\Delta m t) - \Big(\frac{2J_{s1}}{J_0}\sin(2\phi_1) + \eta_y \frac{2J_{s2}}{J_0}\cos(2\phi_1)\Big)\sin(\Delta m t)\Big]\Big\}. \quad (1.52)$$

J_{s2} measures the overlap of the imaginary part of the amplitudes for $\mathrm{B}^0 \to \mathrm{D}^{*-}\mathrm{D}^{*+}\mathrm{K}^0_\mathrm{S}$ and $\overline{\mathrm{B}}^0 \to \mathrm{D}^{*-}\mathrm{D}^{*+}\mathrm{K}^0_\mathrm{S}$. If this would be a pure 3-body decay then $J_{s2} = 0$ would render a measurement of $\cos(2\phi_1)$ impossible. Measurement of J_{s2} itself would require a complicated 3-body angular analysis which is beyond the scope of this thesis. But [34] predicts $2J_{s2}/J_0$ to be positive. This allows us to determine the sign of $\cos(2\phi_1)$ and resolve the two-fold ambiguity $\phi_1 \to \pi/2 - \phi_1$.

1.6 Previous Measurements

In 2006, the BABAR collaboration reported the following results [35],

$$\mathcal{B}(\mathrm{B}^0 \to \mathrm{D}^{*-}\mathrm{D}^{*+}\mathrm{K}^0_\mathrm{S}) = \Big(4.4 \pm 0.4(\mathrm{stat}) \pm 0.7(\mathrm{syst})\Big) \times 10^{-3} \quad (1.53)$$

They assumed no direct CP violation and did not search for it explicitly. For the time-dependent CP analysis using equation 1.51 they measured

$$\begin{aligned} J_c/J_0 &= 0.76 \pm 0.18(\mathrm{stat}) \pm 0.07(\mathrm{syst}) \\ (2J_{s1}/J_0)\sin(2\phi_1) &= 0.10 \pm 0.24(\mathrm{stat}) \pm 0.06(\mathrm{syst}) \\ (2J_{s2}/J_0)\cos(2\phi_1) &= 0.38 \pm 0.24(\mathrm{stat}) \pm 0.05(\mathrm{syst}) \end{aligned} \quad (1.54)$$

and excluded a negative sign of $\cos(2\phi_1)$ at the 94 % confidence level.

In 2011, the BABAR collaboration did a measurement of the branching fractions of multiple decay modes with a result of [36]

$$\mathcal{B}(\mathrm{B}^0 \to \mathrm{D}^{*-}\mathrm{D}^{*+}\mathrm{K}^0) = \Big(8.26 \pm 0.43(\mathrm{stat}) \pm 0.67(\mathrm{syst})\Big) \times 10^{-3} \quad (1.55)$$

where K^0 decays with 50 % into K^0_S or K^0_L. This measurement is consistent with their previous result but has significantly smaller errors. No attempt was made to improve the time-dependent CP analysis.

Belle published performed an analysis of this channel in 2007 using $414\,\mathrm{fb}^{-1}$ ($\sim 60\,\%$ of the final data) [37] and measured

$$\mathcal{B}(\mathrm{B}^0 \to \mathrm{D}^{*-}\mathrm{D}^{*+}\mathrm{K}^0_\mathrm{S}) = \Big(3.4 \pm 0.4(\mathrm{stat}) \pm 0.7(\mathrm{syst})\Big) \times 10^{-3} \quad (1.56)$$

They explicitly checked for direct CP violation but found no evidence. In the 3-parameter fit performed int the half-Dalitz space they obtained

$$\begin{aligned} J_c/J_0 &= \quad 0.60^{+0.25}_{-0.28}(\text{stat}) \pm 0.08(\text{syst}) \\ (2J_{s1}/J_0)\sin(2\phi_1) &= -0.17^{+0.42}_{-0.42}(\text{stat}) \pm 0.09(\text{syst}) \\ (2J_{s2}/J_0)\cos(2\phi_1) &= -0.23^{+0.43}_{-0.41}(\text{stat}) \pm 0.13(\text{syst}). \end{aligned} \tag{1.57}$$

Due to the large errors on $(2J_{s2}/J_0)\cos(2\phi_1)$ no conclusion was drawn concerning the sign of $\cos(2\phi_1)$.

As there is no significant constraint on the sign of $\cos(2\phi_1)$ from Belle this is an excellent opportunity to repeat the analysis with the final data set. In addition to the increased statistics since the previous analysis we can profit from an improved reconstruction method for charged particles, especially in the low momentum range.

Chapter 2

The Belle Experiment

The Belle Experiment has been built specifically to make high-precision measurements of the CKM parameters using $B\overline{B}$ decays. It is stationed at the KEKB collider, part of the KEK Research Center in Tsukuba, Japan, and is currently holding the world record on luminosity of $2.11 \times 10^{34}\,\mathrm{cm}^{-2}\mathrm{s}^{-1}$ [38], exceeding the design luminosity by more than a factor of two. In its runtime from 1999 to 20120, the experiment has accumulated $1\,\mathrm{ab}^{-1}$ of integrated luminosity (Figure 2.1) at the various $\Upsilon(n\mathrm{S})$ resonances, with the majority of data at the $\Upsilon(4\mathrm{S})$ resonance which translates into 772 million $B\overline{B}$ pairs.

2.1 KEKB Accelerator

The KEKB-Accelerator [39, 40] is an asymmetric e^+e^--storage ring with a center of mass energy of $\sqrt{s} = 10.58\,\mathrm{GeV}$, the $\Upsilon(4\mathrm{S})$-resonance. It consists of one high-energy ring (HER) at 8 GeV and one low-energy ring (LER) at 3.5 GeV. These rings have a circumference of roughly 3 km and are located 10 m below ground. A linear accelerator is used to bring the electrons and positrons to the required energy before injecting them into the storage rings.

There is one interaction region in which the two beams cross with an angle of 22 mrad to minimize bunch-bunch interactions in the interaction region. Due to the asymmetric beam energies the B mesons have a boost of $\beta\gamma = 0.425$, which results in a mean $\langle \Delta z \rangle = 200\,\mu\mathrm{m}$ (see Eq. 1.43) which has to be resolved in order to measure time dependent CP asymmetries.

2.2 Belle Detector

The Belle detector [12, 41] aims at full reconstruction of all particles and follows the standard layout of most detectors in high-energy physics. It covers an acceptance from $\theta = 17°$ to $150°$, corresponding to 92 % of the solid angle. The basic layout can be seen in Figure 2.3.

The coordinate system used in Belle is defined as right-handed coordinate system with x, y and z axes and the origin at the nominal interaction point (IP). z is defined as being the direction opposite the positron beam and y is pointing upwards. The radial distance,

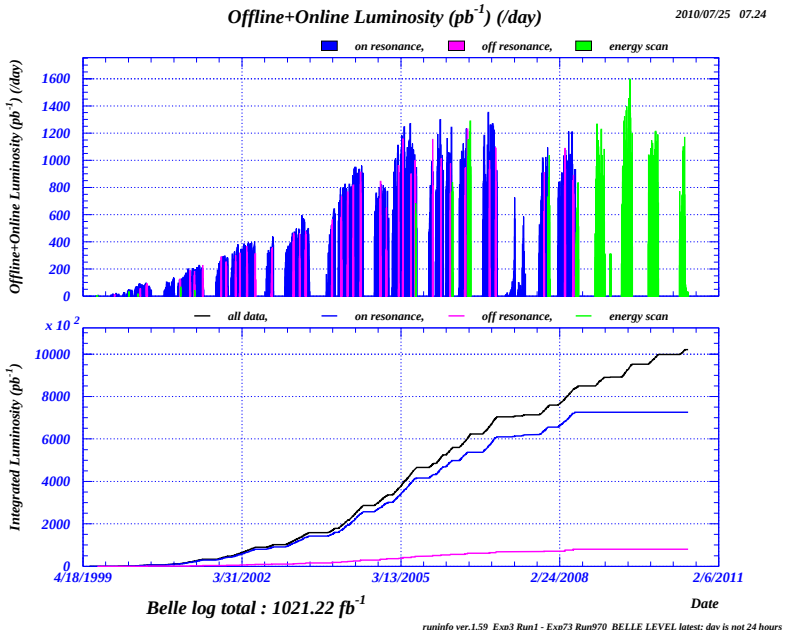

Figure 2.1: Daily recorded luminosity for KEKB.

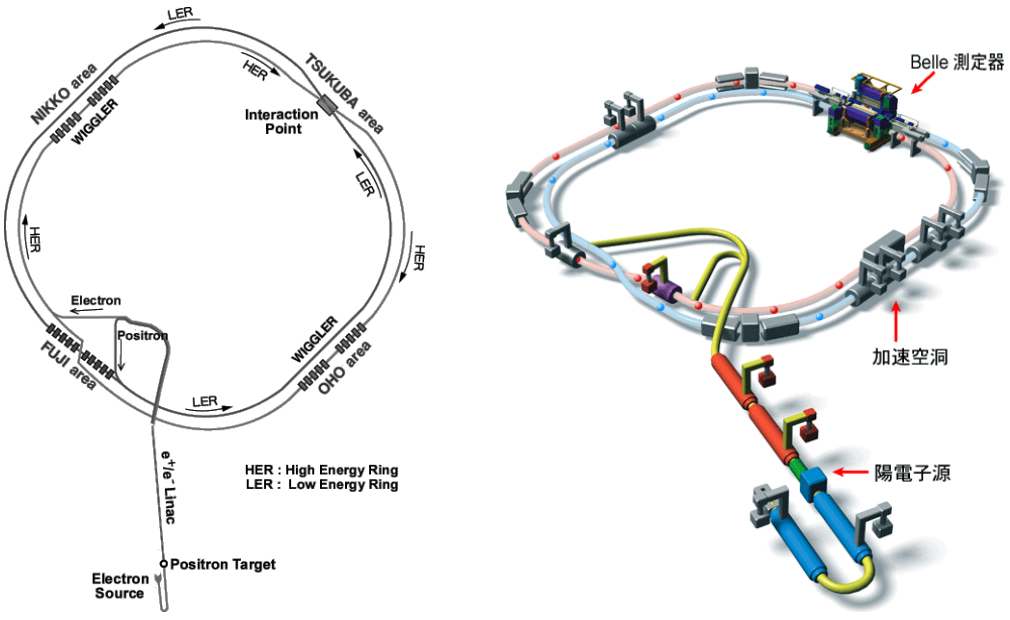

Figure 2.2: Schematic view of the KEKB accelerator.

$r = \sqrt{x^2 + y^2}$, is the distance projected on the xy-plane, θ is the polar angle to the z-axis and ϕ is the azimuthal angle with respect to the positive x-axis.

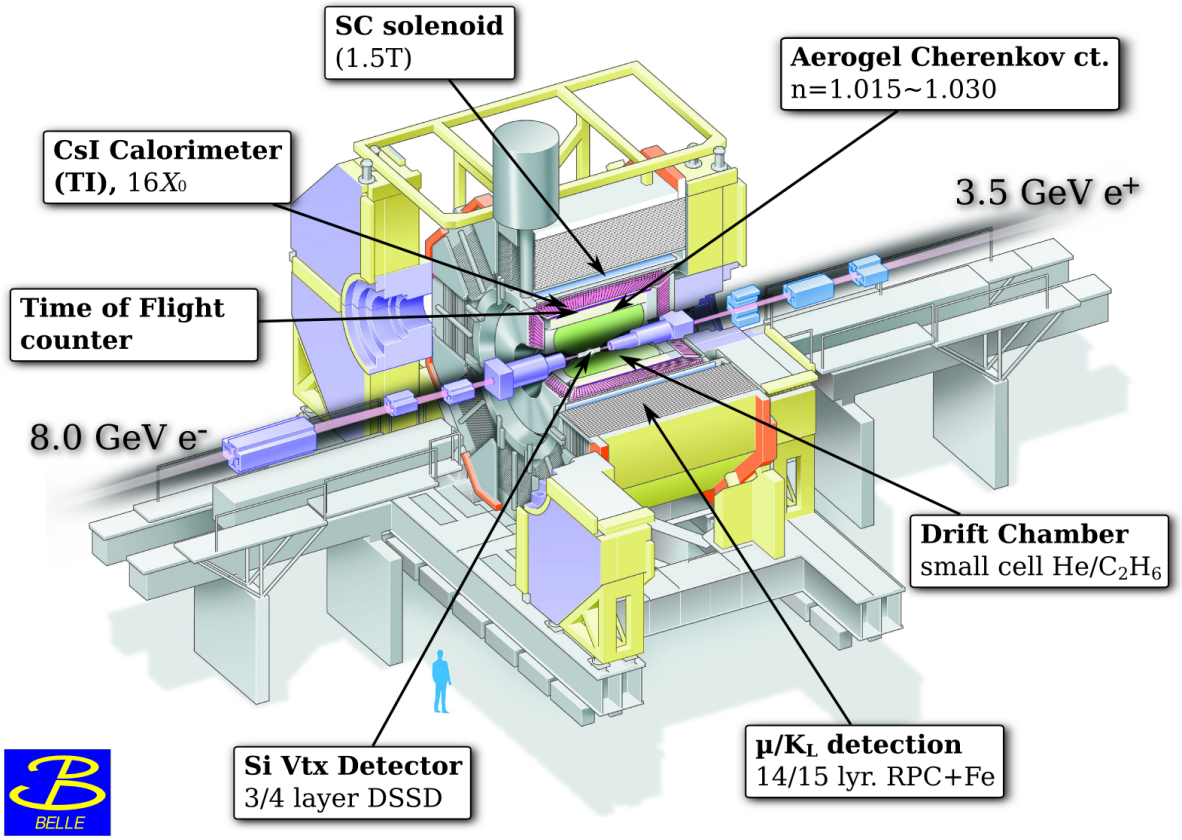

Figure 2.3: Layout of the Belle detector.

2.2.1 Beam Pipe

Although technically not part of the Belle detector, the beam pipe around the interaction point (IP) is the first piece of material all particles must traverse before reaching the detector. Since Coulomb scattering affects track resolution, it is important to minimize the impact of the beam pipe on particle trajectories by choosing a thin material with a low atomic number. In addition, vertexing performance is reduced with increasing distance of the vertex detector from the IP (see below), requiring the diameter of the beam pipe to be as small as possible.

With these considerations in mind, a beryllium beam pipe was chosen, which consists of a dual layer cylinder where the gap between the walls is used as cooling channel. A 20 µm gold foil covers the outer surface to shield low energy X-ray background which otherwise might generate background in the vertex detectors. The total material of the

beam pipe corresponds to 0.3 % and 0.6 % of the radiation length X_0 for the beryllium and the gold foil respectively [12].

The initial beam pipe had an outer radius of 24.25 mm but was replaced after the first 152×10^6 $B\overline{B}$ pairs when the inner detector was re-designed and placed closer to the IP. The new beam pipe has an outer radius of 16.25 mm and a gold foil plating of 10 µm.

2.2.2 Silicon Vertex Detector

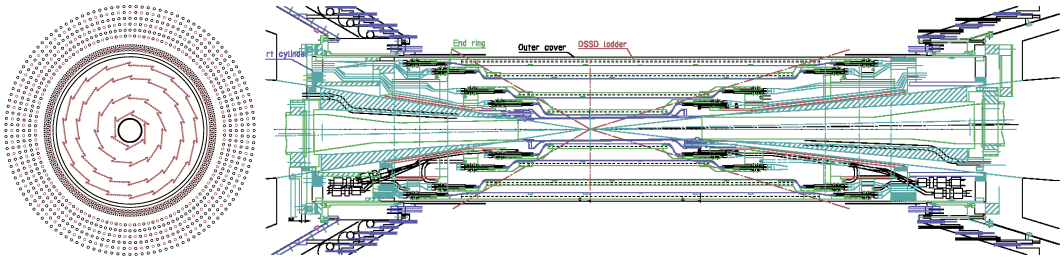

(a) front view (b) side view

Figure 2.4: Structure of the SVD2 [42]. The front view also shows the inner wires of the Drift Chamber.

The Silicon Vertex Detector (SVD) is the innermost subsystem of the Belle detector. Its primary purpose is to determine the decay vertices of the B mesons, making it one of the most important sub-detectors for the measurement of time dependent CP asymmetries. It also contributes to improve the momentum resolution of charged particles.

The original vertex detector (SVD1) consisted of three layers of double sided silicon-strip detectors (DSSD). It was redesigned with four layers (SVD2) in 2001 due to problems with radiation hardness. The main parameters are shown in Table 2.1.

A DSSD is basically a pn-junction with a bias voltage of 75 V applied to the n-side while the p-side is grounded. The n strips are interleaved with p-implants to electrically separate the consecutive strips. A charged particle passing through the n bulk silicon creates electron-hole pairs. The electrons and holes drift to their corresponding biased side of the DSSD, potentially making a 2-dimensional hit signal, as seen in Figure 2.5.

In the SVD2 the number of modules increased by more than a factor of two. To keep the number of readout channels compatible with the existing hardware, the readout channels of all modules in the forward/backward half of one ladder are added together. As a result, complete tracking is required to determine the position of a SVD2 cluster since it may originate from up to three modules.

An important performance indication for the SVD is the resolution of the reconstructed vertex position in $r\phi$ and z direction. These impact parameters are determined using

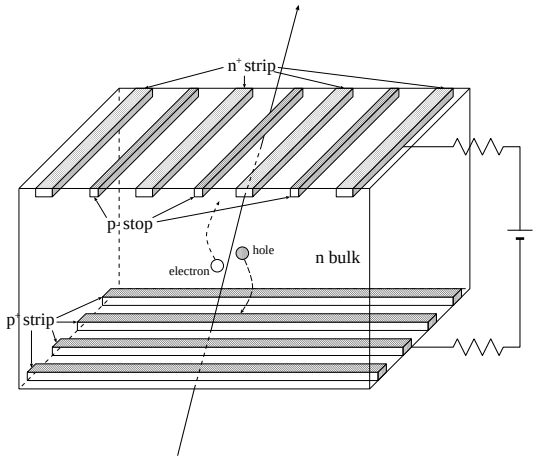

Figure 2.5: Schematic of the working principle of a double sided strip detector.

		SVD1	SVD2
Beam pipe radius	(mm)	20	15
Layers		3	4
Radii of layers	(mm)	30.0/45.5/60.5	20.0/43.5/70.0/88.8
Ladders per layer		8/10/14	6/12/18/18
Modules per ladder		2/3/4	2/3/5/6
Number of Modules		102	246
Module width	(mm)	32.0	25.6 (33.28 for layer 4)
Module length	(mm)	54.5	76.8 (74.75 for layer 4)
Module thickness	(µm)	300	300
Pitch $r\phi$	(µm)	25	50 (65 for layer 4)
Pitch z	(µm)	84	75 (73 for layer 4)

Table 2.1: Parameters of the two different vertex detector configurations [12, 42].

cosmic muons. The resolution of the SVD2 is determined as [42]

$$\sigma_{r\phi} = 22 \oplus 36/\left(p\beta\sin(\theta)^{3/2}\right)\,\mu\text{m}$$
$$\sigma_{z} = 28 \oplus 32/\left(p\beta\sin(\theta)^{5/2}\right)\,\mu\text{m},$$

where p is the momentum and β is the velocity.

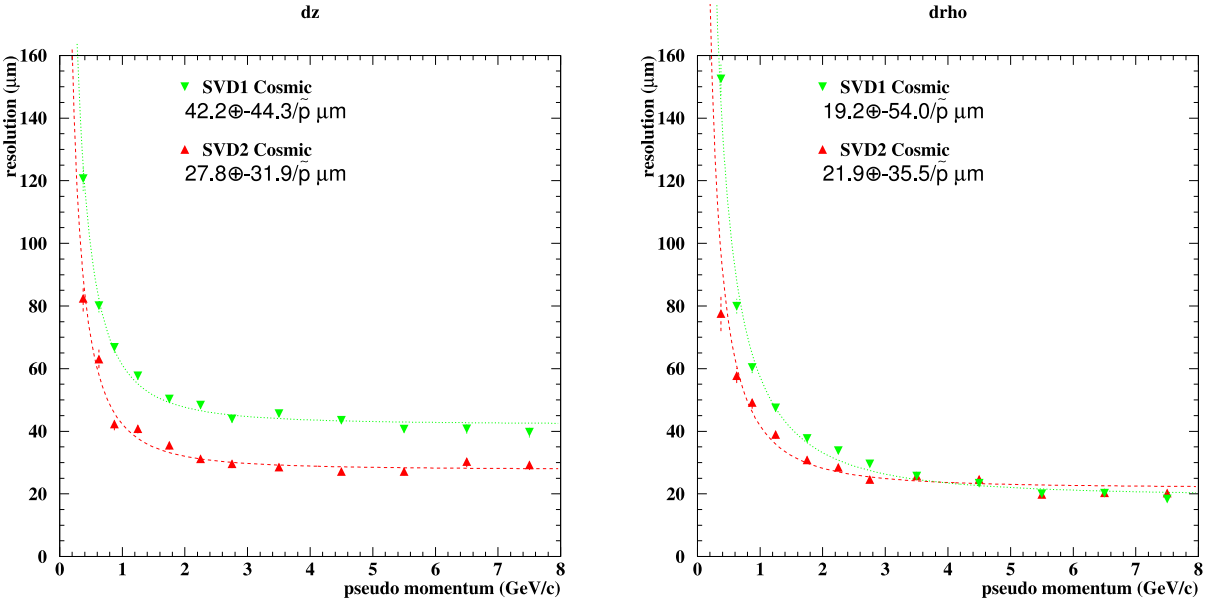

Figure 2.6: Impact parameters of the SVD2 compared to the SVD1 [42]

2.2.3 Central Drift Chamber

The Central Drift Chamber (CDC) is the main tracking subsystem of the Belle detector for measuring the momentum of particles from their curvature in the magnetic field of 1.5 T produced by the solenoid. The CDC also measures dE/dx with an accuracy of 6 % to provide particle identification together with the dedicated ACC and TOF subsystems (see below).

The layout of the CDC can be seen in Figure 2.7. It is filled with a gas mixture consisting of 50 % helium and 50 % ethane. The low-Z gas is chosen to minimize multiple Coulomb scattering and thus ensuring good momentum resolution, especially for low momentum tracks. The CDC contains a total of 8400 drift cells organized in 50 cylindrical layers (Figure 2.8). A drift cell is made up of eight negatively biased field wires providing an electric field which surrounds a positively biased sense wire. Approximately half of the wires are in z direction to provide measurement of the transversal momentum p_t, while the other half is slanted by a small angle of ± 50 mrad. These stereo wires allow to measure the polar angle of the track. The longitudinal momentum can be determined from the measured transversal momentum and the polar angle.

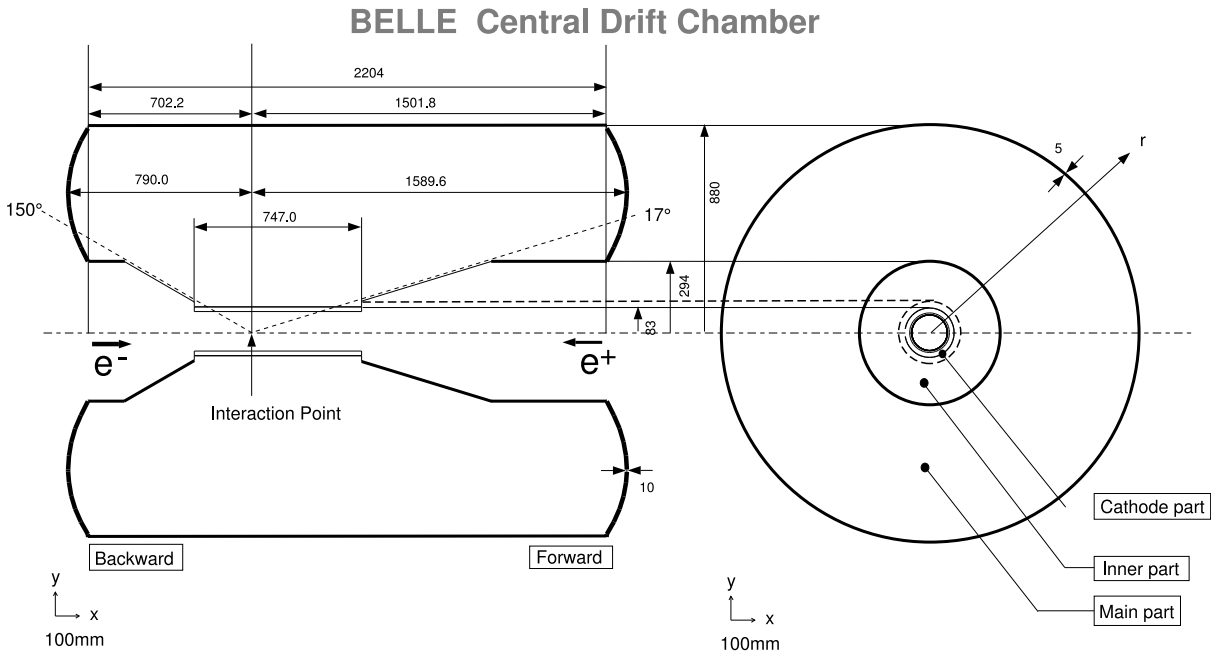

Figure 2.7: Layout of the Central Drift Chamber [12].

When a charged particle passes a drift cell, ionisation electrons from the gas drift towards the sensor wire. Due to the very small diameter of the sense wires (30 µm), the strong electric field close to the wire accelerates the electrons sufficiently to cause secondary ionisations which in turn cause further ionisations resulting in a cascade of charge. This process, called gas amplification, increases the signal by more than 10^6. Before amplification, the electrons have a specific drift velocity, so the measured pulse height and drift time are related to the energy deposit and distance from the sense wire respectively. The resolution of the transverse momenta is [12]

$$\sigma(p_t) = 0.201\% p_t \oplus 0.290\% \beta,$$

where β is the velocity. From the energy deposition and the closest distance to the sensor wire, the drift distance, we can calculate the energy loss dE/dx. The distribution of dE/dx versus momentum is different for different particle types as can be seen in Figure 2.9. For kaons and pions with a momentum between 0.4 GeV/c and 0.6 GeV/c a separation of three standard deviations (σ) can be obtained.

2.2.4 Aerogel Cherenkov Counter

The Aerogel Cherenkov Counter (ACC) is used for particle identification in a momentum range between 1.0 GeV/c and 4.0 GeV/c. It utilizes the effect that particles will emit Cherenkov light when their speed exceeds the speed of light in a medium with refractive

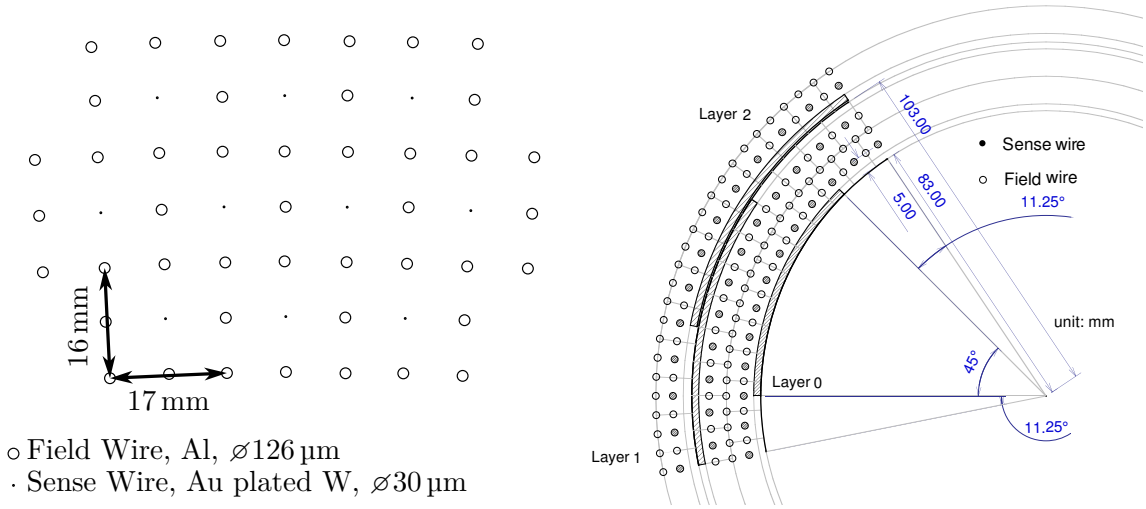

(a) Cell structure (b) Sector configuration

Figure 2.8: Wire configuration in the Drift Chamber [12].

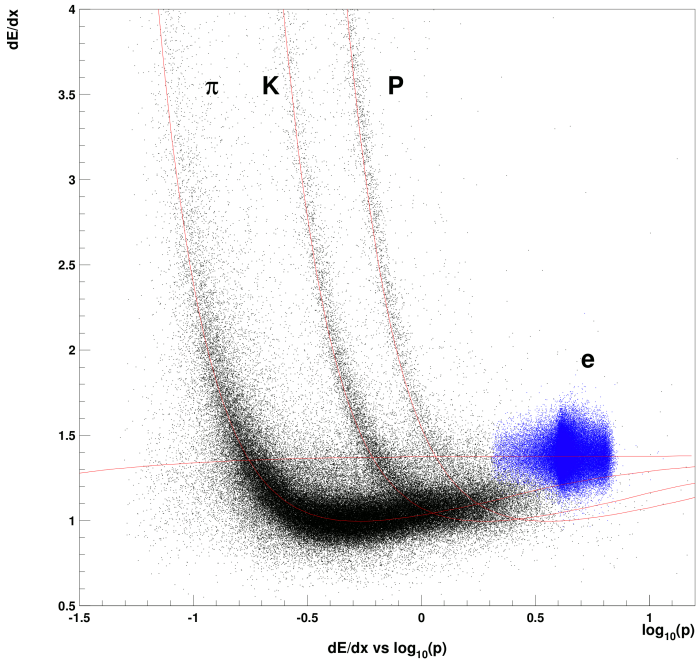

Figure 2.9: Measured dE/dx versus momentum in the CDC [12].

index n

$$n \geq \frac{1}{\beta} = \frac{1}{\sqrt{1 + \left(\frac{m}{p}\right)^2}} \tag{2.1}$$

Due to the different masses, pions can be distinguished from kaons by selecting a material with appropriate refractive index $n < n_0$ so that pions will emit Cherenkov light in the momentum range given above, while the heavier kaons will not. Thus the ACC works as a "threshold Cherenkov counter"

The ACC has 960 separate modules in the barrel region and 228 in the forward endcap, each consisting of an aluminum encased block of silica aerogel with refractive indices of 1.010, 1.013, 1.015, 1.020, 1.028 or 1.030, depending on the polar angle. The layout can be seen in Figure 2.10. One or two photomultiplier tubes are attached to each block to detect the Cherenkov light pulses.

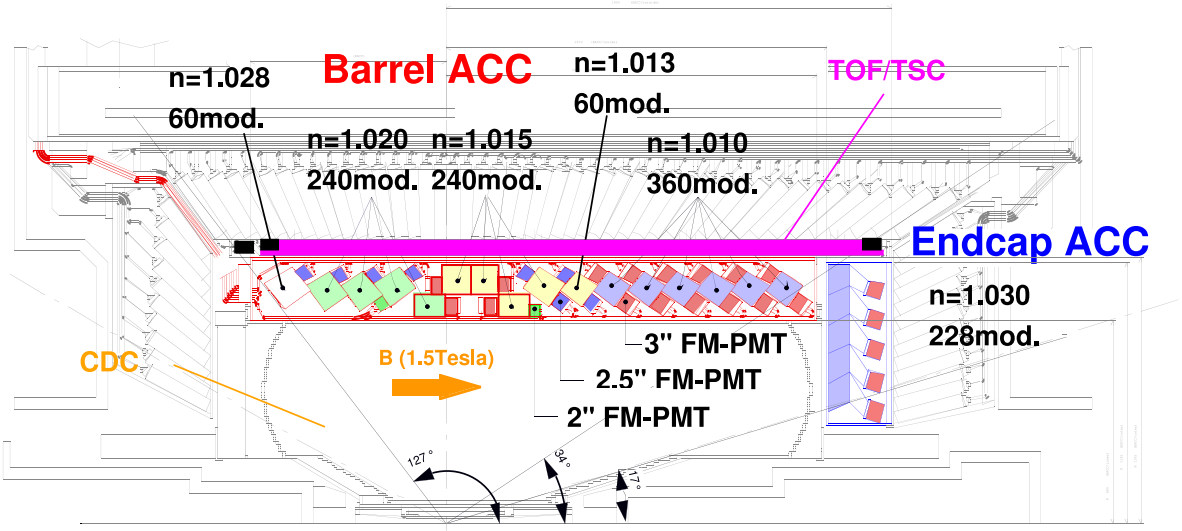

Figure 2.10: Arrangement of the ACC modules [12].

For particles with momenta up to 4 GeV/c, the kaon identification efficiency is 80 % or more while the pion fake rate remains below 10 %. Below the pion threshold of 1 GeV/c electron identification is possible as well.

2.2.5 Time of Flight Counter

The Time of Flight Counter (TOF) gives particle identification for particles below 1.2 GeV/c. The mass m of a particle can be determined from the time T needed to reach the TOF at $L = 1.2$ m from the interaction point, which can be expressed as

$$m^2 = \left(\frac{1}{\beta^2} - 1\right) p^2 = \left(\left(\frac{cT}{L}\right)^2 - 1\right) \tag{2.2}$$

using the momentum p obtained from the CDC measurement. Figure 2.11 shows the mass distribution for each track in hadron events. Clear peaks corresponding to pions, kaons and protons can be seen.

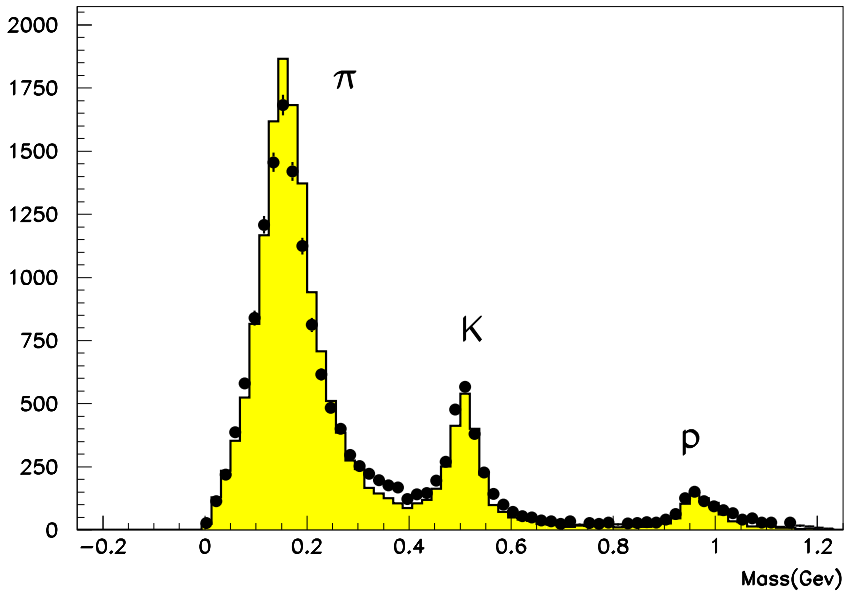

Figure 2.11: Particle identification using TOF measurements showing a clear separation between π, K and p [12].

There are 64 TOF modules in the barrel region, covering the polar region of $33° < \theta < 121°$. Each of the modules consists of plastic scintillation counters attached to photomultiplier tubes and has a time resolution of 100 ps. The TOF also provides fast timing signals for the trigger system. In order to sustain high trigger rates, thin trigger scintillation counters (TSC) are placed just before the TOF modules.

When combining the information from the TOF measurement with the ACC and CDC information on dE/dx described before, a 3σ separation between charged kaons and pions is obtained for a momentum range up to 3.5 GeV/c.

2.2.6 Electromagnetic Calorimeter

The Electromagnetic Calorimeter (ECL) serves to identify electrons and photons by measuring their electromagnetic showers. The ECL consists of 8736 thallium-doped Caesiumiodide (CsI(Tl)) crystal counters. The tower-shaped CsI(Tl) crystals are 30 cm long, which corresponds to 16.2 radiation lengths. Each crystal is positioned to point towards the IP. The ECL is divided into a barrel and end cap part. The barrel part consists of 6624 crystals and the end cap part contains 1152 (960) crystals in the forward (backward) directions. The geometry of the ECL is shown in Figure 2.12.

When an electron or photon hits a crystal, its energy is deposited in electromagnetic showers produced by bremsstrahlung and pair production. Heavy charged particles (pions,

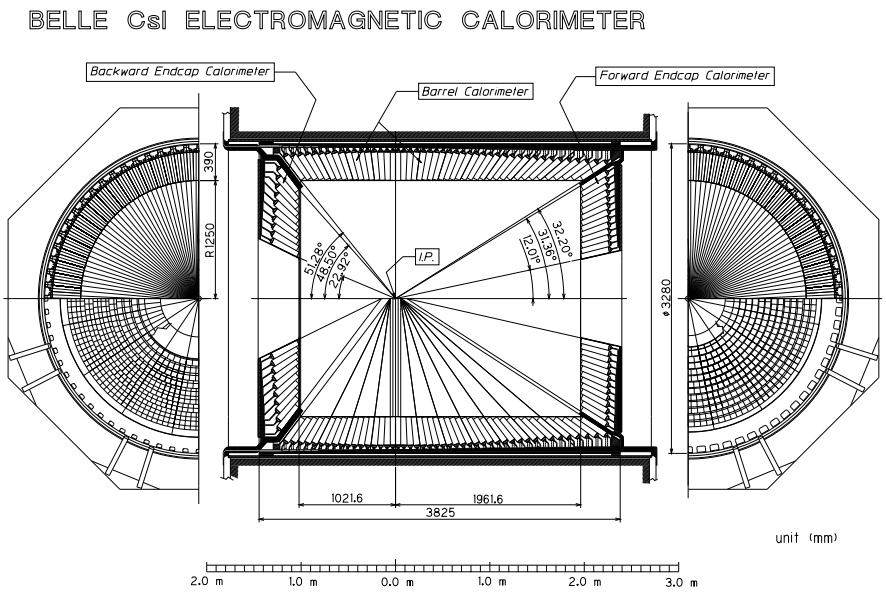

Figure 2.12: Schematics of the Belle Electromagnetic Calorimeter [12].

muons, etc.) deposit only a small amount of energy by ionisation (hadrons only have a small probability to deposit their entire energy in the ECL). Therefore, the ratio of the cluster energy measured by the ECL to the momentum of the charged track momentum as measured by the CDC, E/p, is close to unity for electrons and lower for other particles. In this way, electron identification can be performed.

The energy and position resolutions are given by [12]

$$\sigma_E = \frac{1.3\%}{\sqrt{E}} \qquad \sigma_{pos} = \left(0.27 + \frac{3.4}{E^{1/2}} + \frac{1.8}{E^{1/4}}\right) \text{ mm}$$

2.2.7 Solenoid

The superconducting solenoid provides a magnetic field of 1.5 T parallel to the z direction. The coil consists of a single layer niobium-titanium-copper alloy embedded in a high purity aluminium stabilizer and is wound around the inner surface of an aluminium support cylinder measuring 3.4 m in diameter and 4.4 m in length. Cooling is provided by circulating liquid helium through a tube on the inner surface of the aluminium cylinder.

2.2.8 K_L^0/μ Detector

The K_L^0/μ-Detector (KLM) which is housed in the flux return yoke surrounding the magnet is used to provide μ identification for tracks which reach the KLM ($p_t > 0.6\,\text{GeV}/c$). It is also able to detect the neutral K_L^0. A lot of material is needed to detect these particles efficiently due to their small interaction probability with material.

The KLM is realized as sampling calorimeter consisting of 15 superlayers of resistive plate counters (RPC) interleaved with 14 layers of 4.7 cm thick iron plates. The iron layers also serve as return-yoke for the magnetic field produced by the solenoid. Each RPC superlayer consists of two RPC modules to provide two-dimensional hit information.

Hadrons interacting with the iron plates may produce a shower of ionizing particles that are detected by the RPC layers, resulting in a cluster of hits in the KLM. A K_L^0 candidate can be distinguished from other charged hadrons because it will not leave an associated track in the CDC. Although muons leave a track in the CDC, they can still be distinguished because they do not feel strong interaction and therefore leave an energy according to a minimum ionizing particle.

2.2.9 Trigger System

A large part of the events seen by the Belle detector are not of interest as they originate from background processes like cosmic ray events, synchrotron radiation, beam-gas and beam-beam interactions. During normal operation (luminosity of $L = 10^{34}\,\mathrm{cm}^{-2}\mathrm{s}^{-1}$) the total event rate is around 200 Hz. Out of this rate, 100 Hz are physically interesting events. Besides hadronic events which could originate from a $B\overline{B}$ pair, events of interest are also two photon events, Bhabha scattering and μ pair production as these are also used for luminosity measurements and detector calibration.

A trigger system is used distinguish between interesting events which should be recorded and those to be discarded. It consists of a level 1 hardware trigger, a real-time level 3 software trigger and an off-line level 4 software trigger and obtains an efficiency of more than 99 % for $B\overline{B}$ events.

The Global Decision Logic (GDL) collects trigger signals from the sub-detectors and issues the level 1 decision within 2.2 µs of the beam crossing. It uses track information from CDC and TSC, information about the energy deposit in the ECL and information about muon hits in the KLM. The normal trigger rate is 200 Hz to 250 Hz but the system is designed to sustain a maximum trigger rate of 500 Hz.

The level 3 trigger is software based and used to further reduce the number of events to be stored. It performs a fast track reconstruction to discard events with do not contain a track originating close to the IP. All events which pass the level 3 criteria are stored. After offline reconstruction a level 4 trigger is applied. This trigger works similar to level 3 but can impose stricter requirements.

Chapter 3

Event Selection

This chapter describes how we select the decay $B^0 \to D^{*-}D^{*+}K^0_S$ from the recorded Belle data. For each event, Belle records the response from all sub detectors. The reconstruction software analyses these responses and provides, among other things, all reconstructed tracks from charged particles and a list of reconstructed photons in the calorimeter. Using this information, we now have to identify events which contain the decay $B^0 \to D^{*-}D^{*+}K^0_S$ and reconstruct the B^0 meson for these events.

Although Belle is running at the $\Upsilon(4S)$, not all events will contain a $B\overline{B}$ pair. In fact, only about a third of all hadronic events will produce a $B\overline{B}$ pair, the others will produce $u\overline{u}$, $d\overline{d}$, $s\overline{s}$ and $c\overline{c}$ pairs from e^+e^- annihilation, referred to as $q\overline{q}$ or continuum. A fraction of events will not contain hadrons at all but may come from QED processes, electron positron scattering, two photon processes or background processes like beam gas scattering or synchrotron radiation [43]. Even if we select $B\overline{B}$ events, only a small fraction of those B mesons will decay into $D^{*-}D^{*+}K^0_S$.

In order to optimize the selection of $B^0 \to D^{*-}D^{*+}K^0_S$ events we will use simulated events. This provides us a clean sample of events and allows to estimate the reconstruction efficiency (fraction of all signal events that we actually select). By optimizing the selection and the analysis on simulated events we avoid a possible bias: Knowing the input to the simulation, we can check if we are able to reproduce the correct values.

3.1 Data Sample

For this analysis we use the full data recorded by Belle running at the $\Upsilon(4S)$ between 2000 and 2008, a total of $703\,\text{fb}^{-1}$ which is equivalent to $(771.581 \pm 10.566) \times 10^6$ $B\overline{B}$ pairs. This data is divided into two parts: $(151.965 \pm 1.241) \times 10^6$ $B\overline{B}$ pairs ($141\,\text{fb}^{-1}$) collected with the old vertex detector SVD1 and $(619.620 \pm 9.441) \times 10^6$ $B\overline{B}$ pairs ($563\,\text{fb}^{-1}$) with the newer SVD2 vertex detector.

Decay		relative $\mathcal{B}$	generated $\mathcal{B}$
B^0	$\to D^{*+}D^{*-}K^0_S + cc$	$(0.41 \pm 0.35)\,\%$	$100.00\,\%$
D^{*+}	$\to D^0\pi^+_{slow}$	$(67.70 \pm 0.50)\,\%$	$68.80\,\%$
	$\to D^+\pi^0_{slow}$	$(30.70 \pm 0.50)\,\%$	$32.20\,\%$
D^0	$\to K^-\pi^+$	$(3.87 \pm 0.05)\,\%$	$15.03\,\%$
	$\to K^-\pi^+\pi^0$	$(13.90 \pm 0.50)\,\%$	$53.71\,\%$
	$\to K^-\pi^+\pi^+\pi^-$	$(8.07 \pm 0.20)\,\%$	$31.26\,\%$
D^+	$\to K^-\pi^+\pi^+$	$(9.13 \pm 0.19)\,\%$	$100.00\,\%$
K^0_S	$\to \pi^+\pi^-$	$(69.20 \pm 0.05)\,\%$	$100.00\,\%$

Table 3.1: World average branching fractions according to [46] and generated branching fractions for the signal B^0. The generated branching fractions are the central values of the measured ones normalized to 100 %. For the charged conjugates for D mesons (D^{*-}, $\overline{D}^0$, D^-) the charges of pions and kaons are reversed.

3.2 Event Generation

As mentioned, we perform reconstruction and analysis first on simulated $B^0 \to D^{*-}D^{*+}K^0_S$ events. This signal Monte Carlo (MC) production occurs in two stages. Firstly, the physical decay process is simulated using EvtGen[44]. In a second step the response of the Belle detector is modelled with GEANT[45], a software package designed to simulate interactions between particles and matter. GEANT traces the particles provided by EvtGen through a simulated detector and returns a signal event resembling a real detector output.

The signature of $B^0 \to D^{*-}D^{*+}K^0_S$ decays may differ for both versions of the SVD, so signal MC was generated under both, SVD1 and SVD2 conditions. A set of 15×10^6 events was simulated for each SVD.

We generated exclusively events which contain $\Upsilon(4S) \to B^0\overline{B}^0$. One B meson decays generically and the other decays exclusively into $B^0 \to D^{*-}D^{*+}K^0_S$ where the products will continue to decay as seen in Table 3.1. We generate the events without CP violation and distributed flat in phase space.

3.3 $B\overline{B}$ Event Selection

A standard set of selection criteria, defined in [43], is used to suppresses non-hadronic and hadronic events.

- At least three "good" charged tracks must exist. A "good" charged track is defined as

$$p_T > 0.1\,\mathrm{GeV}/c \qquad dr < 2.0\,\mathrm{cm} \qquad |dz| < 4.0\,\mathrm{cm}$$

where p_T is the transverse momentum, dr and dz are the radial and the z distance of the closest approach to the IP.

- At least two "good" neutral cluster in the barrel region of the ECL, defined as

$$E_{cluster} > 0.1\,\text{GeV} \qquad -0.7 < \cos\theta < 0.9$$

where $E_{cluster}$ is the energy deposit and θ is the polar angle

- The sum of momentum magnitudes in the z direction calculated in the $\Upsilon(4S)$ rest frame, p_z^{CMS}, must be less than half the total available energy, $\sqrt{s}$,

$$\sum |p_z^{CMS}| \leq 0.5\sqrt{s}$$

- The primary vertex calculated from the "good" charged tracks must satisfy

$$dr < 1.5\,\text{cm} \qquad |dz| < 3.5\,\text{cm}$$

- Assuming the pion mass for "good" charged tracks, the total visible energy in the $\Upsilon(4S)$ rest frame, E_{vis}^{CMS}, should be,

$$E_{vis}^{CMS} > 0.18\sqrt{s}$$

- The total energy of "good" neutral clusters in the $\Upsilon(4S)$ rest frame, $E_{cluster}^{CMS}$, has to be inside,

$$0.1\sqrt{s} < \sum E_{cluster}^{CMS} < 0.8\sqrt{s}$$

- The invariant mass of the particles in each hemisphere defined as perpendicular to the boost, M_{jet}, must satisfy,

$$M_{jet} > 1.8\,\text{GeV}/c^2$$

These selection criteria retain more than 99 % of $B\overline{B}$ events while reducing the contamination from non-hadronic processes to less than 5 %. The fraction of non-$B\overline{B}$ hadronic events ($q\overline{q}$, continuum) is reduced by 20 %

3.4 CP Side Reconstruction

As mentioned in Section 1.4.3 we have two B^0 mesons. The one decaying into the final-state $B^0 \to D^{*-}D^{*+}K_S^0$, is called the CP side, B_{CP}. This is the B^0 meson we will fully reconstruct. The other B meson is called the tag side, B_{tag}.

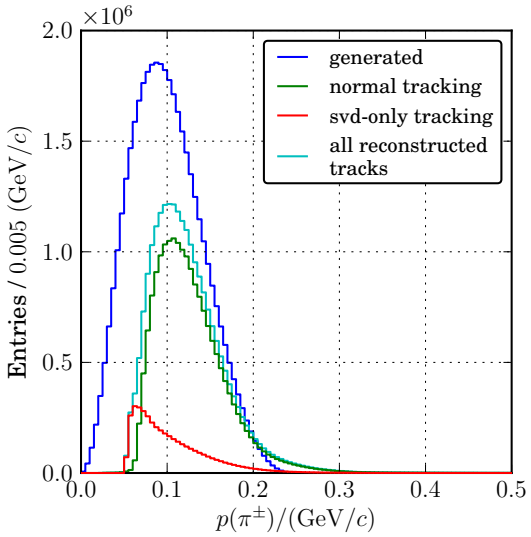

Figure 3.1: Momentum spectrum in the lab frame for slow pions from $D^{*+} \to D^0\pi^+_{slow}$ for generated and correctly reconstructed tracks.

3.4.1 Track Selection

In this analysis we differentiate between two distinct classes of pions: "normal" pions used in the reconstruction of D and K^0_S mesons and "slow" pions which are used to reconstruct D^* mesons. Those two classes of pions are in a very different momentum range so that we have to apply different cuts to them.

For "normal" tracks, a loose selection criteria is applied to reject poorly reconstructed tracks,

$$dr < 0.4\,\text{cm} \qquad\qquad |dz| < 5\,\text{cm}$$

where dr and $|dz|$ represent the distance of closest approach between the track and the IP in the xy plane and the z direction respectively. Due to the small mass difference between $D^{*\pm}$ and D mesons, the pions from the decay $D^{*\pm} \to D^0\pi^\pm_{slow}$ are almost at rest in the $D^{*\pm}$ frame. Phase space restrictions in $B^0 \to D^{*-}D^{*+}K^0_S$ also causes the $D^{*\pm}$ mesons to have a low momentum so that the maximum momentum of these slow pions in the lab system is around $250\,\text{MeV}/c$ (see Figure 3.1). Since one or two of these are required for the reconstruction of each event, an extra tracking algorithm, which tries to reconstruct tracks only from hits in the SVD, is enabled for this analysis. However, this leads to a higher fake track rate so these SVD only tracks are not taken into account for the reconstruction of D mesons as the momentum of their children is high enough that the SVD only tacking does not give significant improvement.

No cut on dr and $|dz|$ is performed and no SVD hits are required for slow pion tracks but the momentum of those tracks is restricted to be

$$p(\pi^\pm_{slow}) < 0.3\,\text{GeV}/c.$$

3.4.2 Particle Identification

Pions and kaons cannot be distinguished unambiguously. However, the CDC, ACC and TOF sub-detectors are able to provide a likelihood that a charged track is one or the other, a likelihood ratio is constructed,

$$\mathcal{P}\left(\mathrm{K}:\pi\right) = \frac{\mathcal{L}_{\mathrm{K}}}{\mathcal{L}_{\mathrm{K}} + \mathcal{L}_{\pi}}.$$

$\mathcal{P}\left(\mathrm{K}:\pi\right)$ is the likelihood that a track is a kaon compared against a pion hypothesis. $\mathcal{L}_i$ $(i = \mathrm{K}, \pi)$ is the likelihood that the particle is of type i and is calculated as

$$\mathcal{L}_i = \mathcal{L}_i^{CDC} \times \mathcal{L}_i^{TOF} \times \mathcal{L}_i^{ACC}$$

where each component $\mathcal{L}_i^{DET}$ is the likelihood that the particle is of type i in the respective sub-detector. The resulting likelihood ratio for all reconstructed tracks is shown in Figure 3.2

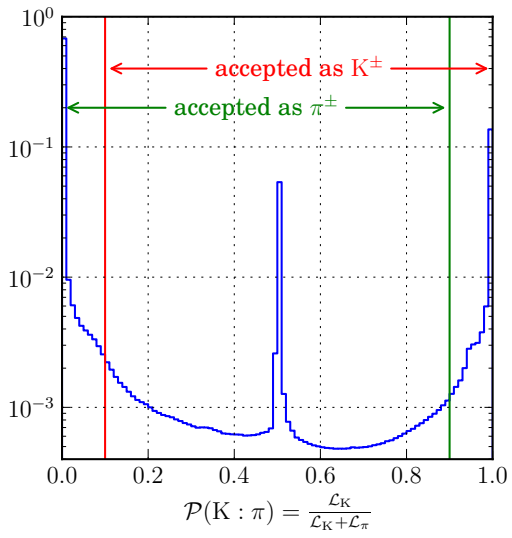

Figure 3.2: Particle identification likelihood ratio for all reconstructed tracks. The peak at 0.5 is caused by tracks for which no particle id information is available, such as tracks reconstructed only in the SVD.

For a track to be accepted as a pion it must satisfy

$$\mathcal{P}\left(\mathrm{K}:\pi\right) < 0.9$$

which means the track will be accepted as a pion unless there is a greater than 90 % likelihood that the track is a kaon. For a track to be accepted as a kaon

$$\mathcal{P}\left(\mathrm{K}:\pi\right) > 0.1$$

Momentum (GeV)	dr (cm)	$d\phi$ (rad)	z_{dist} (cm)	fl (cm)
< 0.5	> 0.05	< 0.30	< 0.8	–
$0.5 - 1.5$	> 0.03	< 0.10	< 1.8	> 0.08
> 1.5	> 0.02	< 0.03	< 2.4	> 0.22

Table 3.2: The "goodKs" cuts. dr is the shortest radial distance between any of the two daughter tracks and the IP, $d\phi$ is the azimuthal angle between the momentum vector and decay vertex of a K^0_S candidate, z_{dist} is the distance between the two K^0_S daughter tracks at their point of interception and fl is the flight length of the K^0_S in the xy plane.

This cuts are quite loose and therefore there is a region of overlap where tracks can be considered to be both, a pion and a kaon. No particle identification (PID) cut is applied for slow pion tracks due to their low momentum and possible SVD-only reconstruction,

3.4.3 π^0 Candidates

The π^0 is reconstructed as

$$\pi^0 \to \gamma\gamma$$

and is subject to the following cuts:

$$E_\gamma > 0.03\,\text{GeV}$$

$$p(\pi^0) > 0.2\,\text{GeV}/c \qquad\qquad p(\pi^0_{\text{slow}}) < 0.3\,\text{GeV}/c$$

where E_γ is the energy of each γ and $p(\pi^0)$ the momentum of the reconstructed π^0, both in the laboratory frame. These cuts help to reduce the effects of misreconstruction as they remove contributions from noise in the calorimeter. A cut on the invariant mass was also applied. It will be discussed in Section 3.4.8.

3.4.4 K^0_S Candidates

K^0_S candidates are already provided by the Belle software. They are reconstructed from two charged tracks without any particle ID requirement and only a loose mass window of $\pm 30\,\text{MeV}/c^2$ around the PDG mass value is applied. In addition, we require all K^0_S candidates to pass the "`goodKs`" criteria [47], which are momentum dependent cuts on several variables of the reconstructed K^0_S; they are summarized in in Table 3.2. Furthermore the invariant mass is subject to a cut similar to the π^0; see Section 3.4.8.

3.4.5 D^0 and $D^\pm$ Candidates

D^0 and $D^\pm$ mesons are reconstructed by combining pion and kaon tracks according to the decay channels in Table 3.1 and applying a cut on the invariant mass. This cut will be discussed in Section 3.4.8.

A vertex fit is performed on the resulting D candidate to get the optimal vertex resolution.

To achieve a good vertex resolution only tracks with a sufficient amount of hits in the vertex detector are selected for vertexing of D mesons. The number of associated hits, N^{SVD}, must be

$$N_{r\phi}^{SVD} \geq 1 \qquad\qquad N_{z}^{SVD} \geq 2.$$

All tracks used for in the D reconstruction that satisfy this condition are fitted on a common vertex and all other tracks are constrained to originate from the same vertex. Then a new D momentum is calculated using the updated track information. No vertex fit is performed if less than two tracks fulfil this requirement.

3.4.6 $\mathrm{D}^{*\pm} \to \mathrm{D}^0\pi^{\pm}_{\mathrm{slow}}$, $\mathrm{D}^+\pi^0_{\mathrm{slow}}$ Candidates

The $\mathrm{D}^{*\pm}$ is reconstructed from a D meson and a slow pion. As mentioned, the $\pi^{\pm}_{\mathrm{slow}}$ is not subject to PID or track quality cuts and also the π^0_{slow} is not subject to the π^0 momentum threshold cut. Both, $\pi^{\pm}_{\mathrm{slow}}$ and π^0_{slow} are required to have a momentum smaller than $0.3\,\mathrm{GeV}/c$. In the case of $\mathrm{D}^{*\pm}$ it is better to cut on the mass difference between the reconstructed $\mathrm{D}^{*\pm}$ and the daughter D meson as the resolution of the resulting distribution is much better. The cut on the mass difference will be explained in more detail in Section 3.4.8.

The lifetime of the $\mathrm{D}^{*\pm}$ is less than $10^{-23}\,\mathrm{s}$ so we can safely assume its vertex position to be identical with that of the B meson. Since the momentum resolution of the slow pions is poor compared to the tracks used to reconstruct the D vertex we do not perform a vertex fit at this point as it would not improve the vertex resolution.

3.4.7 $\mathrm{B}^0 \to \mathrm{D}^{*-}\mathrm{D}^{*+}\mathrm{K}^0_{\mathrm{S}}$ Candidates

Now we can reconstruct $\mathrm{B}^0 \to \mathrm{D}^{*-}\mathrm{D}^{*+}\mathrm{K}^0_{\mathrm{S}}$ from all $\mathrm{D}^{*\pm}$ and $\mathrm{K}^0_{\mathrm{S}}$ candidates. To reduce background, only one of the $\mathrm{D}^{*\pm}$ mesons may decay into $\mathrm{D}^{\pm}\pi^0_{\mathrm{slow}}$. The B^0 vertex is determined by fitting only the granddaughter D pseudo tracks for which the vertex fit was successful. The $\mathrm{K}^0_{\mathrm{S}}$ is excluded due to it's long flight length and the $\pi^{\pm}_{\mathrm{slow}}$ are excluded due to their bad momentum resolution. To improve the vertex position we constrain the fit to be consistent with the IP Profile [48], which is modelled as a three dimensional gaussian and determined from hadronic events every 10 000 to 60 000 events. Its size is typically

$$\sigma_x = 100\,\mu\mathrm{m} \qquad\qquad \sigma_y = 5\,\mu\mathrm{m} \qquad\qquad \sigma_z = 3\,\mathrm{mm}.$$

To account for the finite flight length of the B meson and avoid a bias on the z position of the vertex, the IP profile is added to the fit as a virtual straight track along the boost axis called IP tube. The position uncertainty of this tube is size of the IP profile in the xy plane, smeared by an additional

$$\mathrm{IP}_{\mathrm{smear}} = 21\,\mu\mathrm{m}$$

to account for the transverse B decay length. After the vertex fit, the excluded K^0_S and the slow pions are constrained to come from the same vertex and the B^0 momentum is calculated using these updated momenta.

From 2-body kinematics we know that the energy of the B meson in the $\Upsilon(4S)$ frame, E_B^{CMS} must be half the total energy of the e^+e^- system in this frame: the beam energy E_{beam}^{CMS}. We can thus increase the resolution of the invariant mass of the B by not using the measured energy but by constraining it to the beam energy (beam constrained mass, M_{bc}):

$$M_{\text{bc}} = \sqrt{\left(E_{\text{beam}}^{CMS}\right)^2 - \left(p_B^{CMS}\right)^2}. \tag{3.1}$$

The difference between M_{bc} and the invariant mass is shown in Figure 3.3. One can clearly see the big improvement when using M_{bc} instead of the invariant mass. In addition, we use the difference between the reconstructed energy and the beam energy,

$$\Delta E = E_B^{CMS} - E_{\text{beam}}^{CMS}. \tag{3.2}$$

We retain only candidates which satisfy

$$5.24\,\text{GeV}/c^2 \leq M_{\text{bc}} \leq 5.30\,\text{GeV}/c^2 \quad \text{and} \quad -0.15\,\text{GeV} \leq \Delta E \leq 0.10\,\text{GeV}. \tag{3.3}$$

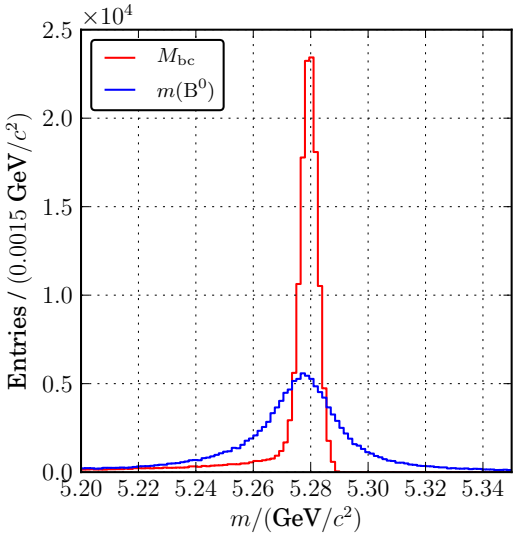

Figure 3.3: Comparison between the beam constrained mass (M_{bc}, red) and the invariant mass of the B^0 candidate for correctly reconstructed signal MC events.

Due to the combinatorial nature of the reconstruction there is a possibility that more than one B^0 can be reconstructed per event. This is called "B^0 multiplicity" and for signal MC it is 2.3 (see Figure 3.4). However, there can only be one reconstructed

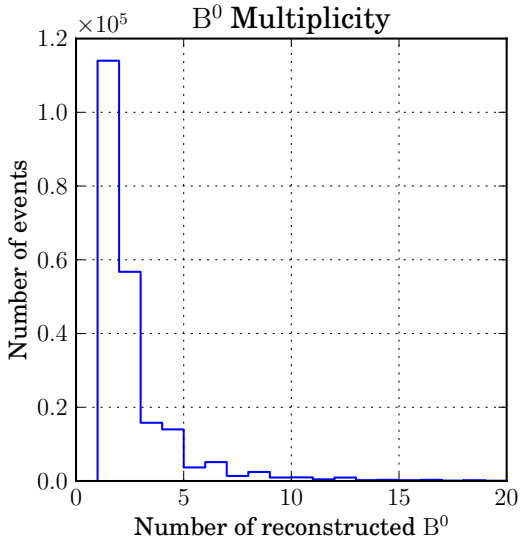

Figure 3.4: The number of reconstructed B^0 candidates per event in signal Monte Carlo.

$B^0 \to D^{*-}D^{*+}K^0_S$ per event. So it is necessary to choose the best candidate using the so called "Best B" selection which will be detailed in Section 3.4.9.

One B^0 is considered "correct" in signal MC when all tracks which were used to determine the vertex can be matched to a corresponding generated particle. Thus the K^0_S, the slow pions and any π^0 are not required to be correctly reconstructed. This results in a correct reconstruction efficiency of 75.1 % on signal MC.

3.4.8 Invariant Mass Windows

To avoid systematic uncertainties due to a possible difference between MC and real data the invariant mass windows for π^0, K^0_S, D and $D^{*\pm}$ were determined from an inclusive data sample and chosen to be large enough that any remaining difference between MC and data can be ignored. We selected 10 million events from the complete Belle data, evenly distributed over the recorded luminosity. Reconstruction was performed identical to the analysis reconstruction described so far but only up to and including $D^{*\pm}$ reconstruction using very wide mass windows in all channels.

The invariant mass of the particles is then modeled using

$$\mathcal{P}(m) = f_{\text{sig}} \cdot \mathcal{P}_{\text{sig}}(m) + (1 - f_{\text{sig}})\mathcal{P}_{\text{bkg}}(m) \tag{3.4}$$

where $\mathcal{P}_{sig}(m)$ is a sum of Gaussian distributions (see Section 4.2.1),

$$\mathcal{P}_{\text{sig}}(m) = \sum_i^N w_i \cdot G(m; \sigma_i, \mu_i) / \sum_i^N w_i, \tag{3.5}$$

and $\mathcal{P}_{bkg}(m)$ is either a linear function in case of π^0, K^0_S or D or a threshold function in case of $D^{*\pm}$,

$$\mathcal{P}_{\text{bkg}}(m) = \begin{cases} p_0 \cdot m + p_1 & \text{for } \pi^0,\ K^0_S \text{ or D}, \\ m^{p_0} \cdot e^{p_1 m + p_2 m^2} & \text{for } D^{*\pm}. \end{cases} \tag{3.6}$$

The mass window is then determined from this distributions by taking the symmetric area around the maximum of $\mathcal{P}_{\text{sig}}(m)$ which contains 95 % of the area of $\mathcal{P}_{\text{sig}}(m)$ The different fits for all decay channels can be seen in Figures 3.5, 3.6 and 3.7.

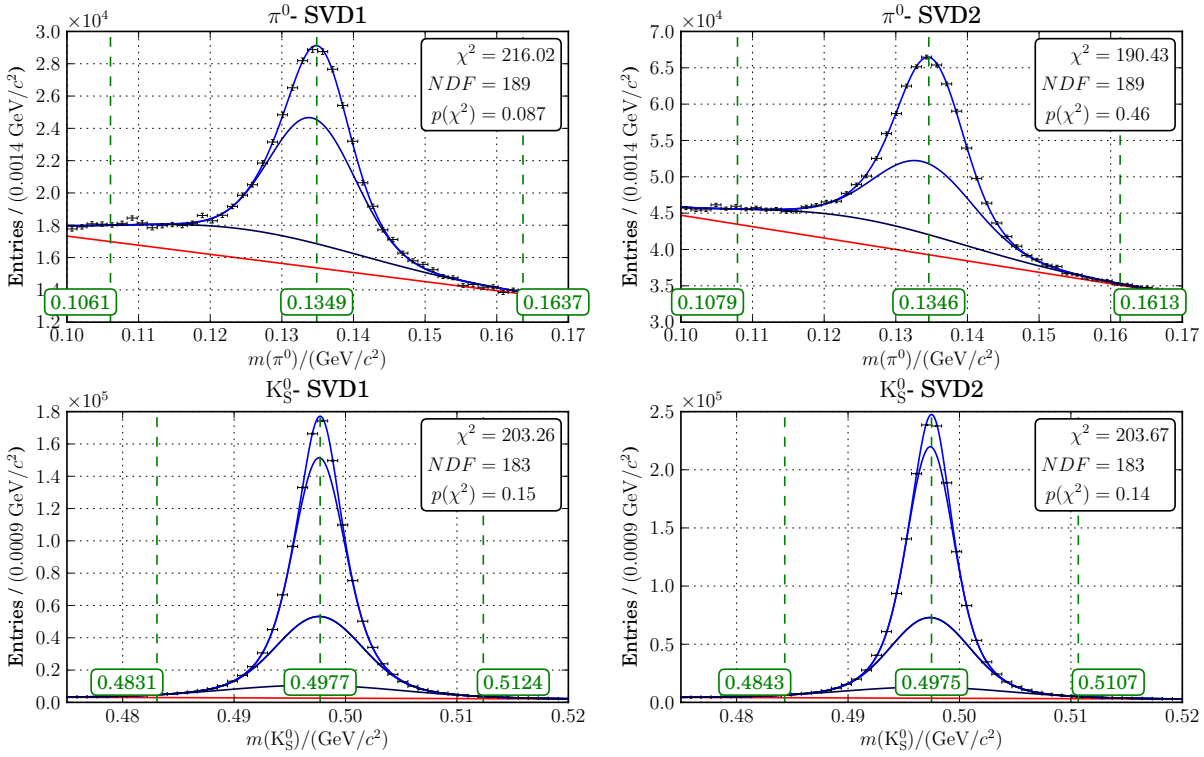

Figure 3.5: Mass limits for π^0 and K^0_S candidates. Red line denotes the background distribution, $\mathcal{P}_{\text{bkg}}(m)$, and the other lines show the separate gaussian distributions of $\mathcal{P}_{\text{sig}}(m)$.

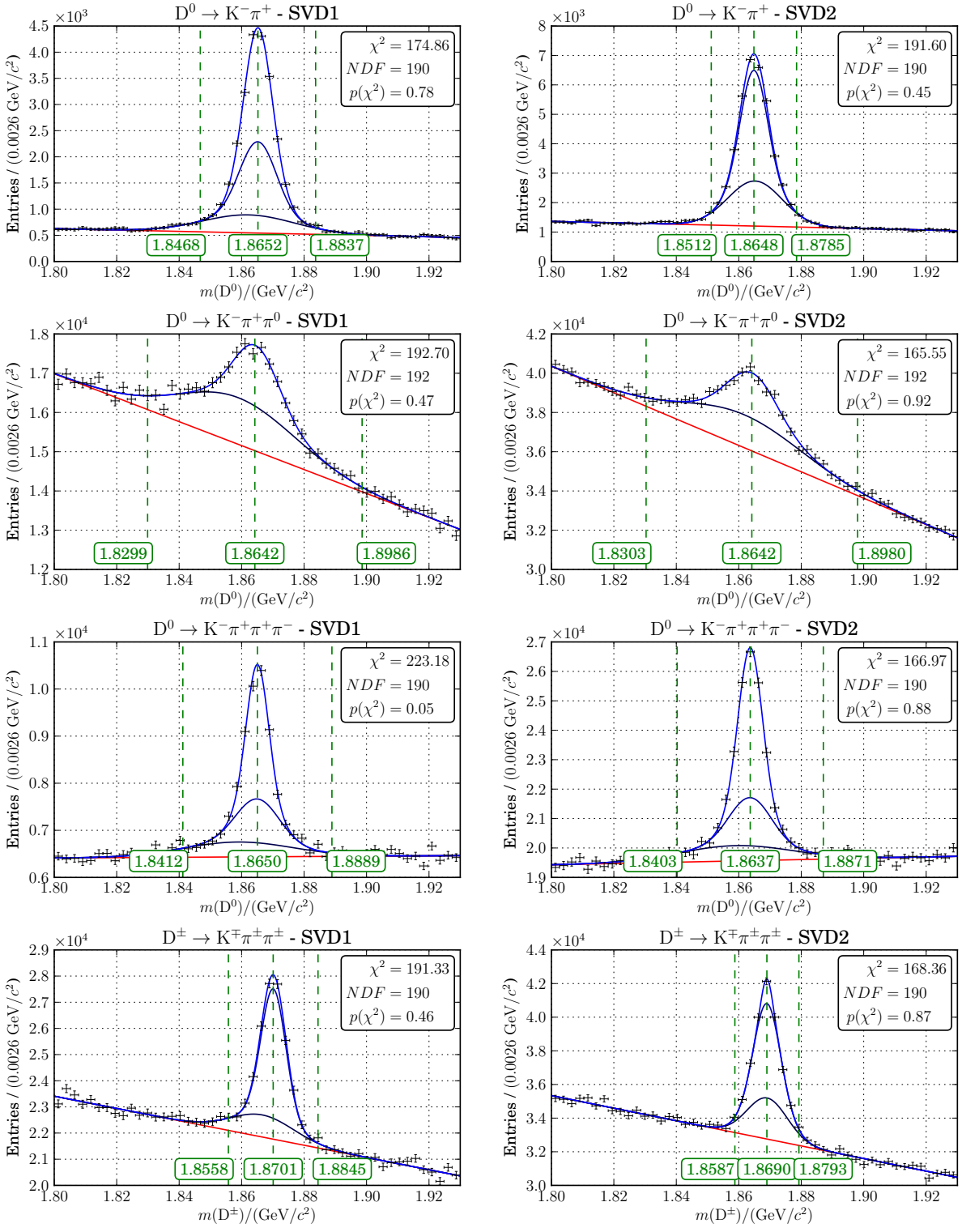

Figure 3.6: Mass limits for D candidates. Red line denotes the background distribution, $\mathcal{P}_{\text{bkg}}(m)$, and the other lines show the separate gaussian distributions of $\mathcal{P}_{\text{sig}}(m)$.

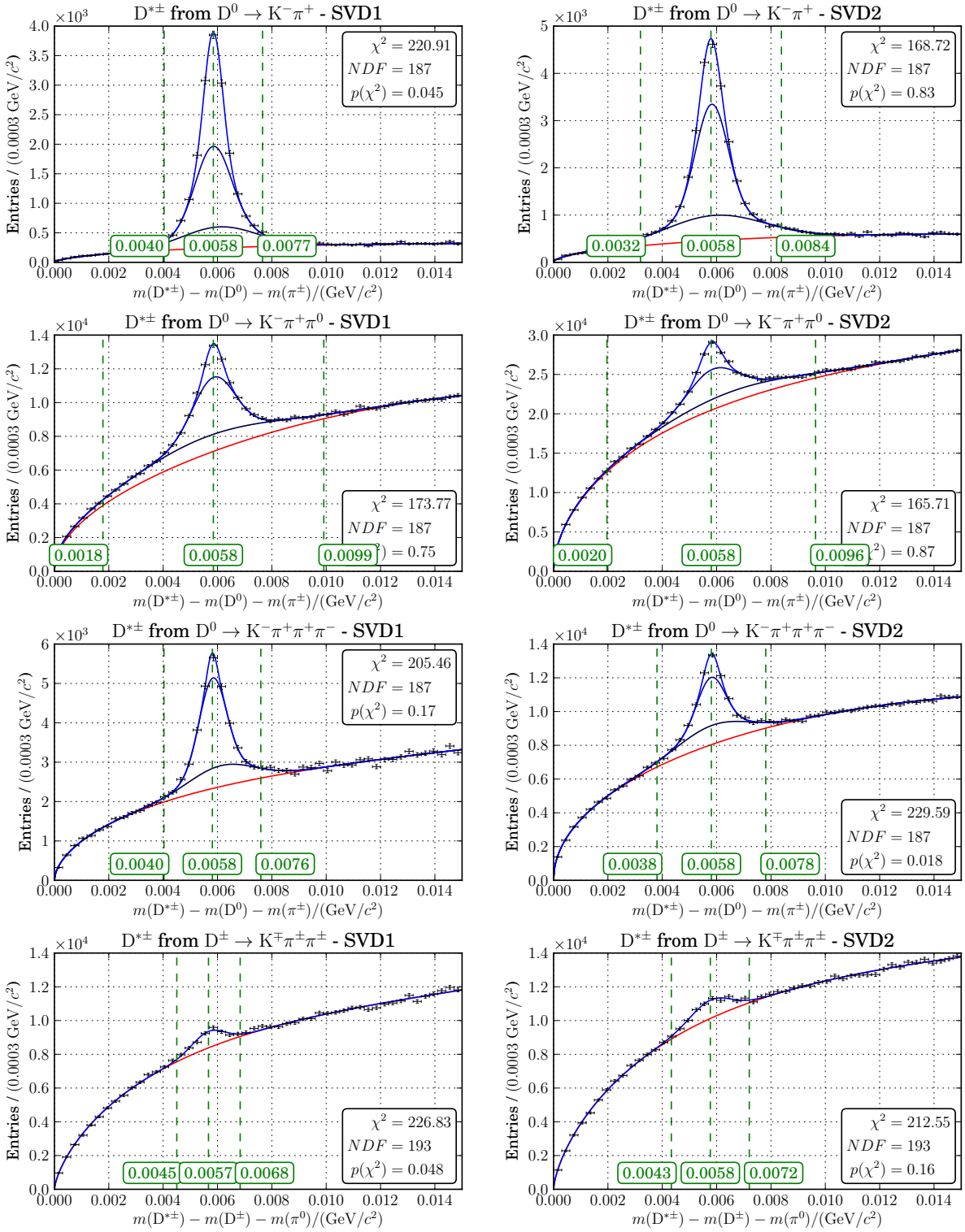

Figure 3.7: Mass limits for D* candidates. Red line denotes the background distribution, $\mathcal{P}_{\text{bkg}}(m)$, and the other lines show the separate gaussian distributions of $\mathcal{P}_{\text{sig}}(m)$.

		SVD1		SVD2	
Candidate	N	center	width	center	width
π^0	3	0.1349	0.0288	0.1346	0.0267
K^0_S	5	0.4977	0.0146	0.4975	0.0132
$D^0 \to K^-\pi^+$	3	1.8652	0.0185	1.8648	0.0137
$D^0 \to K^-\pi^+\pi^0$	2	1.8642	0.0343	1.8642	0.0339
$D^0 \to K^-\pi^+\pi^+\pi^-$	3	1.8650	0.0239	1.8637	0.0234
$D^\pm \to K^\mp\pi^\pm\pi^\pm$	3	1.8701	0.0143	1.8690	0.0103
$D^{*\pm}$ from $D^0 \to K^-\pi^+$	3	0.1454	0.0018	0.1454	0.0026
$D^{*\pm}$ from $D^0 \to K^-\pi^+\pi^0$	3	0.1454	0.0041	0.1454	0.0038
$D^{*\pm}$ from $D^0 \to K^-\pi^+\pi^+\pi^-$	3	0.1454	0.0018	0.1454	0.0020
$D^{*\pm}$ from $D^\pm \to K^\mp\pi^\pm\pi^\pm$	1	0.1406	0.0012	0.1407	0.0014

Table 3.3: Mass limits in GeV/c^2 for all reconstructed candidates given as the center value and the width accepted on each side. N denotes the number of Gaussians used for the signal shape in the fit to the inclusive data sample.

3.4.9 Best B Selection

For the Best B selection we use the mass likelihoods defined in Equation 3.5 to construct a likelihood for the B candidate:

$$\mathcal{L}_{B^0} = \mathcal{P}_{sig}^{D^{*+}} \times \mathcal{P}_{sig}^{D_{(+)}} \times \mathcal{P}_{sig}^{D^{*-}} \times \mathcal{P}_{sig}^{D_{(-)}} \times \mathcal{P}_{sig}^{K^0_S} \tag{3.7}$$

where $D_{(\pm)}$ denotes to the daughter D of the corresponding $D^{*\pm}$ and can either be a D^0 or $D^\pm$ depending on the reconstruction chain. The B candidate with the larges likelihood is taken as the correct B candidate. On signal MC this procedure results in the selected B candidate to be the correctly reconstructed (see Section 3.4.7) on 91.8 % of the time. The likelihoods for D and $D^{*\pm}$ candidates can be seen in Figure 3.8.

Figure 3.9 shows a flow chart of the full reconstruction of the B^0 meson CP side to give a quick overview of all cuts and reconstruction steps.

3.5 Tag Side Reconstruction

After successful reconstruction of the B_{CP}, all remaining tracks are assumed belong to the B_{tag} meson. To be able to extract CP information we need to determine the flavour and the decay vertex of this B_{tag}.

3.5.1 Flavour Tagging

First, we try to determine the flavour of the B_{tag} by using a flavour tagging algorithm called Hamlet [49]. It uses a binned multi dimensional likelihood method to estimate the flavour q and expected flavour dilution factor r which ranges from zero for no discrimination up

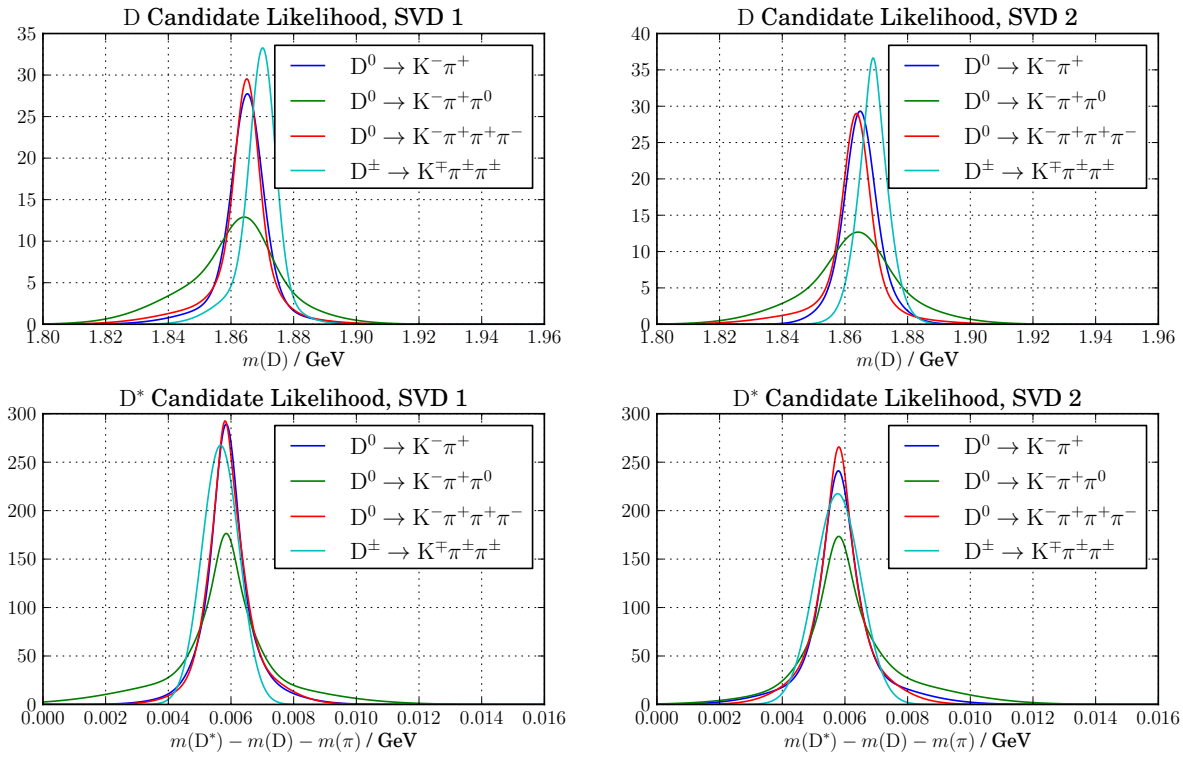

Figure 3.8: Likelihood for $D^\pm$, D^0 and $D^{*\pm}$ candidates used in BestB selection.

to one for unambiguous flavour assignment. Using a multi-dimensional lookup table, the signed probability, $q \cdot r$, is given by

$$q \cdot r = \frac{N(B^0) - N(\overline{B}^0)}{N(B^0) + N(\overline{B}^0)} \tag{3.8}$$

where $N(B^0)$ $\left(N(\overline{B}^0)\right)$ are the number of $B^0(\overline{B}^0)$ events in the corresponding bin of the lookup table prepared from a large sample of simulated events.

In a first stage all tracks are classified into four categories, Λ-like, slow-pion-like, lepton-like and kaon-like, and $(q \cdot r)_X$ is estimated using a set of kinematic variables for each category as discriminants. In the second stage, the $(q \cdot r)_X$ with the largest modulus is taken from the slow-pion-like and lepton-like categories while the kaon-like and Λ-like categories are combined using

$$(q \cdot r)_{K/\Lambda} = \frac{\prod[1 + (q \cdot r)_i] - \prod[1 - (q \cdot r)_i]}{\prod[1 + (q \cdot r)_i] + \prod[1 - (q \cdot r)_i]} \tag{3.9}$$

to account for the cases with multiple s quarks in an event. These variables are used to estimate the final event $q \cdot r$ from a second lookup table.

The flavour tagging procedure is not unambiguous. Depending on the flavour dilution factor, r, there is a certain fraction of events for which the flavour tag will be wrong.

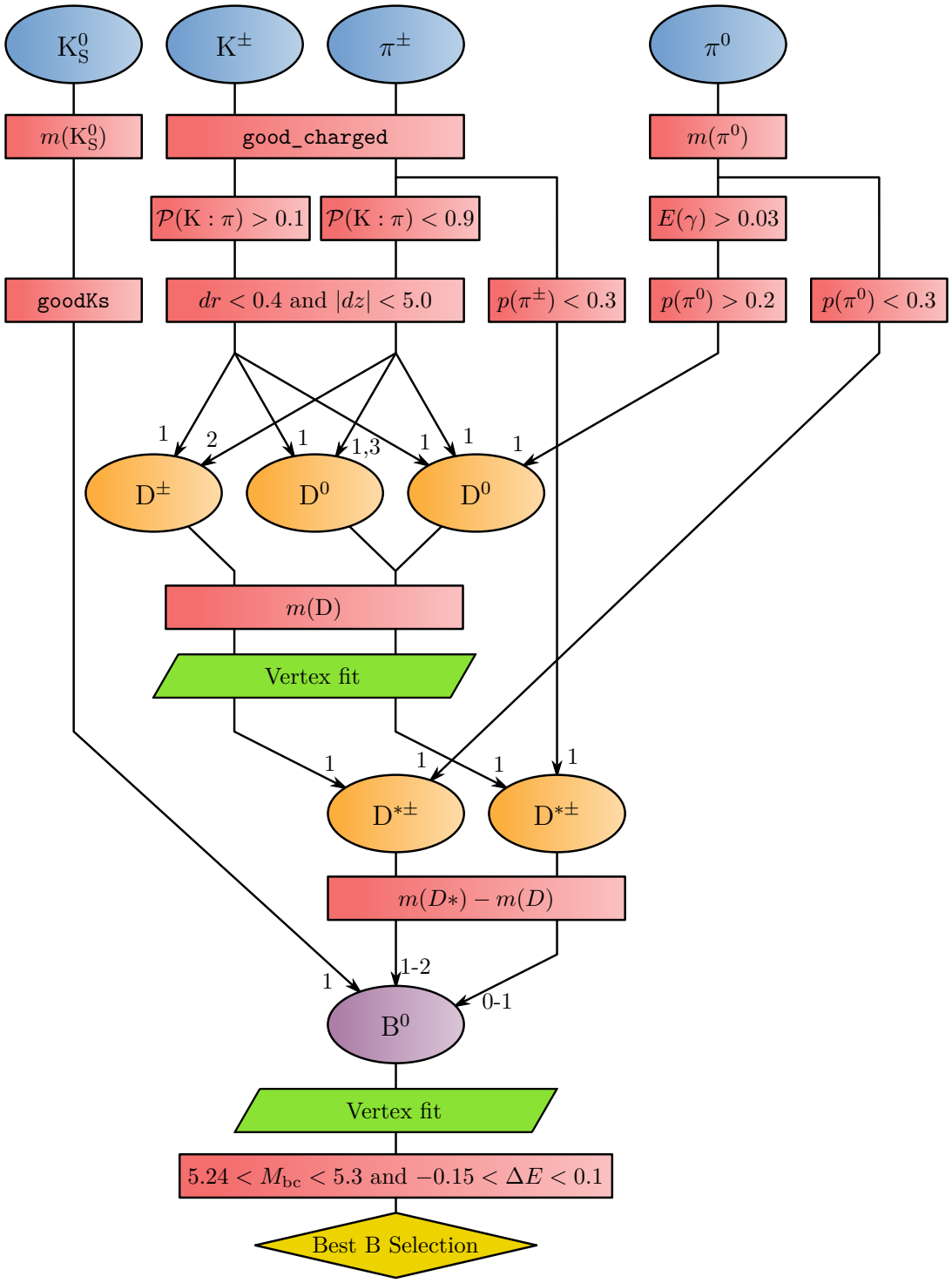

Figure 3.9: Flowchart of the full event selection and reconstruction. Blue circles show the reconstructed candidates already provided by the Belle software, orange circles are intermediate particles of the B^0 candidates (purple). The red boxes symbolize cuts on the candidates.

	SVD1		SVD2	
region of r	w	Δw	w	Δw
0.0 – 0.1	0.5	0.0	0.5	0.0
0.1 – 0.25	0.419	0.057	0.419	-0.009
0.25 – 0.5	0.330	0.013	0.319	0.010
0.5 – 0.625	0.234	-0.015	0.223	-0.011
0.625 – 0.75	0.171	-0.001	0.163	-0.019
0.75 – 0.875	0.100	0.009	0.104	0.002
0.875 – 1.0	0.023	0.005	0.025	-0.004

Table 3.4: Wrong tag fractions and differences, w and Δw, for SVD1 and SVD2 determined from $B^0 \to D^{*-}\ell^+\nu$ and its charge conjugate.

Furthermore this fraction might be different for $q = +1$ and $q = -1$ tags because the detector may not be completely charge-symmetric. This fraction is called wrong tag fraction, w, with the difference $\Delta w = w_{q=+1} - w_{q=-1}$.

Since the flavour tagging procedure is independent of the CP side we can determine w by looking at the decay of a flavour eigenstate instead of a CP eigenstate on the CP side and compare the flavour tag to the reconstructed flavour. In Belle the wrong tag fractions and differences, w and Δw are determined for seven different regions of r. For events with $|r| \leq 0,1$, there is negligible flavour discrimination so the wrong tag fraction is set to $w_0 = 0.5$. In all other regions, w and Δw are determined directly from data using the semi-leptonic decay $B^0 \to D^{*-}\ell^+\nu$ and its charge conjugate.

3.5.2 Tag Side Vertexing

After successful flavour tagging, the tag side vertex is determined. For this we use all tracks which were not used to reconstruct B_{CP} and fulfill the following requirements [50]:

- The number of hits, N^{SVD}, in the vertex detector associated with the track needs to be

$$N_{r\phi}^{SVD} \geq 1 \qquad\qquad N_{z}^{SVD} \geq 2$$

- The z-resolution of the track, σ_z, is required to fulfill

$$\sigma_z < 500\,\mu\text{m}.$$

- The radial distance to the B_{CP} vertex, dr_{CP}, has to be

$$dr_{CP} < 500\,\mu\text{m}.$$

Using the same IP tube constraint described in Section 3.4.7, those tracks are fitted on a combined vertex. While the χ^2 per degree of freedom is larger than 20, the track with the highest contribution to the χ^2 is removed and the fit is repeated. Tacks which have been identified as high p_T leptons are never discarded as they have a high probability to originate from the B_{tag} vertex.

3.6 Vertex Quality Cuts

Time dependent CP parameters are extracted from the Δt distribution which can be calculated from the z distance between the B_{CP} and B_{tag} vertices,

$$\Delta t = \frac{\Delta z}{\beta\gamma c} = \frac{z_{CP} - z_{\text{tag}}}{\beta\gamma c} \tag{3.10}$$

where $\beta\gamma = 0.425$ is the Lorentz boost of the $\Upsilon(4S)$.

Normally, the quality of the vertex fit is determined by the standard χ^2/ndf of the vertex fit. However, this value is correlated with the z-position of the vertex due to the IP constraint in the xy plane and would bias the Δt distribution if used as quality indicator. We therefore introduce a new measure of vertex quality

$$h = \frac{\sum_{i=1}^{n} \chi_i^2}{2n - 2} \tag{3.11}$$

with n, χ_i^2 being the number of tracks and the χ^2 contribution of the ith track respectively. This basically corresponds to the reduced χ^2 without the IP constraint taken into account and has been shown to be unbiased [51].

The following selection criteria are imposed on the vertex quality for both CP side and tag side vertices [50]

- Vertexing procedure has to be successful.
- The z-error of the vertex, σ_z, has to fulfil $\sigma_z < 0.2\,\text{mm}$ and we require $h < 50$ for multi track vertices.
- For single track vertices we require $\sigma_z < 0.5\,\text{mm}$.

and in addition we impose

$$-70\,\text{ps} \leq \Delta t \leq 70\,\text{ps}. \tag{3.12}$$

Chapter 4

Branching Fraction Measurement

The branching fraction of $B^0 \to D^{*-}D^{*+}K^0_S$ assuming equal production of B^0–$\overline{B}^0$ and B^+–B^- pairs is given by,

$$\mathcal{B}\left(B^0 \to D^{*-}D^{*+}K^0_S\right) = \frac{Y\left(B^0 \to D^{*-}D^{*+}K^0_S\right)}{\epsilon\left(B^0 \to D^{*-}D^{*+}K^0_S\right) N(B\overline{B})}. \tag{4.1}$$

The signal yield, $Y(B^0 \to D^{*-}D^{*+}K^0_S)$, is the number of $B^0 \to D^{*-}D^{*+}K^0_S$ events found in the total data set, $N(B\overline{B})$. Since we will not be able to reconstruct all signal events that may have occurred we also need to evaluate the efficiency $\epsilon(B^0 \to D^{*-}D^{*+}K^0_S)$. This term is the probability of detecting any $B^0 \to D^{*-}D^{*+}K^0_S$ event. It also includes the fact that we only reconstruct a small part of the possible $B^0 \to D^{*-}D^{*+}K^0_S$ decay modes.

Normally, one global reconstruction efficiency is used. But in our case the structure in the Dalitz plot in data is not known and the reconstruction efficiency is dependent on the Dalitz variables. Because of this the reconstruction efficiency has to be determined as function of the Dalitz variables. Since we need a first estimation of the reconstruction efficiency we will assume flat phase space distribution for now and correct the efficiency once the Dalitz structure can be determined (see Section 4.8.

4.1 Reconstruction Efficiency

The raw reconstruction efficiency can be obtained easily by counting the number of events which were reconstructed correctly and divide it by the number of total simulated events

$$\epsilon^{(\mathrm{SVD1})}_{raw} = (1.862 \pm 0.011) \times 10^{-3} \qquad \epsilon^{(\mathrm{SVD2})}_{raw} = (6.943 \pm 0.022) \times 10^{-3}. \tag{4.2}$$

However, not all possible decays for $B^0 \to D^{*-}D^{*+}K^0_S$ are reconstructed. In fact, only a very small fraction of those decays can be reconstructed efficiently. Since we only simulate these specific decay modes we have to weight the raw reconstruction efficiency with the branching fraction of decay modes that we actually simulated with respect to the total

$B^0 \to D^{*-}D^{*+}K^0_S$ branching fraction. Given the simulated branching ratios for D^{*+},

$$\mathcal{B}_{sim}\Big(D^{*+} \to D^0\pi^+_{\text{slow}}\Big) = \mathcal{B}\Big(D^{*+} \to D^0\pi^+_{\text{slow}}\Big) \times \sum_i \mathcal{B}\Big({D^0}_i\Big) \tag{4.3}$$

$$\mathcal{B}_{sim}\Big(D^{*+} \to D^+\pi^0_{\text{slow}}\Big) = \mathcal{B}\Big(D^{*+} \to D^+\pi^0_{\text{slow}}\Big) \times \sum_i \mathcal{B}\Big({D^+}_i\Big) \tag{4.4}$$

where ${D^+}_i$ and ${D^0}_i$ denote to the ith reconstructed decay channel for the D meson, and assuming the same branching fraction for the charge conjugated decays it follows that

$$\mathcal{B}_{sim}\Big(B^0 \to D^{*-}D^{*+}K^0_S\Big) = \Big(\mathcal{B}_{sim}\Big(D^{*+} \to D^0\pi^+_{\text{slow}}\Big) + \mathcal{B}_{sim}\Big(D^{*+} \to D^+\pi^0_{\text{slow}}\Big)\Big)^2 \times \mathcal{B}\Big(K^0_S \to \pi^+\pi^-\Big). \tag{4.5}$$

With the individual branching ratios given in Table 3.1, the simulated fraction of the total $B^0 \to D^{*-}D^{*+}K^0_S$ branching ratio is

$$\mathcal{B}_{sim}\Big(B^0 \to D^{*-}D^{*+}K^0_S\Big) = 2.851 \times 10^{-2} \tag{4.6}$$

and the total reconstruction efficiency for Monte Carlo is:

$$\epsilon^{(\text{SVD1})}_{MC} = (5.309 \pm 0.032) \times 10^{-5} \qquad \epsilon^{(\text{SVD2})}_{MC} = (19.792 \pm 0.061) \times 10^{-5}. \tag{4.7}$$

The large difference between SVD1 and SVD2 can be explained by the SVD only track finding which is only possible for SVD2.

Due to small differences between simulated events and real data the efficiency can be different between MC and data. To correct for this effect we define an correction factor,

$$\xi_{CF} = \frac{\epsilon_{\text{Data}}}{\epsilon_{MC}}, \tag{4.8}$$

which is defined for a given set of cuts and has to be determined in a separate study. Four methods used in this analysis have associated correction factors: particle identification [52], low momentum tracking [53, 54], π^0 reconstruction [55] and K^0_S reconstruction [56]. All these corrections are provided for given momentum spectra of the final state particles used for reconstruction. For each possible decay we calculate the correction factors using the corresponding momentum spectra from signal MC and then calculate a weighted average between all the decay channels. We use the number of reconstructed events in one channel over the number of total reconstructed events as weight. The total correction factor for the reconstruction efficiency is simply the product of all ξ^i_{CF} and the final reconstruction efficiency becomes

$$\epsilon_{\text{Data}} = \epsilon_{MC} \prod_i \xi^i_{CF}, \tag{4.9}$$

with the individual ξ^i_{CF} from table 4.1. So assuming flat phase space distribution for $B^0 \to D^{*-}D^{*+}K^0_S$ events, the total, corrected reconstruction efficiency for data is

$$\epsilon^{(\text{SVD1})}_{\text{Data}} = (5.026 \pm 0.030) \times 10^{-5} \qquad \epsilon^{(\text{SVD2})}_{\text{Data}} = (17.902 \pm 0.055) \times 10^{-5}. \tag{4.10}$$

	SVD1	SVD2
particle identification	0.973	0.992
track reconstruction	0.972	0.927
π^0 reconstruction	1.023	1.004
K^0_S reconstruction	0.978	0.979
combined	0.947	0.905

Table 4.1: Reconstruction efficiency correction factors between MC and data for different sources obtained from control studies.

4.2 Data Model

The branching fraction is extracted from the data using a two dimensional extended unbinned maximum likelihood fit to M_{bc} and ΔE. The fit is performed the whole range accepted by the event selection (see Eq. 3.3) to determine the signal yield $Y(\mathrm{B}^0 \to \mathrm{D}^{*-}\mathrm{D}^{*+}\mathrm{K}^0_S)$.

With multiple components l which each have a probability density function (PDF) $\mathcal{P}_l(x;\theta)$ and a yield Y_l, the likelihood for a given set of parameters θ and yields Y_l is defined as

$$\mathcal{L}(\theta, Y_l) = \frac{\left(\sum_l Y_l\right)^N e^{-\sum_l Y_l}}{N!} \prod_{i=1}^{N} \frac{\sum_l Y_l \mathcal{P}_l(x_i;\theta)}{\sum_l Y_l}, \tag{4.11}$$

but it is more convenient to work with the logarithmic likelihood

$$\ln \mathcal{L}(\theta, Y_l) = \sum_{i=0}^{N} \ln\left(\sum_l Y_l \mathcal{P}_l(x_i;\theta)\right) - \sum_l Y_l - \ln N! \tag{4.12}$$

where we drop the constant term $\ln N!$ and finally minimize the objective function,

$$-2\ln \mathcal{L}(\theta) = 2\left(\sum_l Y_l - \sum_{i=0}^{N} \ln\left(\sum_l Y_l \mathcal{P}_l(x_i;\theta)\right)\right), \tag{4.13}$$

using the MINUIT software [57].

The two parts of the Belle data for SVD1 and SVD2 have different shapes in M_{bc} and ΔE due to the different vertex detector and tracking algorithms. Because of this we have a separate model for SVD1 and SVD2 and perform a simultaneous fit on both datasets. Unless otherwise stated, the two datasets have the same model but an independent set of parameters. For convenience we will only show the sum of both models and datasets. Separate plots for SVD1 and SVD2 can be found in Appendix A.1.

4.2.1 Probability Density Functions

A probability density function (PDF) describes the relative likelihood for a continuous random variable to take a given value. As such a PDF is nonnegative and is normalized to unity over the whole range. We will quickly define the different base PDFs used to construct the full Data Model.

Gaussian Distribution

The standard Gaussian PDF is defined as

$$G(x;\mu,\sigma) = \frac{1}{N} \cdot e^{-\frac{(x-\mu)^2}{2\sigma}} \tag{4.14}$$

with a suitable normalization factor N. As an extension, we introduce an bifurcated gaussian

$$G_b(x;\mu,\sigma_L,\sigma_R) = \frac{1}{N} \cdot e^{-\frac{(x-\mu)^2}{2\sigma}}, \quad \sigma = \begin{cases} \sigma_L & \text{if } x \leq \mu, \\ \sigma_R & \text{otherwise,} \end{cases} \tag{4.15}$$

which is is similar to the normal distribution but has a different width σ_L, σ_R on the left or ride side of the mean respectively.

Argus Distribution

The Argus Distribution is an empirical function introduced by the ARGUS collaboration [58] and is used to model the invariant mass of a decayed particle on continuum background. It is defined as

$$\text{Argus}(x;a,c) = \frac{1}{N} \cdot x \cdot \sqrt{1-\frac{x^2}{c^2}}\, e^{a\cdot\left(1-\frac{x^2}{c^2}\right)}, \tag{4.16}$$

with the curvature parameter $a < 0$ and the cut-off energy $c > 0$ with a suitable normalization factor N.

In our case the cut-off parameter is the beam energy which is an event dependent variable so we will omit it in the future

$$\text{Argus}(x;a) = \text{Argus}(x;a,E_{beam}) \tag{4.17}$$

Chebychev Polynomials

Chebychev Polynomials [59] are an orthogonal set of polynomials which can be used to approximate any function in a given interval using a sufficient high order. We use Chebychev Polynomials of the first kind which are defined as

$$\text{Cheb}_n(x;c_1,c_2,\ldots,c_n) = \frac{1}{N} \cdot \left(T_0(x) + \sum_{i=1}^{n} c_i \cdot T_i(x)\right), \tag{4.18}$$

where N is a suitable normalization factor and the $T_i(x)$ are defined using the recurrence relation

$$T_0(x) = 1 \qquad T_1(x) = x \qquad T_{n+1}(x) = 2x \cdot T_n(x) - T_{n-1}(x) \tag{4.19}$$

Component	$\rho_{M_{\mathrm{bc}},\Delta E}$
Signal	0.089
Misreconstructed	0.039
BBbar	0.011
Continuum	0.008

Table 4.2: Pearson correlation coefficients between M_{bc} and ΔE for all model components.

4.2.2 Correctly Reconstructed Events

The main signal model is determined from correctly reconstructed signal MC events (see Section 3.4.7). The correlations between the fit variables in this category are shown in Table 4.2. There is a significant correlation between M_{bc} and ΔE.

To model the core, we use the sum of three Gaussians in ΔE,

$$\mathcal{P}_{sig,core}(\Delta E) = \sum_{i=0}^{3} f_i G(\Delta E; \mu_i + \mu_{\Delta E}^{CF}, \sigma_i \cdot \sigma_{\Delta E}^{CF}) / \sum_{i=1}^{3} f_i, \tag{4.20}$$

and two Gaussians in M_{bc}. To account for the correlation between M_{bc} and ΔE, the wider Gaussian in M_{bc} is correlated with ΔE using a linear dependence for the mean and a quadratic dependence for the width,

$$\begin{aligned}\mathcal{P}_{sig,core}(M_{\mathrm{bc}}|\Delta E) = f \cdot G(M_{\mathrm{bc}}; \mu_1 + \mu_{M_{\mathrm{bc}}}^{CF}, \sigma_1) \\ + (1-f) \cdot G\Big(M_{\mathrm{bc}}; \mu_2 + \mu_{M_{\mathrm{bc}}}^{CF} + \mu_2' \cdot \Delta E, (\sigma_2 + \sigma_2' \cdot \Delta E^2) \cdot \sigma_{M_{\mathrm{bc}}}^{CF}\Big).\end{aligned} \tag{4.21}$$

$\mu_{M_{\mathrm{bc}}}^{CF}$, $\mu_{\Delta E}^{CF}$, $\sigma_{M_{\mathrm{bc}}}^{CF}$ and $\sigma_{\Delta E}^{CF}$ are correction parameters to account for possible differences between the shape in data and MC. When estimating the shape from MC these parameters are fixed to zero for the mean correction ($\mu_{M_{\mathrm{bc}}}^{CF}$, $\mu_{\Delta E}^{CF}$) and one for the width correction ($\sigma_{M_{\mathrm{bc}}}^{CF}$, $\sigma_{\Delta E}^{CF}$) but they are then freed in the final fit to the data. Due to the low number of expected signal events for SVD1 these correction parameters are shared between SVD1 and SVD2, so both models have the same value for all correction parameters.

To model the outliers we use an Argus function in M_{bc} and a single gaussian in ΔE,

$$\mathcal{P}_{sig,outlier}(M_{\mathrm{bc}}, \Delta E) = \mathrm{Argus}(M_{\mathrm{bc}}; a) \times G(\Delta E; \mu_1, \sigma_1), \tag{4.22}$$

and the complete signal model is then given as

$$\begin{aligned}\mathcal{P}_{sig}(M_{\mathrm{bc}}, \Delta E) = & f_{core} \cdot \mathcal{P}_{sig,core}(\Delta E) \times \mathcal{P}_{sig,core}(M_{\mathrm{bc}}|\Delta E) \\ & + (1 - f_{core}) \cdot \mathcal{P}_{sig,outlier}(M_{\mathrm{bc}}, \Delta E)\end{aligned} \tag{4.23}$$

and the results of the fit to signal MC events can be seen in Figure 4.1.

4.2.3 Misreconstructed Signal Events

Events which were reconstructed from signal MC but are not correctly reconstructed are classified as Misreconstructed. To model the core part we use a single Gaussian in ΔE

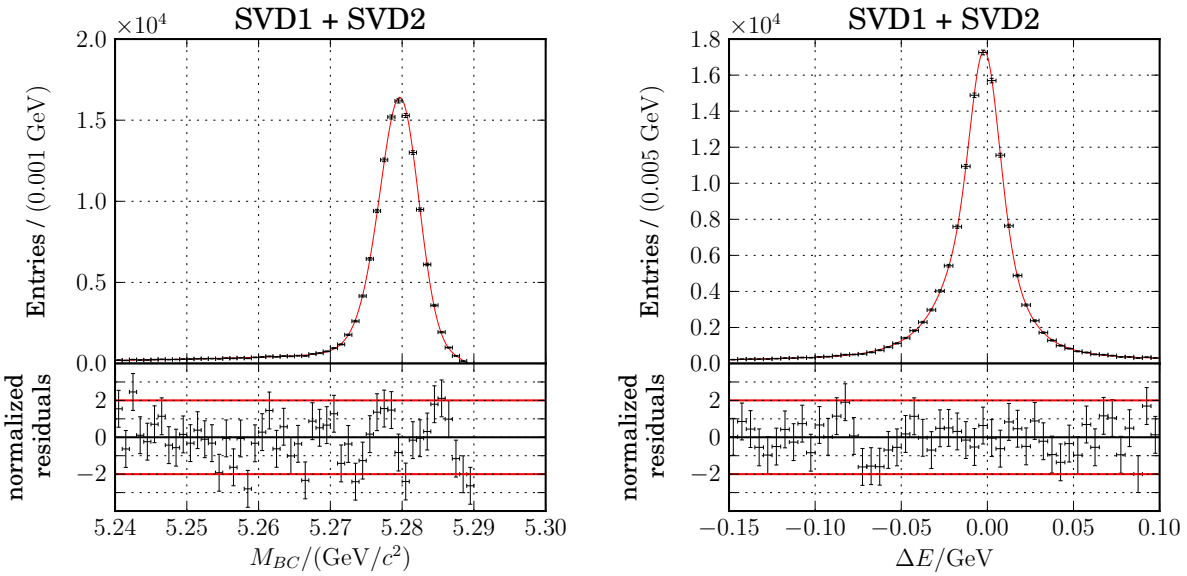

Figure 4.1: Projections to M_{bc} and ΔE after fitting the Signal component to MC.

and a bifurcated Gaussian in M_{bc}

$$\mathcal{P}_{mis,core}(M_{\mathrm{bc}}, \Delta E) = G_B(M_{\mathrm{bc}}; \mu_1, \sigma_{1L}, \sigma_{1R}) \times G(\Delta E; \mu_2, \sigma_2) \tag{4.24}$$

and for the outliers we use an Argus function in M_{bc} and a single gaussian in ΔE as we did for the signal component

$$\mathcal{P}_{mis,outlier}(M_{\mathrm{bc}}, \Delta E) = \mathrm{Argus}(M_{\mathrm{bc}}; a) \times G(\Delta E; \mu_1, \sigma_1) \tag{4.25}$$

resulting in a total PDF given by

$$\mathcal{P}_{mis}(M_{\mathrm{bc}}, \Delta E) = f \cdot \mathcal{P}_{mis,core}(M_{\mathrm{bc}}, \Delta E) + (1 - f) \cdot \mathcal{P}_{mis,outlier}(M_{\mathrm{bc}}, \Delta E). \tag{4.26}$$

and shown in 4.2. We fix the yield of misreconstructed events, Y_{mis}, relatively to the signal yield, Y_{sig}, from MC,

$$Y_{mis} = f_{mis} \cdot Y_{sig}, \tag{4.27}$$

where f_{mis} turns out to be 0.998 for SVD1 and 0.161 for SVD2.

4.2.4 Events Reconstructed from Generic $B\overline{B}$ Decays

To model events from other B decay channels we reconstructed generic $B\overline{B}$ MC provided by the Belle-Collaboration with ten times the statistics compared to real data. We use "mixed" and "charged" MC which contains B^0 and B^+ pairs decaying to generic charm final states. We combine these to MC sets into a single component called BBbar.

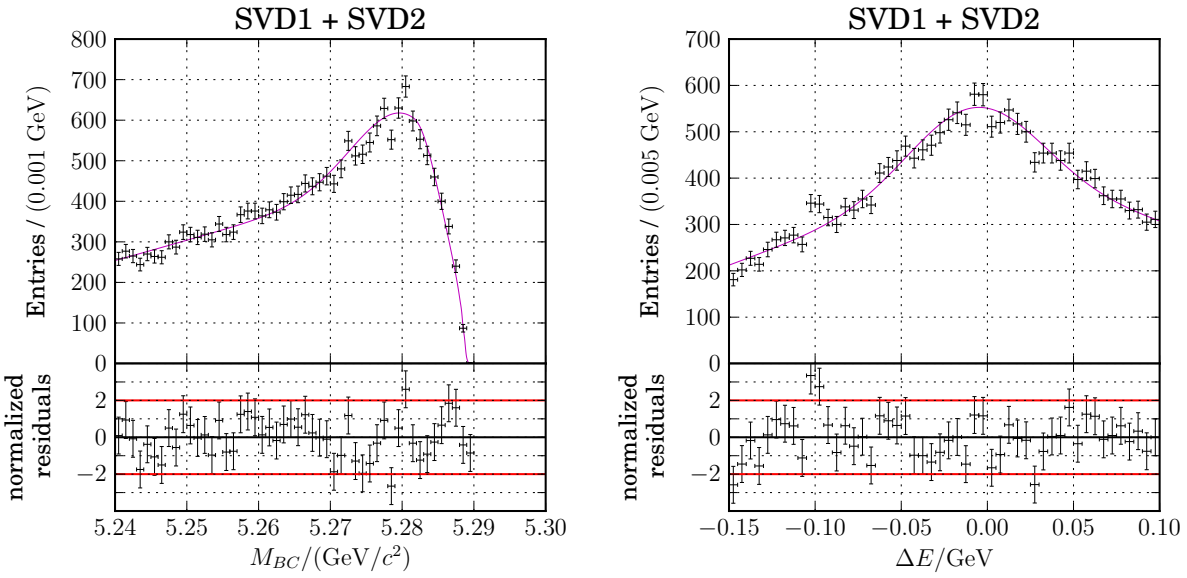

Figure 4.2: Projections to M_{bc} and ΔE after fitting the Misreconstructed component to MC.

Events from BBbar are mainly modelled using an Argus function in M_{bc} and a Chebychev polynomial of second order in ΔE,

$$\mathcal{P}_{bb,main}(M_{\mathrm{bc}}, \Delta E) = \mathrm{Argus}(M_{\mathrm{bc}}; a_{bb}) \times \mathrm{Cheb}_2(\Delta E; c_1, c_2). \tag{4.28}$$

On top of this a small fraction of events are peaking at $M_{\mathrm{bc}} \sim 5.28$ and $\Delta E \sim 0$ and are modelled as a single gaussian in M_{bc} and ΔE,

$$\mathcal{P}_{bb,peak}(M_{\mathrm{bc}}, \Delta E) = G(M_{\mathrm{bc}}; \mu_1, \sigma_1) \times G(\Delta E; \mu_2, \sigma_2) \tag{4.29}$$

resulting in the total PDF,

$$\mathcal{P}_{bb}(M_{\mathrm{bc}}, \Delta E) = f \cdot \mathcal{P}_{bb,main}(M_{\mathrm{bc}}, \Delta E) + (1 - f) \cdot \mathcal{P}_{bb,peak}(M_{\mathrm{bc}}, \Delta E). \tag{4.30}$$

Figure 4.3 shows the result for the fit to the Monte Carlo data.

4.2.5 Background from Generic $q\overline{q}$ Events

To estimate background from generic $q\overline{q}$ interactions we can use a special feature of the Belle experiment. Since we run at the $\mathrm{B\overline{B}}$ production threshold we can lower the beam energies to get below this threshold. The resulting events should be very similar to events from normal operation except that no B mesons can be produced. Belle collected "off-resonance" events at an energy of 60 MeV below the $\Upsilon(4\mathrm{S})$. The recorded luminosity amounts to around one tenth of the collected $\Upsilon(4\mathrm{S})$ luminosity.

Due to the high track multiplicity of $\mathrm{B}^0 \to \mathrm{D}^{*-}\mathrm{D}^{*+}\mathrm{K}^0_{\mathrm{S}}$, only very few events are reconstructed from this off-resonance data. Due to the low statistics so we do not have

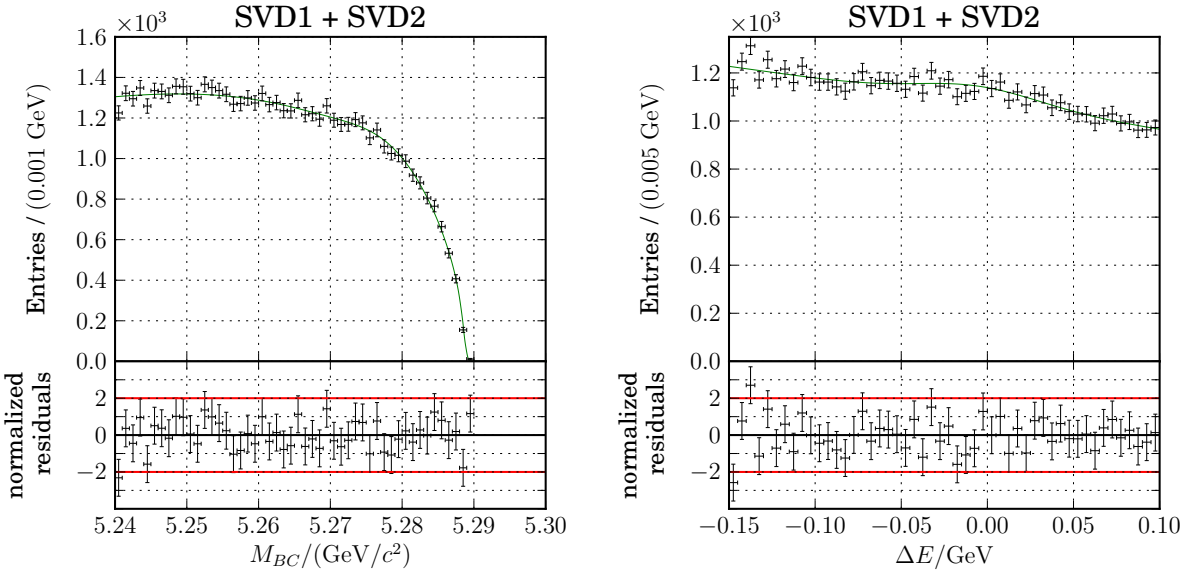

Figure 4.3: Projections to M_{bc} and ΔE after fitting the BBbar component to MC.

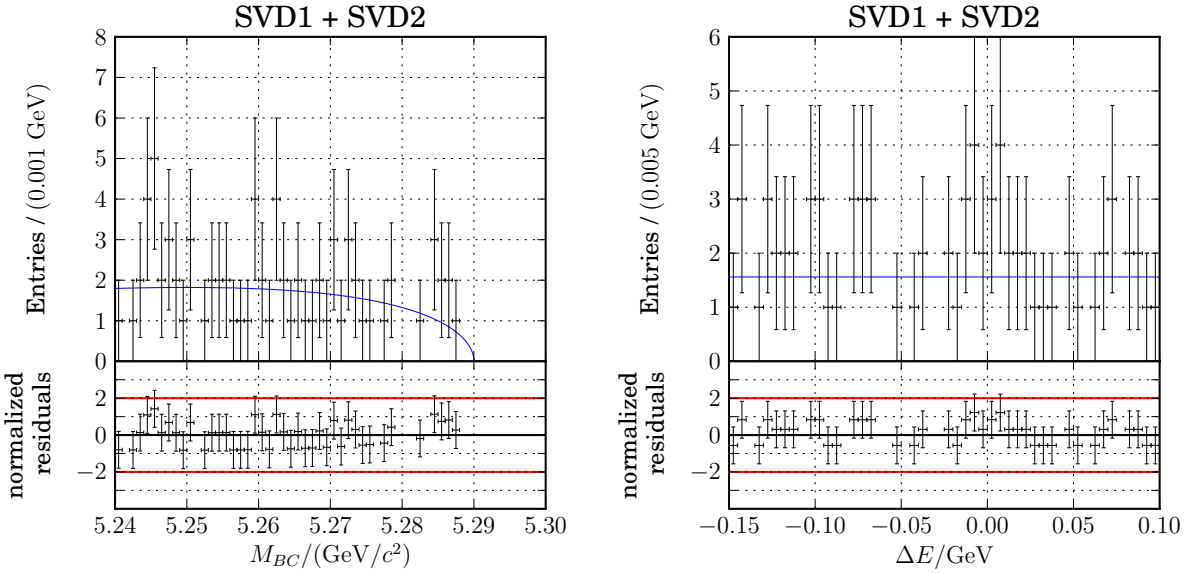

Figure 4.4: Projections to M_{bc} and ΔE after fitting the Continuum component to MC.

Component	SVD1	SVD2
Signal	31 (34)	455 (96)
Misrecon	3	70
BBbar	140	5470
Continuum	20	760

Table 4.3: Approximate number of expected Events for the final fit for correctly reconstructed signal events (Signal), misreconstructed signal events (Misrecon), reconstructed events from other $B\overline{B}$ decays (BBbar) and events reconstructed from generic $q\overline{q}$ decays (Continuum). The numbers in parentheses represent the yield obtained in the old Belle analysis [37].

sufficient statistics to determine the model independently from BBbar. We chose to model the Continuum as a horizontal line in ΔE and an Argus in M_{bc} where the curvature parameter of the Argus is taken from BBbar component,

$$\mathcal{P}_{qq}(M_{\mathrm{bc}}, \Delta E, \Delta t) = \mathrm{Argus}(M_{\mathrm{bc}}; a_{bb}) \times \mathrm{Cheb}_0(\Delta E). \tag{4.31}$$

Due to the expected low statistics of this component and the similarity to BBbar events, the yield of Continuum events, Y_{qq}, is fixed relatively to the yield of BBbar events, Y_{bb}

$$Y_{qq} = f_{qq} \cdot Y_{bb}. \tag{4.32}$$

We fix this fraction from MC and the scaling factor between on and off-resonance data.

4.3 Expected Yields

Using the reconstruction efficiency from Equation 4.7 and Equation 4.1 we can obtain a number of expected signal events from the real dataset,

$$Y\left(\mathrm{B}^0 \to \mathrm{D}^{*-}\mathrm{D}^{*+}\mathrm{K}^0_{\mathrm{S}}\right) = \mathcal{B}\left(\mathrm{B}^0 \to \mathrm{D}^{*-}\mathrm{D}^{*+}\mathrm{K}^0_{\mathrm{S}}\right) \epsilon\left(\mathrm{B}^0 \to \mathrm{D}^{*-}\mathrm{D}^{*+}\mathrm{K}^0_{\mathrm{S}}\right) \times N(\mathrm{B}\overline{\mathrm{B}}). \tag{4.33}$$

For the other components we know the ratio between MC and data so we can estimate the expected number of events in the final dataset. The expected yields for all components can be seen in Table 4.3

4.4 Toy Monte Carlo Studies

To validate the full model we performed toy Monte Carlo studies. For these studies we generated many datasets with the number of events expected in the real data for each component. For each event we randomly picked the M_{bc} and ΔE values from a fully simulated event. Due to the limited statistics for continuum events we generate these events from PDF.

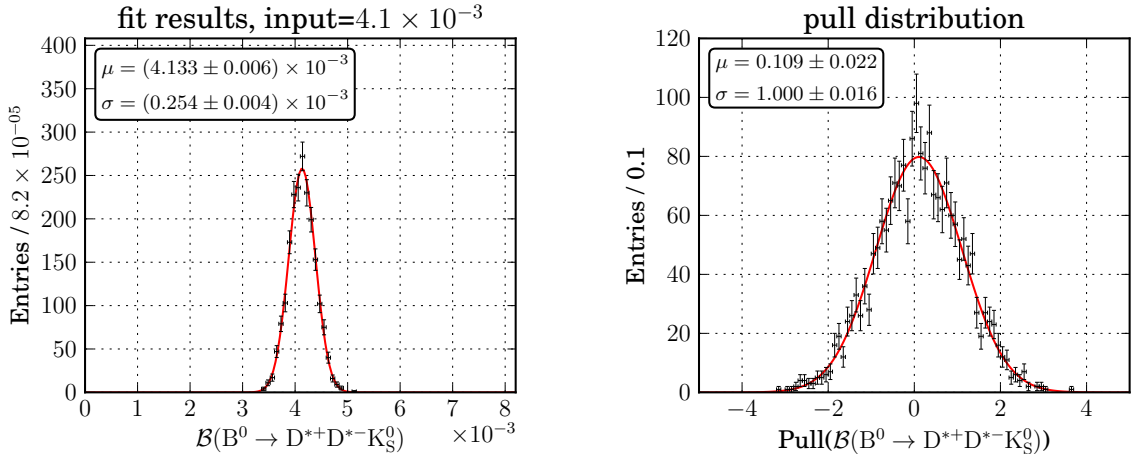

Figure 4.5: Results of the ToyMC tests for the branching fraction. On the left are shown the raw fit results and on the right is the pull distribution. The mean and width of the distributions are determined from a single gauss fit.

We set the branching fraction to the current world average value and generated 2000 experiments. We then fitted each of these experiments. In these fits, we only free the yields for the Signal and BBbar components. The results can be seen in Figures 4.5, the raw fit result on the left and the pull distribution on the right side. The pull distribution is defined as the error weighted residuals between the fit input and output value

$$\text{Pull}(x) = \frac{x_{out} - x_{in}}{\Delta x}, \tag{4.34}$$

and for unconstrained fit parameters this should yield a standard normal distribution, that is a gaussian distribution with a mean of zero and a width of one.

It can be clearly seen that the fit result reproduces the input value with good precision. The pull distribution is in agreement with a standard normal distribution and only a very small bias of 0.1 standard deviations can be observed. The width of the result distribution is equal the expected statistical error of the final fit and it is noteworthy that the expected errors are half of the errors obtained in the previous analysis [37].

4.5 Linearity Tests

The ToyMC test only shows that the result is unbiased if the branching fraction we measure is close to the world average. To verify that the fit also works for different values we performed linearity tests. We created 20 000 experiments where the branching fraction is generated uniform between 2.0×10^{-3} and 6.0×10^{-3}. From the results in Figure 4.6 we can conclude that the fit reproduces the input branching fraction over a large range with only an insignificant bias of less then 0.2 σ over the full range.

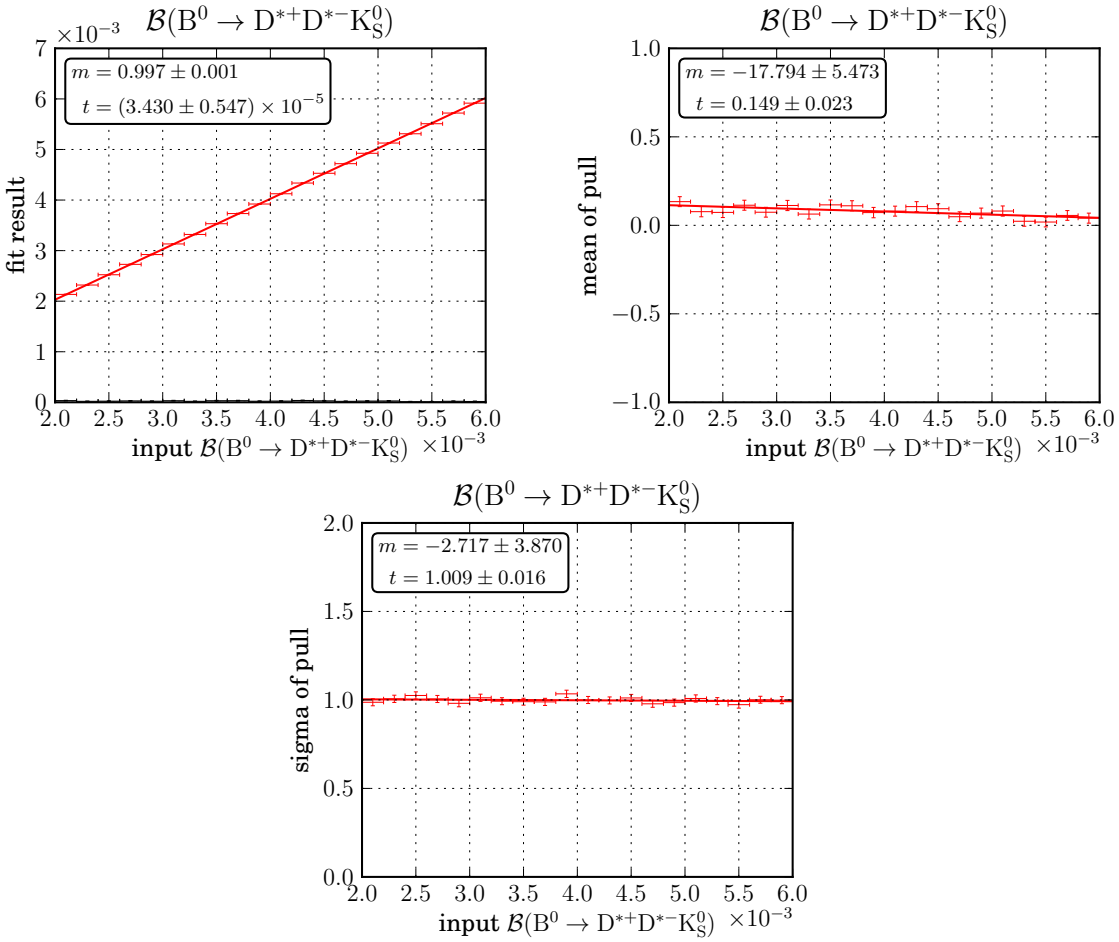

Figure 4.6: Results of the linearity tests for branching fraction. On the top left are the fit results and the residuals, top right shows mean and the bottom plot shows the the width of the pull distribution.

4.6 Control Sample

A valuable source for cross checking the analysis is the use of a control sample which servers two purposes. First to gain confidence in the chosen analysis method by being able to produce expected results in the control sample. Possible problems with the method intended for the mode of interest can be seen on time and rectified. In addition, the control sample shares many properties with the mode of interest and may thus aid in the physics parameter extraction.

A perfect control sample would have certain properties

- It should have roughly an order of magnitude more events
- It must topologically resemble the mode of interest
- It should show the same sensitivity to CP violation
- It must contain all the combinations of daughter decays as the mode of interest

The most obvious choice for a control sample would be $B^+ \to D^{*-}D^{*+}K^+$ but this mode is colour suppressed. This means its branching fraction is too small to be useful. Furthermore, the requirement on the topology rules out everything except double charm decays.

The 3-body decay $B^0 \to D^{*-}D^{*+}K^0_S$ is sensitive to CP violation but if it contains a resonance in D^{*+} K^0_S it ceases to be a CP eigenstate and thus the indirect CP asymmetry is lost. Therefore the control sample must also contain a 3-body decay. Applying also the last requirement, $B^0 \to D^{*-}D^0K^+$ remains the only sensible solution.

4.6.1 Event Selection

Signal MC for the control sample was generated the same way as for the mode of interest, assuming flat phase space distribution and no CP violation. Since there is only one D^*, the reconstruction efficiency is much higher so we generated only two million events for each SVD1 and SVD2.

Apart from that, the event selection criteria is exactly the same as for the signal channel, described in Chapter 3.3. The Best B likelihood in Equation 3.7 is adapted by dropping the second D^* likelihood.

4.6.2 Reconstruction Efficiency

There are two differences in the control sample which directly effect the reconstruction efficiency: There is only one D^* and no K^0_S. This means that there are two fewer tracks to be reconstructed and the remaining tracks will have higher momentum on average, increasing the reconstruction efficiency. So, assuming flat phase space distribution of the events, we can determine the raw reconstruction efficiency analog to Section 4.1,

$$\epsilon_{raw}^{(\mathrm{SVD1})} = (18.568 \pm 0.096) \times 10^{-3} \qquad \epsilon_{raw}^{(\mathrm{SVD2})} = (33.383 \pm 0.129) \times 10^{-3}. \tag{4.35}$$

	SVD1	SVD2
particle id	0.973	1.000
track reconstruction	0.992	0.968
π^0 reconstruction	1.012	1.003
combined	0.977	0.971

Table 4.4: Reconstruction efficiency correction factors between MC and data for the control sample.

Following the same procedure of calculating the simulated branching fraction and using the world averages from [46] as in Section 4.1, we obtain

$$\mathcal{B}_{sim}\left(\mathrm{B}^0 \to \mathrm{D}^{*-}\mathrm{D}^{*+}\mathrm{K}^0_\mathrm{S}\right) = 5.245 \times 10^{-2}, \tag{4.36}$$

which results in a total reconstruction efficiency of

$$\epsilon^{(\mathrm{SVD1})}_{MC} = (97.382 \pm 0.505) \times 10^{-5} \qquad \epsilon^{(\mathrm{SVD2})}_{MC} = (175.082 \pm 0.678) \times 10^{-5} \tag{4.37}$$

for the control sample. One can clearly see that there is less difference between SVD1 and SVD2 as for the signal mode. This is to be expected as the SVD only tracking is only used to improve the slow pion efficiency and we have only one slow pion in the control sample.

As for the mode of interested the reconstruction efficiency has to be corrected to account for differences between MC and data (see Section 4.1). As there is no K^0_S in the control sample only corrections for particle identification, tracking and π^0 reconstruction are needed. With the corrections from Table 4.4 the final reconstruction efficiency is

$$\epsilon^{(\mathrm{SVD1})}_{\mathrm{data}} = (95.143 \pm 0.494) \times 10^{-5} \qquad \epsilon^{(\mathrm{SVD2})}_{\mathrm{data}} = (169.969 \pm 0.658) \times 10^{-5} \tag{4.38}$$

With these numbers we can estimate the expected signal yield for the control sample, see Table 4.5. Compared to the expectation from the mode of interest the signal yield is a factor 10 (5) higher for SVD1 (SVD2). But we also notice that the yields from the backgrounds increased dramatically by more than two orders of magnitudes. Nevertheless we chose to keep the event selection criteria unchanged for the control sample to have minimal differences to the real analysis.

4.6.3 Changes to the Data Model

The data model for the control channel is kept as similar to the signal mode as possible. The only change is that there is a small peak in the distribution of BBbar events at $M_\mathrm{bc} \approx 5.28\,\mathrm{GeV}/c^2$ and $\Delta E \approx -0.15\,\mathrm{GeV}$ which has been added to the PDF in Equation 4.28 as an uncorrelated, 2D Gaussian,

$$\begin{aligned}\mathcal{P}_{bb,main}(M_\mathrm{bc}, \Delta E) = f \cdot \Big(&\mathrm{Argus}(M_\mathrm{bc}; c) \times \mathrm{Cheb}_2(\Delta E; c_1, c_2)\Big) \\ &+ (1-f) \cdot \Big(G(M_\mathrm{bc}; \mu_{1,peak}, \sigma_{1,peak}) \times G(\Delta E; \mu_{2,peak}, \sigma_{2,peak})\Big).\end{aligned} \tag{4.39}$$

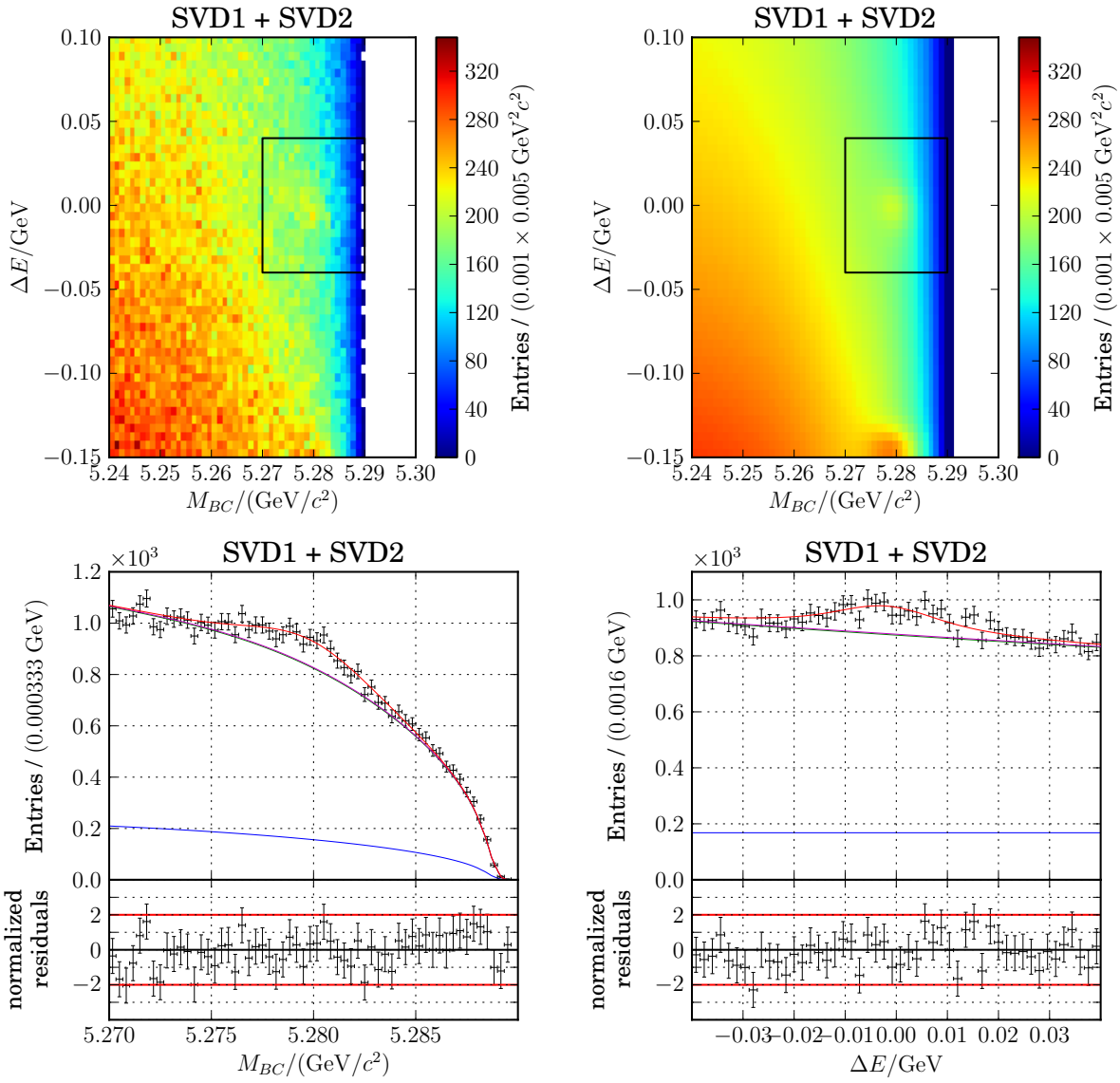

Figure 4.7: Results for the control sample: Top row shows the data (left) and the total PDF (right) for the full fit region in M_{bc} and ΔE. The bottom row shows the projections on M_{bc} and ΔE. Due to the high background levels, the projections are limited to $M_{\mathrm{bc}} > 5.26\,\mathrm{GeV}/c^2$ and $-0.05\,\mathrm{GeV} < \Delta E < 0.05\,\mathrm{GeV}$, marked by the black rectangle.

Component	SVD1	SVD2
Signal	360	2600
Misreconstructed	90	900
BBbar	27000	340000
Continuum	6400	120000

Table 4.5: Approximate number of expected Events for the different components for the final fit of the control sample.

4.6.4 Control Sample results

The fit is performed by freeing the yields for signal and background components as well as the correction parameters for the signal shape. We obtain

$$\mathcal{B}(B^0 \to D^{*-}D^0K^+) = (2.276 \pm 0.131) \times 10^{-3} \tag{4.40}$$

where the error is statistical only. This result is compatible with the world average of $\mathcal{B}(B^0 \to D^{*-}D^0K^+) = (2.47 \pm 0.21) \times 10^{-3}$ within 1.5 standard deviations (σ). The method can then be considered approved. Even in a much less clean environment we were able to reproduce the world average result.

4.7 $B^0 \to D^{*-}D^{*+}K^0_S$ Signal Yield

To finally obtain the signal yield, we perform the fit to the real data. We free the signal yield, the number of BBbar events and the correction factors for the signal shape. As mentioned, the ratio between the Signal and Misreconstructed yields as well as the ratio between the BBbar and Continuum yields remain fixed. The results for the signal yields are

$$Y_{\text{sig}}^{\text{SVD1}} = 32.433^{+7.677}_{-6.861} \qquad Y_{\text{sig}}^{\text{SVD2}} = 714.370^{+48.492}_{-46.772}. \tag{4.41}$$

Figure 4.8 shows the projections of this fit in M_{bc} and ΔE.

As mentioned in 4.2.2, the overall mean and width of the signal shape are free in the final fit. While the mean and width in M_{bc} and the mean in ΔE are consistent with the values obtained from the fit to MC, the width of the signal shape in ΔE $(51 \pm 13)\,\%$ wider than in MC which is an deviation of almost 4σ. Also the yield for SVD2, which we estimated to be around 450 events assuming flat phase space distribution, is higher than expected.

4.8 Corrected Reconstruction Efficiency

As stated in Section 4.8.3, we have to correct the reconstruction efficiency to account for a possible difference between the Dalitz distribution in MC and data. To do this, we chose to bin the Dalitz plot into several bins with similar reconstruction efficiency. To maximize significance we chose to aim for similar signal yield in each bin.

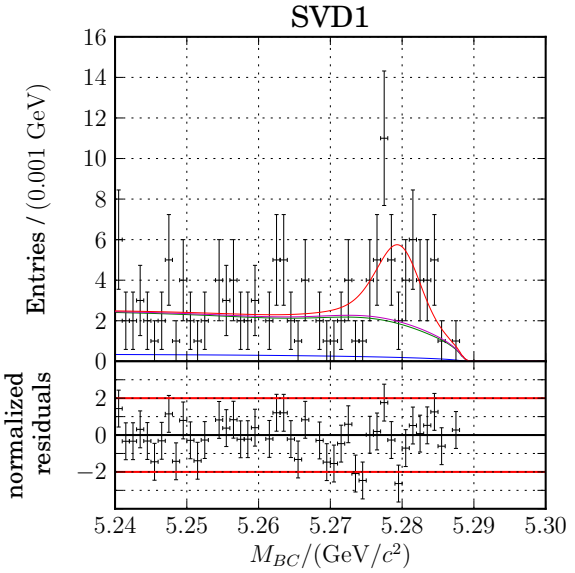

(a) Projection on M_{bc}, SVD1

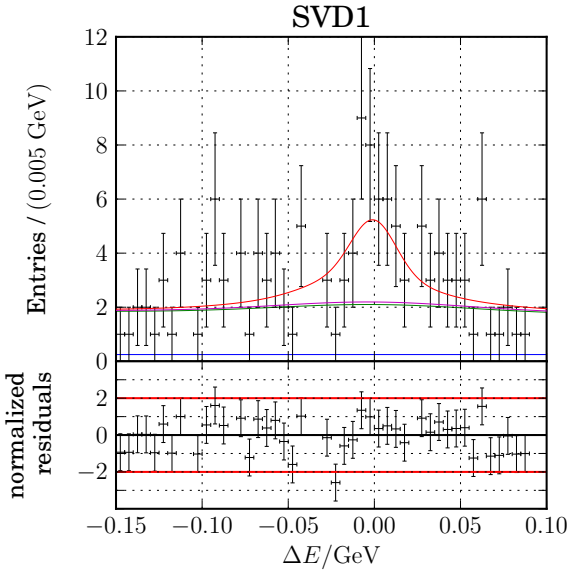

(b) Projection on ΔE, SVD1

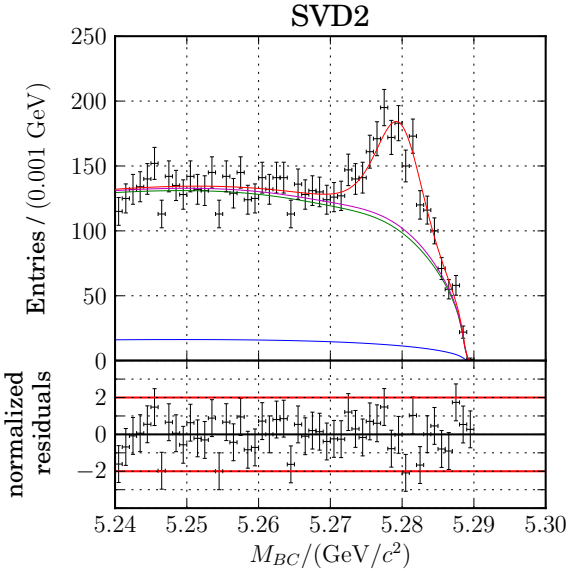

(c) Projection on M_{bc}, SVD2

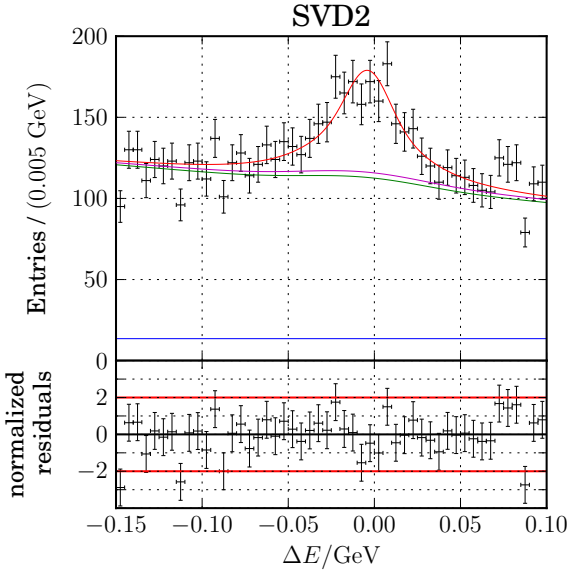

(d) Projection on ΔE, SVD2

Figure 4.8: Results of the fit for the $\mathrm{B}^0 \to \mathrm{D}^{*-}\mathrm{D}^{*+}\mathrm{K}^0_S$ signal yield in the full dataset.

4.8.1 Binning of Dalitz Plot

When looking at the raw reconstruction efficiency with respect to the Dalitz variables we see a strong dependence as shown in Figure 4.9(a). To avoid statistical fluctuations, we smooth this distribution using a bivariate cubic spline fit [60, 61] (Figure 4.9(b)).

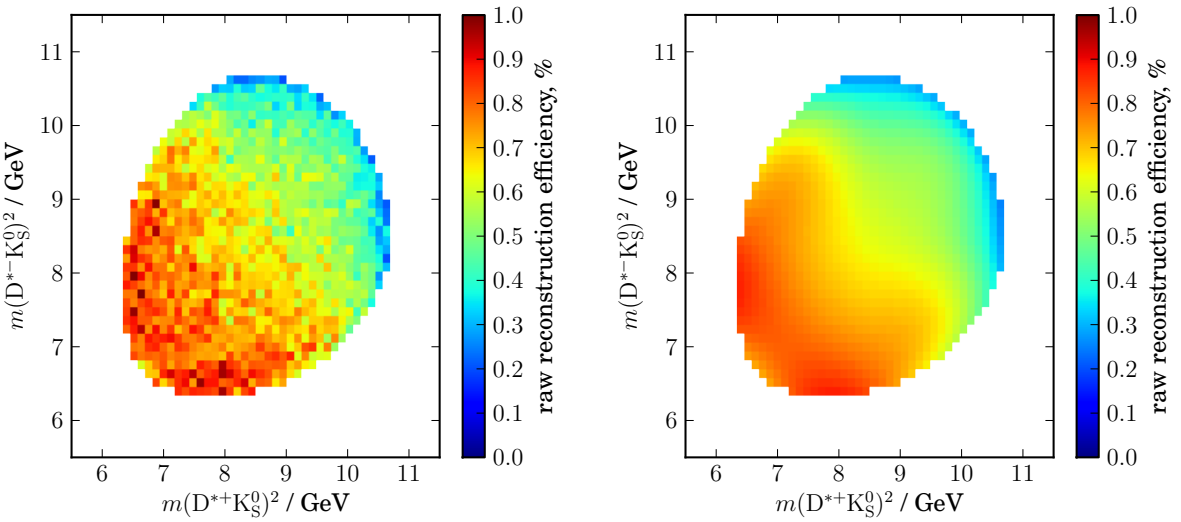

(a) obtained from signal MC

(b) smoothed using a cubic spline

Figure 4.9: Raw reconstruction efficiency in percent with respect to the Dalitz variables. To remove statistical fluctuations we performed a bivariate cubic spline fit on the distribution obtained from signal MC.

For correction of the reconstruction efficiency obtained in Section 4.8.3 we have to determine the signal yield in areas of similar reconstruction efficiency. This allows us to calculate a weighted average of the reconstruction efficiencies in all areas using the yields as weights. How we define these areas is arbitrary but the error of an weighted average will be minimal if all weights are of equal size. Because of that we decided to aim for comparable signal yield in all bins.

To get a rough idea of the Dalitz distribution for signal events we can produce a background subtracted Dalitz plot using the sPlot technique [62]. Note that the background subtraction is not necessarily correct as the Dalitz variables are not statistically independent to M_bc and ΔE. But we use the background subtracted Dalitz plot only as a hint to determine the bin boundaries. The yield in all bins will be determined in a separate fit to the data. Figure 4.10 shows the full Dalitz plot and the background subtracted version.

We choose contour levels on the spline fit to the reconstruction efficiency (Figure 4.9(b)) in such a way that the sum of entries in the background subtracted Dalitz plot (Figure 4.10(b)) is equal for each bin. Based on the obtained signal yield (Equation 4.41) we chose 7 bins to have an expected yield of roughly 100 events in each bin. The resulting bin boundaries can be seen in Figure 4.11.

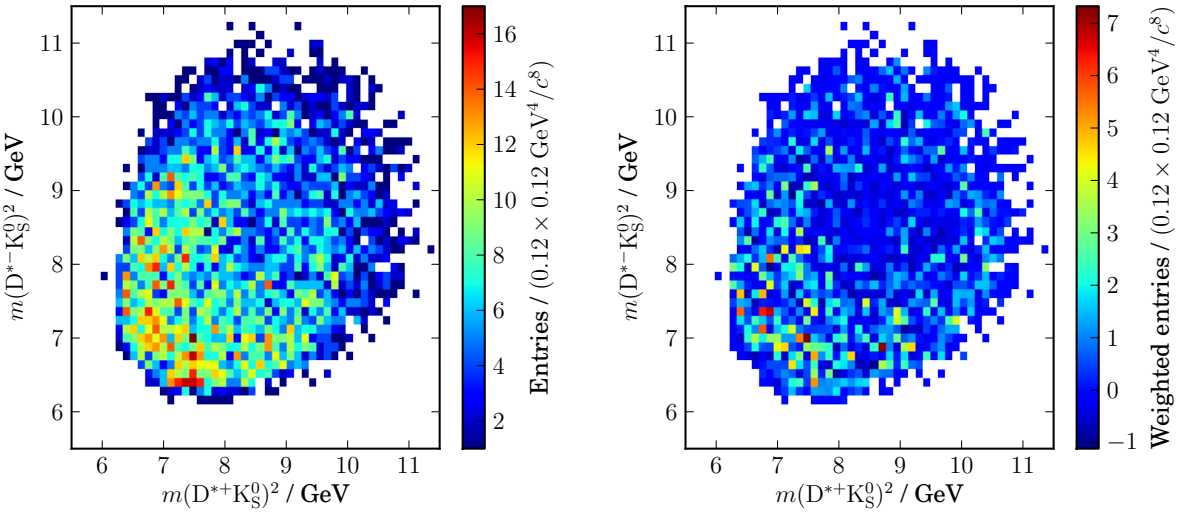

(a) all events (b) background subtracted

Figure 4.10: Dalitz distribution of the data.

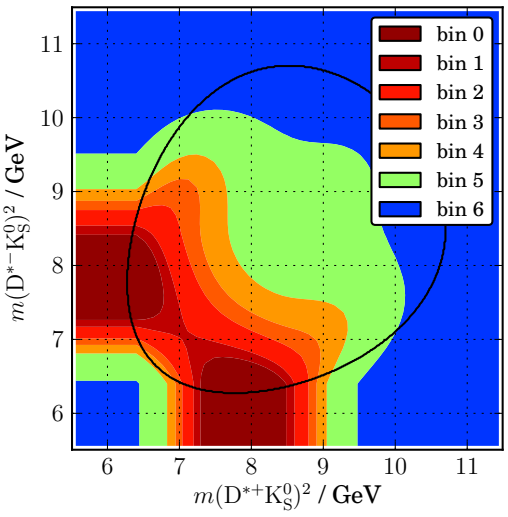

Figure 4.11: Binning of the Dalitz region to correct reconstruction efficiency. The black line shows the analytical Dalitz boundary.

4.8.2 Modification of the Data Model

Since we do not require a mass fit on the B^0, there is a correlation between ΔE and the Dalitz variables, $s^+ = m(D^{*+}K_S^0)^2$ and $s^- = m(D^{*-}K_S^0)^2$. This correlation can be best seen in the BBbar component but is to a lesser degree also present in the other components. Figure 4.12 shows the BBbar MC shapes of ΔE in all Dalitz bins. For the Dalitz bin with the lowest reconstruction efficiency (bin 6, shown in black) we see a strong deviation with respect to the shape of the other bins. Also for bin 5 we see a slight drop off for events with negative ΔE. The Signal and Misreconstructed components show a similar behaviour but due to the prominent peak at $\Delta E = 0\,\text{GeV}$ the effect is much less pronounced. We modified the data model to correct for this dependency.

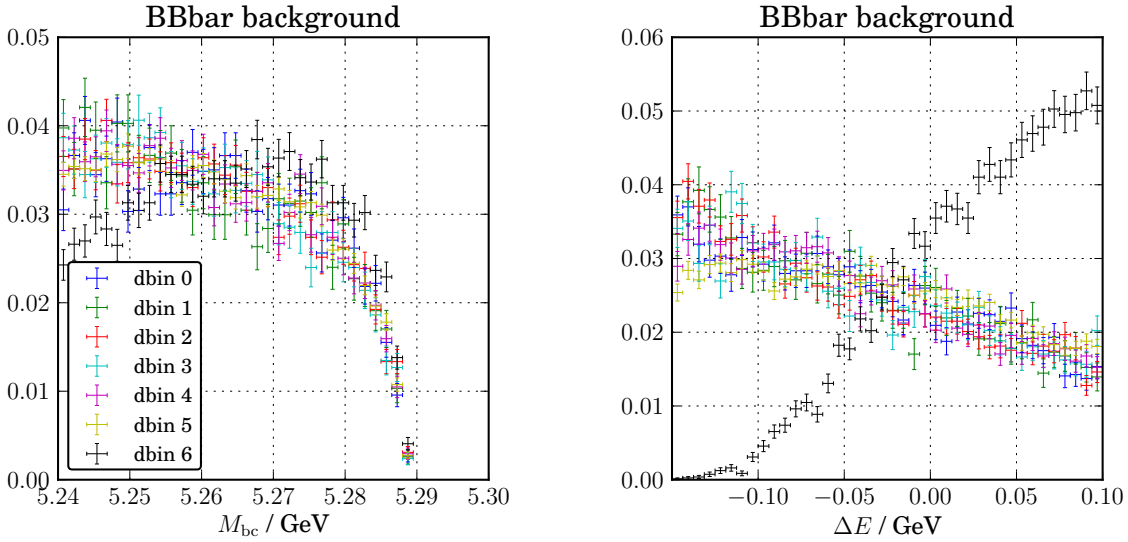

Figure 4.12: Normalized M_{bc} (left) and ΔE (right) distributions for reconstructed BBbar MC events for each Dalitz bin.

The model for the Signal component is unchanged but we introduce a separate set of parameters for the ΔE shape in the last bin. All other bins still share the same shape parameters. For the Misreconstructed component the expected statistics are small enough that the effect is not significant and all bins share the same shape.

For the BBbar we change the model in the last bin, common for SVD1 and SVD2. In M_{bc} we describe the shape using a single Argus function and in ΔE we use a scaled and slightly shifted Chebychev polynomial of the third order where zeroth, first and second order terms are fixed to zero,

$$\mathcal{P}_{bb,bin7}(M_{bc}, \Delta E) = \text{Argus}(M_{bc}; a_{bin6}) \times \text{Cheb}_3\Big(c_{scale} \cdot (\Delta E + c_{shift}); 0, 0, c_3\Big). \quad (4.42)$$

In bin 6 we do not modify the shape but use a separate set of parameters for the Chebychev polynomial in ΔE to account for the drop for negative ΔE seen in Figure 4.12. All other parameters are shared with the other bins which retain the model defined in Section 4.2.4.

For Continuum we do not have enough statistics to estimate a corrected model. We repeated the fit to obtain the signal yield where we fixed the fraction of Continuum events, f_{qq}, to zero. The result is compatible with the yield obtained in the original fit within 0.2 σ and all Continuum events are absorbed into BBbar. As such we chose to remove the continuum events when determining the yield in each Dalitz bin.

4.8.3 Final Reconstruction Efficiency

To determine the yield in each Dalitz bin we perform a simultaneous fit to all Dalitz bins where we free the yields, Y_l^i, for signal and background in all bins but constrain the sum of the yields to be unchanged from the previous result,

$$Y_{\text{sig}} = \sum Y_{\text{sig}}^i. \tag{4.43}$$

Due to the low statistics in SVD1 we share the yield fractions, $f_{\text{sig}}^i = Y_{\text{sig}}^i / Y_{\text{sig}}$, between SVD1 and SVD2. Results for the fit in each bin can be seen in Appendix A.3. In addition to the fractions itself we obtain and their corresponding covariance matrix, $\text{cov}(f_{\text{sig}}^i, f_{\text{sig}}^j)$. Following Sections 4.1 we can now determine the reconstruction efficiency in each Dalitz bin and calculate a weighted average using the obtained Yields as weights.

For a given set of uncorrelated variables x_i with a given error Δx_i, weights w_i and a covariance matrix for the weights $\text{cov}(w_i, w_j)$, the weighted average is defined as

$$x = \frac{\sum_i w_i \cdot x_i}{\sum_i w_i} \tag{4.44}$$

and the error on this value, Δx, can be computed using

$$\Delta x = \frac{\sqrt{(w_i \cdot \Delta x_i)^2 + \sum_i \sum_j (x_i - x)(x_j - x)\text{cov}(w_i, w_j)}}{\sum_i w_i}. \tag{4.45}$$

Using the results from Table 4.6 this leads to the Dalitz corrected reconstruction efficiency for data,

$$\epsilon_{\text{Data}}^{(\text{SVD1})} = (5.818 \pm 0.068) \times 10^{-5} \qquad \epsilon_{\text{Data}}^{(\text{SVD2})} = (21.109 \pm 0.220) \times 10^{-5}, \tag{4.46}$$

which is 15 % and 18 % higher than the value for SVD1 and SVD2 from Equation 4.10 when assuming flat phase space distribution.

4.9 Systematic Uncertainties

In addition to the statistical error we have to consider several sources of systematic uncertainties which have to be added to the final result.

		SVD1			SVD2		
	f^i_{sig}	$\epsilon_{MC}/10^{-5}$	ξ_{CF}	$\epsilon_{\text{Data}}/10^{-5}$	$\epsilon_{MC}/10^{-5}$	ξ_{CF}	$\epsilon_{\text{Data}}/10^{-5}$
bin 0	0.16	7.28 ± 0.15	0.969	7.05 ± 0.15	27.62 ± 0.30	0.922	25.46 ± 0.28
bin 1	0.14	6.47 ± 0.16	0.965	6.24 ± 0.16	25.88 ± 0.33	0.922	23.86 ± 0.30
bin 2	0.17	6.60 ± 0.11	0.962	6.35 ± 0.11	24.54 ± 0.22	0.918	22.53 ± 0.20
bin 3	0.15	6.04 ± 0.13	0.953	5.76 ± 0.12	23.89 ± 0.25	0.910	21.74 ± 0.23
bin 4	0.15	5.92 ± 0.10	0.952	5.64 ± 0.09	22.29 ± 0.19	0.907	20.21 ± 0.18
bin 5	0.16	5.22 ± 0.05	0.941	4.91 ± 0.05	19.13 ± 0.10	0.900	17.21 ± 0.09
bin 6	0.07	3.71 ± 0.05	0.943	3.50 ± 0.05	13.42 ± 0.10	0.896	12.03 ± 0.09
total		6.08 ± 0.07	0.956	5.82 ± 0.07	23.12 ± 0.23	0.912	21.11 ± 0.22

Table 4.6: Yield fraction, reconstruction efficiency on MC, Efficiency correction and reconstruction efficiency for data in all Dalitz bins for SVD1 and SVD2. The last row shows the weighted average for all bins. The errors on the efficiencies in each are the statistical uncertainties.

4.9.1 Number of $B\overline{B}$ Events

The total number of $B\overline{B}$ events in the Belle data is determined using off-resonance data which has been recorded 60 MeV below the $\Upsilon(4S)$. Due to the small energy difference these events should behave identical to on-resonance data except for the fact that no $B\overline{B}$ pairs can be produced. A scale factor between on-resonance and off-resonance data is determined by comparing the number of $e^+e^- \to \mu^+\mu^-$ events. To determine the number of $B\overline{B}$ events, the scaled number of off-resonance events is subtracted from the number of on-resonance events. This total number of $B\overline{B}$ events is used to determine the branching fraction $\mathcal{B}(B^0 \to D^{*-}D^{*+}K^0_S)$ in equation 4.1. As such, the error of $\Delta N(B\overline{B}) = 1.37\,\%$ is considered as an systematic error on the branching fraction.

4.9.2 Reconstruction Efficiency

The reconstruction efficiency is determined by counting the number of reconstructed events over the number of generated events. As the number of generated events is not infinite, the efficiency has a statistical error and, since we use the reconstruction efficiency $\epsilon(B^0 \to D^{*-}D^{*+}K^0_S)$ in Equation 4.1 to determine the branching fraction, it is also considered to be a source of systematic errors. This also includes the uncertainties from the yield fractions in each Dalitz bin as explained in Section 4.8.3.

4.9.3 Daughter Branching Fractions

All branching ratios used in Equation 4.5 have an error associated with their world average, given in [46]. These branching ratios, $\mathcal{B}$, and their errors, $\Delta\mathcal{B}$, are shown in Table 3.1 and

can be written as

$$\mathcal{B} = \begin{pmatrix} \mathcal{B}\left(\mathrm{D}^{*+} \to \mathrm{D}^0\pi^+_{\mathrm{slow}}\right) \\ \mathcal{B}\left(\mathrm{D}^{*+} \to \mathrm{D}^+\pi^0_{\mathrm{slow}}\right) \\ \mathcal{B}\left(\mathrm{D}^0 \to \mathrm{K}^-\pi^+\right) \\ \mathcal{B}\left(\mathrm{D}^0 \to \mathrm{K}^-\pi^+\pi^0\right) \\ \mathcal{B}\left(\mathrm{D}^0 \to \mathrm{K}^-\pi^+\pi^+\pi^-\right) \\ \mathcal{B}\left(\mathrm{D}^+ \to \mathrm{K}^-\pi^+\pi^+\right) \\ \mathcal{B}\left(\mathrm{K}^0_{\mathrm{S}} \to \pi^+\pi^-\right) \end{pmatrix} = \begin{pmatrix} 67.7 \pm 0.5 \\ 30.7 \pm 0.5 \\ 3.87 \pm 0.05 \\ 13.9 \pm 0.5 \\ 8.07 \pm 0.2 \\ 9.13 \pm 0.19 \\ 69.2 \pm 0.05 \end{pmatrix} \times 10^{-2}. \tag{4.47}$$

As such, the total simulated branching ratio, $\mathcal{B}_{sim}(\mathrm{B}^0 \to \mathrm{D}^{*-}\mathrm{D}^{*+}\mathrm{K}^0_{\mathrm{S}})$, also has an error which we need to take into consideration. From global fits performed by [46], which constrain the sum of all branching fractions for a given particle to unity, we can obtain correlations between the daughter branching fractions of D^{*+} and D^0 used in this analysis. We assume that all branching ratios are uncorrelated to the branching ratios of different particles. This allows us to obtain the correlation matrix between all daughter branching fractions from [46]:

$$\mathrm{corr}\,(\mathcal{B}) = \begin{pmatrix} 1 & -0.66 & 0 & 0 & 0 & 0 & 0 \\ -0.66 & 1 & 0 & 0 & 0 & 0 & 0 \\ 0 & 0 & 1 & -0.04 & 0.22 & 0 & 0 \\ 0 & 0 & -0.04 & 1 & 0.55 & 0 & 0 \\ 0 & 0 & 0.22 & 0.55 & 1 & 0 & 0 \\ 0 & 0 & 0 & 0 & 0 & 1 & 0 \\ 0 & 0 & 0 & 0 & 0 & 0 & 1 \end{pmatrix}. \tag{4.48}$$

The error on the total simulated branching ratio $\mathcal{B}_{sim}\left(\mathrm{B}^0 \to \mathrm{D}^{*-}\mathrm{D}^{*+}\mathrm{K}^0_{\mathrm{S}}\right)$ can then be calculated using standard error propagation,

$$\Delta y = \sqrt{\sum_{i=1}^{n}\sum_{j=1}^{n}\left(\frac{\partial y}{\partial x_i}\right)\left(\frac{\partial y}{\partial x_j}\right)\cdot \mathrm{cov}(x_i, x_j)}, \tag{4.49}$$

were the covariance matrix, $\mathrm{cov}(\mathcal{B})$, is obtained by multiplying the correlation matrix $\mathrm{corr}(\mathcal{B})$ with a diagonal matrix containing the errors on the branching fractions, $\mathrm{diag}(\Delta\mathcal{B})$ from both sides

$$\mathrm{cov}(\mathcal{B}) = \mathrm{diag}(\Delta\mathcal{B})\mathrm{corr}(\mathcal{B})\mathrm{diag}(\Delta\mathcal{B}) \tag{4.50}$$

With Equations 4.5 and 4.49 the total error turns out to be

$$\Delta\mathcal{B}_{rec}\left(\mathrm{B}^0 \to \mathrm{D}^{*-}\mathrm{D}^{*+}\mathrm{K}^0_{\mathrm{S}}\right) = 4.4\,\%. \tag{4.51}$$

4.9.4 Particle Reconstruction and Identification

When calculating the reconstruction efficiency we introduced correction factors to account for differences between MC and data which were obtained from separate studies. Since

these studies are also limited in their statistics and methods, all these correction factors have an associated error which we have to take into account. Similar to section 4.1, we separately determine the errors for particle identification [52], low momentum tracking [53, 54], π^0 reconstruction [55] and K^0_S reconstruction [56] for each particle in each decay channel from signal MC. The errors in each decay channel are added linearly and we form an weighted average between all channels where we use the number of reconstructed events in each channel as weight.

4.9.5 Model Uncertainties

The data model was obtained from fits to simulated events and all parameters used in these fits have associated uncertainties which have to be taken into account. For each component we obtain a covariance matrix of the parameters from the fit to the simulated data. Assuming that the parameters between different models are uncorrelated we can thus create a global covariance matrix for all model parameters.

We now performed 20 000 fits to the data where the model parameters are varied randomly using a correlated, multidimensional gaussian distribution between all parameters. The resulting yield distribution for SVD1 and SVD2 can be seen in Figure 4.13. To estimate the spread of these distributions we fit them using a bifurcated gaussian (see Section 4.2.1) and choose the larger width as an systematic error on the model uncertainties.

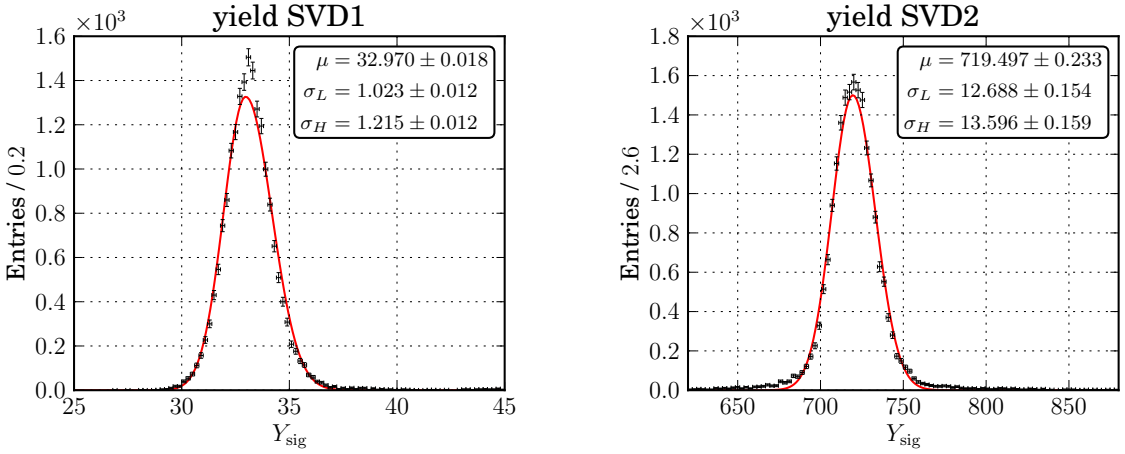

Figure 4.13: Yield distribution for SVD1 and SVD2 when repeating the fit to the data while varying the model parameters according to their covariance matrix

4.9.6 Total Systematics

Table 4.7 shows an overview of all the systematic errors. For some categories a systematic error was calculated for SVD1 and SVD2 and in these cases the systematic is determined

Category	SVD1	SVD2
Number of $B\overline{B}$ events	± 1.37	
Reconstruction efficiency	± 1.18	± 1.05
Daughter branching fractions	± 4.40	
Particle identification	± 3.70	± 5.70
Tracking efficiency	± 7.23	± 4.39
π^0 reconstruction	± 7.64	± 5.46
K^0_S reconstruction	± 1.20	± 1.17
Model uncertainties	± 3.75	± 1.90
Total	± 10.58	

Table 4.7: Systematic uncertainties for the Branching fraction, given in percent of the measured value. The total systematic error is the quadratic sum of all contributions.

by taking the weighted average using the number of $B\overline{B}$ events multiplied with the reconstruction efficiency as weights. The total systematic error is then calculated by summing the systematic uncertainties of each category in quadrature.

4.10 Final Result

With the yields from Equation 4.41 and the corrected reconstruction efficiency from Equation 4.46 we calculate the branching ratio for SVD1 and SVD2 using Equation 4.1,

$$\mathcal{B}^{\mathrm{SVD1}} = 3.667^{+0.868}_{-0.776} \times 10^{-3} \qquad \mathcal{B}^{\mathrm{SVD2}} = 5.460^{+0.371}_{-0.357} \times 10^{-3}. \tag{4.52}$$

To obtain the final result, we form a weighted average between SVD1 and SVD2 where we use the number of $B\overline{B}$ pairs multiplied with the reconstruction efficiency as weights,

$$\mathcal{B}(B^0 \to D^{*-}D^{*+}K^0_S) = \left(5.35^{+0.35}_{-0.34}(\mathrm{stat}) \pm 0.57(\mathrm{syst})\right) \times 10^{-3}. \tag{4.53}$$

Compared to the previous result from Belle the obtained branching ratio is significantly higher. It is interesting to see that the branching ratio from SVD1 is in very good agreement with the old analysis so the difference seems to mainly originate from the SVD2 data. The reconstruction algorithm and systematic studies have been changed significantly between these two results so they have to be considered independent which leads to an agreement within 2 σ. The agreement with the results from BABAR is also within 2 σ.

The statistical error improved from 11.7 % to 6.5 % which is roughly consistent with the increase in statistics. In contrast to the previous analysis the width and mean of the signal peak are free in the final fit which slightly diminishes the separation power between signal and background but helps to avoid systematic error due to shape differences between MC and data.

The systematic errors changed from 19.8 % to 10.7 %. This is in part due to new studies for track reconstruction and the inclusion of correlations for the calculation of the error on the daughter branching fraction.

Chapter 5

CP Violation Measurement

Using the result from the last chapter we can now determine the CP violation parameters defined in Section 1.5. To do this we extend the data model from Section 4.8.2 to also include the lifetime difference Δt.

5.1 Data Model

The CP violation parameters are extracted from a three dimensional unbinned maximum likelihood fit to $M_{\rm bc}$, ΔE and Δt. All parameters of the model on $M_{\rm bc}$ and ΔE are fixed to the values obtained in the branching fraction measurement. Since there are no significant correlations between Δt and $M_{\rm bc}$ or ΔE, the PDF for each component, $\mathcal{P}_l(M_{\rm bc}, \Delta E)$, can easily be extended to

$$\mathcal{P}_l(M_{\rm bc}, \Delta E, \Delta t) = \mathcal{P}_l(M_{\rm bc}, \Delta E) \times \mathcal{P}_l(\Delta t) \tag{5.1}$$

5.1.1 Correctly Reconstructed Signal Events

Considering the effects of incorrectly tagging a B meson, the theoretical time-dependent Δt distribution from Equation 1.52 becomes

$$P_{sig}(\Delta t, q, \eta_y) = \frac{e^{-|\Delta t|/\tau_{\rm B^0}}}{4\tau_{\rm B^0}}\Big\{1 - q\Delta w + q(1-2w) \times \Big[\eta_y \frac{J_c}{J_0}\cos(\Delta m_d \Delta t) - \Big(\frac{2J_{s1}}{J_0}\sin(2\phi_1) + \eta_y \frac{2J_{s2}}{J_0}\cos(2\phi_1)\Big) \cdot \sin(\Delta m_d \Delta t)\Big]\Big\} \tag{5.2}$$

where q is the flavour determined for the $\rm B_{tag}$ meson as described in Section 3.5, w is the probability that this flavour tag is incorrect and Δw is the difference of the wrong tag probability between $\rm B^0$ and $\overline{\rm B}^0$. η_y contains the phase space information and is defined as

$$\eta_y = +1\ (-1) \text{ for } s^+ \geq s^-\ (s^+ \leq s^-) \quad s^+ = (p_{\rm D^{*+}} + p_{\rm K^0_S})^2 \quad s^- = (p_{\rm D^{*-}} + p_{\rm K^0_S})^2. \tag{5.3}$$

J_c/J_0, $(2J_{s1}/J_0)\sin(2\phi_1)$ and $(2J_{s2}/J_0)\cos(2\phi_1)$ represent the CP parameters need to be measured. Note how J_c/J_0 and $(2J_{s2}/J_0)\cos(2\phi_1)$ manifest in the asymmetry $q \cdot \eta_y$ while

$(2J_{s1}/J_0)\sin(2\phi_1)$ is only dependent on q. To be able to observe all three parameters we have to consider the asymmetry between events with $q \cdot \eta_y = +1$ and $q \cdot \eta_y = -1$ in addition to the normal CP asymmetry as explained in Section 1.4.3.

To account for detector and reconstruction effects, P_{sig} is convoluted with a decay mode independent resolution function [48],

$$\mathcal{P}_{sig}(\Delta t, q, \eta_y) = (R_{sig} * P_{sig})(\Delta t, q, \eta_y) = \int_{-\infty}^{\infty} R_{sig}(\tau) P_{sig}(\Delta t - \tau, q, \eta_y)\, d\tau. \tag{5.4}$$

This resolution function consists of three components,

$$R_{sig} = R_{det} * R_{NP} * R_K, \tag{5.5}$$

where R_{det} represents the detector resolution, R_{NP} describes the smearing due to reconstructing the B_{tag} vertex from non-primary tracks and R_K models the effects of the kinematic approximation that neglects the transverse momentum of the B mesons in the centre of mass system.

The result in Figure 5.1 shows a slight problem for SVD2 in the central region. As the amount of simulated data amounts to approximately 200 times the real data we think that this result can be tolerated.

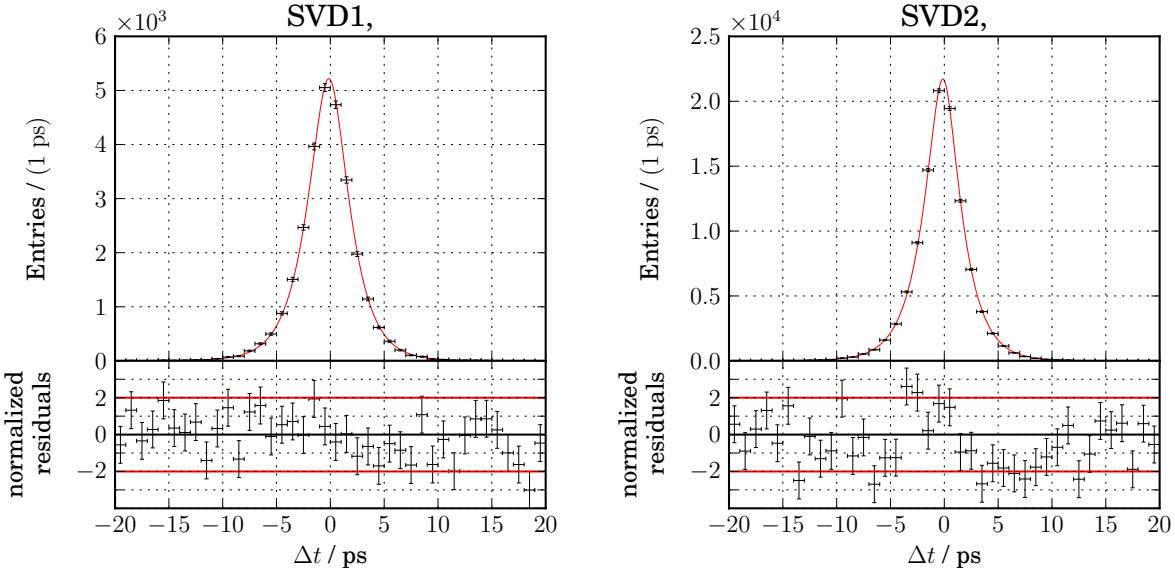

Figure 5.1: Fit to Δt for correctly reconstructed signal MC, integrated over all q and η_y.

5.1.2 Misreconstructed Signal Events

The same lifetime PDF for signal events (Section 5.1.1) is used to model misreconstructed events. The CP parameters are shared with the Signal component. Misreconstruction has

been defined as signal events where at least one track used to determine the B_{CP} vertex is incorrect. As such, there is a high chance that at least one track tends to be taken from the B_{tag} meson. This will shift the reconstructed vertex closer to that of the B_{tag} meson and the effective lifetime of the B_{CP} meson will appear smaller. To account for this effect we free the B^0 lifetime for misreconstructed events when creating the model from MC, resulting in $\tau_{mis} \sim 1\,\text{ps}$.

As with correctly reconstructed events, the fit to MC in Figure 5.2 shows small slight problem in the describing of the central area for the SVD2. Again, we consider this not significant due to the much higher statistics of the MC sample.

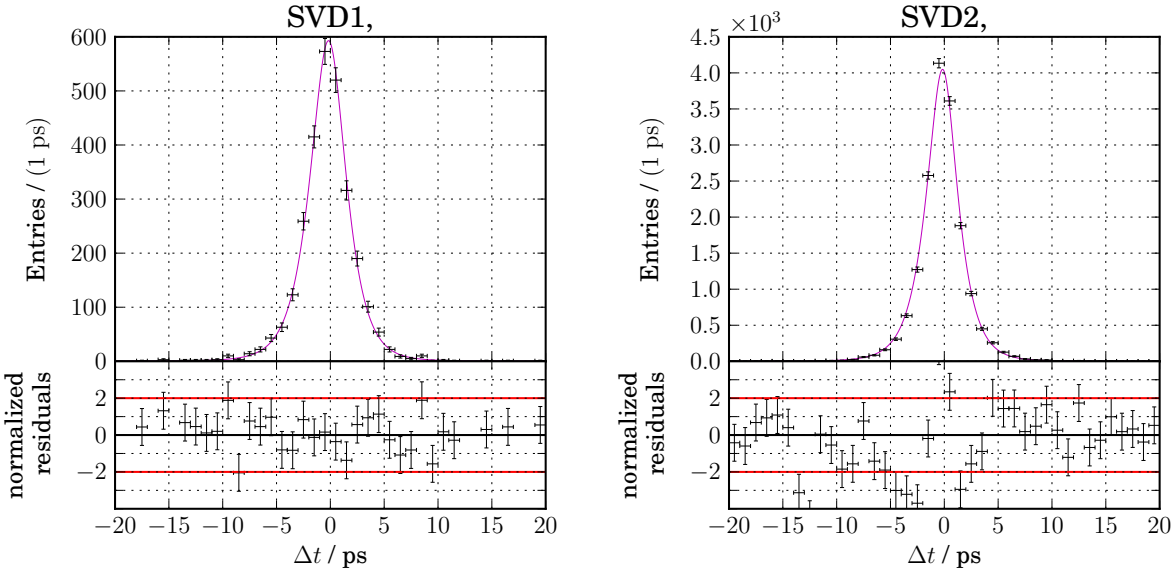

Figure 5.2: Fit to Δt for misreconstructed signal MC, integrated over all q and η_y.

5.1.3 Background Events from $B\overline{B}$ and $q\overline{q}$

To describe Δt for the background components, we use an empirical function consisting of two parts: an prompt part for vertices without a lifetime and an exponential decaying part for reconstructed particles which decay with an effective lifetime τ_{bkg},

$$P_{bkg}(\Delta t) = f_\delta \cdot \delta(\Delta t - \mu_\delta) + (1 - f_\delta) \cdot e^{|\Delta t - \mu_{bkg}|/\tau_{bkg}}, \tag{5.6}$$

where $\delta(x)$ is the Dirac delta function. This function is convoluted with a resolution function to account for the vertex resolution. As the vertex resolution depends on the number of tracks used in the vertex fit we distinguish between two different kinds of events: "Multi-track" events where more than one track is used for the determination of the vertex for B_{tag} and B_{CP} and "Single-track" events where at least one of the two vertices was determined using only one track. For both kinds we assume an double gaussian as

resolution function,

$$R_{bkg}(\Delta t) = (1 - f_{tail}) \cdot G(\Delta t, 0, \sigma \cdot s_{main}) + f_{tail} \cdot G(\Delta t, 0, \sigma \cdot s_{main} \cdot s_{tail}), \tag{5.7}$$

where $\sigma = \sqrt{\sigma_{CP}^2 + \sigma_{\text{tag}}^2}$ is the quadratic sum of the vertex errors given by the reconstruction.

The full lifetime PDF for background events is the convolution of $P_{bkg}(\Delta t)$ and $R_{bkg}(\Delta t)$,

$$\mathcal{P}_{bkg}(\Delta t) = (R_{bkg} * P_{bkg})(\Delta t) = \int_{-\infty}^{\infty} R_{bkg}(\tau) P_{bkg}(\Delta t - \tau)\, d\tau. \tag{5.8}$$

To avoid systematics and due to low statistics in the off-resonance data and possible differences between MC and data, the parameters for the background lifetime function are extracted from a sideband of the real data: A fit is performed on all events outside the signal region,

$$M_{\text{bc}} > 5.26\,\text{GeV}/c^2 \qquad -0.05\,\text{GeV} < \Delta E < 0.05\,\text{GeV}, \tag{5.9}$$

to determine the shape of the background lifetime PDF. The result can be seen in Figure 5.3

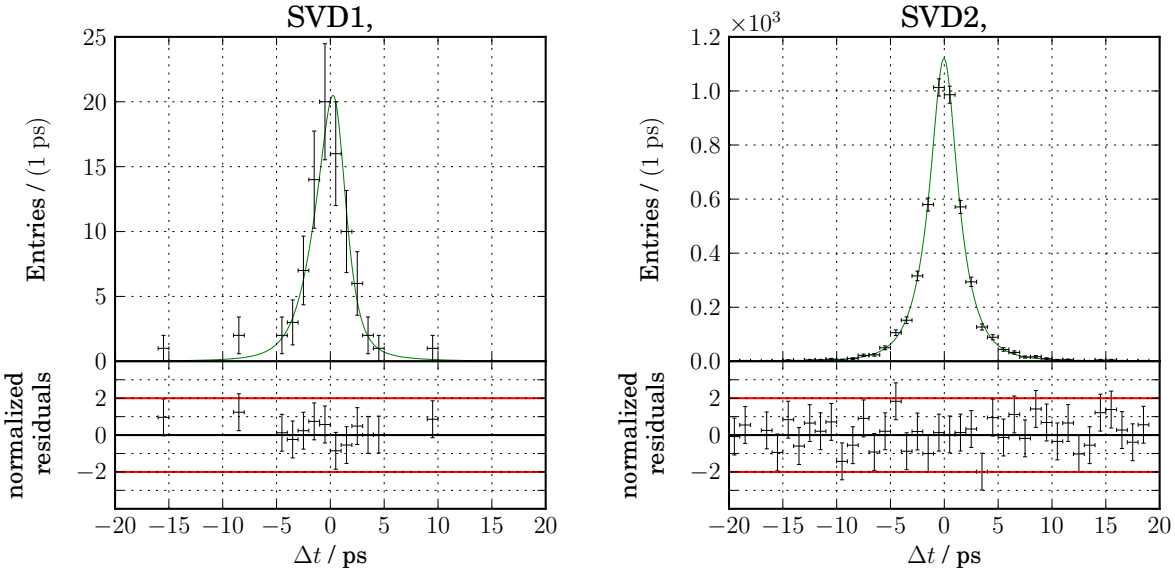

Figure 5.3: Fit to Δt for sideband data, integrated over all q and η_y.

5.2 Toy Monte Carlo Studies

To validate the full model we also performed toy MC studies. We set the CP parameters to the current world average and generated 2000 experiments where lifetime distributions

are generated from PDF and M_{bc} and ΔE are taken randomly from simulated events. We then fitted each of the 2000 experiments freeing only the CP parameters. In contrast to the final fit we also free the B^0 lifetime for the Signal component to check that the nominal B^0 lifetime used as input for the simulation, $\tau_{B^0} = 1.53\,\mathrm{ps}$, can be reproduced. The results can be seen in Figure 5.4 and 5.5, the raw fit results on the left and the pull distributions on the right side.

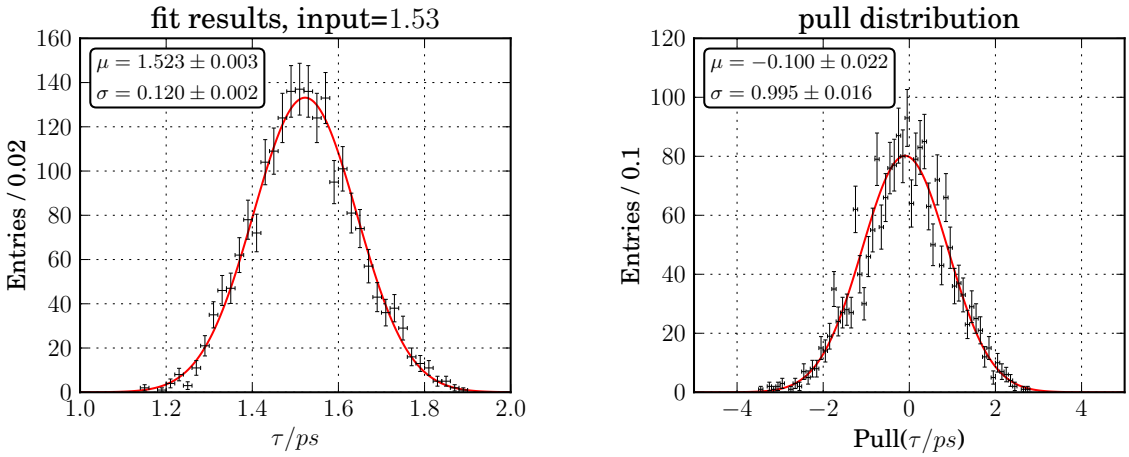

Figure 5.4: Results of the ToyMC tests for the B lifetime. On the left is shown the raw fit result and on the right is the pull distribution. The mean and width of the distributions are determined from a single gauss fit.

It can be seen clearly that for all parameters the fit output is in good agreement with the input values. The pull distribution is consistent with a standard normal distribution and no significant bias can be observed. The width of the result distribution is equal the expected statistical error of the final fit and are half of the errors obtained in the previous analysis [37].

5.3 Linearity Tests

As for the branching fraction measurement we also performed linearity tests to validate the fit procedure over the whole parameter range. We created 20 000 experiments where the CP parameters for each experiment are generated uniformly inside of the unit sphere so that

$$\Big(J_c/J_0\Big)^2 + \Big((2J_{s1}/J_0)\sin(2\phi_1)\Big)^2 + \Big((2J_{s2}/J_0)\cos(2\phi_1)\Big)^2 \leq 1 \tag{5.10}$$

and the B^0 lifetime is fixed to its nominal value.

From the results in Figures 5.6 and 5.7 we can conclude that the fit shows a good behaviour, especially for the CP parameter J_c/J_0. For $(2J_{s1}/J_0)\sin(2\phi_1)$ and $(2J_{s2}/J_0)\cos(2\phi_1)$ a small bias of 11 % and 14 % of the statistical error can be observed over the full range which will be considered as an systematic error.

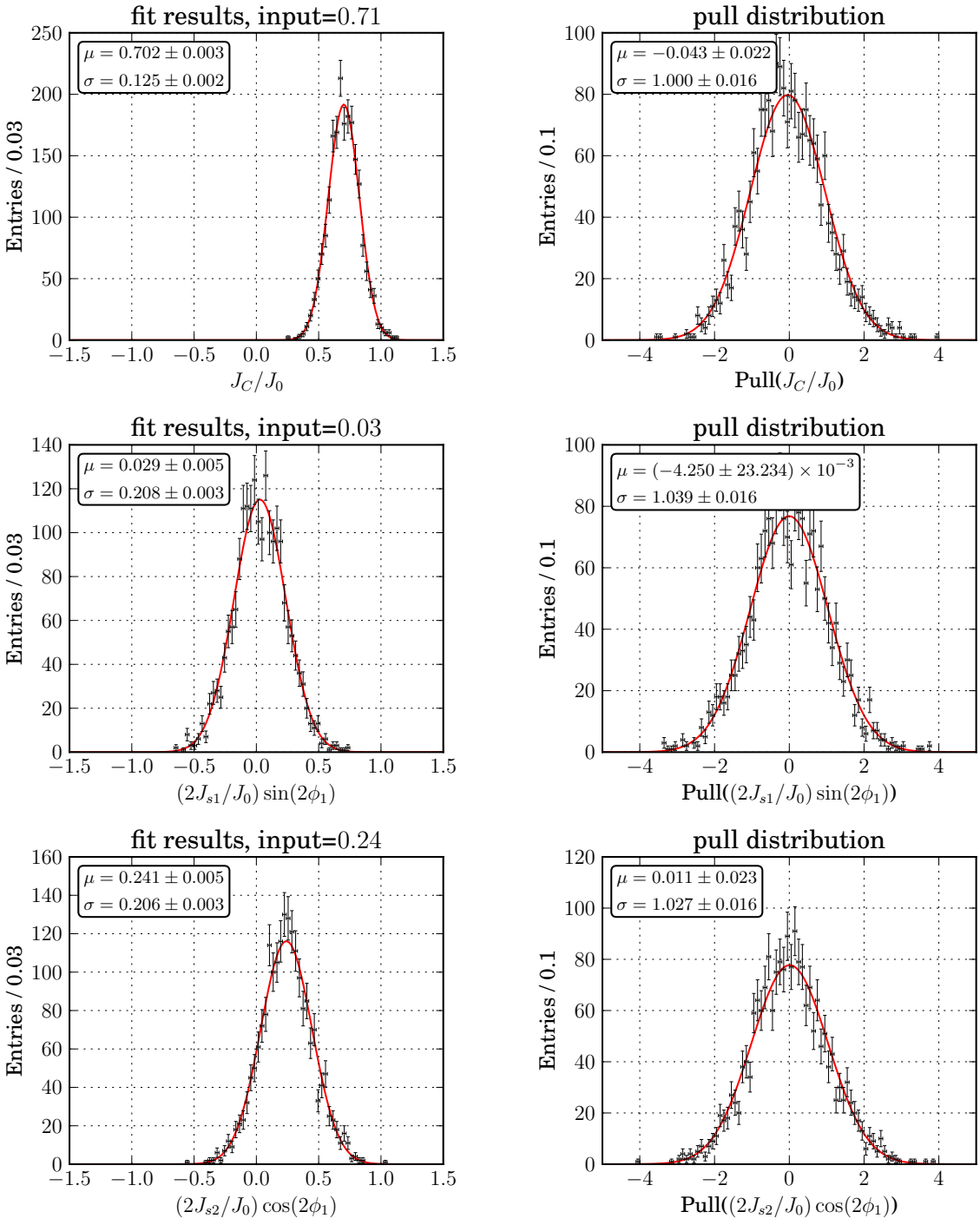

Figure 5.5: Results of the ToyMC tests for the CP parameters J_c/J_0 (top), $(2J_{s1}/J_0)\sin(2\phi_1)$ (middle) and $(2J_{s2}/J_0)\cos(2\phi_1)$ (bottom). On the left are shown the raw fit results and on the right is the pull distribution. The mean and width of the distributions are determined from a single gauss fit.

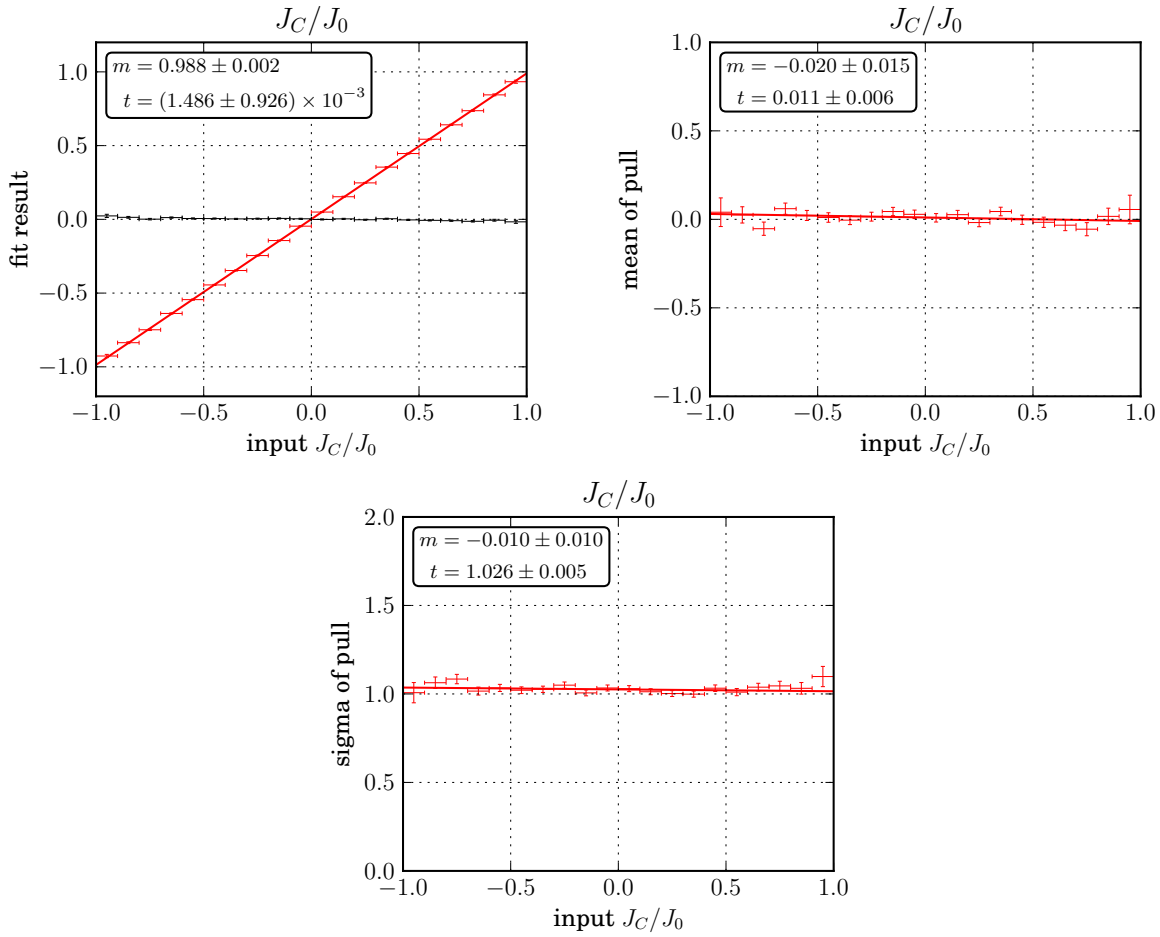

Figure 5.6: Results of the linearity tests the CP parameter J_c/J_0. Top left shows the fit results and the residuals, top right shows the mean and the bottom shows the width of the pull distribution.

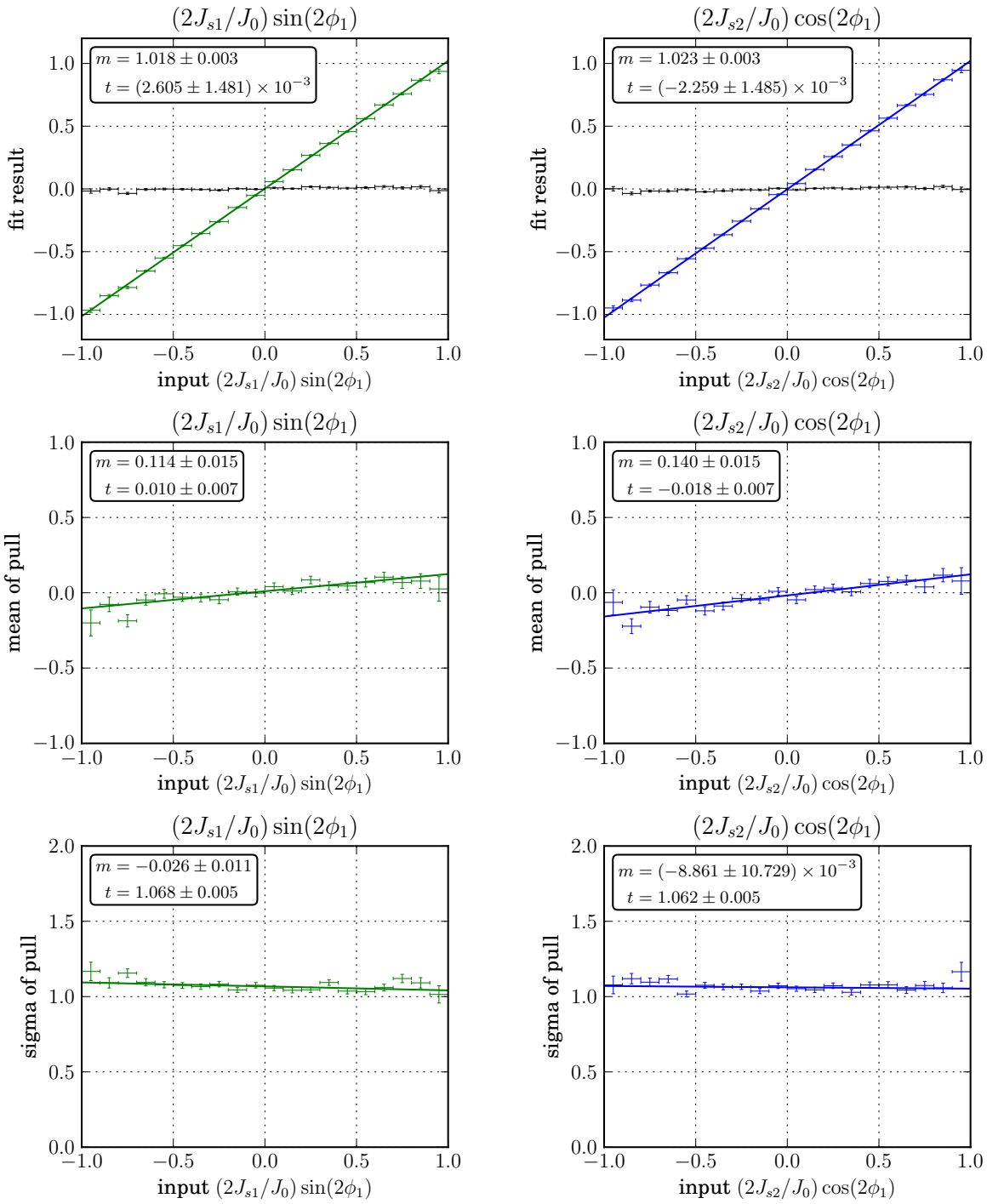

Figure 5.7: Results of the linearity tests for the CP parameters $(2J_{s1}/J_0)\sin(2\phi_1)$ (left) and $(2J_{s2}/J_0)\cos(2\phi_1)$ (right). On the top are the fit results and the residuals, at the middle and bottom is the mean and the width of the pull distribution respectively.

5.4 Control Sample

To validate that the fit can produce the expected results on data we performed the CP violation analysis on the control sample already used in the branching fraction measurement 4.6.

The lifetime PDF used for the mode of interest does not allow for an unequal distribution of $\eta_y = +1$ and $\eta_y = -1$. This is no problem for the signal channel as the Dalitz plot is symmetric but for the control channel the second D^* is replaced by a D meson and the symmetry is lost. Because of that, we chose to change the Δt PDF for signal components (Eq. 5.2) to the more common PDF with only two parameters (Eq. 1.42), removing the η_y dependence:

$$P_{sig}(\Delta t, q, \eta_y) = \frac{e^{-|\Delta t|/\tau_{\mathrm{B}^0}}}{4\tau_{\mathrm{B}^0}}\Big\{1 - q\Delta w + q(1-2w) \times \Big[A_{CP}\cos(\Delta m_d \Delta t) + S_{CP}\cdot\sin(\Delta m_d \Delta t)\Big]\Big\}. \quad (5.11)$$

Everything else is kept identical to the mode of interest. From the fit result shown in Figure 5.8 we obtain

$$\begin{aligned} A_{CP} &= 0.134 \pm 0.092 \\ S_{CP} &= -0.028 \pm 0.131, \end{aligned} \quad (5.12)$$

which is in agreement with the expectation of no CP violation within 1.8σ. The background subtracted CP asymmetry for the control channel can be seen in Figure 5.9 and also shows no evidence for CP violation.

In addition we perform a fit where only the B^0 lifetime is free and we obtain

$$\tau_{\mathrm{B}^0} = 1.342 \pm 0.099 \quad (5.13)$$

which is consistent with the current world average, $\tau_{\mathrm{B}^0} = 1.519 \pm 0.007$ [46], within 1.8 σ.

To further check the stability of this result against possible problems with the modelling of the background lifetime PDF, especially considering the high background level, we repeated the fit of the B^0 lifeftime 1000 times while varying the f_δ and τ_{bkg} parameters of the background PDF within their errors. The results can be seen in Figure 5.10 and shows that the changes to the B^0 lifetime with the variation of the background description amount to 34 % of the statistical error. Given the very large amount of background events in this control sample compared to the mode of interest we can conclude that the extracted lifetime is stable against variations of the background shape.

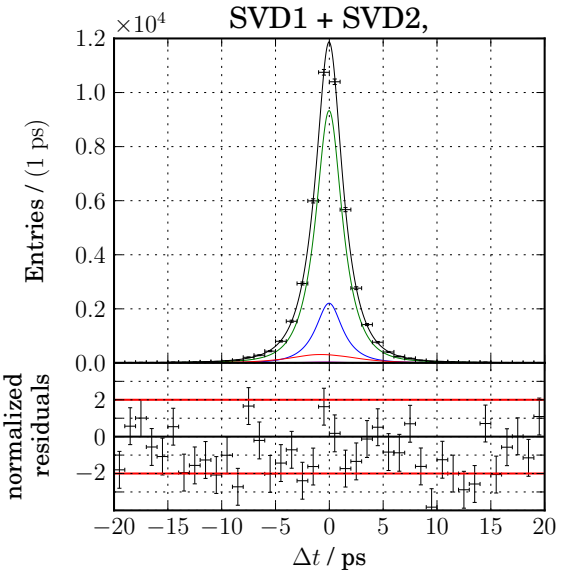

Figure 5.8: Signal enhanced results for the lifetime fit on the control channel, integrated over all q. To enhance the signal fraction we only show the distribution only for events which satisfy $M_{\mathrm{bc}} > 5.26\,\mathrm{GeV}/c^2$ and $-0.05\,\mathrm{GeV} < \Delta E < 0.05\,\mathrm{GeV}$.

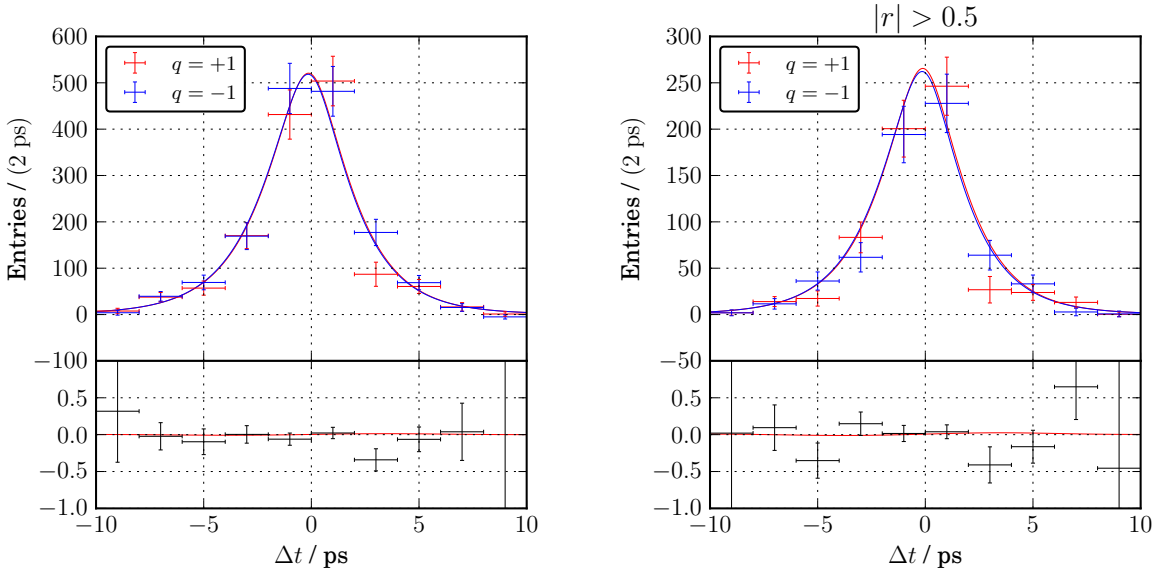

Figure 5.9: Background subtracted Δt lifetime (top) and CP asymmetry (bottom) for the control channel. Left side shows the asymmetry for all events and the right side shows the asymmetry for events with a high quality flavour tag, $|r| > 0.5$.

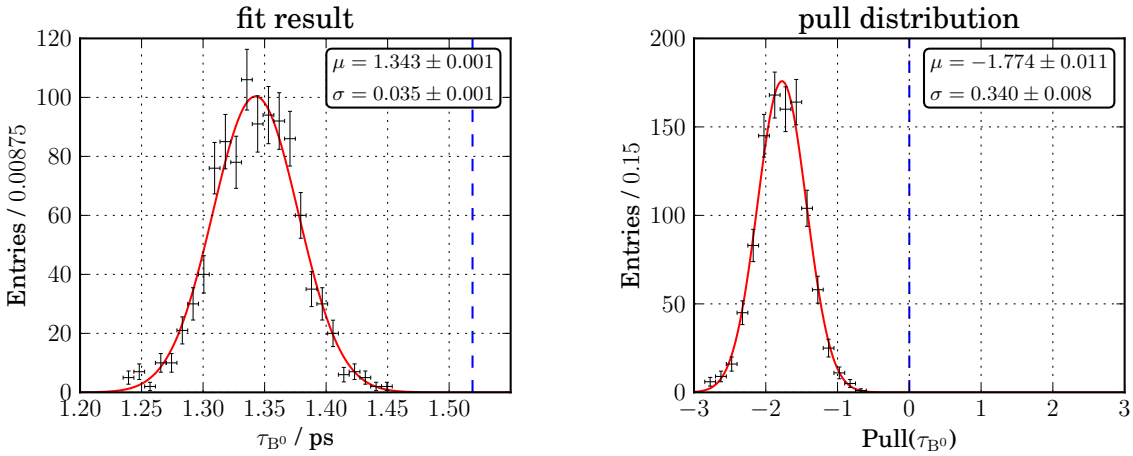

Figure 5.10: Study of the effect on B^0 lifetime when varying the background Δt model. We performed 1000 fits where f_δ and τ_{bkg} were varied within their errors. The resulting B^0 lifetime can be seen on the right and the pull distribution versus the world average on the left. The dotted line shows the position of the world average.

5.5 Results on Partial Data

As a next step we performed the CP analysis on the data which has already been analyzed in the previous analysis[37]. This data contains 449 million $B\overline{B}$ pairs and accounts for 58 % of the full data. Due to the improved reconstruction efficiency in SVD2, especially the addition of the SVD-only track reconstruction, since the previous analysis we expect a significant increase in statistics compared to the previous analysis.

To perform the CP analysis we first repeat the branching fraction measurement on the partial data for SVD2 and obtain

$$Y^{\text{SVD2}}_{\text{sig,partial}} = 314.910^{+32.986}_{-31.148}, \tag{5.14}$$

which is more than three times larger than the total yield for SVD2 in the previous analysis. We use this result for the fit to the CP parameters. The result of the Δt fit is shown in Figure 5.11 and we extract

$$\underbrace{\begin{aligned} J_c/J_0 &= 0.197^{+0.155}_{-0.159}, \\ (2J_{s1}/J_0)\sin(2\phi_1) &= 0.051^{+0.228}_{-0.225}, \\ (2J_{s2}/J_0)\cos(2\phi_1) &= 0.356^{+0.221}_{-0.232}. \end{aligned}}_{\text{this analysis}} \qquad \underbrace{\left(\begin{aligned} J_c/J_0 &= 0.60^{+0.25}_{-0.28} \pm 0.08 \\ (2J_{s1}/J_0)\sin(2\phi_1) &= -0.17^{+0.42}_{-0.42} \pm 0.09 \\ (2J_{s2}/J_0)\cos(2\phi_1) &= -0.23^{+0.43}_{-0.41} \pm 0.13 \end{aligned}\right)}_{\text{previous Belle measurement}} \tag{5.15}$$

Compared to the previous results we notice that J_c/J_0 is significantly closer to zero but agrees within 2.5 σ. $(2J_{s1}/J_0)\sin(2\phi_1)$ and $(2J_{s1}/J_0)\sin(2\phi_1)$ are in good agreement with the previously published results. The background subtracted CP asymmetries are shown in Figures 5.12 and 5.13 for all events and for events with good flavour tag quality

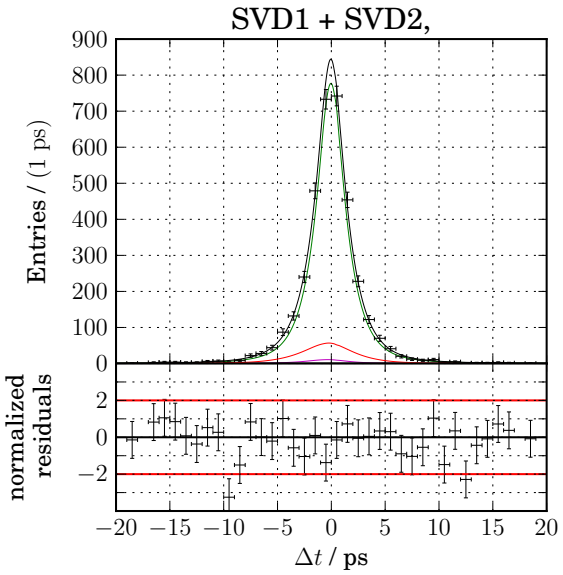

Figure 5.11: Results for the lifetime fit on the partial data containing the first 449 million $B\overline{B}$ events, integrated over all q and η_y.

respectively. In both asymmetries we see a good agreement between the data and the PDFs obtained from the fit.

Similar to the Control channel we also perform a fit to estimate the B^0 lifetime. The result,

$$\tau_{B^0} = 1.601^{+0.146}_{-0.137}, \tag{5.16}$$

is in very good agreement with the current world average, $\tau_{B^0} = 1.519 \pm 0.007$ [46], within 0.6 σ.

5.6 B^0 Lifetime from Full Data

As a final check we extracted the B^0 lifetime from the full data. For this we first perform a fit of the lifetime with blinded CP parameters and then repeat the fit with a free B^0 lifetime for the signal component (shown in Figure 5.14). We extract a lifetime of

$$\tau_{B^0} = 1.472 \pm 0.095, \tag{5.17}$$

which is again in very good agreement with the world average (within 0.5σ).

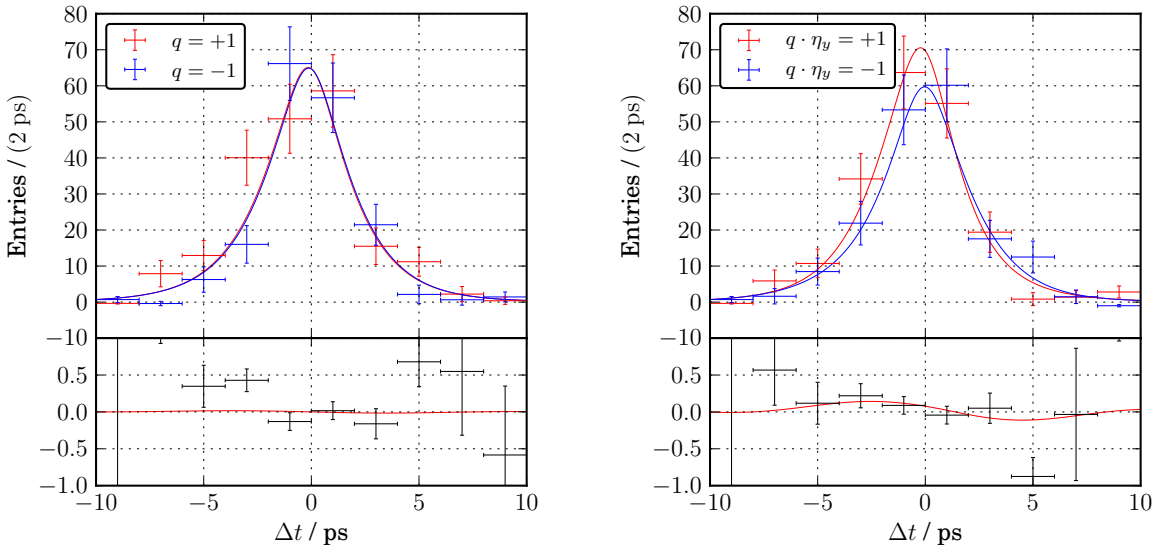

Figure 5.12: Background subtracted Δt lifetime (top) and CP asymmetry (bottom) extracted from the partial data containing the first 449 million $B\overline{B}$ events. Left side shows the asymmetry between different B_{tag} flavour tag, q and the right side shows the asymmetry between the product $q \cdot \eta_y$.

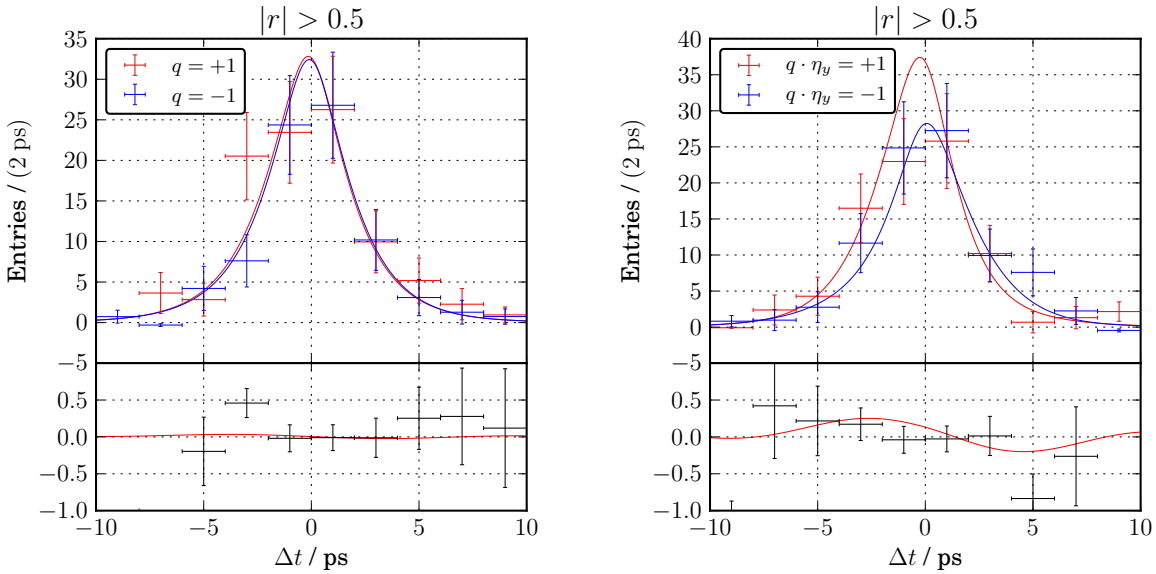

Figure 5.13: Background subtracted Δt lifetime (top) and CP asymmetry (bottom) extracted from the partial data for events with good flavour tag quality, $|r| > 0.5$. Left side shows the asymmetry between different B_{tag} flavour tag, q and the right side shows the asymmetry between the product $q \cdot \eta_y$.

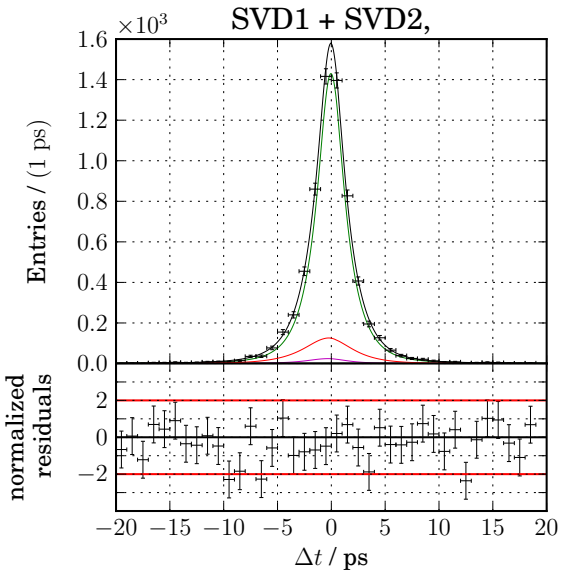

Figure 5.14: Results for the lifetime fit on the full data, integrated over all q and η_y.

5.7 CP Parameter Result from Full Data

Finally we perform the lifetime fit on the full data. We obtain a result of

$$\underbrace{\begin{aligned} J_c/J_0 &= 0.37 \pm 0.10, \\ (2J_{s1}/J_0)\sin(2\phi_1) &= 0.30 \pm 0.16, \\ (2J_{s2}/J_0)\cos(2\phi_1) &= 0.16 \pm 0.16, \end{aligned}}_{\text{this analysis}} \qquad \underbrace{\left(\begin{aligned} J_c/J_0 &= 0.60^{+0.25}_{-0.28} \pm 0.08 \\ (2J_{s1}/J_0)\sin(2\phi_1) &= -0.17^{+0.42}_{-0.42} \pm 0.09 \\ (2J_{s2}/J_0)\cos(2\phi_1) &= -0.23^{+0.43}_{-0.41} \pm 0.13 \end{aligned}\right)}_{\text{previous Belle measurement}} \quad (5.18)$$

which is consistent with the result from the partial data within less then two standard deviations for all three values. Nevertheless we see relative large differences when comparing to the partial data. $(2J_{s1}/J_0)\sin(2\phi_1)$, which was compatible with zero to a very high precision, now shows a deviation of almost two standard deviations. Further studies are needed to verify that this is a statistical fluctuation and no systematic effect.

Figures 5.15 and 5.16 shows the background subtracted data together with the lifetime PDFs for signal events as well as their asymmetries for all events and for events with good vertex tagging, $|r| > 0.5$. In all cases we see a very good agreement between the data points and the lifetime PDF.

5.8 Systematic Uncertainties

As for the branching ratio measurement we have to consider different sources of systematic errors in addition to the statistical error obtained from the fit. Main contributions arise from the vertexing procedure as well as the flavour tagging procedure. But also the

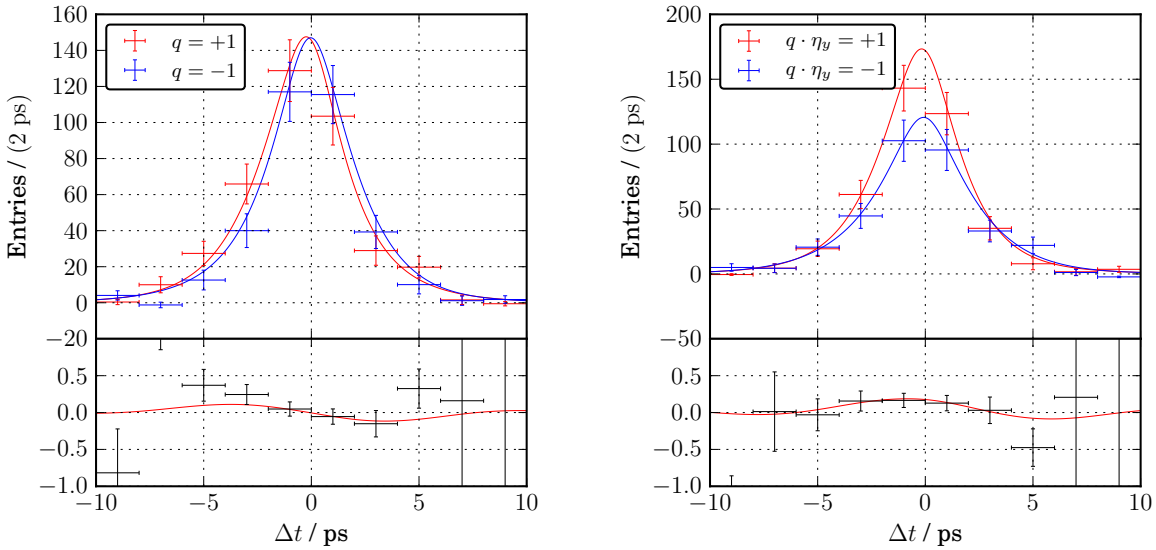

Figure 5.15: Background subtracted Δt lifetime (top) and CP asymmetry (bottom) extracted from the full data. Left side shows the asymmetry between different B_{tag} flavour tag, q and the right side shows the asymmetry between the product $q \cdot \eta_y$.

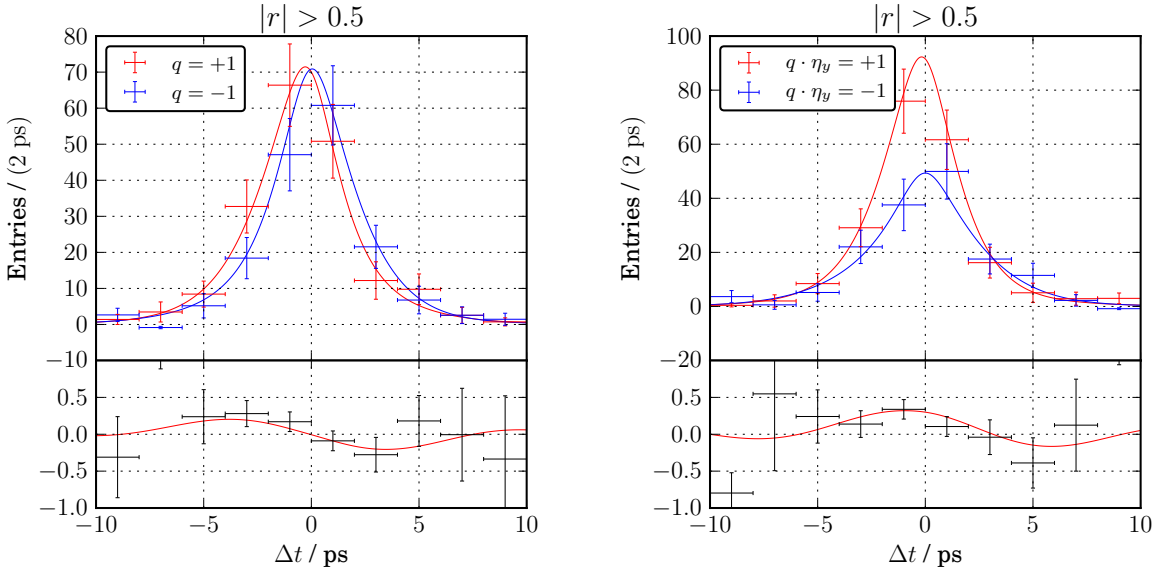

Figure 5.16: Background subtracted Δt lifetime (top) and CP asymmetry (bottom) extracted from full data for events with good flavour tag quality, $|r| > 0.5$. Left side shows the asymmetry between different B_{tag} flavour tag, q and the right side shows the asymmetry between the product $q \cdot \eta_y$.

parametrization of the resolution function for signal and background components as well as the uncertainties on the used physics parameters have to be considered.

Unless otherwise stated, the systematic errors are estimated by varying certain cuts or input values to the fit in a specified interval. We repeat the fit with the new values and the larger deviation from the original fit result is then taken as systematic error. If more than one parameter or cut is varied for a given category the combined systematic is calculated by adding the larger deviation for each parameter in quadrature.

5.8.1 Vertex Reconstruction

Vertex reconstruction plays an essential role in CP violation analysis. As such we have to consider the effect of the vertexing procedure and the applied cuts on the final result

IP Profile

The vertices of the B_{CP} and B_{tag} mesons were reconstructed using an IP tube constraint (see Section 3.4.7). To estimate the systematic error we varied IP_{smear} by $\pm 10\,\mu m$.

B_{tag} Track Selection

The track selection cuts for the B_{tag} vertex described in Section 3.5.2 could also influence the final result so we repeated the analyis and varied the cuts on the z-resolution and $r\phi$-distance by $\pm 10\,\%$.

Vertex Quality Cuts

We also required a vertex quality cuts for both vertices, B_{tag} and B_{CP}, as described in Section 3.6. For the estimation of the systematic error we repeated the fit with $h < 25$ and $h < 100$ and varied the requirements on σ_z by $\pm 10\,\%$.

Δt Range

In Section 3.6 we also imposed $|\Delta t|$ to be within 70 ps. To validate the result against this requirement we repeat the fit with $|\Delta t| \leq 40$ ps and $|\Delta t| \leq 100$ ps.

Misalignment and possible Δz bias.

We have to take into account the possible effects of misalignment for our result. Two possible sources are the internal misalignment within the SVD and a relative misalignment between the SVD and CDC which might cause a bias in the Δz distribution. Both effects can be studied using MC samples with and without misalignment and taking the difference as systematic error. However, these effects are considered to be mode independent so their contribution is taken from the $B^0 \to J/\psi K^0_S$ study [63].

5.8.2 Flavour Tagging

The wrong tag fractions, w, and the B^0– $\overline{B}^0$ wrong tag fraction difference, Δw are described in Section 3.5.1. These fractions are determined from control samples and also have an uncertainty. We estimate the systematic uncertainty by varying the value for w and Δw for each region of r separately and summing the differences in quadrature.

5.8.3 Resolution Function

We vary all parameters used in the resolution function for signal events according to their errors given in [48]. Again, we sum all differences in quadrature.

5.8.4 Model Uncertainties

As for the branching fraction measurement we have to account for the uncertainties in our model parameters. Following the same procedure as described in Section 4.9.5 we estimate the systematic uncertainty arising from model uncertainties by performing 20 000 fits to the data where we vary all model parameters according to their covariance matrix. This includes the uncertainties on the yields from the branching fraction measurement and the shape of the background lifetime obtained from sideband. Figure 5.17 shows the deviation from the original result when varying the model parameters for all three CP parameters. We fitted a bifurcated Gaussian to the resulting distribution and took the larger width as systematic error.

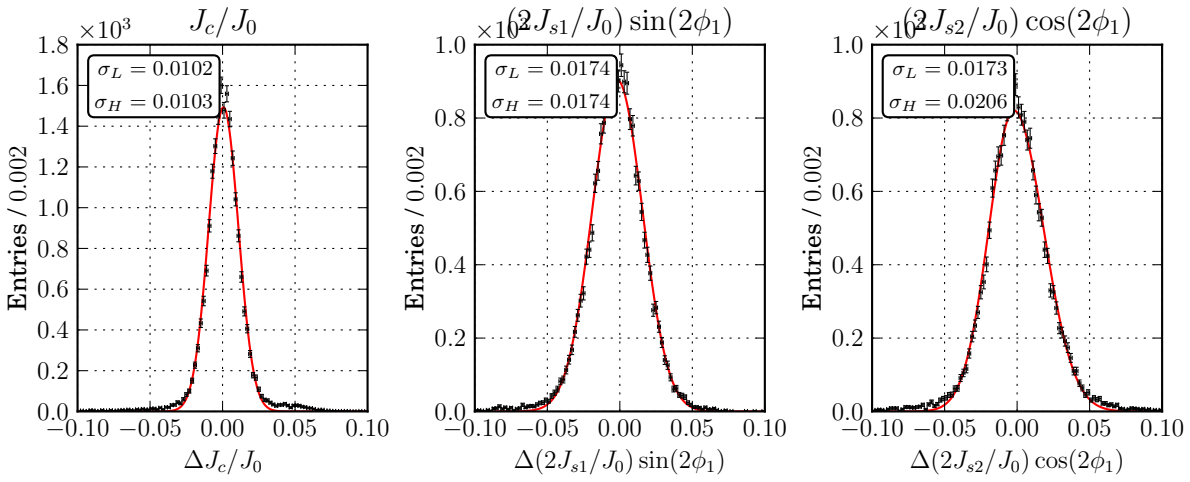

Figure 5.17: Deviations from the CP fit result when randomly varying all model parameters according to their covariance matrix for J_c/J_0 (left), $(2J_{s1}/J_0)\sin(2\phi_1)$ (middle) and $(2J_{s2}/J_0)\cos(2\phi_1)$ (right).

Category	$\Delta J_c/J_0$	$\Delta(2J_{s1}/J_0)\sin(2\phi_1)$	$\Delta(2J_{s2}/J_0)\cos(2\phi_1)$
Vertex reconstruction			
IP profile	0.0002	0.0020	0.0130
B_{tag} track selection	0.0110	0.0068	0.0049
Vertex quality cuts	0.0084	0.0114	0.0160
Δt range	0.0001	0.0005	0.0003
Misalignment	0.0041	0.0024	0.0024
Δz bias	0.0050	0.0039	0.0039
Flavour tagging	0.0014	0.0016	0.0014
Resolution function	0.0100	0.0145	0.0140
Model uncertainties	0.0103	0.0174	0.0206
Physics parameters	0.0010	0.0004	0.0001
Fit bias	0.0030	0.0079	0.0015
Tag side interference	0.0011	0.0015	0.0017
Total	0.0213	0.0280	0.0331

Table 5.1: Absolute values for the systematic uncertainties from different sources for the CP violation measurement. We calculated the total by summing all contributions in quadrature.

5.8.5 Physics Parameters

The world averages for $\Delta m_d = (0.507 \pm 0.004)\,\mathrm{ps}^{-1}$ and $\tau_{B^0} = (1.519 \pm 0.007)\,\mathrm{ps}$ [46] are used in the lifetime PDF in Equation 5.2. We calculate the associated systematic error by varying their values within the errors.

5.8.6 Fit Bias

The toy MC linearity test in Section 5.3 showed a small bias for $(2J_{s1}/J_0)\sin(2\phi_1)$ and $(2J_{s2}/J_0)\cos(2\phi_1)$. The expected deviations from the real values are taken as a systematic error.

5.8.7 Tag Side Interference

While the flavor of the B_{tag} is usually determined using flavour specific events there contributions CKM-suppressed decays. The interference between these amplitudes gives deviations from the standard time evolution [64]. The correction to the time-dependent PDF is estimated with a $B^0 \to D^*\ell\nu$ sample. Toy MC is generated with and without tag side interference and the difference is taken as the systematic error.

5.8.8 Total Systematics

A summary of all obtained systematics for the time-dependent CP analysis is given in Table 5.1. The different contributions are summed in quadrature.

5.9 Final Result

Together with the values from Equation 5.18 and the systematic errors from Table 5.1 we obtain a fnal result of

$$\begin{aligned} J_c/J_0 &= 0.37 \pm 0.10(\text{stat}) \pm 0.02(\text{syst}) \\ (2J_{s1}/J_0)\sin(2\phi_1) &= 0.30 \pm 0.16(\text{stat}) \pm 0.03(\text{syst}) \\ (2J_{s2}/J_0)\cos(2\phi_1) &= 0.16 \pm 0.16(\text{stat}) \pm 0.03(\text{syst}). \end{aligned} \tag{5.19}$$

These measurements agree with the previous results from BABAR [35]:

$$\begin{aligned} J_c/J_0 &= 0.76 \pm 0.18(\text{stat}) \pm 0.07(\text{syst}), \\ (2J_{s1}/J_0)\sin(2\phi_1) &= 0.10 \pm 0.24(\text{stat}) \pm 0.06(\text{syst}), \\ (2J_{s2}/J_0)\cos(2\phi_1) &= 0.38 \pm 0.24(\text{stat}) \pm 0.05(\text{syst}), \end{aligned}$$

and Belle [37],

$$\begin{aligned} J_c/J_0 &= \quad 0.60^{+0.25}_{-0.28}(\text{stat}) \pm 0.08(\text{syst}), \\ (2J_{s1}/J_0)\sin(2\phi_1) &= -0.17^{+0.42}_{-0.42}(\text{stat}) \pm 0.09(\text{syst}), \\ (2J_{s2}/J_0)\cos(2\phi_1) &= -0.23^{+0.43}_{-0.41}(\text{stat}) \pm 0.13(\text{syst}). \end{aligned}$$

within two standard deviations. The statistical uncertainties of our measurement are less than half of the previous Belle result. We could also decrease the systematic uncertainties by roughly a factor of two due to improvements in the reconstruction and vertexing procedures. This currently the most precise measurement of the time dependent CP violation parameters for $B^0 \to D^{*-}D^{*+}K^0_S$ decays.

As J_{s2}/J_0 is predicted to be positive [34] we can determine an exclusion limit for a negative sign for $\cos(2\phi_1)$. We perform a series of fits where $(2J_{s2}/J_0)\cos(2\phi_1)$ is fixed to different values and record the likelihood. We convolute this distribution with using a gaussian distribution with a width of $\sigma = 0.033$ to account for the systematic error, shown in Figure 5.18. From this result we can exclude a negative result for $(2J_{s2}/J_0)\cos(2\phi_1)$ with a significance of 1.03 σ. This corresponds to a confidence level of 85 %.

Although our measurement of $(2J_{s2}/J_0)\cos(2\phi_1)$ has smaller uncertainties, the central value is closer to zero when compared to the BABAR results. Because of this our constraint on the sign of $\cos(2\phi_1)$ is weaker then the one obtained by BABAR (94 %).

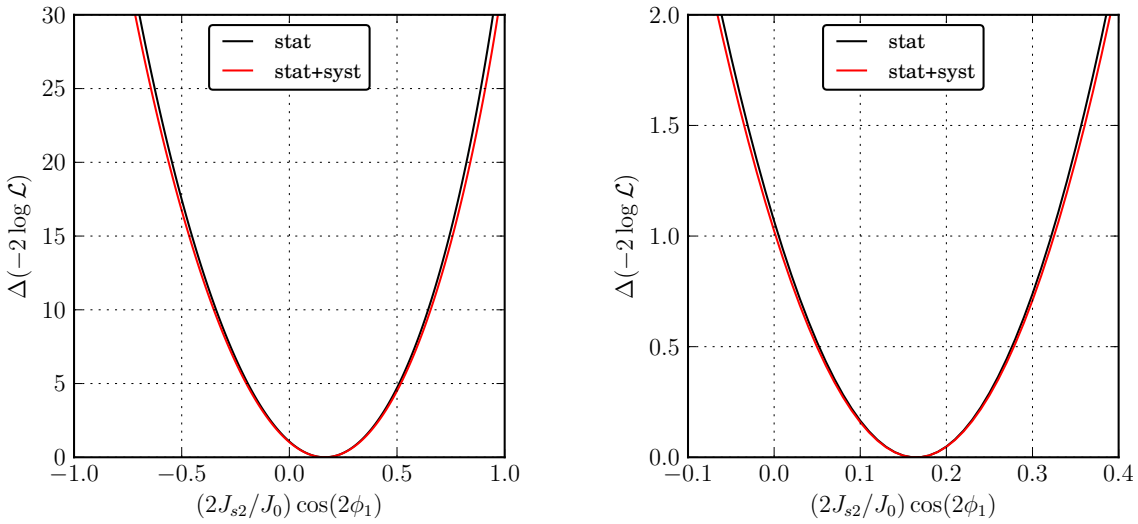

Figure 5.18: Likelihood distribution for $(2J_{s2}/J_0)\cos(2\phi_1)$, full range (left) and around the minimum (right). The black line is the likelihood distribution obtained from the fit and the red line shows the final result including systematic errors.

Chapter 6

Belle II Vertex Detector Simulation

The SuperKEKB project [65, 66] , which is scheduled to start data-taking in 2016, is an upgrade of the original Belle Experiment. The accelerator will be upgraded to SuberKEKB [17, 67] and targets a luminosity of $8 \times 10^{35}\,\mathrm{cm}^{-2}\mathrm{s}^{-1}$. To exploit this luminosity the Belle detector will be upgraded [17, 42]. Among these changes there is a completely new vertex detector which consists of a two layer pixel detector (PXD) and a four layer double sided strip detector (SVD). With this new configuration we expect an improvement of more than a factor of two for the single track impact parameter resolution compared to Belle.

To be able to simulate events we need to implement a precise description of the geometry and material in the Belle II software framework. The simulation for Belle II is based on Geant4 [68], an improved C++ version of the GEANT toolkit used for Belle.

This chapter presents the implementation of the simulation geometry for the combined Belle II vertex detector (VXD).

6.1 The SuperKEKB Accelerator

In order to achieve the targeted luminosity of $8 \times 10^{35}\,\mathrm{cm}^{-2}\mathrm{s}^{-1}$, the SuperKEKB accelerator will employ the "Nano-beam" scheme [69], which was first proposed for the Super B factory in Italy [70]. A relatively large crossing angle of 83 mrad between the two beams and a very small horizontal emittance allow to minimize the longitudinal overlap region of the two beams at the interaction point. New superconducting quadrupole systems close to the vertex allow to squeeze the vertical beta function at the IP, β_y^*, by almost a factor of 20 compared to Belle.

In addition, the beam energies have been changed to 7.0 GeV for the electron beam and 4.0 GeV for the positron beam compared to 8.0 GeV and 3.5 GeV at Belle. This is due to decrease the effects from Touschek (intra-beam) scattering [71] which limits the beam lifetime.

6.2 The Belle II Detector

The Belle II detector will retain the basic layout of the Belle detector. An overview of all sub-detectors is shown in Figure 6.1. It consists of a pixel detector and a double sided strip detector to determine the vertices and a central drift chamber (CDC) for tracking of charged particles. The Belle particle ID systems TOF and ACC are replaced by a time of propagation counter (TOP) in the barrel region and an Aerogel RICH detector in the forward endcap. These are encased by the electromagnetic calorimeter (ECL), the 1.5 T solenoid and the K_L^0/μ detection system (KLM). The ECL, solenoid and KLM get reused from Belle but receive significant updates. In this section we will focus only on the vertex detectors. More information on the other sub-detectors can be found in [17].

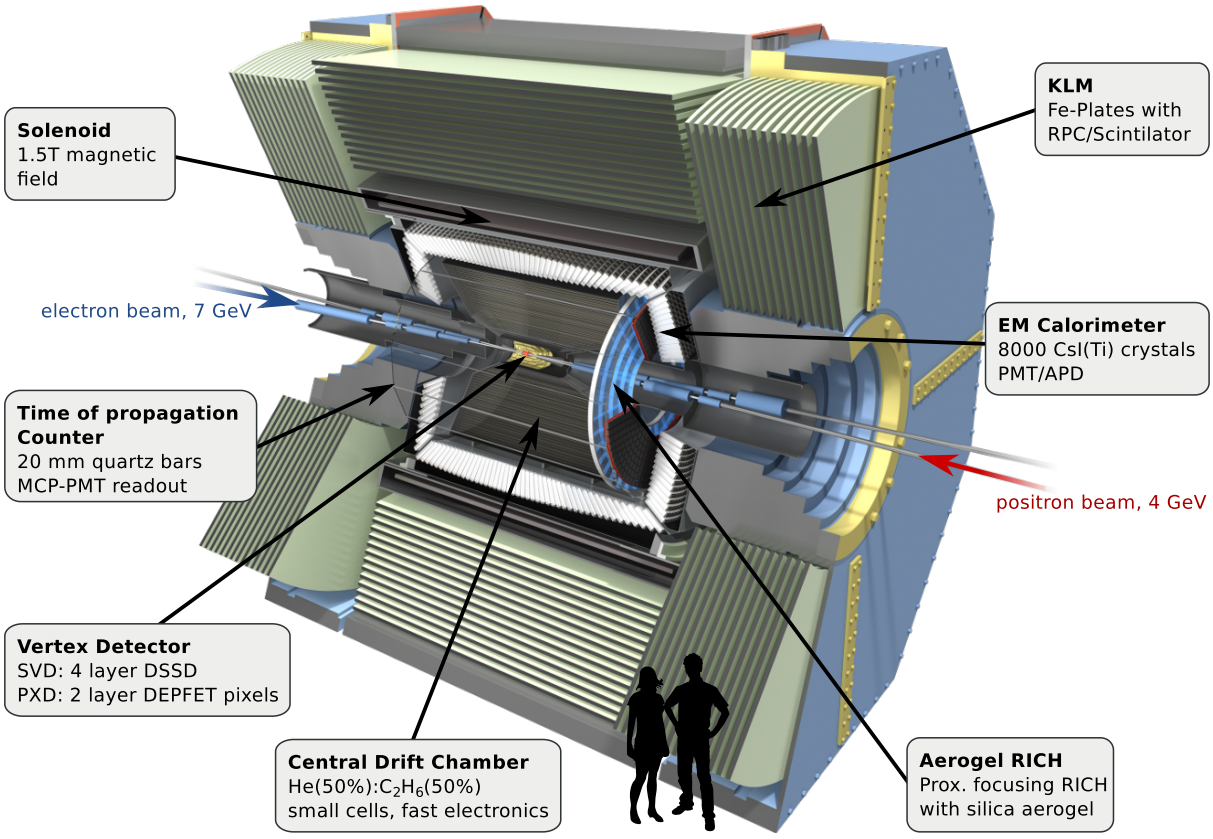

Figure 6.1: Overview of the Belle II detector.

6.2.1 Coordinate system

The global coordinate system of Belle II is defined as a right-handed coordinate system with x, y and z-axes. The origin is located at the nominal interaction point (IP) with the z-axis pointing along the axis of the magnetic solenoid. The y axis is pointing upwards and the x-axis lies in the accelerator plane and points away from the accelerator center.

The radial distance, $r = \sqrt{x^2 + y^2}$, is the distance to the origin projected on the xy-plane, θ is the polar angle to the z-axis and ϕ is the azimuthal angle with respect to the positive x-axis. As for Belle, the acceptance is defined as

$$17° \leq \theta \leq 150°. \tag{6.1}$$

The directions forward and backward denote the $z > 0$ and $z < 0$ sides of the detector respectively. Both beams have an inclination of 41.5 mrad with respect to the z axis while the electron beam goes in the forward direction and the positron beam goes in the backward direction.

For local coordinates of the sensors in the PXD and SVD, the convention is the right-handed coordinate system with the axes u, v and w. u points along the global $r\phi$ direction, v is in the direction of the global z axis and w is pointing away from the IP.

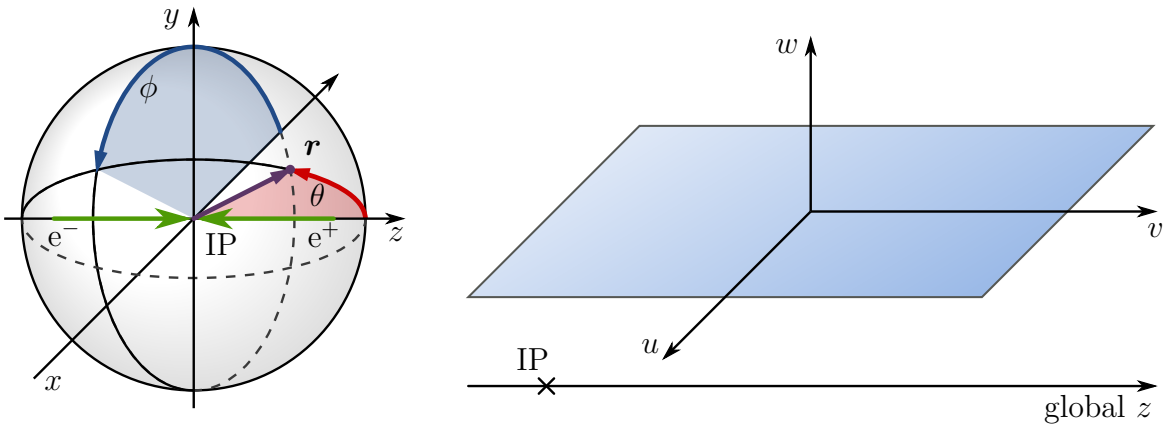

(a) Global coordinates. (b) Local coordinates.

Figure 6.2: Belle II coordinate system.

6.2.2 Beam Pipe

The beam pipe design for Belle II is very similar to the one used in Belle (Section 2.2.1): A dual layer of Beryllium cylinders with a cooling gap in between and a 10 µm gold plating on the inside to shield low energy X-ray background. In contrast to Belle, the outer radius has been reduced from 16.25 mm to 12.0 mm.

6.2.3 Pixel Detector

The pixel detector is a completely new sub-detector in Belle II. It consists of two layers of DEPFET [72, 73] pixel sensors. A schematic view of the geometrical sensor arrangement can be found in Figure 6.3 and a detailed description of all the PXD components can be found in [74].

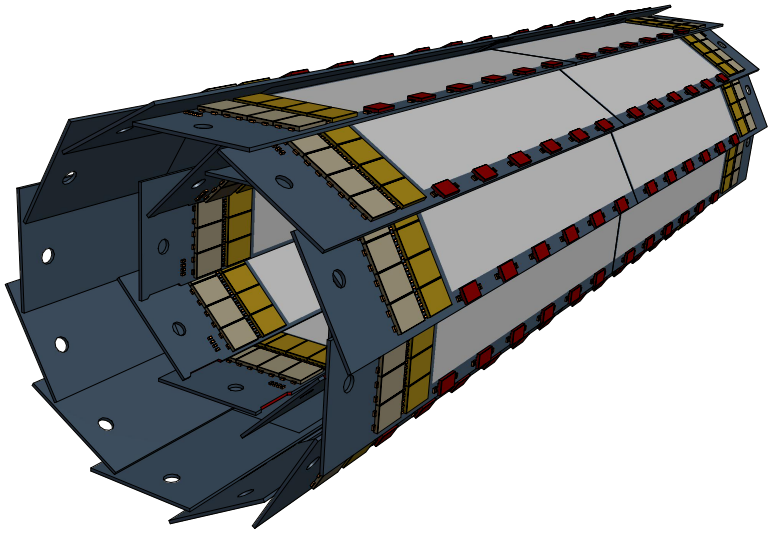

Figure 6.3: Schematic view of the geometrical arrangement of the sensors for the PXD. The light gray surfaces are the sensitive pixel area. The yellow and red structures are the readout chips placed directly on the pixel sensor.

The first layer of sensors is at a distance of 14 mm from the IP and the second layer is at 22 mm. The PXD has 40 sensors and a total of 7.68 million pixels. The pixel size is 50 µm in $r\phi$ direction for both layers. In z direction, the sensors are segmented and have two different pixel sizes, where the smaller pixels are closer to the center of the detector. The size of the pixels in z direction ranges from 55 µm to 85 µm and the actual values are summarized in Table 6.1. Each sensor is read out row by row from one side and is equipped with different kinds of readout chips: eight chips at the end for the actual readout and six along the sensor side to control the readout of different rows, so-called switchers (Figure 6.4).

To reduce the amount of material, the sensitive area of the silicon sensors, which contains the actual pixels, is thinned down to 75 µm. Around the sensitive area, the silicon retains a thickness of 525 µm to provide mechanical stability as can be seen in Figure 6.5. This figure also shows how two sensors are glued together using an adhesive joint to form one ladder. This joint is reinforced using small ceramic inserts to increase the mechanical stability. Apart from these inserts, the silicon sensors are self-supporting: no additional mechanical structure is present within the acceptance region.

Eight (twelve) of these ladders are placed radially around the z-axis to form the inner (outer) layer of the PXD. In forward and backward directions, both layers are mechanically supported by a common endflange outside of the acceptance region. This endflange also provides cooling for the readout chips using liquid CO_2 flowing through internal channels (see Figure 6.6). For cooling of the switcher chips in the acceptance region a number of small carbon tubes are running between the forward and backward endflanges and provide cold air through small holes along their sides.

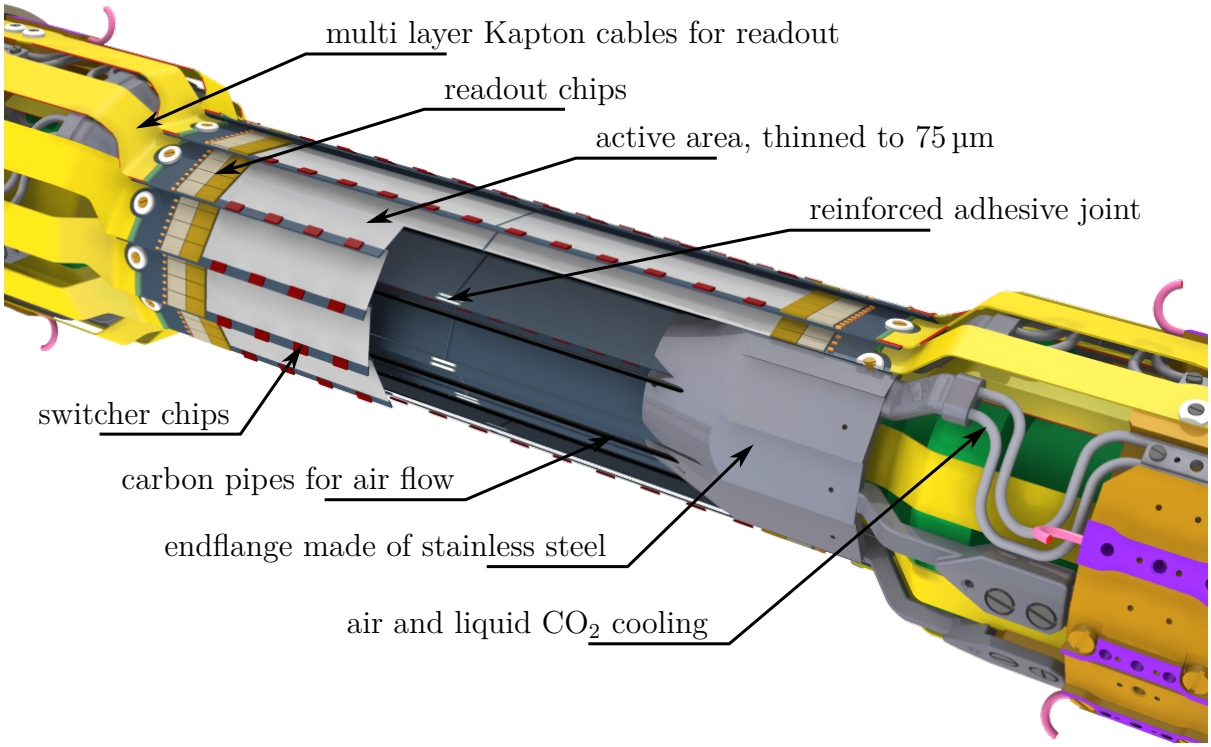

Figure 6.4: Rendering of the mechanic design of the PXD. A part of the the sensors in the outer layer has been cut away to show the endlange and the carbon tubes for air cooling.

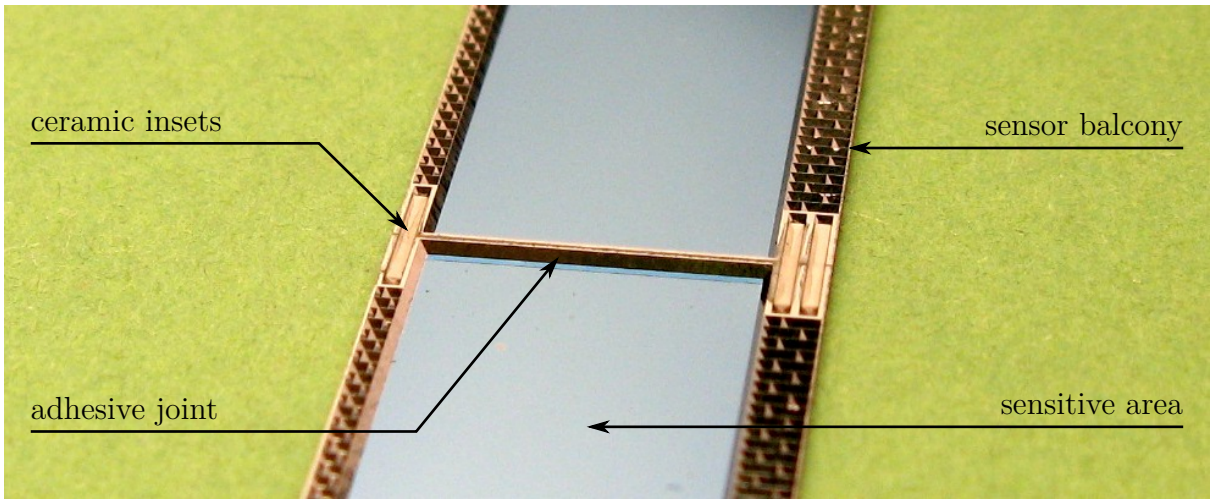

Figure 6.5: Back view of the joint between two PXD sensors. The connection is done with an adhesive joint, reinforced using three small ceramic inserts. In addition, one can see the thinning of the active area compared to the sensor border.

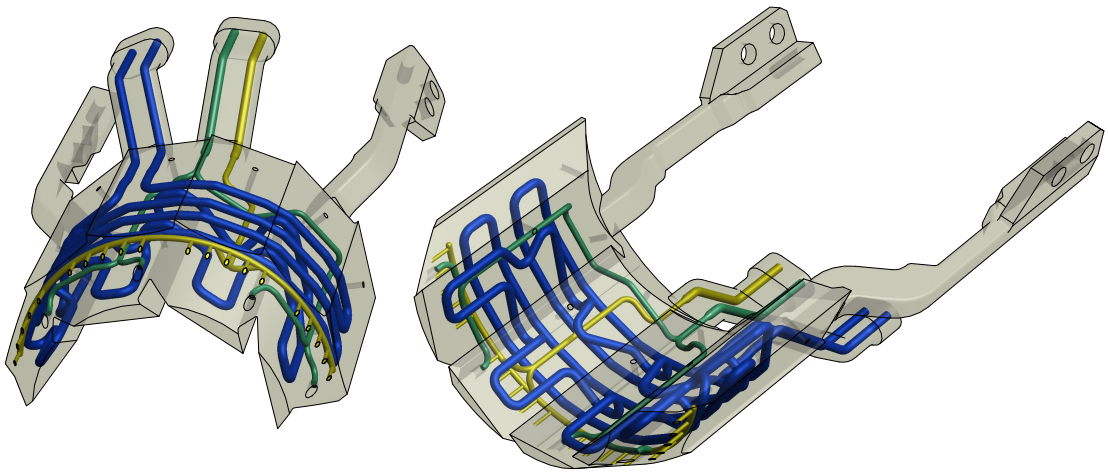

Figure 6.6: Mechanical design of the PXD endflange. The internal blue lines are the for liquid CO_2 cooling and green and yellow lines are for airflow cooling.

6.2.4 Silicon Vertex Detector

The silicon vertex detector (SVD) shares some similarities with the Belle SVD described in Section 2.2.2: It uses a double sided strip technology and has four layers of silicon sensors. However, the distance to the IP has been increased to provide sufficient space for the PXD. In all but the innermost layer, the forward region is slanted towards the z-axis, as can be seen in Figure 6.7, to reduce the number of required sensors. The parameters for the different layers is summarized in Table 6.1.

In the SVD, one ladder consists of two to five silicon sensors which are glued on two composite sandwich carbon fiber ribs. Both ribs are made of a 3 mm core of low mass, but rigid foam (Airex). A 140 µm thick layer of carbon fiber is laminated on each side.

To read out the central sensors in each ladder, the SVD employs the so-called "Origami chip-on-sensor" concept [17]: The readout chips of both sides are placed on a single flexible circuit, mounted on the top of the sensor. The strips on the top side (measuring the z coordinate) are connected by a pitch adapter and the strips on the opposite side (for $r\phi$ measurement) are attached by small flexible fanouts wrapped around the edge of the sensor. Figure 6.8 shows drawings of top and side views for an Origami chip-on-sensor module, including the mechanical support ribs. A stainless steal cooling pipe with an outer diameter of 1.5 mm and a wall thickness of 50 µm is placed on top of the readout chips to provide sufficient cooling using liquid CO_2.

The outer sensors are read out using readout boards outside of the acceptance. The complete ladders are fixed on stainless steel endrings (see Figure 6.9), which also provide cooling for the readout boards. A carbon fiber structure, which can be seen in Figure 6.10, is used to connect all the endrings and encase the SVD.

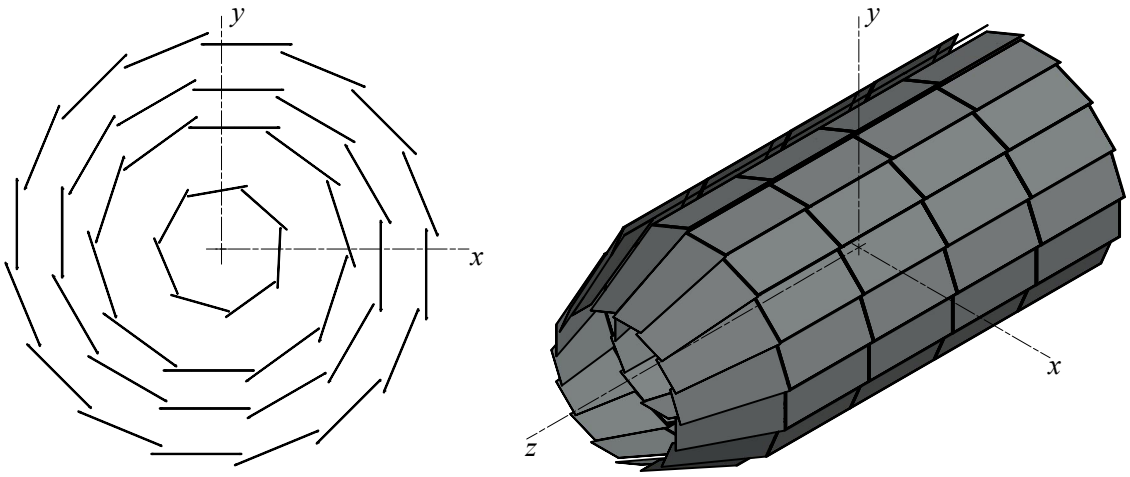

(a) front view without slanted sensors (b) isometric projection

Figure 6.7: Schematic view of the geometrical arrangement of the sensors for the SVD. Only the silicon sensors are shown, all other components have been omitted.

layer		radius (mm)	slant angle	ladders	sensors /ladder	pitch $r\phi$ (µm)	pitch z (µm)	width (mm)	length (mm)
PXD	1	14	-	8	2	50	55, 60	12.5	44.80
	2	22	-	12	2	50	70, 85	12.5	61.44
SVD	3	38	-	7	2	50	160	38.52	120.02
	4	80	11.9°	10	3	75	240	57.72	122.90
	5	105	16.0°	12	4	75	240	57.72	122.90
	6	135	21.1°	16	5	75	240	57.72	122.90

Table 6.1: Belle II vertex detector configuration. The width and length are only for the sensitive area. The slanted sensors are trapezoidal shaped and have a variable $r\phi$ pitch from 50 µm to 75 µm, a sensitive width from 38.42 mm to 57.59 mm and a sensitive length of 122.76 mm.

a) Top view:

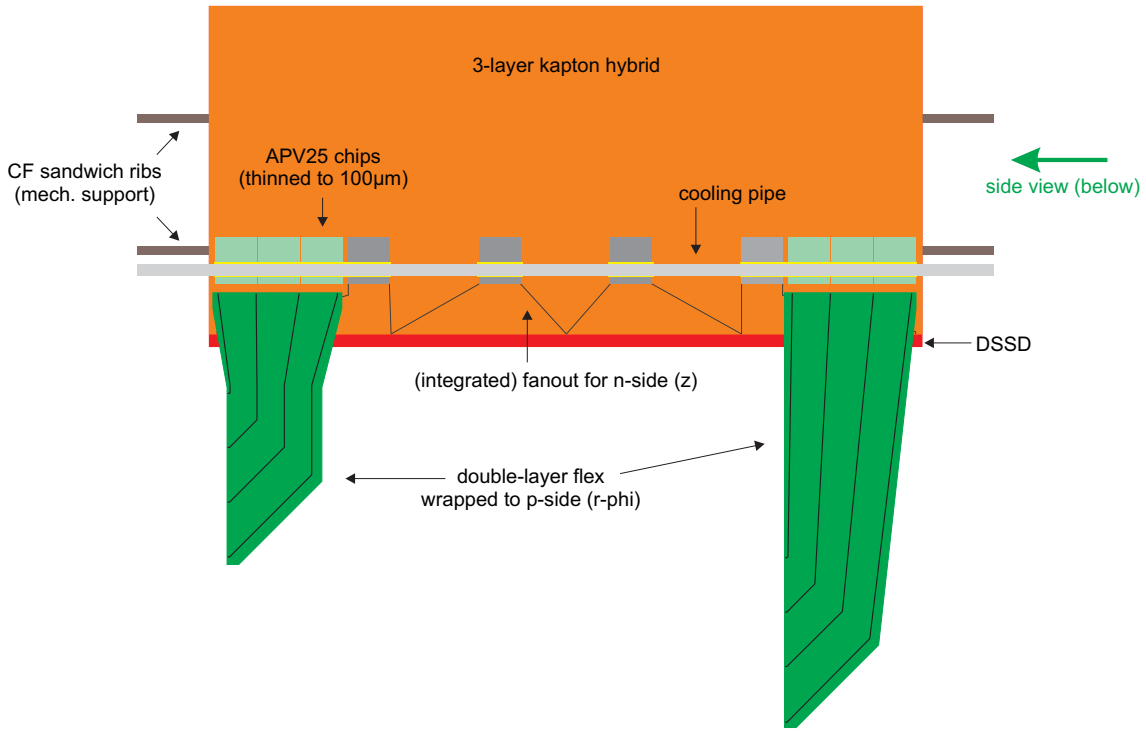

b) Side view (cross section):

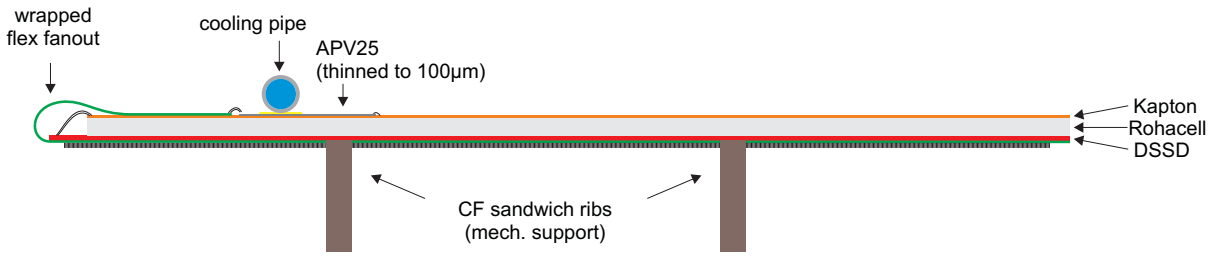

Figure 6.8: Top and side views of the Origami chip-on-sensor concept. The flex pieces to be wrapped around the sensor edge are unfolded in the top view [17].

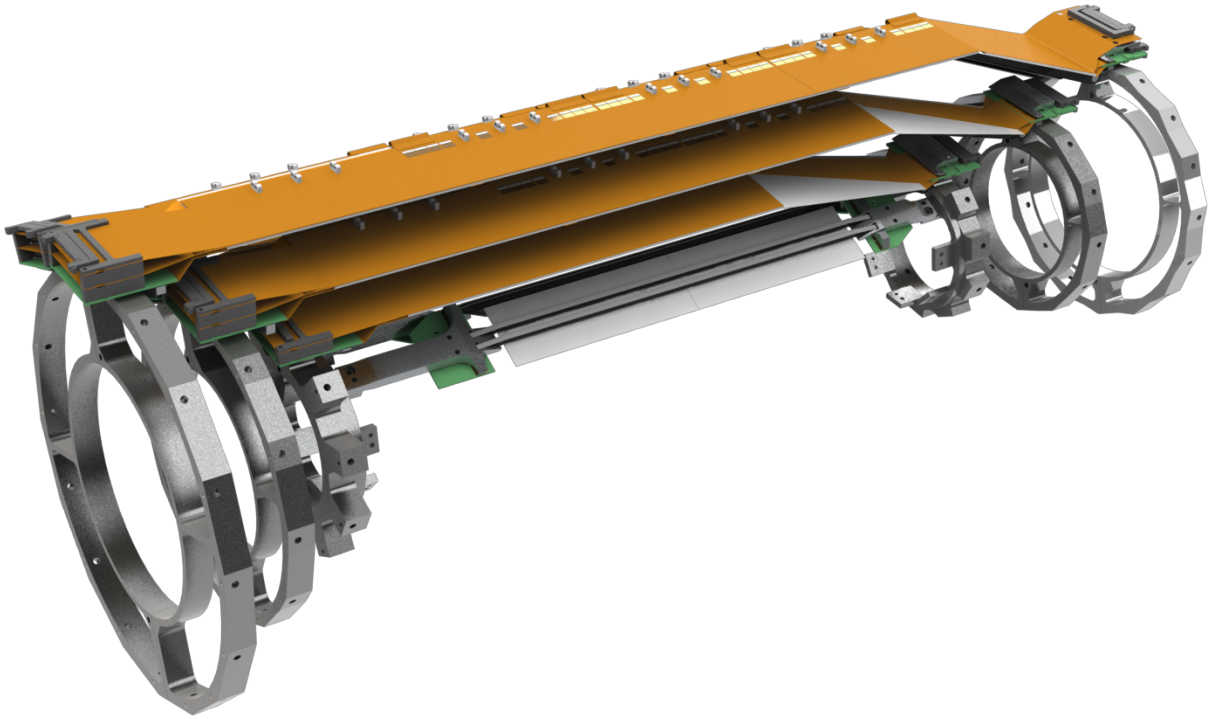

Figure 6.9: Rendering of endring stucture for the SVD. The readout boards (green) for the outer modules are places directly on these endrings.

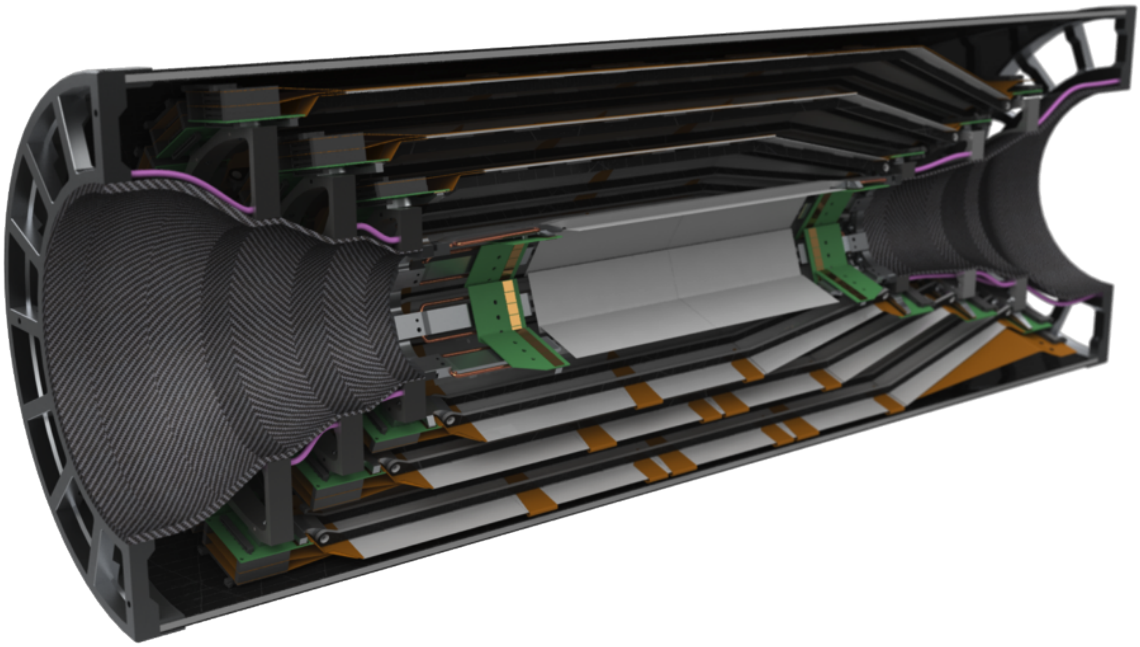

Figure 6.10: Rendering of the mechanical design of half the SVD including all components.

6.3 Belle II Software Framework

The Belle II software framework is called basf2 [75]. It is a modular C++ framework utilizing the recent C++11 standard [76]. All tasks like reading and writing data files, simulation, reconstruction or user analysis are performed by so-called "Modules". Figure 6.11 shows the basic data flow during computation. The Modules can write and read objects to and from a common data store. So-called "Paths" are used to define the execution order of different Modules and conditions can be set to switch between Paths depending on the result in each Module.

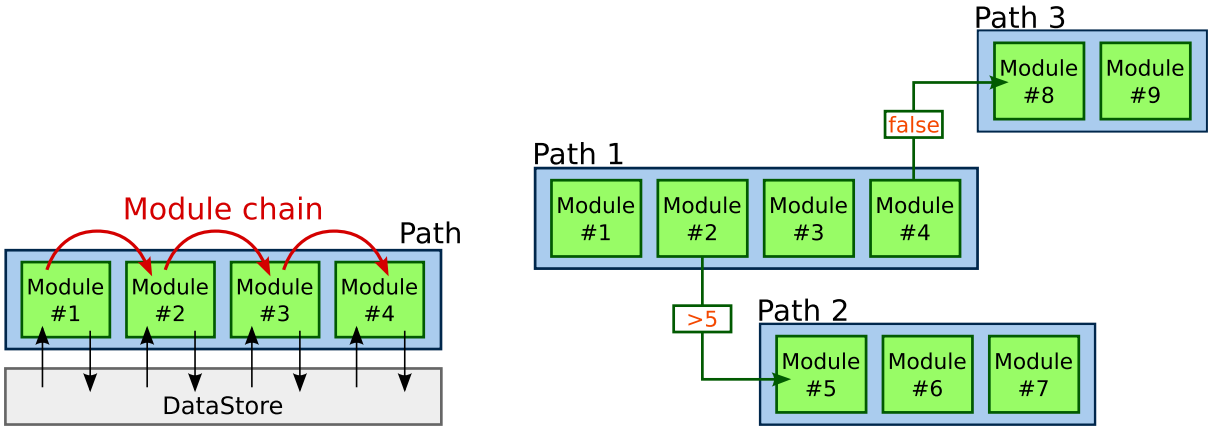

(a) Module execution (b) Path conditions

Figure 6.11: Schematic view of the execution flow in the Belle II software framework. Code is divided into modules which can be placed in Paths. Modules can (a) communicate by reading from and writing to a common DataStore and (b) return a result to change the execution flow between different paths.

6.3.1 Configuration Parameters

For unified access to configuration parameters, basf2 provides a module called "Gearbox" [75]. This module provides a simple interface to query a tree structure of parameters using a subset of the XML Path Language, XPath [77]. At the time of this writing, the configuration parameters are stored in plain human-readable XML files [78]. Configurations for different sub-detectors reside in separate files and are included into the global configuration space using the XInclude [79] mechanism to decouple the parameters for different sub-detectors.

Usage of the generic XPath language allows each each sub-detector to freely choose the configuration parameters and structure best suited for them. This allows us to parametrize the geometry of the PXD and SVD in an optimal way and independently of any other sub-detector.

6.3.2 Simulation Geometry

The overall detector geometry used in the Belle II simulation is implemented using the geometry primitives provided by Geant4 [68]. Geant4 utilises "constructive solid geometry". Basic, simple primitives like box, sphere or tube are provided and more complicated shapes can be created using the boolean operations union, intersection and difference as shown in Figure 6.12. Finally, a nested structure of volumes is created where each volume is the combination of a shape with a physical material and is placed inside a mother volume. To improve efficiency, volume hierarchies can be reused and placed multiple times.

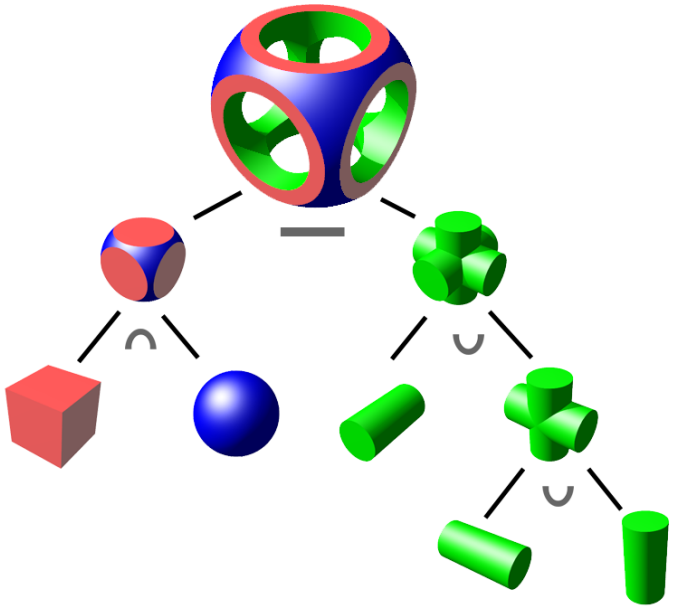

Figure 6.12: Principle of constructive solid geometry [80]. Complicated shapes are constructed using intersection ($\cap$), union ($\cup$), and difference ($-$) between different shapes.

The integration of the geometry from all sub-detectors into a common data structure is done by a common module simply called "Geometry". This module is responsible for setting up the world volume in which all other volumes will be placed. The Geometry module then reads the configuration parameters to determine what materials should be created and how to call the sub-detector specific code responsible for the creation of the respective geometry.

6.3.3 Materials

All Materials used in the simulation have to be created with the correct atomic properties. Geant4 already defines all known chemical elements using the isotopic abundances and properties derived from the NIST database on Atomic Weights and Isotopic Compositions [81]. For each element Geant4 also defines a pure material using the NIST database of

material properties. In addition, a number of frequently used materials are also predefined. This means that the definition of new materials usually just requires to specify the correct composition of the already defined materials.

We implemented a Material provider which is responsible for the creation of new materials from the configuration parameters and then providing an easy access to all defined Materials. The definition for each new material provides a name and a weighted list of chemical elements or already defined materials. Optionally, the density, temperature and pressure can be specified. An overview of all available parameters can be found in AppendixB.1

6.4 Common Vertex Detector Geometry

Very detailed, three-dimensional mechanical designs already exist for both vertex detectors, PXD and SVD. However we chose not to attempt to directly use these in the simulation for various reasons:

- Although a software exists to convert mechanical designs to Geant4 geometry [82], this approach has some drawbacks. In its current implementation all shapes would be converted to polygon meshes. This would either greatly increase the number of required primitives or result in a loss of precision.

  In addition, the current Belle II tracking software also needs a geometry description to account for material effects but uses a different representation. This representation can be automatically generated from Geant4 objects but does not support the use of polygon meshes.

- The mechanics were designed were created with a focus on the assembly and the manufacturing processes. This does not necessarily coincide with the optimal structure for a simulation geometry. For example, a certain part might be modelled in the mechanical design by removing material from a base object to mimic the actual production process. In the simulation geometry, instead, it might be much easier to just build the same part using a few simple, adjacently placed geometrical objects.

- The simulation geometry should not be to complex to not needlessly slow down the speed of simulation while the mechanical design needs to be as detailed as possible.

Nevertheless, close collaboration with the mechanical engineers is very important for the decision about how to implement the simulation geometry. For example, information about the mechanical tolerances and degrees of freedom for different parts can help to optimize the geometry implementation for alignment purposes. Moreover familiarity with the details of the mechanical design helps to avoid errors and easily identify the common structures in both sub-detectors:

- Both have a number of layers.

- Each layer consists of identical structures called ladders placed around the IP in a so-called "windmill" structure in $r\phi$ direction.
- The ladders of each layer consist of two to four separate silicon sensors and there is only a small number of different sensor layouts for PXD and SVD.
- Additional structures like readout cables or chips might be placed on top or bottom of the sensor.
- For mechanical and assembly reasons, both detectors are divided into two halves. The PXD is split horizontally while the SVD is divided vertically.
- Each detector half has an independent structure to mechanically support all layers and ladders.

Of course, there are also differences or unique features in the design of both sub-detectors:

- The PXD has a common mechanical support for all layers in each half while the SVD separately supports each layer on separate endrings.
- The ladders of the PXD are self supporting while the SVD ladders need an additional mechanical support structure.
- Controlled air cooling is provided only for the PXD using small carbon tubes between both layers.
- The SVD employs liquid CO_2 cooling for the readout chips using stainless steel pipes along the ladders of the outer three layers.
- The PXD sensors are thinned down to 75 µm in the sensitive area.

Since none of the differences are strongly conflicting we decided to develop a common code which is able to create both geometries. This slightly increases the complexity of the code but simplifies the validation and greatly increases the maintainability as code duplication between the two sub-detectors can be avoided.

6.4.1 Preparation for Alignment Studies

The final detector assembly can only be performed with finite precision, leading to deviations from the nominal positions for all sensors. To achieve an optimal vertex performance this effect has to be taken into account. This is usually done using track based alignment procedures [83–88].

These procedures can benefit from additional knowledge about the expected mechanical tolerances. For example, the internal structure of one ladder is very rigid so it is unlikely that large displacements will occur between the sensors in one ladder but it is very plausible that the whole ladder might be displaced relative to the other ladders in the layer.

To allow for studies of the alignment procedure we prepared the simulation geometry for misplacement with respect to the nominal position. We defined a hierarchy of position corrections for all geometrical components: sensors, ladders, half-layers and the whole sub-detector. Each of these components has six degrees of freedom: three displacements from the nominal position and three rotations around the local coordinate axes. All of these position corrections are applied relative to the nominal position of the containing structure. A misplacement of a ladder will also shift all sensors in that ladder and a misplacement of the whole detector will affect all structures simultaneously.

Care has to be taken to make sure that these position corrections do not cause an overlap between different volumes as this leads to undefined behaviour of Geant4. To avoid that we made sure that there is always sufficient distance between different components. This should guarantee an overlap free geometry for small displacements as expected from alignment. For larger displacements, the volumes of the PXD and SVD need to be checked for overlaps prior to simulation.

6.4.2 Structure of Geometrical Components

The geometry of both detectors can be described using a common hierarchy: We have to distinguish between components placed on sensors, single sensors, ladders, half layers and half detectors. For all of these we define a common set of parameters for PXD and SVD.

Component

A number of additional components like readout cables and chips might be placed directly on the sensors, either on top or below. In addition, the thinning of the PXD Sensors and the ceramic inserts have to be taken into account.

All components used in the current design can be approximated by rectangular or trapezoidal outline with a certain thickness and a given material. For the thinning of the sensitive area of the PXD sensors we also need to allow for tapering of the component along w.

We define a set of parameters to describe all components placed on or in the sensor, summarized in Table 6.2. Each component definition can contain zero or more sub-components. These sub-components are placed relative to the center of their parent component using the parameters shown in Table 6.3. Figure 6.13 illustrates the parameters for component definition and placement. An example an be found in Appendix B.2.

Sensor Definition

For both sub-detectors we need to define all existing sensors. A sensor is one piece of silicon which has an active area where the detector is sensitive to traversing particles. In addition, a number of components like readout cables and chips might be placed directly on the sensor, either on top or below. To implement and the thinning of the PXD Sensors and the ceramic inserts we also may need to place components inside the sensor volume.

Parameter	Description
name	Unique name to identify the component
Material	Name of the material to be used
width	Size of the component in u direction at the backward side
width2	Width at the forward side. If not present, the value of *width* is taken to create a rectangular outline
length	Size of the component in z direction
height	Thickness of the component
angle	Angle for tapering. If not specified, no taper is assumed

Table 6.2: Parameters defined for the creation of components.

Parameter	Description
type	Name of the component to be placed
u	Local u coordinate where the component should be placed with respect to the center of the parent component
v	Local v coordinate where the component should be placed with respect to the center of the parent component
w	Vertical placement, can have one of the values “above”, “top”, “center”, “bottom” and “below” to place the component either above the parent component, inside the parent component and aligned to the top, center or bottom or below the parent component respectively

Table 6.3: Parameters defined for the placement of components.

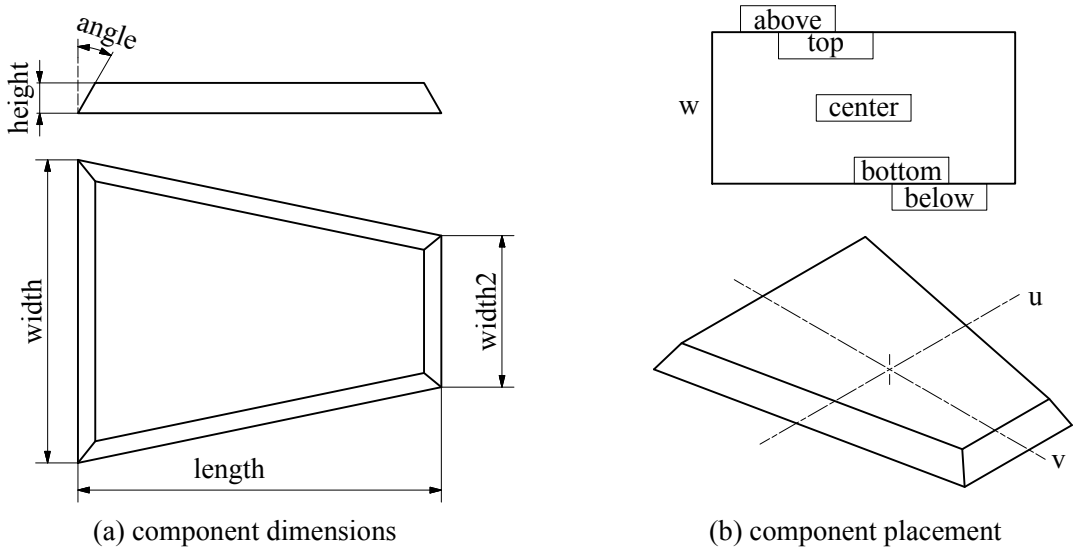

Figure 6.13: Illustration of the parameters for (a) component definition and (b) component placement.

Exploiting the definition of components above, we can define a sensor using the same parameters shown in Table 6.2. In addition, we require exactly one additional component, the active area, and allow for zero or more components placed on or in the sensor. Each sensor definition has a unique name which allows easy placement on the ladders.

Ladder Definition

One ladder configuration is needed for each layer to specify where to place the sensors of each ladder, summarized in Table 6.4. For each ladder we need to know the shift in $r\phi$ direction to create the windmill structure and the radial distance from the IP. Furthermore we need to know the sensor types and their z position in each ladder. For the slanted sensors, we additionally need to declare its inclination angle and the radial distance of the sensor center to the z-axis. Finally, each sensor in a ladder is given a numerical id, starting at one for the forward sensor and increasing along opposite z direction. Figure 6.14 illustrates all these parameters.

Additionally, the PXD sensors of each ladder are mirror-symmetric and the inner layer is facing towards the IP. To facilitate this, we also define three parameters to allow reflection of the sensors when placing them in the ladder. To make sure that the active area conforms to the local coordinate definition in Section 6.2, the reverse transformation is applied to the active area when it is placed in the sensor volume.

Parameter	Description
shift	Offset of the ladder center when placing
radius	Distance of the sensor to the IP
slanted.angle	Inclination angle for the slanted sensor
slanted.radius	Distance of the slanted sensor center to the IP
sensor.type	Name of the sensor type
sensor.id	numerical ID if the sensor within the ladder
sensor.z	global z position of the sensor center with respect to the IP
sensor.flipU	if present, mirror the sensor at the vw plane
sensor.flipV	if present, mirror the sensor at the uw plane
sensor.flipW	if present, mirror the sensor at the local uv plane

Table 6.4: Parameters for the definition of ladders. The parameters prefixed with "sensor." need to be specified for each sensor in the ladder. If slanted.angle and slanted.radius are given, the first sensor in the ladder will be slanted. Otherwise all sensors will be placed along z

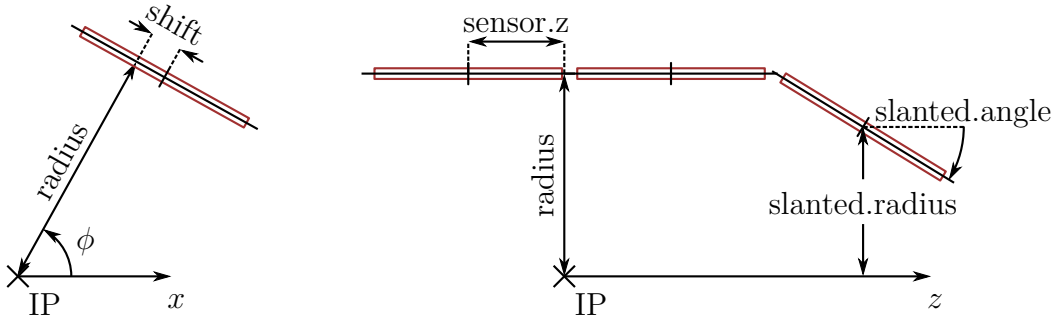

(a) xy view (b) rz view

Figure 6.14: Illustration of the parameters used to define the ladders for each layer.

Layer definition

As both detectors are divided into two halves we also define the ladder position per half layer as a list of the polar angle, ϕ, and the numerical id of each ladder. Ladders are numbered per full layer, starting at one for the sensor with the smallest positive polar angle and increasing along $r\phi$ direction.

The layers for each detector half share a common numbering for PXD and SVD. With increasing distance from the IP, the PXD layers are defined as one and two and the SVD layers start at three and go up to the outer most layer with number six.

6.5 PXD Geometry

Using the scheme described above we implemented the full PXD geometry, including the complete mechanical support close to the acceptance. Readout cables and support structures further away from the IP than the ladder endflange are not implemented at this stage.

6.5.1 Sensor Design

We only have two different sensor types for the PXD, one for the inner and one for the outer layer. However, each ladder consists out of two sensors, one mirrored at the uw-plane. In addition, the inner layer faces inward (readout chips point towards the IP) while layer 2 points outward. For both layers we implemented only one sensor facing outward and apply the appropriate reflection along the uw and or vw plane when placing them in the ladder.

Each sensor is equipped with different of readout chips, eight at the end to do the actual readout and six along the side to switch the readout between different rows. Figure 6.15 shows the resulting simulation geometry for one ladder from layers 1 and two where the inner ladder has been rotated by $\phi = 180°$ to show the top side.

The thinning of the PXD sensitive area to a thickness of 75 µm has been implemented by placing an appropriately sized component containing air inside the sensor volume and the ceramic inserts are separated for each sensor. The ceramic inserts, which span across two sensors in the mechanical design, have been split into independent parts for each sensor.

6.5.2 Mechanical Support

The PXD ladders are self-supporting, so no additional structures apart from the small inserts are needed for mechanical stability. Only the forward and backward endflange shown in Section 6.2.3 has to be provided.

To implement the shape in the simulation we produced a simplified version using the CAD system used for the mechanical design of the PXD. This allowed us to derive the dimensions directly from the original design. We omitted the holding arms and the cooling inlets and smoothed the contact surface for the outer layer. The contact surfaces for

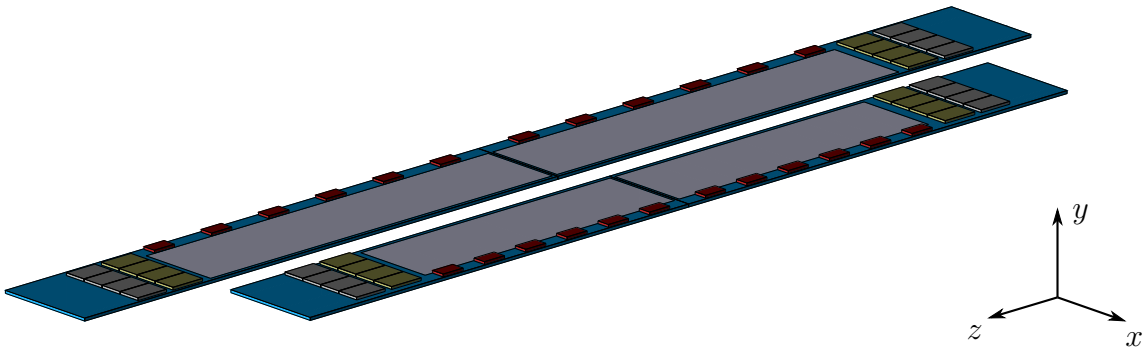

Figure 6.15: Ladder geometry for both PXD ladders. The smaller ladder represents layer 1 and has been rotated by $\phi = 180°$. Each ladder consists of two sensors joined at the middle. The sensitive area is shown in light gray and the different readout chips are in dark gray, yellow and red.

the inner layer were implemented by intersecting box shaped volumes with a rotational symmetric shape. Figure 6.16 shows a comparison between the original endflange and the simplified version used for the simulation geometry. Appendix B.3 lists the parameters for this simplified version.

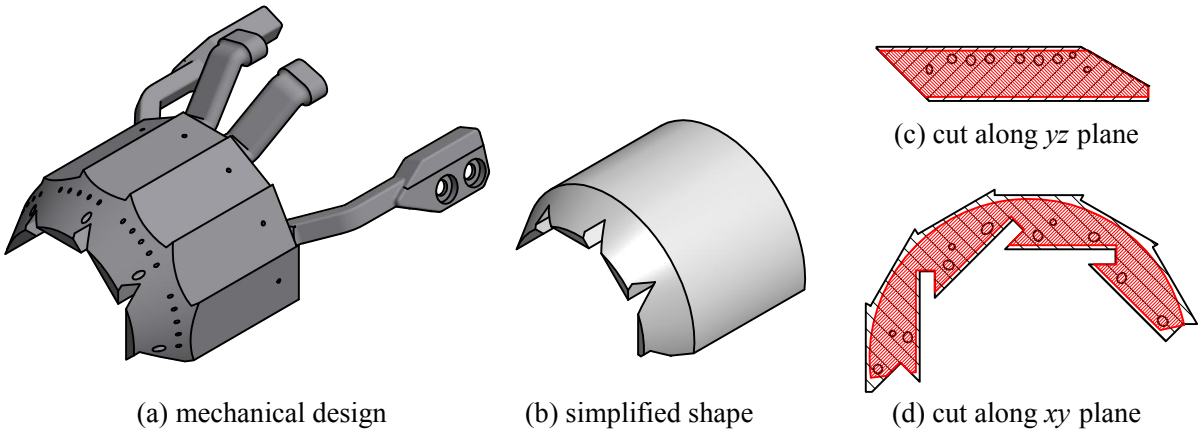

Figure 6.16: Comparison between the original mechanical endflange design and our simplified geometry. In (c) and (d) the mechanical design is shown in black while the simplified geometry is overlaid in red.

As the simplified geometry is smaller than the original design we used the CAD system to calculate the volume of the original endflange, V_{CAD}, and our simplified geometry, V_{sim}. We then scaled the density of the material in the simulation by the ratio between these volumes,

$$\rho_{\mathrm{sim}} = \rho_{\mathrm{steel}} \cdot \frac{V_{\mathrm{CAD}}}{V_{\mathrm{sim}}}, \tag{6.2}$$

to obtain the correct mass in the simulation.

We also added the air cooling tubes running between the forward and backward endflange to the simulation. The full mechanical support and cooling implemented for both halves can be seen in Figure 6.17. This figure also shows all ladders for the lower half of the PXD.

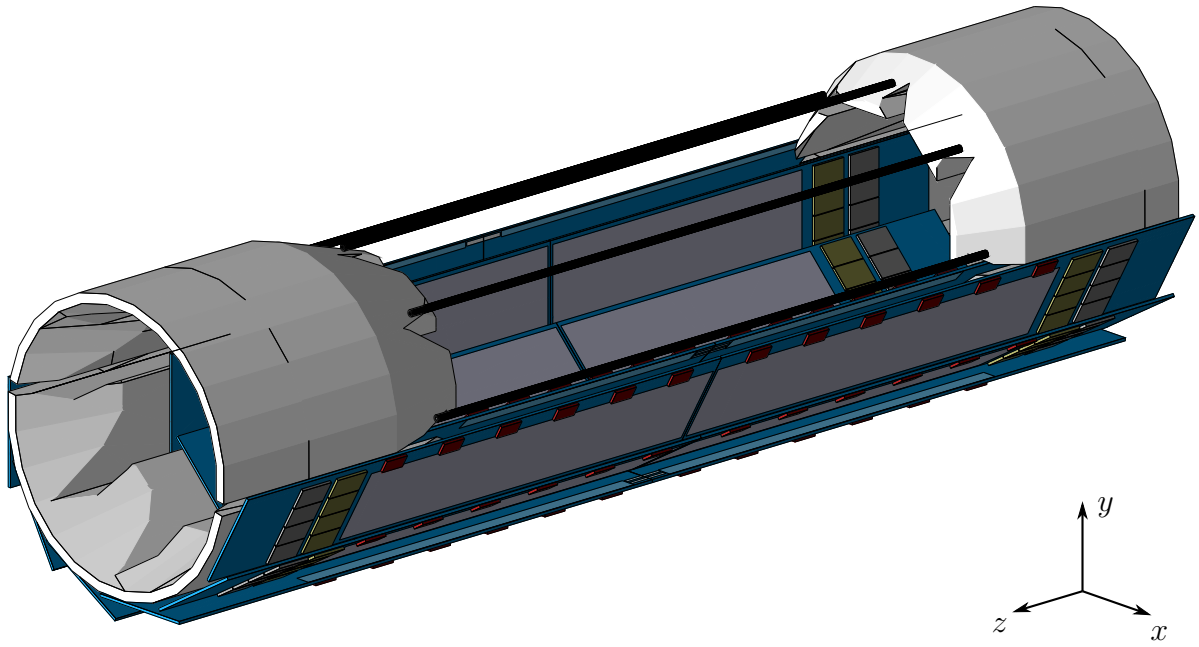

Figure 6.17: Simulation geometry of the PXD mechanical support, together with all ladders in the lower half. The large, light gray structures are the stainless steel endflanges and the black lines between them are carbon tubes for air cooling.

6.6 SVD Geometry

The geometry of the SVD is much more complex as the SVD has four layers with up to five sensors per ladder. Instead of two distinct sensors and combined support for both layers, as for the PXD, we have seven different sensors, separate support structures for each layer and additional mechanical support for each layer.

6.6.1 Sensor Design

The design of the sensors for layer 3 is straightforward. We have two identical sensors per ladder and the readout is done to the side, outside of the acceptance. For layers four to six we have a trapezoidal shaped sensor in the forward direction and two to four identical, rectangular sensors along the ladder. But we also have to distinguish between the edge sensors, which are read out to the side, and the central sensors using the Origami

chip-on-sensor concept. In addition, there is a different number of readout cables on top of each sensor depending on its position inside the ladder since the data of the central sensors has to pass along the outer sensors. This results in a total of seven different sensor types.

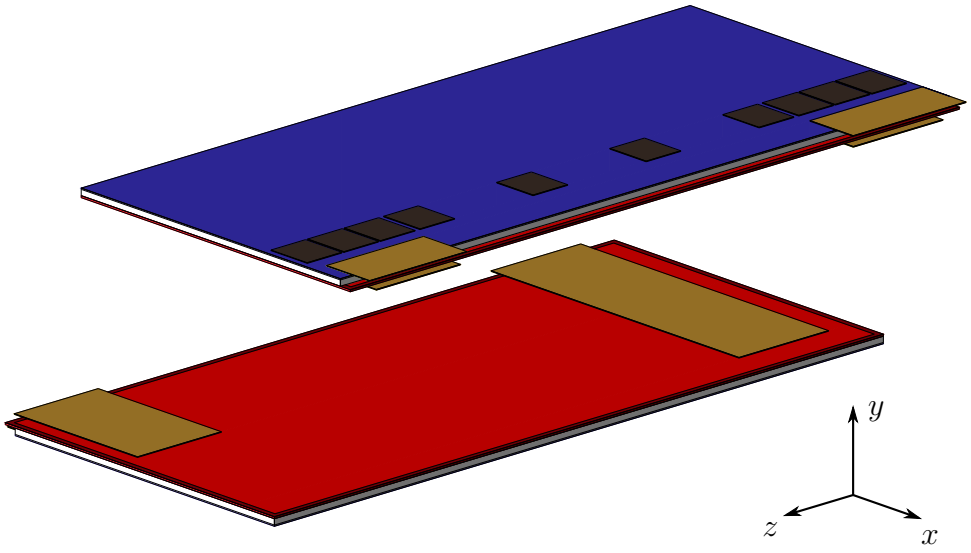

Figure 6.18: Simulation geometry showing top and bottom for an Origami sensor. Silicon is shown in red, Origami hybrid in blue, readout chips in gray and the flex cables connecting the bottom strips in orange. One can see that the flex cables slightly extend over the sensor edge to emulate the bending around the sensor.

For Origami readout, we have two additional Kapton flex cables to connect the strips on the bottom side to the readout chips. We implemented these cables using two pieces of Kapton, one on top and one on bottom, which are extended slightly over the sensor edge. We simplified the form of these cables to be rectangular instead of the more complicated shape in the drawings (Figure 6.8) but kept the surface area identical. Figure 6.18 shows one of these Origami sensors as implemented in the simulation geometry.

6.6.2 Mechanical Support

All ladders in the SVD have additional mechanical support but at the time of this implementation there was no design for the support of layer 3. For all other layers, we implemented the support rib structure described in Section 6.2.4 as a union of simple box shapes for the straight and the slanted part.

The readout boards for the readout on of the edge sensors is not implemented in the current geometry. As these boards are outside of the acceptance region we deem this acceptable for now.

Figure 6.19 shows layer 6 ladders with silicon sensors shown in red. The readout cables for the Origami sensors are colored blue while the flex cables for the Origami readout are

colored orange. One can also see the readout chips on the three center modules and the Airex/carbon fiber ribs for mechanical support.

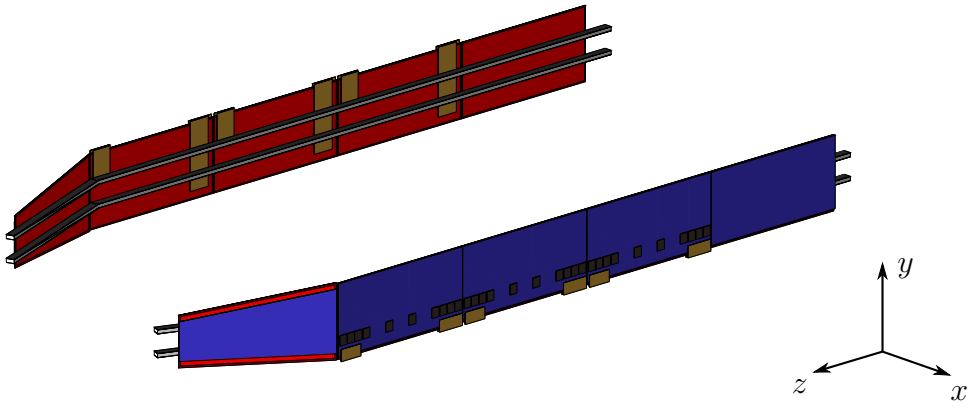

Figure 6.19: Simulation geometry for two ladders from layer 6 including the mechanical support ribs. The inner sensors use the Origami concept while the edge sensors are read out to the forward and backward side.

All ladders are mounted on stainless steel endrings at both sides which are glued on a carbon fiber structure as shown in Figure 6.20 together with the first ladder in each layer. Notice that the endrings and support structure are divided vertically to allow displacement between the two detector halves. We also added a small gap between the base of the endrings and the carbon fiber support structures to allow for misalignment of the complete half layers.

The SVD also has an outer cover made out of an Airex cylinder with carbon fiber laminated on both sides. This outer cover connected to the lower support structure using an endflange outside of the acceptance region in forward and backward direction (see Figure 6.10). We included the outer cover in the simulation geometry but no design was available for the forward and backward endflange so they were omitted from the current implementation.

6.6.3 Cooling

The SVD uses liquid CO_2 to cool the readout chips. The cooling for the edge modules provided by the endrings so no additional geometry components were necessary. For the Origami modules the CO_2 flows through a stainless steel pipe with an outer diameter of 1.5 mm and a wall thickness of 50 µm, placed directly on the chips. One meandering pipe is used per half layer to cool all ladders. Both ends of this pipe are connected at the backward side. The simulation geometry for the two cooling pipes of layer 6 together with one ladder are show in Figure 6.21. There is ongoing discussion about the thickness and material of these cooling pipes and a switch to titanium pipes with 100 µm wall thickness seems likely. As the thickness and materials are defined in the parameter files the change in the simulation geometry would be trivial (see Appendix B.4).

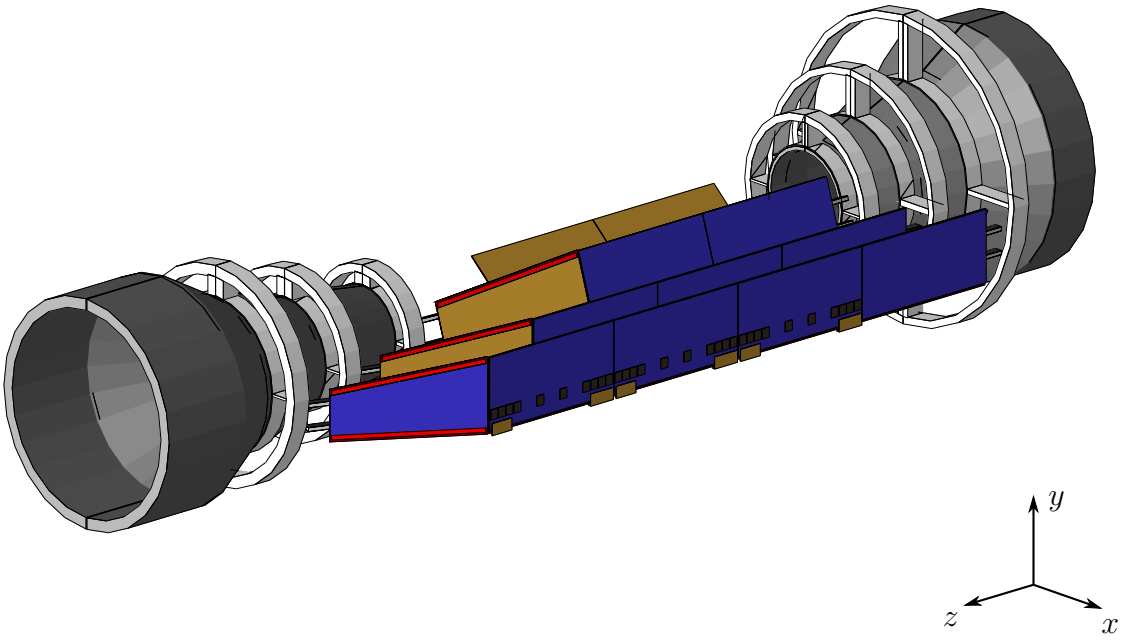

Figure 6.20: Simulation geometry of the SVD carbon support structure including endrings. In addition we show the first ladder of each layer.

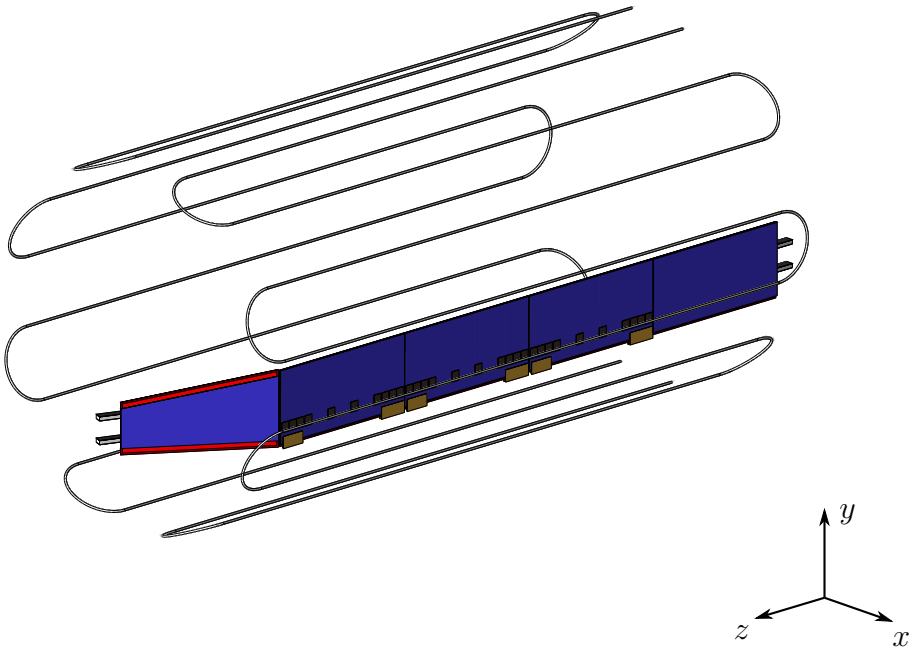

Figure 6.21: Simulation geometry of the two CO_2 cooling pipes for layer 6 together with one layer 6 ladder.

Finally, Figure 6.22 shows one half of the complete simulation geometry for PXD and SVD including the SVD outer cover.

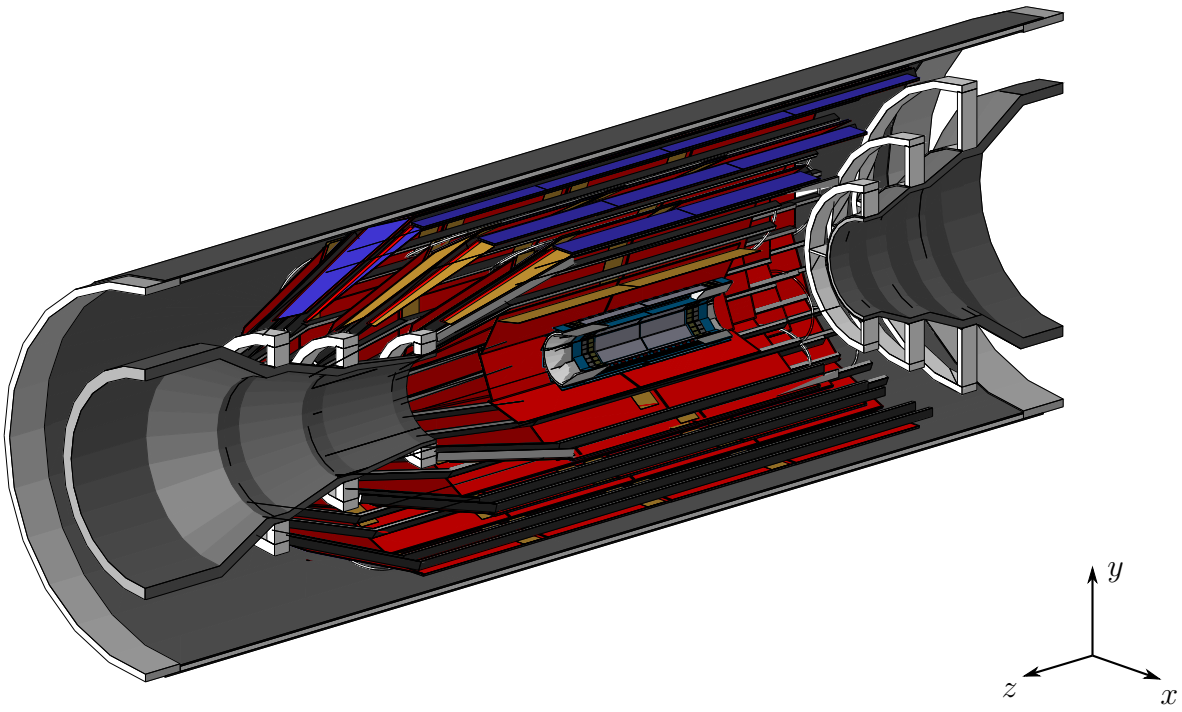

Figure 6.22: Cut view of the final vertex detector simulation geometry, including the SVD outer cover.

6.7 Material Budget

The simulation geometry for PXD and SVD shown in Figure 6.22 can be used to study the amount of material that a particle has to pass when traversing the detector, the so-called "material budget". In order to achieve this, we simulate virtual particles called "Geantino". These particles do not interact with any matter or field but can be used to record the amount of material they encounter.

To determine the material budget we generate a large number of these virtual particles at the IP and shoot them uniformly in θ and ϕ, covering the full acceptance. For each particle, we collect the amount of material it passed when traversing the detector.

Figure 6.23 shows the material budget over the full acceptance in units of radiation length, X_0, versus the polar angle, θ, and averaged over the polar angle, ϕ. For PXD and SVD the material budget is divided into different categories: silicon sensors, readout cables, readout chips, mechanical support and cooling structures. Table 6.5 summarizes the respective contributions in percent of one radiation length for perpendicular incident and averaged over the whole acceptance. For both detectors, the silicon itself (blue) is the biggest contribution to the overall material budget.

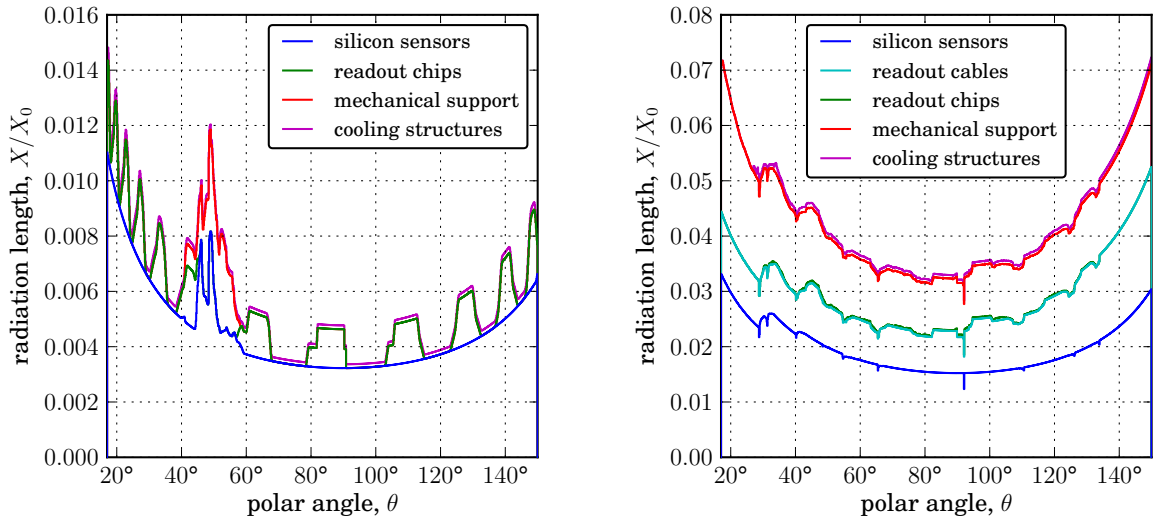

(a) PXD

(b) SVD

Figure 6.23: Cumulative material budget in units of radiation length, X_0 versus the polar angle, θ, for PXD and SVD.

In the PXD, we can see the ceramic inserts around the joint region (40° to 60°) in red. The silicon material is also enhanced in this region as the thinning of the active area does not extend directly to the sensor edge (see Figure 6.5). The contributions from the switcher chips (green) are clearly visible while the carbon fibers for air cooling (purple) are not significant.

In the SVD, the material budget is much more homogeneous. The dip at around 30° is due to the transition from slanted to straight sensors. On top of the silicon, we have a relative large contribution from the readout cables (cyan) which increases in backward direction (large θ values). This is due to the fact that most Origami sensors are read out on the backward side and so the number of cables on top of the sensors in backward direction is higher. The SVD readout chips (green) are thinned down to 100 µm so they are barely visible. The CO_2 cooling pipes (purple) do not extend below 30° due to the meandering structure which is only connected at the backward side.

The Belle II technical design report [17] quotes a value of 0.55 % X_0 for one Origami sensor at perpendicular incident. This would naively result in a total Material budget of 2.2 % X_0 for the four layers of the SVD. However, this calculation assumes perpendicular incident on ϕ and θ and does not take into account any overlaps. Furthermore, the outer cover is missing from the calculation and some of the design parameters seem to have changed in the mechanical design so that the overall budget of 3.2 % X_0 seems reasonable.

This is similar for the PXD where a number of 0.19 % X_0 is given per sensor. In the calculation, the switchers are averaged over the full sensor and the cooling pipes are not included so that we can reproduce the quoted value to a good precision.

	$\theta = 90°$		full acceptance	
Category	PXD	SVD	PXD	SVD
silicon sensors	0.32	1.52	0.46	1.97
readout cables	-	0.65	-	1.00
readout chips	0.14	0.05	0.08	0.02
mechanical support	0.00	0.93	0.03	1.27
cooling structures	0.01	0.06	0.02	0.07
total	0.48	3.21	0.59	4.33

Table 6.5: Material budget in percent of one radiation length for PXD and SVD at perpendicular incident, $\theta = 90°$, and averaged over the full acceptance.

Finally, Figure 6.24 shows the overall material budget for both vertex detectors and the beam pipe. We estimate the total material budget for perpendicular incident to 4.5 % X_0, which contains the beam pipe contribution of 0.8 % X_0. Averaged over the whole acceptance we obtain 6.0 % X_0 (beam pipe: 1.1 % X_0). Since the mechanical support for layer 3 is still missing these numbers will increase slightly for the final detector design.

This simulation geometry also provides the basis for the estimation of the PXD occupancy: the fraction of fired pixels per readout cycle. This occupancy is dominated by background, most prominently QED processes. The PXD readout system cannot sustain more than 3 % of occupancy, so detailed studies are necessary to guarantee a save operation of the device. The current estimation of the occupancy is around 1 % (0.5 %) for layer 1 (layer 2) [74] and thus well in the limits for safe operation.

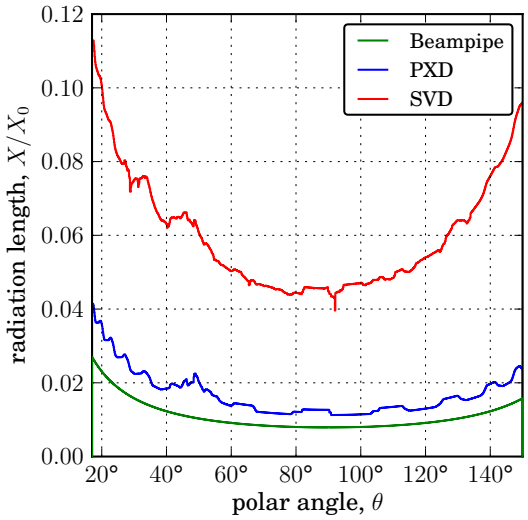

Figure 6.24: Cumulative material budget for the beam pipe, the PXD and the SVD in units of radiation length, X_0 versus the polar angle, θ.

Conclusion and Outlook

Two different subjects have been presented in this thesis: the measurement of the branching ratio and of the time dependent CP violation parameters for the decay $B^0 \to D^{*-}D^{*+}K^0_S$ and the implementation of the vertex detector geometry for Belle II experiment.

For the study of the $B^0 \to D^{*-}D^{*+}K^0_S$ decay mode we measured the branching fraction

$$\mathcal{B}\Big(B^0 \to D^{*-}D^{*+}K^0_S\Big) = \Big(5.35^{+0.35}_{-0.34}(\text{stat}) \pm 0.57(\text{syst})\Big) \times 10^{-3}.$$

Although still compatible with the previous measurements at 2.9σ, this measurement is larger than previously measured. Compared to the previous Belle analysis, the relative statistical and systematic uncertainties could be improved by almost a factor of 2.

Performing a three parameter time dependent analysis fit sensitive to $\cos(2\phi_1)$, we extract the CP asymmetry parameters:

$$\begin{aligned} J_c/J_0 &= 0.37 \pm 0.10(\text{stat}) \pm 0.02(\text{syst}), \\ (2J_{s1}/J_0)\sin(2\phi_1) &= 0.30 \pm 0.16(\text{stat}) \pm 0.03(\text{syst}), \\ (2J_{s2}/J_0)\cos(2\phi_1) &= 0.16 \pm 0.16(\text{stat}) \pm 0.03(\text{syst}), \end{aligned}$$

which are in agreement with the previous results from BABAR and the previous Belle measurement within two standard deviations. Since $(2J_{s2}/J_0)$ is predicted to be positive, we can exclude a negative sign of $\cos(2\phi_1)$ at a 85 % confidence level. Although we can significantly improve the statistical and systematical error compared to both previous analyses, our exclusion limit is weaker than the 94 % quoted by BABAR: the reason is the smaller significance of $(2J_{s2}/J_0)\cos(2\phi_1)$ as positive value (BABAR measured a much larger value of $0.38 \pm 0.24 \pm 0.05$).

Concerning the branching ratio measurement: this result is limited by the systematic uncertainties. We plan to investigate strategies to further reduce them. For example, the systematic error coming from the π^0-reconstruction in the D decay is one of the dominant contributions. It might be beneficial then to exclude the decay modes with more than one π^0 from the event selection. As this would affect the reconstruction efficiency, thus increasing the statistical error, we need to perform a detailed study to determine if the overall significance would be improved.

As for the CP violation parameters, we also performed the time dependent CP analysis on the same data used in the previous Belle analysis. These results are compatible within two standard deviations with those from full data. The results need then to be examined carefully in order to be sure that they are statistically acceptable. In the future, we

plan to perform additional checks: one possibility might be to generate MC data with significant CP violation to verify the procedure.

In the last part of the thesis, the implementation of the full vertex detector geometry in the Belle II software is presented. We developed a parameter-driven description of the vertex detector geometry which makes it possible to change most aspects of the simulation geometry with minimal modifications of the code.

All the material inside the acceptance region has been implemented except for the mechanical support of layer three as no design was present at the time of this study, but has been made available in the meantime. Moreover some detector components outside the acceptance region have been omitted in the implementation presented here. In the future, we plan to update the geometry description for both detectors using the latest design iterations and complete the remaining components, most prominently the support for layer three.

Finally, studies of the material budget for the new geometry are presented. We obtained 0.6 % of a radiation length, X_0, for the pixel detector and 4.3 % X_0 for the silicon strip detector. These values are determined using rays originating at the interaction point and are averaged over the full acceptance region. These results are consistent with the analytical calculated values for one sensor under perpendicular incident of 0.19 % X_0 for the pixel detector and 0.55 % X_0 for the silicon strip detector.

Precise knowledge of the material budget is essential for optimizing the tack impact parameters and vertex resolution, which could be shown to improve a factor of 2 with respect to the Belle experiment.

Appendix A

Branching Fraction Measurement

A.1 Data Model

In Section 4.2 we showed the combined results of the fits for all model components to MC. In addition, separate results for SVD1 and SVD2 are provided for the components Signal (Figures A.1 and A.2), Misreconstructed, (Figures A.3 and A.4) and BBar (Figures A.5 and A.6). Due to the low statistics from off-resonance data for SVD1 we omit the separate results for the Continuum component.

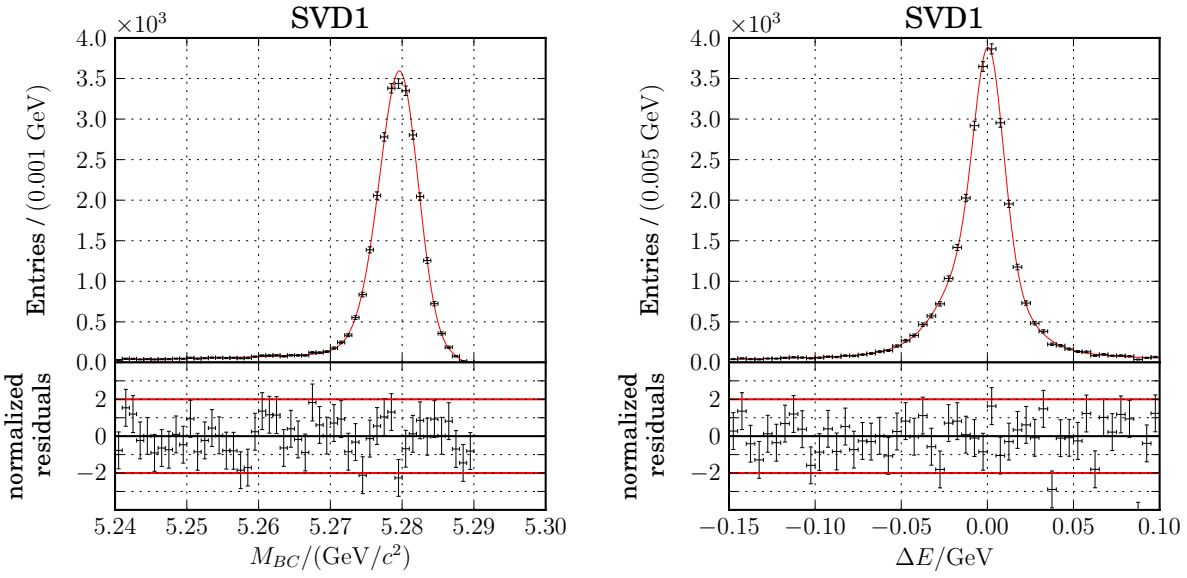

Figure A.1: Projections to M_{bc} and ΔE after fitting the Signal component to MC. Only SVD1.

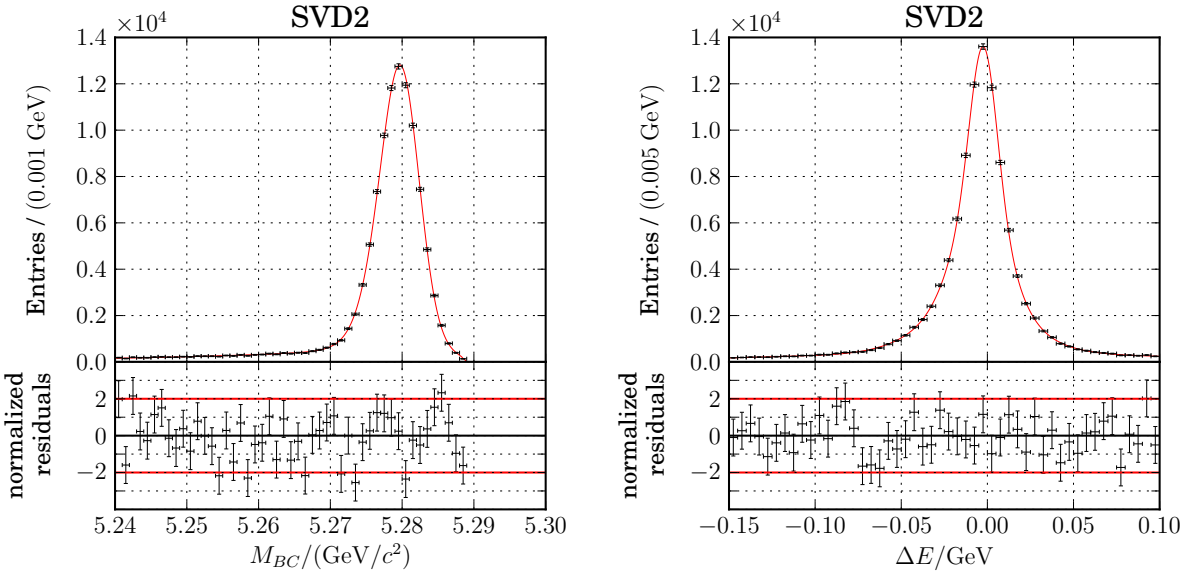

Figure A.2: Projections to M_{bc} and ΔE after fitting the Signal component to MC. Only SVD2.

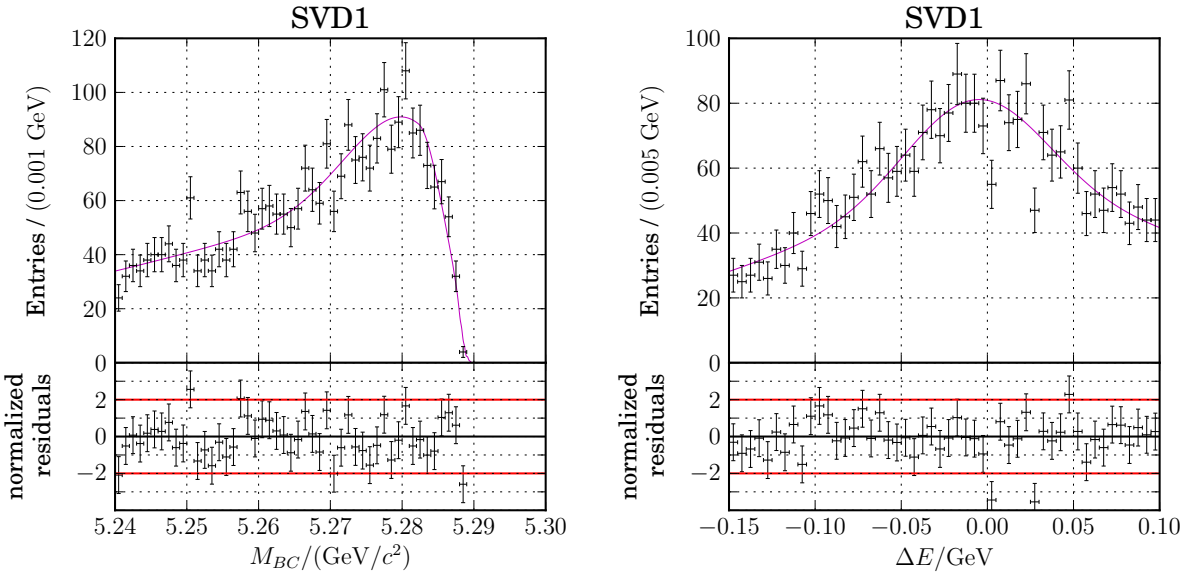

Figure A.3: Projections to M_{bc} and ΔE after fitting the Misreconstructed component to MC. Only SVD1.

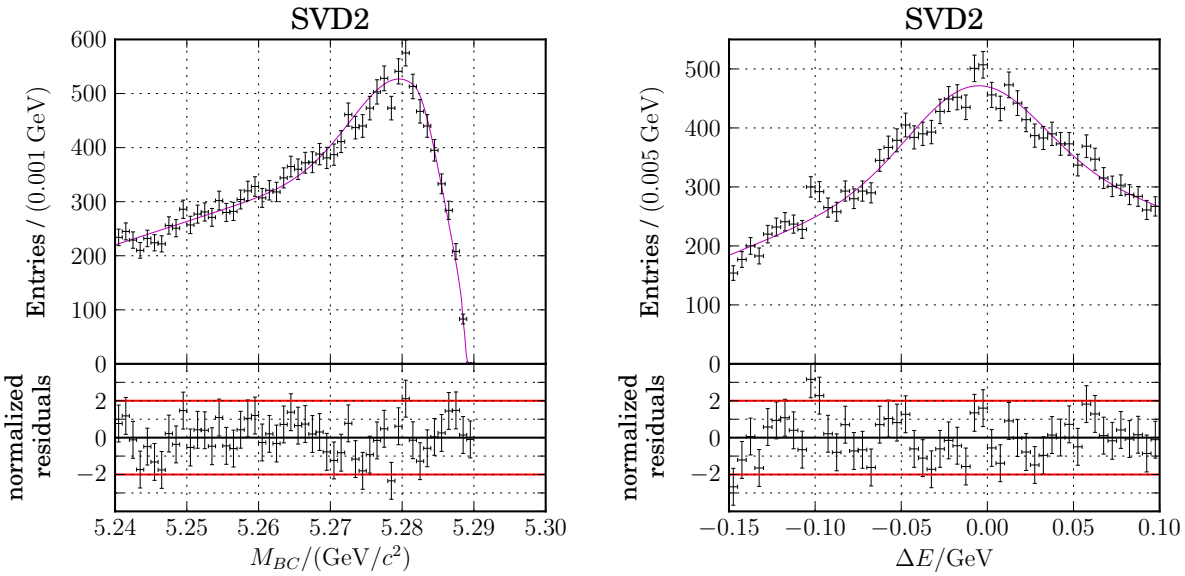

Figure A.4: Projections to M_{bc} and ΔE after fitting the Misreconstructed component to MC. Only SVD2.

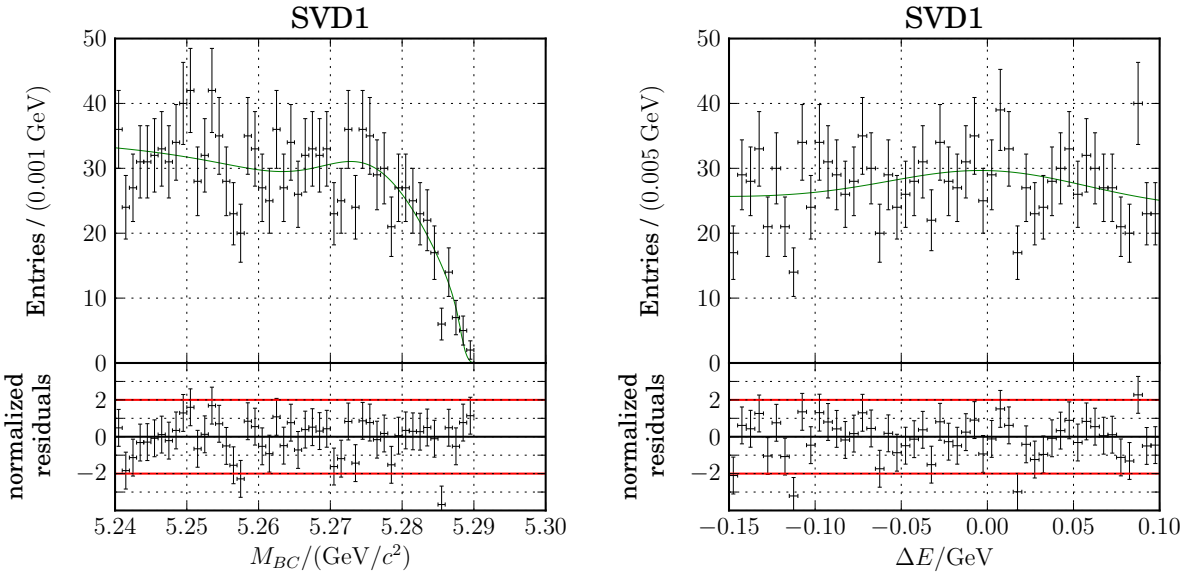

Figure A.5: Projections to M_{bc} and ΔE after fitting the BBbar component to MC. Only SVD1.

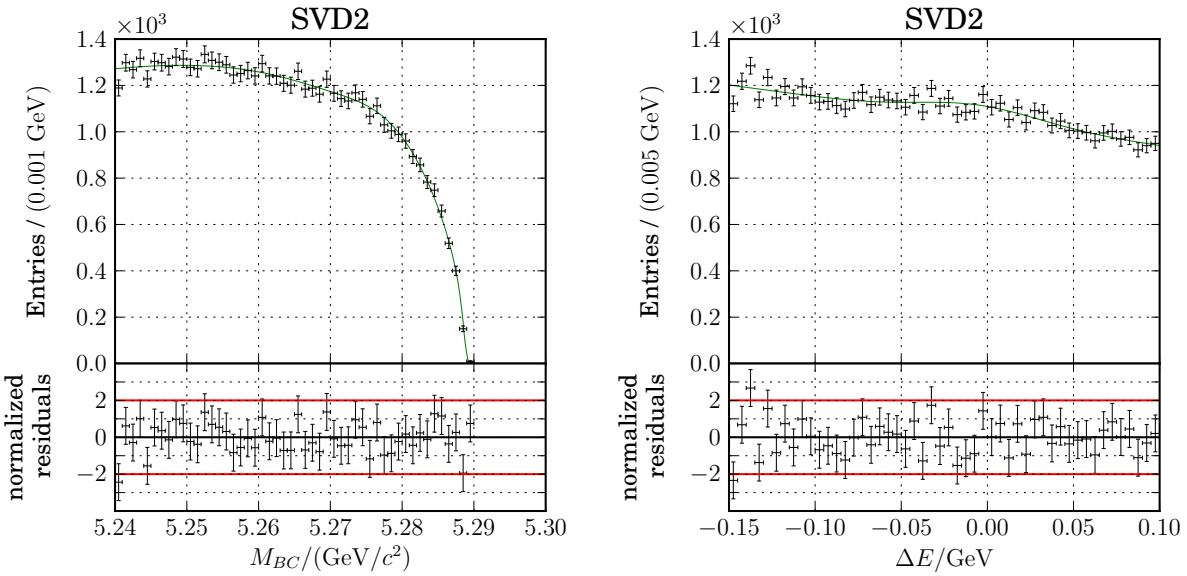

Figure A.6: Projections to M_{bc} and ΔE after fitting the BBbar component to MC. Only SVD2.

A.2 Control Sample

Figures A.7, A.8, A.9 and A.10 show the control sample result of the Signal, Misreconstructed, BBar and Continuum components when fitting the model to MC.

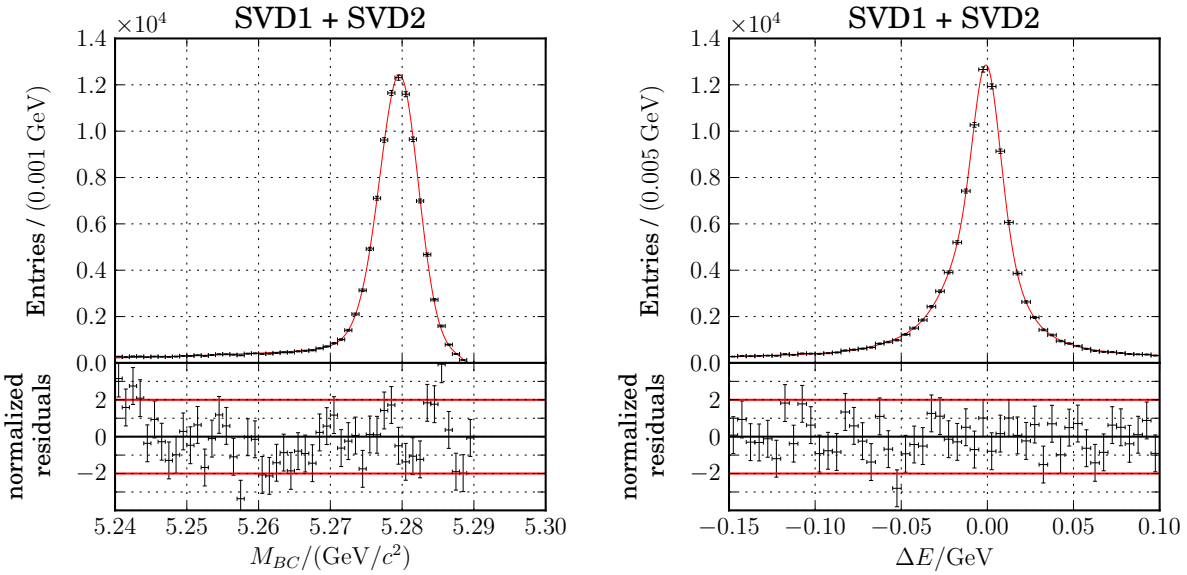

Figure A.7: Control sample: Projections to M_{bc} and ΔE after fitting the Signal component to MC.

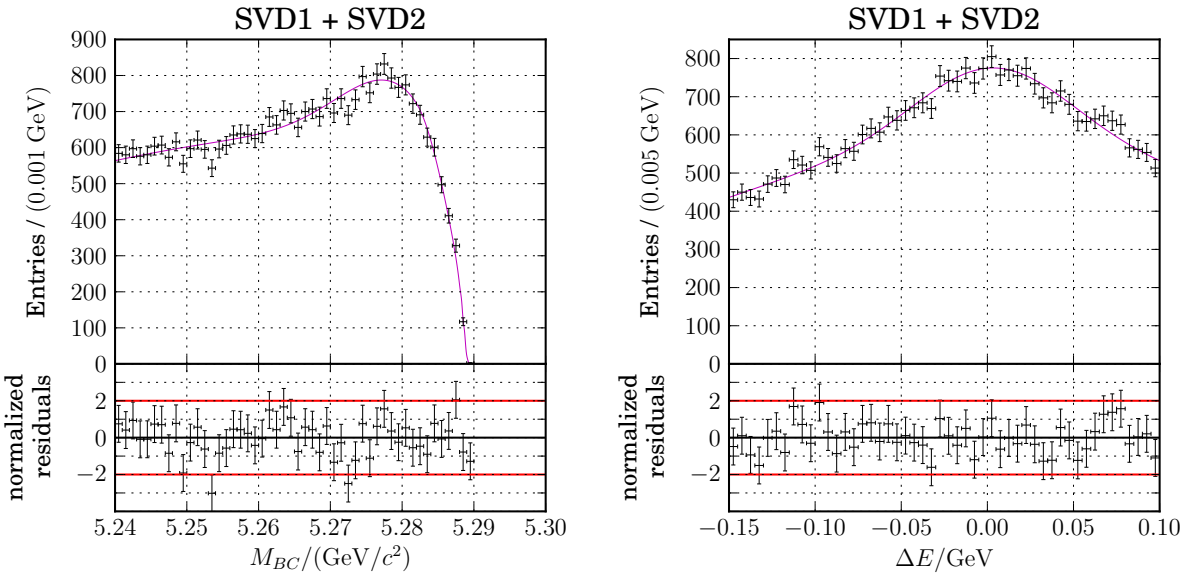

Figure A.8: Control sample: Projections to M_{bc} and ΔE after fitting the Misreconstructed component to MC.

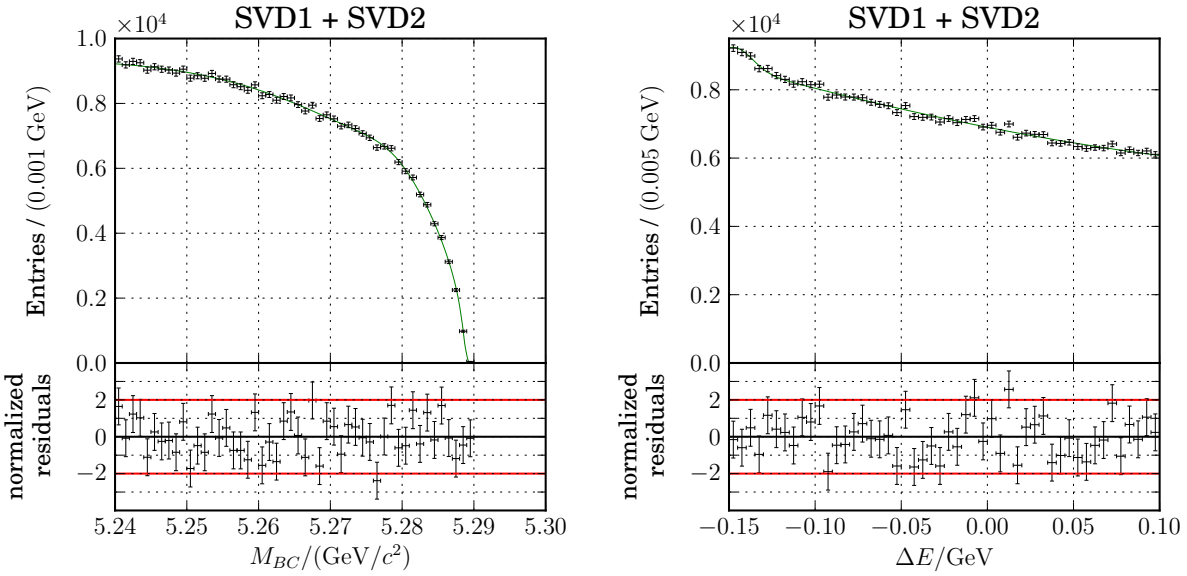

Figure A.9: Control sample: Projections to M_{bc} and ΔE after fitting the BBbar component to MC.

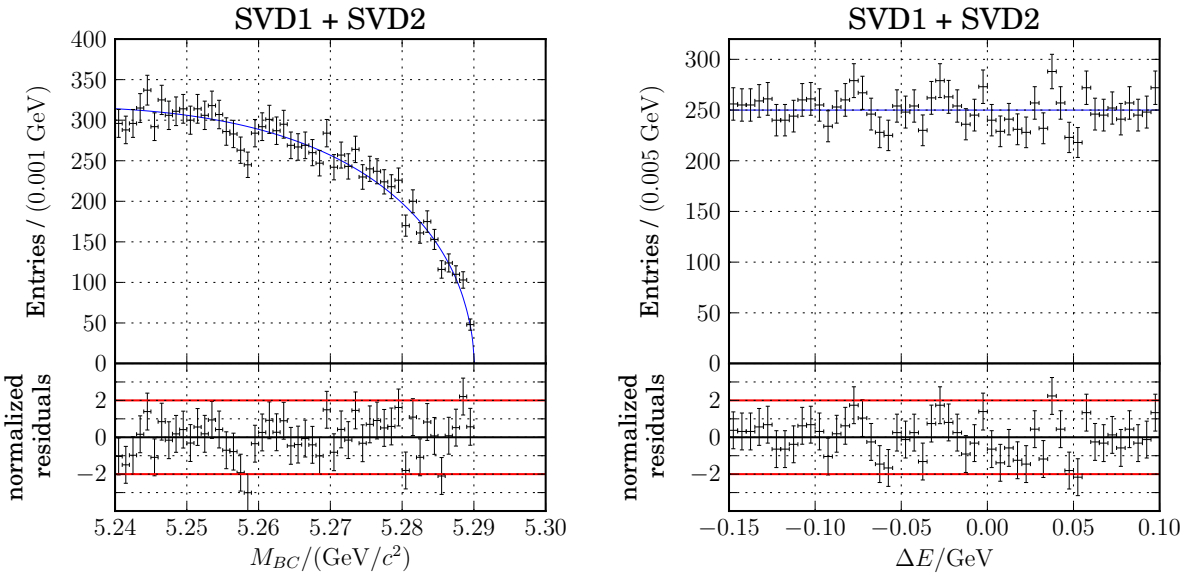

Figure A.10: Control sample: Projections to M_{bc} and ΔE after fitting the Continuum component to MC.

A.3 Final Results in all Dalitz Bins

After modifying the data model to incorporate the Dalitz bin dependency in Section 4.8.2, we performed a simultaneous fit to extract the yield fraction for each Daltiz bin. Figures A.11 to A.17 show the fit projections on M_{bc} and ΔE in each Dalitz bin.

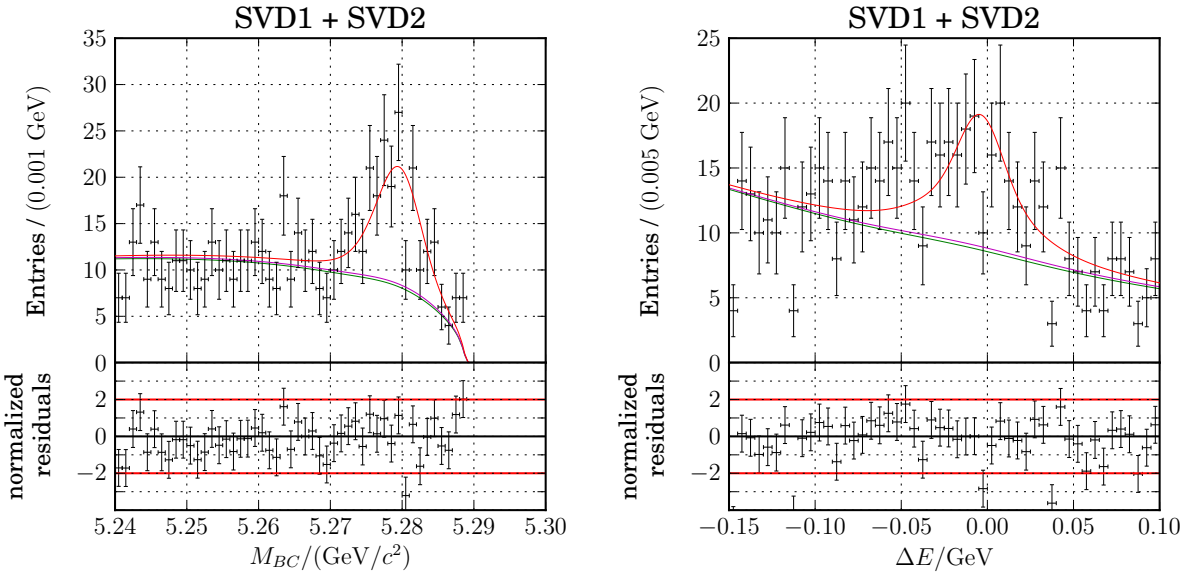

Figure A.11: Projections to M_{bc} and ΔE for the fit to the data in Dalitz bin 0.

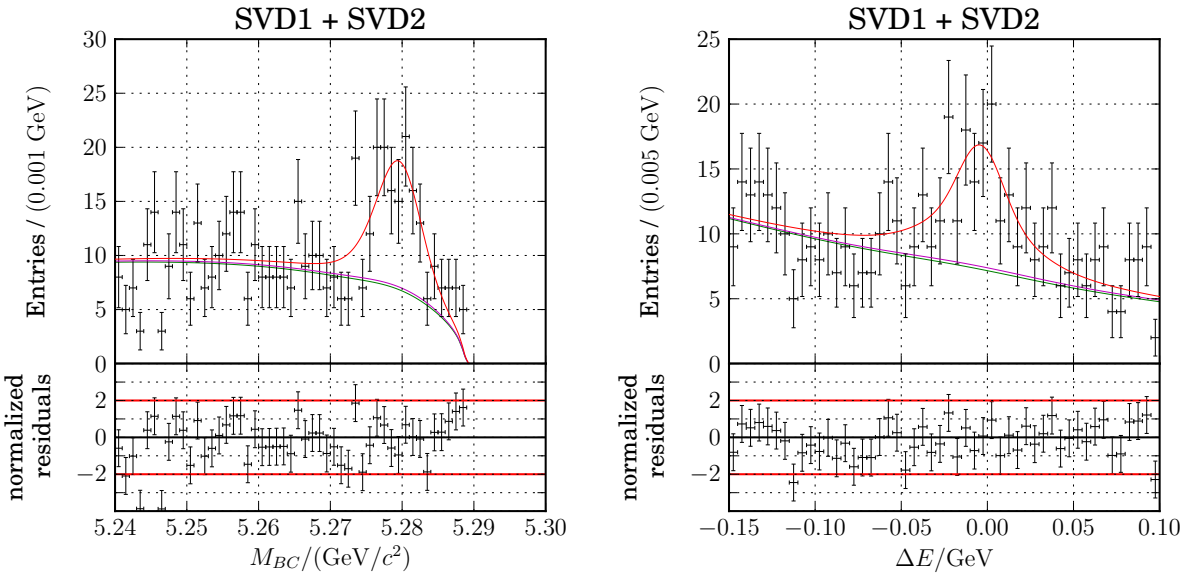

Figure A.12: Projections to M_{bc} and ΔE for the fit to the data in Dalitz bin 1.

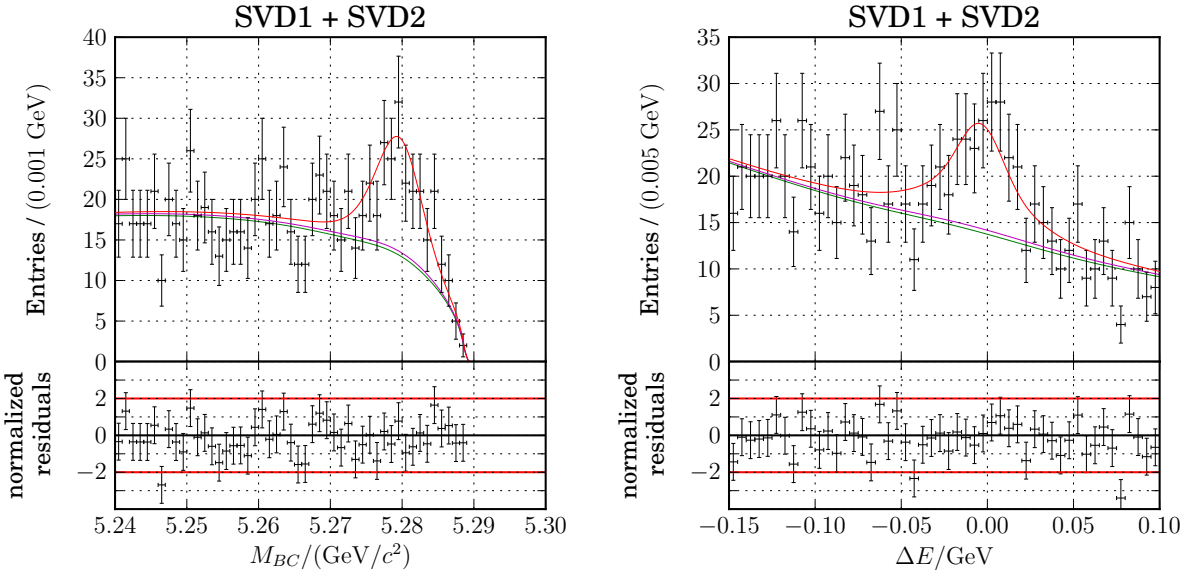

Figure A.13: Projections to M_{bc} and ΔE for the fit to the data in Dalitz bin 2.

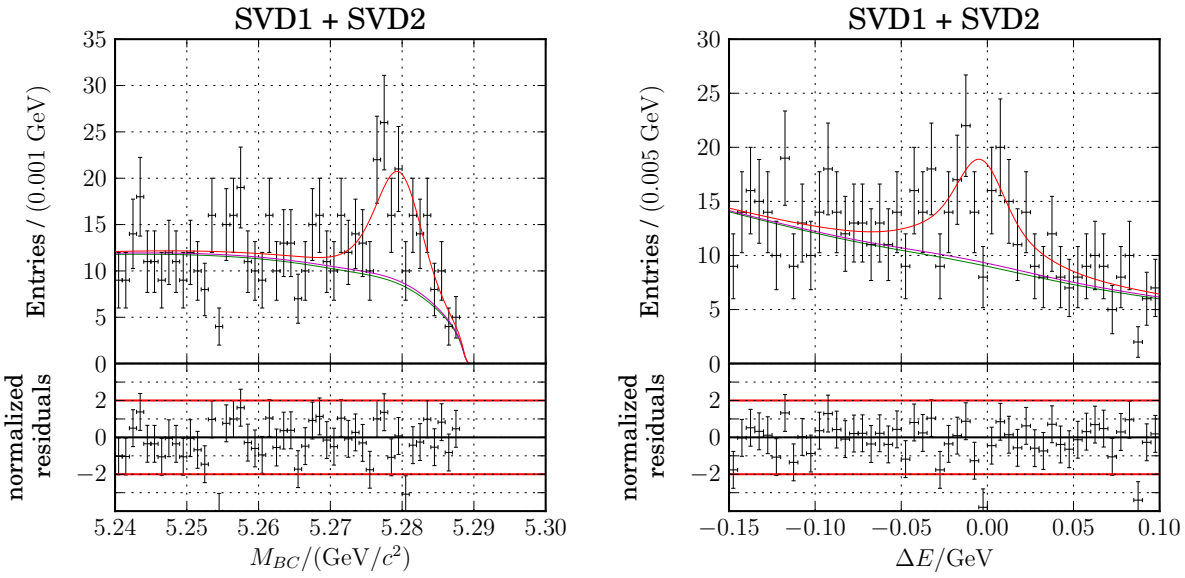

Figure A.14: Projections to M_{bc} and ΔE for the fit to the data in Dalitz bin 3.

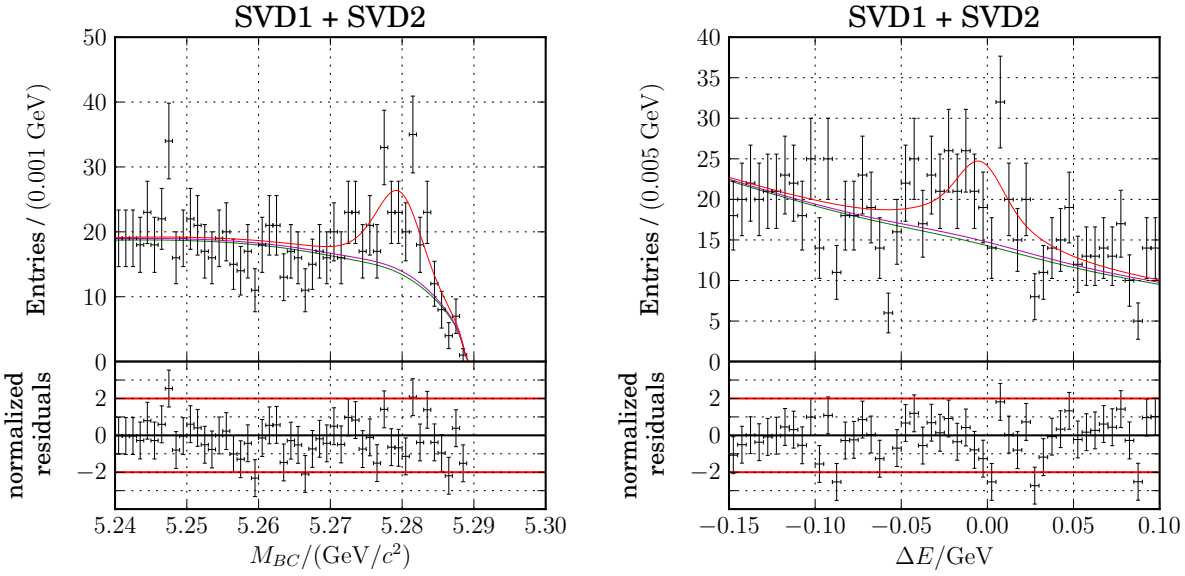

Figure A.15: Projections to M_{bc} and ΔE for the fit to the data in Dalitz bin 4.

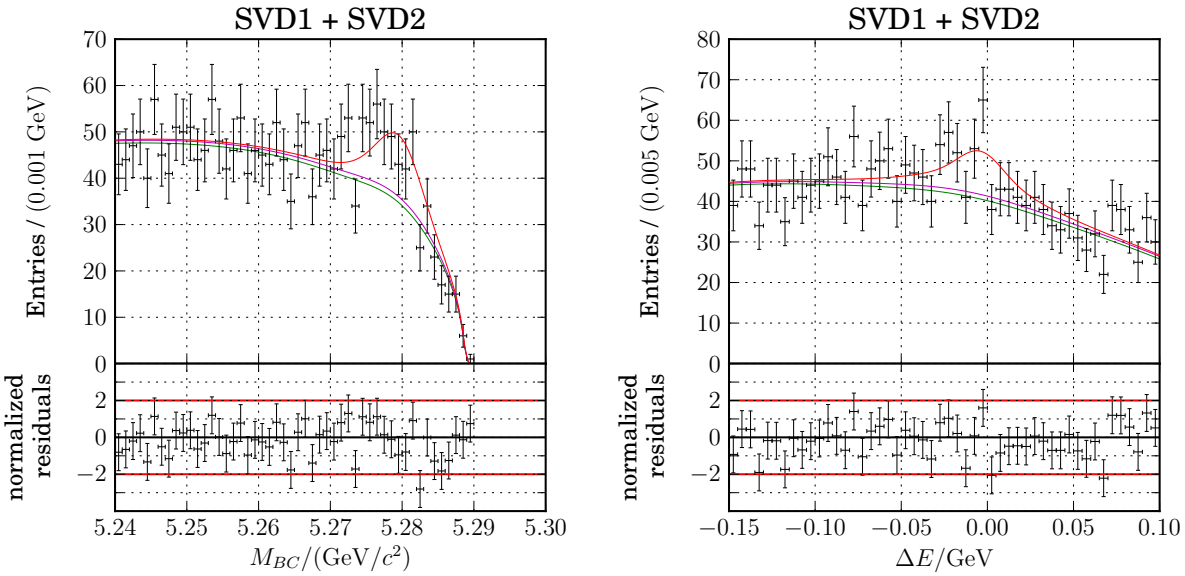

Figure A.16: Projections to M_{bc} and ΔE for the fit to the data in Dalitz bin 5.

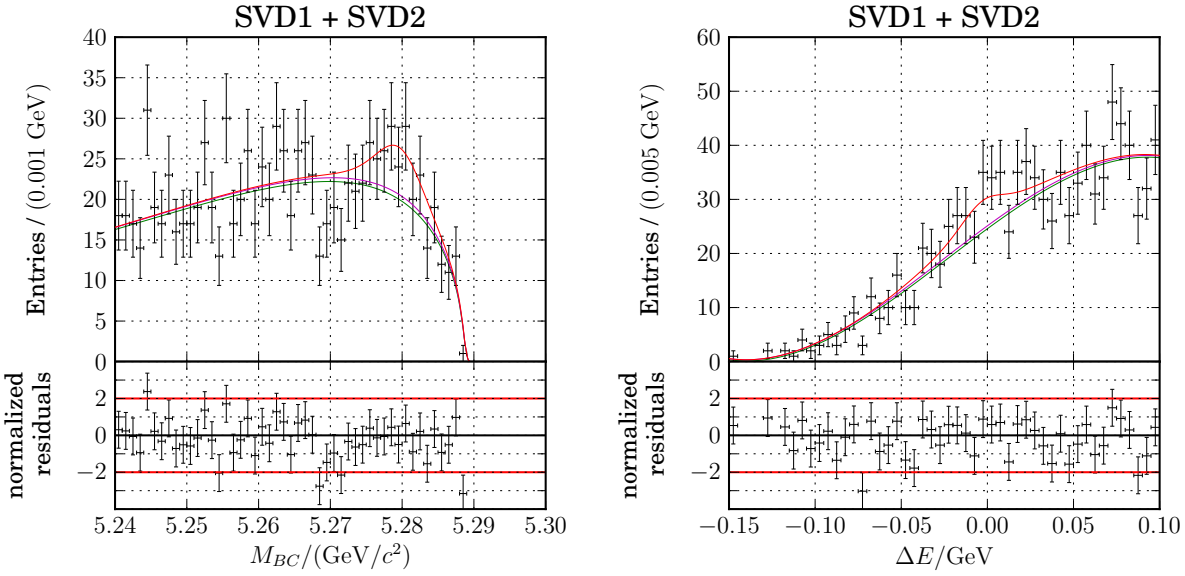

Figure A.17: Projections to M_{bc} and ΔE for the fit to the data in Dalitz bin 6.

Appendix B

Belle II Vertex Detector Simulation

B.1 Material Definition

The creation of new materials in the Belle II Software framework was summarized in Section 6.3.3. All parameters available for the definition of new materials are listed in Table B.1. Each material is constructed of chemical elements or other materials. For each constituent the name and relative fraction have to be specified. Figure B.1 shows example code for the definition of three materials: ethane, the gas mixture used in the CDC and the material used for the quartz bars of the TOP detector.

Parameter	Description
name	Unique name to identify the material
density	Density of the material. If this material is constructed by combining already defined materials it can be omitted. The weighted average of the densities from all components will be used
state	Physical state of the material. Can be one of “gas”, “liquid”, “solid” or “undefined”
temperature	Temperature of the material in Kelvin. If this parameter is omitted a standard temperature of 273.15 K is assumed.
pressure	Pressure in atm. If omitted, 1.0 atm is used.
Components	list of at least one element or material which should be used to construct the new material
Property	additional energy-dependent optical properties like the refractive index. Each property has a name and a list of energy/value pairs.

Table B.1: Parameters defined for the creation of components.

```
<?xml version="1.0" encoding="utf-8"?>
<Materials>
    <Material name="Ethane">
        <state>Gas</state>
        <density unit="g/cm3">1.356e-3</density>
        <temperature>273</temperature>
        <pressure>1.0</pressure>
        <Components>
            <Element fraction="0.7989">C</Element>
            <Element fraction="0.2011">H</Element>
        </Components>
    </Material>
    <Material name="CDCGas">
        <state>Gas</state>
        <density unit="g/cm3">7.67e-4</density>
        <Components>
            <Element fraction="0.500">He</Element>
            <Material fraction="0.500">Ethane</Material>
        </Components>
    </Material>
    <Material name="TOPSiO2">
        <state>Solid</state>
        <density unit="g/cm3">2.62</density>
        <Components>
            <Element fraction="0.5326">O</Element>
            <Element fraction="0.4674">Si</Element>
        </Components>
        <Property name="RINDEX" unit="eV">
            <value energy="1.39999998">1.45196021</value>
            <value energy="1.40999997">1.45205235</value>
            <value energy="1.41999996">1.45214438</value>
            <!-- additonal entries omitted for readability -->
            <value energy="3.97999763">1.48473752</value>
            <value energy="3.98999763">1.48493171</value>
            <value energy="3.99999762">1.48512673</value>
        </Property>
    </Material>
</Material>
```

Figure B.1: Example XML code for a material definition.

B.2 Component Definition

To provide an example for the component definition presented in Section 6.4.2 we show the XML code defining the Kapton flexes on the underside of the SVD Orgiami sensors in Figure B.2. Notice that the material for material was omitted the "OrigamiPitchAdapter" component. This means that the default material for the SVD, cold air, will be used. Also shown is the possibility to define the components directly as sub-components inside of another component. In this case all parameters shown in Tables 6.2 and 6.3 can be used instead of the "type" parameter.

```
<?xml version="1.0" encoding="utf-8"?>
<!-- Origami flexes on bottom of sensors. The real shape is
     more complicated but we approximate it by using
     rectangular shapes -->
<Component name="OrigamiPitchAdapter">
    <width  unit="mm">54.891</width>
    <length unit="mm">116.154</length>
    <Component name="LongOrigamiPitchAdapter">
        <Material>SVD-KaptonPitchAdapter</Material>
        <u      unit="mm">  0.000</u>
        <v      unit="mm">-48.890</v>
        <width  unit="mm"> 54.891</width>
        <length unit="mm"> 18.374</length>
        <height unit="mm">  0.100</height>
    </Component>
    <Component name="ShortOrigamiPitchAdapter">
        <Material>SVD-KaptonPitchAdapter</Material>
        <u      unit="mm">-13.800</u>
        <v      unit="mm"> 49.477</v>
        <width  unit="mm"> 27.291</width>
        <length unit="mm"> 17.200</length>
        <height unit="mm">  0.100</height>
    </Component>
</Component>
```

Figure B.2: Definition for the Kapton flexes on the underside of SVD Origami sensor.

B.3 PXD Endflange

The simplified shape for the PXD endflange (see Section 6.5.2) is created from a rotational symmetric shape around the z axis. In Figure B.3 we define an inner and outer radius at various z positions. These points are combined to form an outline. If we rotate this outline around the z axis between a given start and end angle ϕ we obtain the base volume of the PXD endflange. To make room for the PXD ladders we have to cut away rectangular

shapes by intersecting the base volume with appropriately sized box volumes. The width, height, radius and ϕ position of these boxes are defined in B.4. The length is calculated automatically to extend along the full endflange.

```
<?xml version="1.0" encoding="UTF-8"?>
<Endflange name="backward">
    <Material>PXD-Support</Material>
    <minPhi unit="deg">-7.125</minPhi>
    <maxPhi unit="deg">168.049</maxPhi>
    <Plane>
        <posZ unit="mm">-66.580</posZ>
        <innerRadius unit="mm"> 21.080</innerRadius>
        <outerRadius unit="mm"> 21.080</outerRadius>
    </Plane>
    <Plane>
        <posZ unit="mm">-60.520</posZ>
        <innerRadius unit="mm"> 14.940</innerRadius>
        <outerRadius unit="mm"> 21.080</outerRadius>
    </Plane>
    <Plane>
        <posZ unit="mm">-38.933</posZ>
        <innerRadius unit="mm"> 14.940</innerRadius>
        <outerRadius unit="mm"> 21.080</outerRadius>
    </Plane>
    <Plane>
        <posZ unit="mm">-31.000</posZ>
        <innerRadius unit="mm"> 14.940</innerRadius>
        <outerRadius unit="mm"> 16.420</outerRadius>
    </Plane>
</Endflange>
```

Figure B.3: Definition of the base shape for the PXD backward endflange.

B.4 SVD Cooling Pipes

To emphasize the simplicity of the change of the SVD cooling pipes (see Section 6.6.3) the parameters for the SVD cooling pipes are shown in Figure B.5. The geometry code just requires the number of pipes, the radius, the start angle and angle between neighboring pipes and the z position of the start for the forward and backward winding. The winding itself will be calculated automatically.

```
<?xml version="1.0" encoding="UTF-8"?>
<Cutout>
    <count>5</count>
    <width unit="mm">17.073</width>
    <height unit="mm">2.520</height>
    <rphi unit="mm"> 13.680</rphi>
    <shift unit="mm">-3.084</shift>
    <startPhi unit="deg">-135.000</startPhi>
    <deltaPhi unit="deg">45.000</deltaPhi>
</Cutout>
```

Figure B.4: Definition of the boxes intersecting with the base shape for the PXD endflange.

```
<?xml version="1.0" encoding="utf-8"?>
<CoolingPipes>
    <Material>StainlessSteel</Material>
    <outerDiameter unit="mm">1.500</outerDiameter>
    <wallThickness unit="mm">0.050</wallThickness>
    <Layer id="4">
        <!-- number of pipes for this layer/halfshell -->
        <nPipes>5</nPipes>
        <!-- phi angle of the center of the first pipe -->
        <startPhi unit="deg">-71.118</startPhi>
        <!-- phi angle between two pipes -->
        <deltaPhi unit="deg"> 36.000</deltaPhi>
        <!-- distance between IP and center of the pipes -->
        <radius   unit="mm">  87.000</radius>
        <!-- beginning of pipe in z -->
        <zstart   unit="mm">-155.100</zstart>
        <!-- end of pipe in z -->
        <zend     unit="mm">  96.880</zend>
    </Layer>
    <!-- the definitions for layers 5 and 6 have been omitted for
         readability -->
</CoolingPipes>
```

Figure B.5: Cooling pipe parameters defined for the SVD.

List of Figures

List of Tables

Bibliography

[1] A. Sakharov. "Violation of CP Invariance, C Asymmetry, and Baryon Asymmetry of the Universe". *JETP Lett* 5 (1967), p. 24. URL: http://www.jetpletters.ac.ru/ps/1643/article_25089.pdf.

[2] G. W. Bennett et al. "Measurement of the Negative Muon Anomalous Magnetic Moment to 0.7 ppm". *Phys. Rev. Lett.* 92.16 (Apr. 2004), p. 161802. DOI: 10.1103/PhysRevLett.92.161802.

[3] C. Amsler et al. "Review of Particle Physics". *Physics Letters B* 667.1-5 (2008). Review of Particle Physics, pp. 1–6. ISSN: 0370-2693. DOI: 10.1016/j.physletb.2008.07.018.

[4] E. Komatsu et al. "Five-Year Wilkinson Microwave Anisotropy Probe (WMAP) Observations: Cosmological Interpretation". *Astrophys. J.* 180 (Feb. 2009), pp. 330–376. DOI: 10.1088/0067-0049/180/2/330. arXiv: 0803.0547.

[5] P. Ade et al. "Planck 2013 results. I. Overview of products and scientific results" (2013). arXiv: 1303.5062 [astro-ph.CO].

[6] J. H. Christenson et al. "Evidence for the 2π Decay of the $K2$ Meson". *Phys. Rev. Lett.* 13.4 (July 1964), pp. 138–140. DOI: 10.1103/PhysRevLett.13.138.

[7] M. Kobayashi and T. Maskawa. "CP-Violation in the Renormalizable Theory of Weak Interaction". *Prog. Theor. Phys.* 49.2 (1973), pp. 652–657. DOI: 10.1143/PTP.49.652.

[8] A. B. Carter and A. I. Sanda. "CP Nonconservation in Cascade Decays of B Mesons". *Phys. Rev. Lett.* 45 (12 Sept. 1980), pp. 952–954. DOI: 10.1103/PhysRevLett.45.952.

[9] A. B. Carter and A. I. Sanda. "CP violation in B-meson decays". *Phys. Rev. D* 23 (7 Apr. 1981), pp. 1567–1579. DOI: 10.1103/PhysRevD.23.1567.

[10] I. Bigi and A. Sanada. "Notes on the observability of CP violations in B decays". *Nucl. Phys. B* 193.1 (1981), pp. 85–108. ISSN: 0550-3213. DOI: 10.1016/0550-3213(81)90519-8.

[11] B. Aubert et al. "The BABAR detector". *Nucl. Instrum. Methods Phys. Res. Sect. A* 479.1 (2002), pp. 1–116. ISSN: 0168-9002. DOI: 10.1016/S0168-9002(01)02012-5.

[12] A. Abashian et al. "The Belle detector". *Nucl. Instrum. Methods Phys. Res. Sect. A* 479.1 (2002), pp. 117–232. ISSN: 0168-9002. DOI: 10.1016/S0168-9002(01)02013-7.

[13] K. Abe et al. "Observation of large CP violation in the neutral B meson system". *Phys. Rev. Lett.* 87 (2001), p. 091802. DOI: 10.1103/PhysRevLett.87.091802.

[14] B. Aubert et al. "Observation of CP Violation in the B Meson System". *Phys. Rev. Lett.* 87.9 (Aug. 2001), p. 091801. DOI: 10.1103/PhysRevLett.87.091801.

[15] C. S. Fong, E. Nardi, and A. Riotto. "Leptogenesis in the Universe". *ArXiv e-prints* (Jan. 2013). arXiv: 1301.3062 [hep-ph].

[16] T. E. Browder et al. "New Physics at a Super Flavor Factory" (2008). arXiv: 0802.3201 [hep-ph].

[17] T. Abe et al. "Belle II Technical Design Report". *ArXiv e-prints* (Nov. 2010). arXiv: 1011.0352 [physics.ins-det].

[18] E. Noether. "Invariante Variationsprobleme". *Nachr. d. König. Gesellsch. d. Wiss. zu Göttingen* (1918), pp. 235–257.

[19] T. D. Lee and C. N. Yang. "Question of parity conservation in weak interactions". *Phys. Rev.* 104 (1956), pp. 254–258.

[20] C. S. Wu et al. "Experimental test of parity conservation in beta decay". *Phys. Rev.* 105 (1957), pp. 1413–1415.

[21] L. Landau. "On the conservation laws for weak interactions". *Nucl. Phys.* 3 (1957), pp. 127–131.

[22] G. Lüders. "Proof of the TCP theorem". *Ann. Phys.* 2 (1957), p. 1.

[23] N. Cabibbo. "Unitary Symmetry and Leptonic Decays". *Phys. Rev. Lett.* 10.12 (June 1963), pp. 531–533. DOI: 10.1103/PhysRevLett.10.531.

[24] Wikipedia. *Quark — Wikipedia, The Free Encyclopedia*. [Online; accessed 2009-09-24]. 2009. URL: http://en.wikipedia.org/w/index.php?title=Quark&oldid=315864017.

[25] I. Bigi and A. Sanda. *Cp Violation*. Cambridge: Cambridge University Press, 2009. ISBN: 9780521847940.

[26] G. Branco, L. Lavoura, and J. Silva. *Cp Violation*. Vol. 103. International series of monographs on physics. Oxford: Clarendon Press, 1999. ISBN: 9780198503996.

[27] L. Wolfenstein. "Parametrization of the Kobayashi-Maskawa Matrix". *Phys. Rev. Lett.* 51.21 (Nov. 1983), pp. 1945–1947. DOI: 10.1103/PhysRevLett.51.1945.

[28] C. Jarlskog. "Commutator of the Quark Mass Matrices in the Standard Electroweak Model and a Measure of Maximal CP Nonconservation". *Phys. Rev. Lett.* 55.10 (Aug. 1985), pp. 1039–1042. DOI: 10.1103/PhysRevLett.55.1039.

[29] J. Charles et al. "CP violation and the CKM matrix: Assessing the impact of the asymmetric B factories". *Eur.Phys.J.* C41 (2005). Updated results and plots available at: http://ckmfitter.in2p3.fr, pp. 1–131. DOI: 10.1140/epjc/s2005-02169-1. arXiv: hep-ph/0406184 [hep-ph].

[30] T. Browder et al. "On the Physics Case of a Super Flavour Factory". *JHEP* 02 (2008), p. 110. DOI: 10.1088/1126-6708/2008/02/110. arXiv: 0710.3799 [hep-ph].

[31] A. J. Buras. "Flavor dynamics: CP violation and rare decays" (2001). arXiv: hep-ph/0101336.

[32] T. E. Browder and K. Honscheid. "B mesons". *Progress in Particle and Nuclear Physics* 35 (1995), pp. 81–219. ISSN: 0146-6410. DOI: 10.1016/0146-6410(95)00042-H.

[33] K.-F. Chen et al. "Observation of time-dependent CP violation in B0 –> eta' K0 decays and improved measurements of CP asymmetries in B0 –> Phi K0, K0(S) K0(S) K0(S) and B0 –> J/psi K0 decays". *Phys. Rev. Lett.* 98 (2007), p. 031802. DOI: 10.1103/PhysRevLett.98.031802. arXiv: hep-ex/0608039.

[34] T. E. Browder et al. "Measuring β in $B \to D^{(*)+}D^{(*)-}K_s$ decays". *Phys. Rev. D* 61 (5 Feb. 2000), p. 054009. DOI: 10.1103/PhysRevD.61.054009.

[35] B. Aubert et al. "Measurement of the Branching Fraction and Time-Dependent CP Asymmetry in the Decay $B^0 \to D^{*+}D^{*-}K_s^0$". *Phys.Rev.* D74 (2006), p. 091101. DOI: 10.1103/PhysRevD.74.091101. arXiv: hep-ex/0608016 [hep-ex].

[36] P. del Amo Sanchez et al. "Measurement of the $B \to \overline{D}^{(*)}D^{(*)}K$ branching fractions". *Phys.Rev.* D83 (2011), p. 032004. DOI: 10.1103/PhysRevD.83.032004. arXiv: 1011.3929 [hep-ex].

[37] J. Dalseno et al. "Measurement of branching fraction and time-dependent CP asymmetry parameters in $B^0 \to D^{*+}D^{*-}K_S^0$ decays". *Phys. Rev. D* 76 (7 Oct. 2007), p. 072004. DOI: 10.1103/PhysRevD.76.072004.

[38] *Using Crab Cavities, KEKB Breaks Luminosity World Record*. URL: http://www.kek.jp/intra-e/press/2009/KEKBluminosity2.html.

[39] T. Abe et al. "Achievements of KEKB". *Prog. Theor. Exp. Phys.* 2013.3 (2013). 03A001 (2013) and following articles up to 03A011. DOI: 10.1093/ptep/pts102.

[40] S. Kurokawa and E. Kikutani. "Overview of the KEKB accelerators". *Nucl. Instrum. Methods Phys. Res. Sect. A* 499.1 (2003). And other papers included in this Volume. ISSN: 0168-9002. DOI: 10.1016/S0168-9002(02)01771-0.

[41] J. Brodzicka et al. "Physics achievements from the Belle experiment". *Prog. Theor. Exp. Phys.* 2012.1 (2012). DOI: 10.1093/ptep/pts072.

[42] K. Abe et al. *Letter of Intent for KEK Super B Factory. Part II: Detector*. Tech. rep. KEK Report 04-4, 2004. URL: http://superb.kek.jp/documents/loi/img/LoI_detector.pdf.

[43] B. Casey. "HadronB". *BELLE Note* 390 (2001). Accessible only by Belle members. URL: http://belle.kek.jp/secured/belle_note/gn390/bn390_012901.ps.gz.

[44] D. J. Lange. "The EvtGen particle decay simulation package". *Nucl. Instrum. Methods Phys. Res. Sect. A* 462.1-2 (2001), pp. 152–155. ISSN: 0168-9002. DOI: 10.1016/S0168-9002(01)00089-4.

[45] R. Brun et al. "GEANT3". *CERN-DD-EE-84-1* (1987).

[46] J. Beringer et al. "Review of Particle Physics". *Phys. Rev. D* 86 (1 July 2012), p. 010001. DOI: 10.1103/PhysRevD.86.010001.

[47] F. Fang. "Study of $Ks \to \pi^+\pi^-$ selection". *BELLE Note* 323 (2000). Accessible only by Belle members. URL: http://belle.kek.jp/secured/belle_note/gn323/note323.ps.gz.

[48] H. Tajima et al. "Proper-time resolution function for measurement of time evolution of B mesons at the KEK B-Factory". *Nucl. Instrum. Methods Phys. Res. Sect. A* 533.3 (2004), pp. 370–386. ISSN: 0168-9002. DOI: 10.1016/j.nima.2004.07.199.

[49] H. Kakuno et al. "Neutral flavor tagging for the measurement of mixing-induced violation at Belle". *Nucl. Instrum. Methods Phys. Res. Sect. A* 533.3 (2004), pp. 516–531. ISSN: 0168-9002. DOI: 10.1016/j.nima.2004.06.159.

[50] T. Higuchi. *Time-Dependent CP Violation*. Belle Analysis School. Accessible only by Belle members. 2012. URL: http://kds.kek.jp/getFile.py/access?contribId=8&resId=1&materialId=slides&confId=9641.

[51] T. Higuchi. *Resolution Function Study*. Belle Analysis Meeting. Accessible only by Belle members. 2010. URL: http://kds.kek.jp/getFile.py/access?contribId=63&resId=0&materialId=slides&confId=4932.

[52] S. Nishida. "Study of Kaon and Pion Identification Using Inclusive D^* Sample". *BELLE Note* 779 (2005). Accessible only by Belle members. URL: http://belle.kek.jp/secured/belle_note/gn779/bn779.ps.gz.

[53] B. Bhuyan. "High P_T Tracking Efficiency Using Partially Reconstructed D^* Decays". *BELLE Note* 1165 (2011). Accessible only by Belle members. URL: http://belle.kek.jp/secured/belle_note/gn1165/BN1165_v1.pdf.

[54] W. Dungel. "Systematic investigation of the reconstruction efficiency of low momentum $\pi^\pm$ and π^0". *BELLE Note* 1176 (2011). Accessible only by Belle members. URL: http://belle.kek.jp/secured/belle_note/gn1176/bn1176.pdf.

[55] P. C. S.W. Lin and H.C.Huang. "Update of π^0 Systematics Using Inclusive η (78/fb)". *BELLE Note* 645 (2003). Accessible only by Belle members. URL: http://belle.kek.jp/secured/belle_note/gn645/pi0-syst.ps.gz.

[56] E. White. "Determination of K_S Efficiency and Systematic Uncertainty". *BELLE Note* 1207 (2011). Accessible only by Belle members. URL: http://belle.kek.jp/secured/belle_note/gn1207/bn1207_v2.ps.

[57] F. James and M. Roos. "Minuit: A System for Function Minimization and Analysis of the Parameter Errors and Correlations". *Comput.Phys.Commun.* 10 (1975), pp. 343–367. DOI: 10.1016/0010-4655(75)90039-9.

[58] H. Albrecht et al. "Exclusive hadronic decays of B mesons". *Z. Phys. C* 48.4 (1990), pp. 543–551. ISSN: 0170-9739. DOI: 10.1007/BF01614687.

[59] *NIST Digital Library of Mathematical Functions*. http://dlmf.nist.gov/, Release 1.0.6 of 2013-05-06. Online companion to [89]. URL: http://dlmf.nist.gov/18.

[60] P. Dierckx. "An Algorithm for Surface-Fitting with Spline Functions". *IMA Journal of Numerical Analysis* 1.3 (1981), pp. 267–283. DOI: 10.1093/imanum/1.3.267.

[61] E. Jones, T. Oliphant, P. Peterson, et al. *SciPy: Open source scientific tools for Python*. 2001–. URL: http://www.scipy.org/.

[62] M. Pivk and F. L. Diberder. "sPlot: A statistical tool to unfold data distributions". *Nucl. Instrum. Methods Phys. Res. Sect. A* 555.1–2 (2005), pp. 356–369. ISSN: 0168-9002. DOI: http://dx.doi.org/10.1016/j.nima.2005.08.106.

[63] I. Adachi et al. "Precise measurement of the CP violation parameter $\sin 2\phi_1$ in $B^0 \to (c\bar{c})K^0$ decays". *Phys.Rev.Lett.* 108 (2012), p. 171802. DOI: 10.1103/PhysRevLett.108.171802. arXiv: 1201.4643 [hep-ex].

[64] O. Long et al. "Impact of tag-side interference on time-dependent CP asymmetry measurements using coherent B^0B^0 pairs". *Phys. Rev.* D68 (2003), p. 034010. DOI: 10.1103/PhysRevD.68.034010. arXiv: hep-ex/0303030 [hep-ex].

[65] S. Hashimoto et al. *Letter of Intent for KEK Super B Factory. Part I: Physics*. Tech. rep. KEK Report 04-4, 2004. URL: http://superb.kek.jp/documents/loi/img/LoI_physics.pdf.

[66] T. Aushev et al. "Physics at Super B Factory". *ArXiv e-prints* (Feb. 2010). arXiv: 1002.5012 [hep-ex].

[67] J. W. Flanagan and other. *Letter of Intent for KEK Super B Factory. Part III: Accelerator Design*. Tech. rep. KEK Report 04-4, 2004. URL: http://superb.kek.jp/documents/loi/img/LoI_accelerator.pdf.

[68] S. Agostinelli et al. "GEANT4: A Simulation toolkit". *Nucl.Instrum.Meth.* A506 (2003), pp. 250–303. DOI: 10.1016/S0168-9002(03)01368-8.

[69] P. Raimondi. *Status on SuperB effort*. talk given at the 2nd SuperB workshop, Frascati, 2006. URL: http://www.lnf.infn.it/conference/superb06/talks/raimondi1.ppt.

[70] SuperB Collaboration et al. "SuperB Technical Design Report". *ArXiv e-prints* (June 2013). arXiv: 1306.5655 [physics.ins-det].

[71] C. Bernardini et al. "Lifetime and Beam Size in a Storage Ring". *Phys. Rev. Lett.* 10 (9 May 1963), pp. 407–409. DOI: 10.1103/PhysRevLett.10.407.

[72] J. Kemmer and G. Lutz. "New detector concepts". *Nucl. Instrum. Methods Phys. Res. Sect. A* 253.3 (1987), pp. 365–377. ISSN: 0168-9002. DOI: 10.1016/0168-9002(87)90518-3.

[73] R. Richter et al. "Design and technology of DEPFET pixel sensors for linear collider applications". *Nucl. Instrum. Methods Phys. Res. Sect. A* 511.1–2 (2003), pp. 250–256. ISSN: 0168-9002. DOI: 10.1016/S0168-9002(03)01802-3.

[74] The DEPFET Collaboration. "The PXD Whitebook". unpublished. 2012. URL: http://twiki.hll.mpg.de/twiki/bin/viewfile/DepfetInternal/WhiteBookStructure?rev=1;filename=PXDwb20130712.pdf.

[75] A. Moll. "The Software Framework of the Belle II Experiment". *Journal of Physics: Conference Series* 331.3 (2011), p. 032024. DOI: 10.1088/1742-6596/331/3/032024.

[76] ISO. *ISO/IEC 14882:2011 Information technology — Programming languages — C++*. Geneva, Switzerland: International Organization for Standardization, Feb. 28, 2012, 1338 (est.) URL: http://www.iso.org/iso/iso_catalogue/catalogue_tc/catalogue_detail.htm?csnumber=50372.

[77] S. DeRose and J. Clark. *XML Path Language (XPath) Version 1.0*. W3C Recommendation. W3C, Nov. 1999. URL: http://www.w3.org/TR/1999/REC-xpath-19991116.

[78] T. Bray et al. *Extensible Markup Language (XML) 1.0 (Fifth Edition)*. W3C Recommendation. W3C, Nov. 2008. URL: http://www.w3.org/TR/2008/REC-xml-20081126/.

[79] J. Marsh, D. Veillard, and D. Orchard. *XML Inclusions (XInclude) Version 1.0 (Second Edition)*. W3C Recommendation. W3C, Nov. 2006. URL: http://www.w3.org/TR/2006/REC-xinclude-20061115/.

[80] Wikipedia. *Constructive solid geometry — Wikipedia, The Free Encyclopedia*. [Online; accessed 20-November-2013]. 2013. URL: http://en.wikipedia.org/w/index.php?title=Constructive_solid_geometry&oldid=581321406.

[81] J. S. Coursey et al. *Atomic Weights and Isotopic Compositions*. Ed. by NIST. 2010. URL: http://www.nist.gov/pml/data/comp.cfm.

[82] C. M. Poole et al. "A CAD Interface for GEANT4". *Australasian Physical & Engineering Science in Medicine* (2012). DOI: 10.1007/s13246-012-0159-8. URL: http://www.springerlink.com/content/u563877422284578.

[83] V. Blobel. "Software alignment for tracking detectors". *Nucl. Instrum. Methods Phys. Res. Sect. A* 566.1 (2006). TIME 2005 - Proceedings of the 1st Workshop on Tracking in High Multiplicity Environments, pp. 5–13. ISSN: 0168-9002. DOI: 10.1016/j.nima.2006.05.157.

[84] T. Lampén. "General alignment concept of the CMS". *Nucl. Instrum. Methods Phys. Res. Sect. A* 566.1 (2006). TIME 2005 - Proceedings of the 1st Workshop on Tracking in High Multiplicity Environments, pp. 100–103. ISSN: 0168-9002. DOI: 10.1016/j.nima.2006.05.030.

[85] V. Re et al. "Performance of the BABAR silicon vertex tracker". *Nucl. Instrum. Methods Phys. Res. Sect. A* 501.1 (2003). Proceedings of the 10th International Workshop on Vertex Detectors, pp. 14–21. ISSN: 0168-9002. DOI: 10.1016/S0168-9002(02)02005-3.

[86] V. Karimaki et al. "Sensor Alignment by Tracks" (2007). arXiv: physics/0306034v2.

[87] H. Ishino, A. Kibayashi, and T. K. Takahashi. "Alignment Method for the SVD2 and Its Performance". *BELLE Note* 715 (2005). Accessible only by Belle members. URL: http://belle.kek.jp/secured/belle_note/gn715/svd2_alignment.ps.gz.

[88] G. Flucke et al. "CMS silicon tracker alignment strategy with the Millepede II algorithm". *J. Instrum.* 3.09 (2008), P09002. DOI: 10.1088/1748-0221/3/09/P09002.

[89] F. W. Olver et al., eds. *NIST Handbook of Mathematical Functions*. Print companion to [59]. New York, NY: Cambridge University Press, 2010.